Mixed Mode Failure Analysis of Adhesively Bonded Composite Systems Using the Modified Iosipescu Test Method

Shiliang Ding
B.S., Xi'an Jiaotong University, 1983
M.S., Xi'an Jiaotong University, 1986

A dissertation submitted to the faculty of the
Oregon Graduate Institute of Science & Technology
in partial fulfillment of the
requirements for the degree of
Doctor of Philosophy
in
Materials Science and Engineering

April 1995

The dissertation "Mixed Mode Failure Analysis of Adhesively Bonded Composite Systems Using the Modified Iosipescu Test Method" by Shiliang Ding has been examined and approved by the following Examination Committee:

Maciej S. Kumosa, Thesis Advisor
Associate Professor

David G. Atteridge
Professor

Lemmy L. Meekisho
Assistant Professor

F.-G. Buchholz
Acting Professor, Dr.-Ing.
Academic Director

ACKNOWLEDGEMENTS

First of all, I would like to thank my thesis adviser, Dr. Maciej S. Kumosa, for his time, attention, academic guidance, and financial aid throughout the course of this work. I am grateful to Dr. F.-G. Buchholz for providing me with an opportunity to work in his research group for seven months, for his help during my stay in Germany, and for his time in reviewing this work. Special thanks are due to Dr. Lemmy L. Meekisho for the useful suggestions in the finite element calculations, for evaluating this thesis, and in daily life matters. I sincerely appreciate the time and effort of Dr. David G. Atteridge in reviewing the manuscript as well as asking me, "How's your baby doing," every time he saw me.

I would like to recognize the financial support by the National Science Foundation under research grants MSS-9102763 and CMS-9414740 during the course of this work.

Whenever I felt like being lazy, I remembered my master's thesis advisor and role model, Prof. Muyao Tang, who showed me how to be a maybe-not-the-greatest but a devoted scientist. This memory was a constant driving force encouraging me to work harder and harder.

I greatly appreciate the help I received from the OGI faculty, namely, Drs. Bill Wood, Jack Devletian, Margaret Ziomek-Moroz, Karen Vaught-Alexander, Antonio Baptista and Lawrence Ruby, and from the OGI staff, in particular, Drs. Wenyu Shen, Lu Fang, Rajesh Dighde, Nu Yu, Yabin Lei, Mrs. Roxanne Metzker, Ms. Margaret Day, Ms. Julie Wilson, Ms. Mary Vatne and Mrs. Julianne Williams.

I would like to thank my OGI fellow students who provided me with a lot of help and with whom I have developed friendships during the last four years, namely, Bansal, Bala, Jun, Qiong, Ibo, Hursha, Andreas, Mengnie, Qinghua, Yuding, Nong, Xihong, Ming, Youping, Hua, Hui, Xiaoyan, Wen, Jodi, Heidi, Venki, Don, Jeff, Jim, Jinshu, Henry, and Weiran. I would also like to give my special thanks to Badih, Feng, Gang,

Yijin, Zhouyu, Cangsong, and Chris (my basketball buddies), who made my OGI life more enjoyable.

I gratefully acknowledge my German colleagues and friends, Dr. Peter Pawliska, Hui Wang, Manfred Buerger, Hindrik van Lengen, Burkhardt May, and Xiaogang Gao, for their help and friendship.

I owe a lot to Helen and Walter Friesen, Vernon Bissell, and the Chens, who have continuously helped my family since we came to the United States.

I heartily thank my wife, Xiaoyan, for all the support, patience, and understanding; my son, Anton, for his "participation" in the dissertation writing; and my parents for their long-distance emotional support, even though they did not fully understand what their son was doing in the United States.

To Anton, Xiaoyan
and my parents

TABLE OF CONTENTS

LIST OF FIGURES

LIST OF TABLES

ABSTRACT

Mixed Mode Failure Analysis of Adhesively Bonded Composite Systems
Using the Modified Iosipescu Test Method

Shiliang Ding
Oregon Graduate Institute of Science & Technology, 1995

Supervising Professor: Maciej S. Kumosa

Adhesive bonding is widely used as a joining method for important structural components, particularly in aerospace, automotive, and microelectronic applications. The design of adhesive joints requires an adequate understanding of their ultimate strengths and failure mechanisms under various combinations of applied shear and normal loads. There are several test configurations currently available for the testing of adhesive joints under various loading conditions. However, all of these methods have serious disadvantages, ranging from a prohibitive cost of specimen preparation and testing to questionable stress fields in the adhesive layers. Adhesively bonded composite systems consist of bimaterial interface corners, which are generally a source of singular stress fields. These singularities lead to premature failure, thereby making it difficult to characterize the mechanical behavior and to establish the proper failure/fracture criteria of adhesively bonded composite systems.

During the course of this work, the modified Iosipescu test technique was analyzed and applied to investigate the strength of different adhesive joints subjected to biaxial (shear dominated) loadings. The Airy stress function approach, finite element

method (FEM), and the finite element iterative method (FEIM) were applied to investigate macro- and micro-stress fields in the adhesively bonded Iosipescu specimens with different geometries. Analytical and numerical schemes for evaluating the interfacial stress intensity factors, eigenfunctions, eigenvalues, singular zones, and the plastic zones at interface corners were introduced. In the experimental part of this study, adhesively bonded Iosipescu specimens were prepared using a specially designed bonding assembly and were subsequently tested in the modified Iosipescu test fixture. In addition, the fractured surfaces of the specimens tested under various biaxial loadings were examined using optical and scanning electron microscopy.

It was found that there are two independent composite parameters necessary for characterizing the mechanical properties of a bimaterial interface corner. Furthermore, there exists a critical interface angle beyond which the stress singularity vanishes for all material combinations. It was also observed that at a non-linear bimaterial interface corner, there is a transition zone between the smaller plastic zone and the larger singular zone. The experimental results obtained in this study strongly indicate that the type of notch configuration, biaxial loading conditions, and joint strength for rigid and flexible adhesives are not related. Based on the results obtained in this study, an optimized adhesive joint Iosipescu specimen is proposed. The specimen should be ideal for mechanical testing of adhesive joints since it is free from stress singularities.

CHAPTER 1
INTRODUCTION

1.1. Adhesively Bonded Composite Systems

Modern industrial development necessitates the use of functional and efficient materials. Composites, which have a high specific modulus and strength, are potential materials for extensive use in structural applications. As a matter of fact, the structural efficiency of a composite structure is established, with very few exceptions, by its joints, rather than by its basic structure. There are many joining methods used in structural engineering such as welding, brazing, soldering, bolting, riveting, fastening, and adhesive bonding. Among these methods, adhesive bonding has gained considerable popularity in the manufacture of composite structural systems, especially in the past two decades.

Adhesive bonding for primary load-bearing structures was developed several decades ago, but it has only recently gained importance as an economical and effective method for joining materials. Cage [1] has illustrated the extensive use of adhesives in the aircraft industry, and Vinson [2] has also been listed several advantages of using adhesive bonding techniques. Generally, such adhesively bonded materials can be considered as a composite system that offers superior stiffness, lower density, lower fabrication cost, and improved damage tolerance when compared to other joining techniques. Although adhesively bonded structures are extensively used in the aircraft, automotive, and electronic industries [1-4,38-41,56-70], the mechanism of interface delamination of adhesively bonded structures and the corresponding criterion are not well understood. This is primarily due to the absence of a reliable test method to characterize mechanical properties of the adhesives and joints being used.

1.2. Test of Adhesively Bonded Joints

The ability to predict the mechanical properties and to understand the failure mechanisms in adhesively bonded joints under mixed mode loading conditions is important for the further development of adhesively bonded composite structures. Some of the important requirements for adequate predictions are adhesive properties, joint shear and tensile strengths, delamination initiation criterion, crack propagation condition, and response of different adhesives under mixed mode loading situations. Currently, many adhesive joint test methods are available, including single-lap test, double-lap test, step-wised-lap test, scarf-lap test, cone and plate test, Arcan test, and Iosipescu-type specimen test. Unfortunately, none of these methods is able to generate a uniform stress state (especially pure shear) inside the adhesive layer [71-77] and therefore are unable to reliably characterize the adhesive properties.

Kumosa [78-79], after an in-depth study of pure shear and mixed mode testing of composite materials using the modified Iosipescu test fixture, introduced a new method for adhesive joint mixed mode testing: an Iosipescu specimen with an adhesive joint (to be mixed-mode tested using the modified Iosipescu test fixture), which is considered to be capable of generating a uniform stress state inside the adhesive layer. In order to understand and exploit the potential of this method, extensive study on the global and local stress distribution of the **adhesive joint Iosipescu specimen** has been conducted. Special attention has been given to the interfaces and interface corners where most failures are initiated.

1.3. Interfacial Stress Singularities

1.3.1. Importance

The majority of recently developed advanced materials and engineering structures

is comprised of more than one phase. Very often, an interface can be defined between any two phases, for example, an adhesive joint, as a bonding surface where a discontinuity of some kind occurs. The discontinuity may be sharp or gradual. In general, the interface is an essentially two-dimensional region through which material parameters such as concentration of an element, crystal structure, atomic registry, elastic modulus, density, and coefficient of thermal expansion, change from one side to another. Clearly, a given interface may involve one or more of these items and plays a major role in the mechanical and physical properties of the material or structure. Here, the mechanical behavior, namely the stress singular power, the stress intensity factor, the shape and size of the singular stress dominating zone, and the plastic zone shape and size (if the interface consists of elasto-plastic materials) of an interface, is the main concern.

In composite systems, the existence of interfaces is one of the most important features. The properties of the composite systems are largely determined by the interfaces. For example, consider an interface of fiber-matrix composite. The large differences between the elastic properties of the matrix and the fibers have to be communicated through the interface; or, in other words, the stresses acting on the matrix are transmitted to the fiber across the interface. The interface is a dominant factor in the fracture toughness properties of composite materials and in their response to aqueous and corrosive environments. Composite materials with weak interfaces have relatively low strength and stiffness but high resistance to fracture, whereas those with strong interfaces have high strength and stiffness but are very brittle. This is related to the ease of debonding and pull-out of fibers from the matrix during crack propagation [1].

Interfacial stress singularity is a major problem [4,64] in the manufacture of electronic components. For example, a silicon integrated-circuit chip is built by contiguously embedding, butting, and overlaying structural elements of a large variety of materials with different elastic and thermal properties. Stresses therefore develop from the thermal cycling of the chip, and large localized stresses are induced in the silicon substrate near the edges and corners of such structural elements. The stress distribution

inside the elements significantly affects their functions and needs to be understood. Hu [4] has done an extensive review of stress-related problems in silicon integrated-circuit chip industry.

In the coating industry, interfaces are created because of the material property differences between the coating and the substrate. Therefore, the fracture of a coated surface is always initiated from the interface corner [6,7,71]. Understanding the mechanical behavior of the interfaces under thermal or external loading is crucial in obtaining high quality coatings.

In normal metal crystal structures, an interface stress singularity is often encountered. The precipitate atomic registry is a good example of stresses arising in the coherent and semi-coherent interface [5]. Twinning is another example, and it is even more complicated because materials around the interface are anisotropic.

Whenever a structure containing an interface is subjected to external traction or thermal loadings, a singular stress field is observed at the interface corner. This singular stress field determines the failure process and failure mode of the structure. Therefore, it is obvious that in order to fully make use of the benefits of advanced materials or structural designs, this singular behavior at the interface corner should be thoroughly understood.

1.3.2. Assumptions

An extensive literature review has revealed that the following assumptions, though not explicitly stated, have been made by researchers in both theoretical and numerical investigations with respect to interfacial stress singularities:

(1) The interface is infinitesimally thin; that is, only two types of materials are involved near the interface.

(2) The bonding between the two materials is perfect, implying that there is no strain discontinuity across the interface.

(3) The materials close to the interface have the same properties as the materials in the bulk form respectively.

1.3.3. Some Definitions

A stress field is said to be **singular** in a regime inside which, theoretically, a point exists around which the stresses become unbounded as the point is approached. The first type of such a stress field can be written as

$$\sigma_{ij}=Qr^{-\lambda}f_{ij}(\theta) \qquad (\lambda>0) \qquad (1.1)$$

where r and θ represent a polar coordinate system; σ_{ij} are the stress components; $f_{ij}(\theta)$ are trigonometric functions; Q and λ are defined below. This type of stress field is referred to as a **power singularity** stress field and is the main topic of this investigation. The second type has the following form:

$$\sigma_{ij}=Q\ln(r)\,f_{ij}(\theta) \qquad (1.2)$$

which is defined as a **logarithmic singularity** stress field.

Q in equations (1.1) and (1.2) is a measure of the intensity of a singular stress field and is called the **stress intensity factor**.

λ in equation (1.1) is called the **singular power** (or **singular strength**).

The region inside which equation (1.1) or (1.2) dominates for stress expressions is defined as the **singular stress zone**.

The domain inside which the material yields is referred to as the **plastic zone**.

1.4. Outline of the Dissertation

In Chapter 2, a literature review is presented that focuses on the topics of adhesive joint test method, modified Iosipescu test method, global stress analysis of adhesive joints, singular stress analysis, and plastic zone evaluation at the interface

corner. The procedures used and results obtained in this research are presented in Chapter 3, where global stress analysis of adhesive joint Iosipescu specimen, singular stress analysis at an interface corner, and evaluation of plastic zones at interface corners are described in detail. In Chapter 4, discussions are made on the subjects of singular power calculation, stress intensity factor calculation, singular stress zone evaluation, plastic zone evaluation, interactions between the singular and plastic zones, and degree of mode mixing of pure and biaxial stresses of adhesive joint Iosipescu specimens. Based on these efforts, the conclusions of this study are listed in the final chapter.

CHAPTER 2
BACKGROUND

2.1. Adhesive Joint Test Methods

There are four types of deformations that are important, namely, shear, tension, cleavage, and peel as shown in Fig. 2.1, when considering adhesively bonded joints [95]. Corresponding to these four types of deformation, there are four types of joint strengths. Among them, the joint shear strength and shear modulus are of great interest to design engineers because most adhesive joints are primarily used to bear shear loads. Therefore, the shear test methods of adhesive joints are the focus of this section.

2.1.1. Single-Lap and Double-Lap Tests

The ASTM standards for single-lap and double-lap joint (Fig. 2.2) tests are D1002-72 and D3528-76 [96], respectively. The main purpose of these tests is to determine the shear strength of adhesives for bonding metals. The tests have been popular for many years and work very well in many industrial applications. However, they cannot provide the shear characteristics of adhesives under consideration because the stresses inside the adhesive layer are unevenly distributed. Fig. 2.3 is a typical example of stress and strain distributions in a double-lap joint under tension loading [57], where the adhesive is assumed to be elasto-perfectly plastic.

2.1.2. Napkin Ring Test

The napkin ring type of test specimen (Fig. 2.4) relies on an uniform distribution

of the almost pure shear resultant stress when the joint is subjected to torsion as the bonded cups are twisted [96]. Because the radial thickness of the adhesive layer is small, the shear stress can be considered to be constant, making the specimen attractive for the determination of shear properties. However, it should be noted that some structural adhesives can withstand 80-100% shear strain. Normal stresses are very likely generated under such conditions so the uniformity and purity of the shear stress state can no longer be taken for granted. When bond-normal loading of the napkin ring specimen was considered, large stress concentrations were found because of the sharp, 90° bimaterial corners formed by the adhesive and adherends at the free surfaces of the specimen [67]. In addition, the bond-line thickness is difficult to control during joint fabrication [96].

2.1.3. Cone and Plate Test

Grant [68,97] proposed the cone and plate specimen (Fig. 2.5) as another torsional shear testing technique. A closed form solution based on the assumption of rigid adherends indicated that the cone and plate geometry should provide a more uniform shear stress than is produced by the standard radial thickness of the napkin ring geometry. Ratios of the moduli of structural metals to those of structural adhesives generally range from 50 to 120. Although it might be thought that the rigidity of adherends would be a reasonable assumption, evidence of combined relaxation and creep phenomena in adhesively bonded joints indicate that it is not. If the adherends in the cone and plate specimen are not rigid, some accommodation must be made between the radial stresses in adherends and the constant stress in the adhesive. FEM analyses [67] have shown that the shear stress in the adhesive is highly nonuniform for an aluminum/epoxy joint and that this non-uniformity leads to normal stresses that are highly concentrated near the center of the specimen, while the solution of a steel/rubber combination approached the closed form result. This observation indicates that the cone and plate specimen is suitable for pure shear testing when the adherend-to-adhesive modulus ratio

is high enough.

2.1.4. Arcan Test

The Arcan test fixture and specimen are shown in Fig. 2.6. Originally, Arcan *et al.* [98,99] invented this fixture to generate a uniform plane shear stress state in the center of the specimen to conduct mode II test for conventional and composite materials. The test was subsequently modified to characterize adhesive shear properties (Fig. 2.6) [70]. This method gained other researchers' attention thereafter, and the purity of the shear stress state in the adhesive layer was also confirmed [67,68]. In addition, this fixture can be used for mixed mode loading [70].

2.1.5. Iosipescu-Type Specimen Test

By the adaptation of Iosipescu shear testing for metals, Wycherley *et al.* [69] developed an Iosipescu-type specimen (Fig. 2.7) for uniform shear stress-strain characterization of adhesives. In order to perform precise tests, the authors designed special instruments and jigs to facilitate sample preparation, bond-line thickness measurement, and shear displacement determinations. Typical shear stress-strain curves for FM-1000 film adhesive [69] measured by this method indicated that the results from this method were reproducible. However, theoretical support (from closed form and/or numerical analyses) is still needed to account for the residual stresses after curing and the stress state within the adhesive and adherends during testing.

2.2. Modified Iosipescu Test Method for Adhesively Bonded Joints

2.2.1. Modified Iosipescu Test Fixture

An ideal test method is one that is relatively simple to conduct, employs small, easily fabricated specimens, and is capable of measuring both shear strength and shear modulus. In 1967, Iosipescu [100] proposed a method to determine the shear properties of metals. In this procedure, a state of pure shear stress is obtained at the mid-length of an isotropic double V-notched planar specimen by the application of two counteracting force couples (Fig. 2.8). A state of constant shear exists in the mid-section of the specimen with the induced moments canceling exactly at the mid-length and thereby producing a pure shear stress state at this location. Fig. 2.8 shows the force, shear and moment diagrams.

Rod test specimens were originally used, with a 90° circumferential V-notch cut completely around the mid-section. This specimen geometry transforms the parabolic shear distribution (associated with beams of constant cross-section) to a uniform shear distribution in the regions between the notches. The reduced area also promotes shear failure in this region [72]. The two sides of the angular notches, which are the isostatics of the stress-free surface, must be inclined at an angle of 45°. Hence, the inclined angle of the V-notch is 90°. The applied force P divided by the net cross-sectional area A between the notch roots gives the nominal shear stress:

$$\overline{\tau} = P/A \qquad (2.1)$$

Walrath and Adams [101-102] developed the Iosipescu shear test method to determine in-plane and through-thickness shear properties of fiber composite materials. This test used flat rectangular specimens with notches machined at the top and bottom edges (Fig. 2.9). Shear strain was measured at the center of the notch axis using two strain gauges oriented at $\pm 45°$ to the longitudinal axis of the specimen. The authors

[103-106] attempted to optimize the Iosipescu specimen geometry and Iosipescu shear test fixture. As a result of comprehensive investigations of the stress distribution in the Iosipescu specimen as a function of the notch geometry and orthotropic ratio, a re-designed University of Wyoming Iosipescu test specimen and fixture was developed [12].

In most engineering applications, structural materials are subjected to biaxial or tri-axial loads. Therefore, it is important to obtain the mechanical properties and failure criteria under multi-axial-stress conditions. Currently, few testing methods are available for the biaxial characterization of materials and all of them have drawbacks [72].

As a result of the study conducted by Broughton *et al.* [90,107], a new in-plane biaxial test fixture, based on the Arcan test method (Fig. 2.6) and the Iosipescu shear test (Figs. 2.8 and 2.9), was designed. The biaxial loading schematic and fixture (marketed by Instron Corporation) are shown in Fig. 2.10.

2.2.2. Biaxial Test of Adhesive Joints

Structural adhesive joints are usually subjected to multi-axial stress loads, like bonded structures of steels or composites; therefore, the characterization of joint mechanical properties and failure procedures under multi-axial stress conditions is crucial to design engineers and fabricators. As stated in Section 2.1, the only available biaxial adhesive joint test is the Arcan test method (Fig. 2.6), which has the shortcomings of fixed loading angles and difficulties in alignment of the specimen and the grip.

Having done comprehensive research on pure shear and mixed mode testing using the modified Iosipescu fixture [74,78,79,88-91,108-111], Kumosa proposed a new mixed mode test method for adhesive joints: an adhesive joint Iosipescu specimen (Fig. 2.11) [78,79]. The specimen can be loaded using the modified Iosipescu fixture in either pure shear or biaxial stress state to conduct the test. To allow for a full understanding of this method, an in-depth investigation of the global and local stress fields, both from a

theoretical and experimental viewpoints, was conducted in the study.

2.3. Global Stress Analysis of Adhesive Joints

Numerous theoretical and numerical analysis methods exist for the global stress analysis of adhesive joints, the details of which are described elsewhere [2,59]. Shear lag analysis methods, FEM schemes, and experimental techniques used in this study are reviewed below.

2.3.1. Shear Lag Analysis

Shear lag analysis was first introduced by Cox [112] for studying the effect of orientation of the fibers on the stiffness and strength of paper and other fibrous materials. This theory explains the stresses inside a fiber based on differential straining of the matrix, with the assumptions of: (1) a perfect bond between the fiber and the matrix, and (2) no load transfer through the ends of the fiber. Later, Holister and Thomas [113] developed this method to determine the stresses and strains within discontinuous fibers in fiber-reinforced materials. However, Hull [3] pointed out that the results from this analysis were not exact; further, finite element analysis and experimental studies suggested that it under-evaluated the shear stress concentration at the ends of the fibers by a factor of at least two [3].

In 1973, Hart-Smith [38,39] used this shear lag concept to develop analysis and design procedures for single lap and double lap joints. Both methods assumed that the adherends remained elastic and that the adhesive stresses were constant through the bond-line thickness. The adhesive was assumed to be elastic or elastic-perfectly plastic to simplify equation development. For single lag joints, the procedure accounted for the bending of the adherend resulting from the eccentricity in the load path; for double lap joints, both balanced and unbalanced adherend combinations were considered. A double

lap joint is said to be balanced when the thickness of the inner adherend is twice that of each outer adherend. Long [40] successfully applied this method to study the static strength of adhesively bonded ARALL-1 joints.

2.3.2. Finite Element Analysis

The FEM has become widely accepted as one of the most popular numerical techniques. A large number of studies have employed FEM [2,6-11,28-30,40,43,56-67,69-71] to solve various interface-related problems using general commercial FEM codes. However, FEM approaches do have certain disadvantages, namely: (1) the global stiffness matrix resulting from finely meshed interface wedge corners tends to yield excessively large number of degrees of freedom; and (2) the validity of the method relies on an accurate input of the adhesive mechanical properties, which are hard to obtain.

2.3.3. Experimental Analysis

Obtaining the global stress distribution of an adhesive joint by the experimental method is difficult because the adhesive thickness is very thin and the stress state within it is generally non-uniform in real applications. However, there have been many attempts to describe the joint stress distribution. Wycherley *et al.* [69] used a self-designed shearometer to measure the stress contours inside an adhesive layer, assuming that stresses were uniformly distributed. Theocaris [75] employed a pseudocaustic technique to obtain complex stress intensity factors of interfacial cracks (the stress field was clearly known when these factors were substituted into the corresponding theoretical formulas). This technique could be extended to interfacial stress intensity factor measurements. Moreover, Kumosa [114] has suggested that photo-elasticity is another potential method for global stress measurement in adhesive joints.

2.4. Singular Stress Analysis

As mentioned above, failures in adhesive joints are often initiated in a very localized region near the interface corners. Closed form and numerical analyses indicated that stresses are singular at these corners [49]. A review with respect to analytical, numerical, and experimental analyses is given in this section.

2.4.1. Closed Form Analysis

A bimaterial wedge consisting of bonded materials 1 and 2 is shown in Fig. 2.12. Materials 1 and 2 have been assigned a wedge angle, Poisson's ratio, and Young's modulus of θ_1, ν_1, E_1 and θ_2, ν_2, E_2 respectively. A polar coordinate system with its origin at the bimaterial wedge corner is employed (Fig. 2.12), where the external traction along the rays $\theta=\theta_1$ and $\theta=\theta_2$ is assumed to be zero. By taking into account the fact that at the interface ($\theta=0°$) the stresses and displacements are continuous in accordance with Newton's third law, the boundary conditions of the 2-dimensional bimaterial wedge in Fig. 2.12 can be expressed in the following form:

$$\sigma_{\theta\theta}^{(1)}(r,\theta_1)=0 \qquad (2.2)$$

$$\sigma_{r\theta}^{(1)}(r,\theta_1)=0 \qquad (2.3)$$

$$\sigma_{\theta\theta}^{(2)}(r,\theta_2)=0 \qquad (2.4)$$

$$\sigma_{r\theta}^{(2)}(r,\theta_2)=0 \qquad (2.5)$$

$$\sigma_{\theta\theta}^{(1)}(r,0)=\sigma_{\theta\theta}^{(2)}(r,0) \qquad (2.6)$$

$$\sigma_{r\theta}^{(1)}(r,0) = \sigma_{r\theta}^{(2)}(r,0) \qquad (2.7)$$

$$u_r^{(1)}(r,0) = u_r^{(2)}(r,0) \qquad (2.8)$$

$$u_\theta^{(1)}(r,0) = u_\theta^{(2)}(r,0) \qquad (2.9)$$

where σ_{ij} are stress components; u_i are the displacement components and the supersuffices (1) and (2) correspond to the material types.

When both materials in Fig. 2.12 are elastic, stresses at the bimaterial wedge corner will be mathematically unbounded. This elastic interfacial stress problem has been examined by many researchers with different analytical methods [6-25]. Knesl *et al.* [6-7] classified these methods into two types (the first two of the following three). By taking into account the Mellin transform method used by Bogy [13,14], there should be three analytical methods, namely: Airy stress function, complex potentials and Mellin transform. These analytical methods are reviewed in the following sections.

2.4.1.1. Airy Stress Function Approach

A biharmonic Airy stress function in a polar coordinate system, given by Williams [34] and employed in [6-11], has the following form:

$$\psi = F(\theta)\, r^{-\lambda+2} \qquad (2.10)$$

where λ is a constant for a specific material combination and fixed geometry and is denoted as the stress singular power.

This stress function can be used to study singular stress fields in the vicinity of an interface corner. In equation (2.10), $F(\theta)$ can be determined from the requirement that ψ has to be biharmonic, *i.e.*,

$$\nabla^2\nabla^2\psi = 0 \tag{2.11}$$

where ∇^2 is the Laplacian operator and has the following form:

$$\nabla^2 = \frac{\partial^2}{\partial r^2} + \frac{1}{r}\frac{\partial}{\partial r} + \frac{1}{r^2}\frac{\partial^2}{\partial \theta^2} \tag{2.12}$$

By applying equation (2.11) to equation (2.10) and solving for $F(\theta)$, then substituting $F(\theta)$ back to equation (2.10), the following can be obtained:

$$\begin{aligned}\psi = r^{-\lambda+2}[&A_1 \sin\lambda\theta + A_2 \cos\lambda\theta \\ &+ A_3 \sin(2-\lambda)\theta + A_4 \cos(2-\lambda)\theta]\end{aligned} \tag{2.13}$$

where A_i are constants to be determined from the boundary conditions.

In terms of the Airy stress function, the stress components take the following form:

$$\sigma_{rr} = \frac{1}{r}\frac{\partial\psi}{\partial r} + \frac{1}{r^2}\frac{\partial^2\psi}{\partial\theta^2} \tag{2.14}$$

$$\sigma_{\theta\theta} = \frac{\partial^2\psi}{\partial^2 r} \tag{2.15}$$

$$\sigma_{r\theta} = -\frac{\partial}{\partial r}\left(\frac{\partial\psi}{r\partial\theta}\right) \tag{2.16}$$

$$\frac{\partial u_r}{\partial r} = \frac{2(1+\nu)}{E}\left[\frac{1}{r}\frac{\partial\psi}{\partial r} + \frac{1}{r^2}\frac{\partial^2\psi}{\partial\theta^2} - \left(1 - \frac{k+1}{4}\right)\nabla^2\psi\right] \tag{2.17}$$

$$\frac{\partial u_\theta}{\partial r} - \frac{u_\theta}{r} + \frac{1}{r}\frac{\partial u_r}{\partial\theta} = \frac{2(1+\nu)}{E}\left(-\frac{1}{r}\frac{\partial^2\psi}{\partial r\partial\theta} + \frac{1}{r^2}\frac{\partial\psi}{\partial\theta}\right) \tag{2.18}$$

where E is the Young's modulus and ν is the Poisson's ratio, u_r and u_θ are the displacements along the radial and circumferential directions respectively, and k has the following values:

$$k=3-4\nu \qquad \textit{for plane strain condition} \qquad (2.19)$$

$$k=\frac{3-\nu}{1+\nu} \qquad \textit{for plane stress condition} \qquad (2.20)$$

After substituting equations (2.14-2.18) into the boundary condition equations (2.2-2.9), eight linear algebraic homogeneous equations are achieved for the eight unknown constants $A_i^{(j)}$ (i=1,2,3,4 and j=1,2 to represent different materials). If $A_i^{(j)}$ are denoted as B_n, n=1,2,..,8, and the coefficients of $A_i^{(j)}$ are denoted as $D_{mn}(\theta_1,\theta_2,\nu_1,\nu_2,E_1,E_2,\lambda)$, m=1,2,..,8, the linear equation system can be written as

$$[D_{mn}][B_n]=0 \qquad (2.21)$$

where m,n= 1,2,..,8.

The existence of a non-zero solution of equation (2.21) requires that the determinant of $[D_{mn}]$ equal zero, that is,

$$|D_{mn}|=f(\theta_1,\theta_2,\nu_1,\nu_2,E_1/E_2,\lambda)=0 \qquad (2.22)$$

Equation (2.22) is a transcendental equation, from which the eigenvalues λ can be obtained. λ may be real or complex and may have infinite number of roots, but only the real part of λ within the interval (0,1) is of interest.

According to equations (2.21) and (2.22), only the relative relationship between the intensity factors $A_i^{(j)}$ can be found; the absolute values of $A_i^{(j)}$ cannot be calculated because equation (2.21) is homogeneous. However, $A_i^{(j)}$ can be computed when the boundary conditions on the other parts of the bimaterial body are considered.

With equations (2.13-2.16), the stresses that have a $\sigma_{ij}\sim r^{-\lambda}$ form can be inspected.

Moreover, taking into account the previous discussion that multiple eigenvalues exist, the stress distribution at the wedge corner can be expressed as

$$\sigma_{ij}=\sum_{n} Q_{ij(n)} f_{ij(n)}(\theta) r^{-\lambda_n} \qquad (2.23)$$

where λ_n is the *n*th singular power, which may be real or complex, and $0<\mathrm{Re}(\lambda_n)<1$ [Re(x) obtains the real part of complex number x] has to be met because of the finite displacement requirement; also, λ_n are the same in both materials; $Q_{ij(n)}$ is the *n*th stress intensity factor, which is only a function of body dimensions and external traction [6-7].

Another kind of singularity problem, namely, logarithmic singularity, was studied by Zwiers et al [26] for free-edge stresses in laminated composites under uniform extension. In this case, the singular behavior has the form of $Q\ln(r)$. This problem, however, is beyond the scope of this work: further details can be found in reference [26].

2.4.1.2. Complex Potentials

The method of complex potentials was used by Theocaris [12,82] for solving the singular stress field at a multi-wedge corner. Knesl [6] also gave a brief description of the method. The process is shown below.

Two analytical complex functions $\phi(z)$ and $\psi(z)$ as sums (over all possible values of λ) of the terms of type shown below are selected as

$$\phi_j(z)=a_{j1}z^{(1-\lambda)}+a_{j2}z^{\overline{(1-\lambda)}} \qquad (2.24)$$

$$\psi_j(z)=b_{j1}z^{(1-\lambda)}+b_{j2}z^{\overline{(1-\lambda)}} \qquad (2.25)$$

where z is a complex variable, $z=x+iy=re^{i\theta}$, j is the index of material types and can be chosen as 1 or 2, $\overline{\lambda}$ is the complex conjugate of λ. The terms a_{jq}, b_{jq} (j,q=1,2) represent eight generally complex potential intensities.

Using the functions in equations (2.24) and (2.25), stresses can be expressed as follows:

$$\sigma_{\theta\theta}^{(j)} + \sigma_{rr}^{(j)} = 2\left[\phi'(z) + \overline{\phi_j'(z)}\right] \qquad (2.26)$$

$$\sigma_{\theta\theta}^{(j)} - \sigma_{rr}^{(j)} + 2i\sigma_{r\theta}^{(j)} = 2e^{2i\theta}\left[\bar{z}\phi_j''(z) + \psi_j'(z)\right] \qquad (2.27)$$

$$\frac{E_j}{1+\nu_j}\left(u_r^{(j)} + iu_\theta^{(j)}\right) = e^{-i\theta}\left[k_j\phi_j(z) - z\overline{\phi_j'(z)} - \overline{\psi_j(z)}\right] \qquad (2.28)$$

where prime denotes a derivative with respect to z, E_j is the Young's modulus, and ν_j is the Poisson's ratio of material j, respectively. k_j had been previously defined in equations (2.19-2.20).

If the stresses and displacements in equations (2.26-2.28) are substituted into the boundary conditions (2.2-2.9), which must be valid for any r, eight (generally complex) linear algebraic homogeneous equations for the eight unknowns a_{jq} and b_{jq} can be obtained. If the eight unknowns a_{jq} and b_{jq} are denoted as C_n, n=1,2,..,8, the eight linear homogeneous equations can be rewritten as

$$[H_{mn}][C_n] = 0 \qquad (2.29)$$

where the coefficients H_{mn} (m=1,2,...,8) are known functions of the known values of θ_j, ν_j, E_j and of the unknown singular power λ.

A non-zero solution of equation (2.29) exists only if the determinant of $[H_{mn}]$ equals zero, that is,

$$|H_{mn}| = f(\theta_1, \theta_2, \nu_1, \nu_2, E_1/E_2, \lambda) = 0 \qquad (2.30)$$

where m,n=1,2,..,8. Equation (2.30) can be rewritten as

$$\lambda = \lambda(\theta_1, \theta_2, \nu_1, \nu_2, E_1/E_2) \qquad (2.31)$$

Equation (2.31) is a transcendental equation. Although it does not have the same form as equation (2.23), they share the same roots of λ. Generally, equation (2.31) can be solved numerically; only in exceptional cases, can it be solved analytically.

Similar to the case of equation (2.22), the absolute values of the potentials' intensities a_{jq} and b_{jq} cannot be determined using only equation (2.29). However, the exact values can be obtained from the boundary conditions of the total area of interest.

Knesl [6] suggested that one possible, although complicated, way to find such a complete solution is to consider the complete solution in polar coordinates as a series of terms of types (2.24) and (2.25) for all eigenvalues λ_n, including the non-singular terms with $\mathrm{Re}(\lambda_n) \geq 1$.

2.4.1.3. Mellin Transform

Mellin transforms have also been used to solve this boundary-value problem in references [13-17]. The Mellin transform of a function f is defined by

$$M\{f;s\}=\int_0^\infty f(r)\, r^{s-1} dr \qquad (2.32)$$

where s is the (complex) transform parameter. In addition, the stress components of the stress field inside the bimaterial wedge should meet the requirement of the regularity conditions [13,14]:

$$\sigma_{ij}=O(r^{-1+h}) \ \text{as} \ r\to\infty \ \text{for every} \ h>0 \qquad (2.33)$$

where $O(.)$ means that the dependent and independent variables are of the same order of infinitesimalness.

With this method, even more complicated problems can be solved as well. Traction can be applied to the two wedge surfaces ($\theta=\theta_1$ and $\theta=\theta_2$); that is, the boundary

conditions of equations (2.2-2.5) can be changed to have the following forms:

$$\sigma_{\theta\theta}^{(1)}(r,\theta_1) = n^{(1)}(r) \tag{2.34}$$

$$\sigma_{r\theta}^{(1)}(r,\theta_1) = t^{(1)}(r) \tag{2.35}$$

$$\sigma_{\theta\theta}^{(2)}(r,\theta_2) = n^{(2)}(r) \tag{2.36}$$

$$\sigma_{r\theta}^{(2)}(r,\theta_2) = t^{(2)}(r) \tag{2.37}$$

where $n^{(j)}(r)$ are the normal traction on the surface $\theta=\theta_j$ and $t^{(j)}(r)$ are the shear traction on the surface $\theta=\theta_j$.

Let $\Psi_j(s,\theta)$, $S_{rr}^{(j)}(s,\theta)$, $S_{\theta\theta}^{(j)}(s,\theta)$, $S_{r\theta}^{(j)}(s,\theta)$, $U_r^{(j)}(s,\theta)$, $U_\theta^{(j)}(s,\theta)$, $N^{(j)}(s)$, $T^{(j)}(s)$ in the order denote the Mellin transforms with respect to r of $\psi_j(r,\theta)$, $r^2\sigma_{rr}^{(j)}(r,\theta)$, $r^2\sigma_{\theta\theta}^{(j)}(r,\theta)$, $r^2\sigma_{r\theta}^{(j)}(r,\theta)$, $ru_r^{(j)}(r,\theta)$, $ru_\theta^{(j)}(r,\theta)$, $r^2n^{(j)}(r)$, and $r^2t^{(j)}(r)$. A formal application of the Mellin transform to (2.12) produces an ordinary differential equation for Ψ_j, the general solution of which is

$$\Psi_j(s,\theta) = a_j(s)\sin(s\theta) + b_j(s)\cos(s\theta)$$

$$+ c_j(s)\sin(s\theta+2\theta) + d_j(s)\cos(s\theta+2\theta) \tag{2.38}$$

Here, functions $a_j(s)$, $b_j(s)$, $c_j(s)$ and $d_j(s)$ are to be determined through the transforms of equations (2.14-2.18) and from the transforms of boundary condition equations (2.6-2.9) and (2.34-2.37). These transformed equations have the following forms when equation (2.38) is taken into consideration:

$$S_{rr}^{(j)}(s,\theta) = \left(\frac{d^2}{d\theta^2} - s\right)\Psi_j(s,\theta) \tag{2.39}$$

$$S_{\theta\theta}^{(j)}(s,\theta) = s(s+1)\,\Psi_j(s,\theta) \tag{2.40}$$

$$S_{r\theta}^{(j)}(s,\theta) = (s+1)\,\frac{d}{d\theta}\Psi_j(s,\theta) \tag{2.41}$$

$$U_r^{(j)}(s,\theta) = \frac{1+\nu_j}{E_j}\Big[s\Psi_j(s,\theta) + (k_j+1)\,c_j(s)\sin(s\theta+2\theta)$$

$$+ (k_j+1)\,d_j(s)\cos(s\theta+2\theta)\Big] \tag{2.42}$$

$$U_\theta^{(j)}(s,\theta) = -\frac{1+\nu_j}{E_j}\Big[-\frac{d}{d\theta}\Psi_j(s,\theta) + (k_j+1)\,c_j(s)\cos(s\theta+2\theta)$$

$$-(k_j+1)\,d_j(s)\sin(s\theta+2\theta)\Big] \tag{2.43}$$

$$S_{\theta\theta}^{(j)}(s,\theta) = N^{(j)}(s) \tag{2.44}$$

$$S_{r\theta}^{(j)}(s,\theta) = T^{(j)}(s) \tag{2.45}$$

$$S_{\theta\theta}^{(1)}(s,0) = S_{\theta\theta}^{(2)}(s,0) \tag{2.46}$$

$$S_{r\theta}^{(1)}(s,0) = S_{r\theta}^{(2)}(s,0) \tag{2.47}$$

$$U_r^{(1)}(s,0) = U_r^{(2)}(s,0) \tag{2.48}$$

$$U_\theta^{(1)}(s,0) = U_\theta^{(2)}(s,0) \tag{2.49}$$

If equations (2.38-2.43) are substituted into equations (2.44-2.49), eight linear equations for the eight unknown functions $a_j(s)$, $b_j(s)$, $c_j(s)$ and $d_j(s)$ can be obtained. The eight unknown functions can be determined by solving the eight equations. If these eight solved functions are substituted back into equations (2.38-2.43), $\Psi_j(s,\theta)$, $S_{rr}^{(j)}(s,\theta)$, $S_{\theta\theta}^{(j)}(s,\theta)$, $S_{r\theta}^{(j)}(s,\theta)$, $U_r^{(j)}(s,\theta)$, $U_\theta^{(j)}(s,\theta)$ (k=1,2) can therefore be obtained. Then, by use of the inversion theorem for the Mellin transform [80], the stress components σ_{ij} and displacements $u_r^{(j)}$ and $u_\theta^{(j)}$ can be eventually found:

$$\sigma_{mn}^{(j)}(r,\theta) = \frac{1}{2\pi i}\int_{c-i\infty}^{c+i\infty} S_{mn}^{(j)}(s,\theta)\, r^{-s-2} ds \qquad (2.50)$$

where mn=rr, $\theta\theta$, rθ and j=1,2; and

$$u_m^{(j)}(r,\theta) = \frac{1}{2\pi i}\int_{c-i\infty}^{c+i\infty} U_m^{(j)}(s,\theta)\, r^{-s-1} ds \qquad (2.51)$$

where m=r, θ and j=1,2.

The path of the integration in the complex line integral is critical to finding the proper solution. The singular power was computed by using the residual theorem. Detailed discussions of the computation procedure can be obtained from references [13-15].

2.4.1.4. Composite Parameters

From the previous descriptions of λ calculation (equations (2.22) and (2.31)), it can be clearly seen that whenever the geometry of the bimaterial wedge is fixed; that is, the angles θ_1 and θ_2 are fixed, and λ depends only on the three parameters: ν_1, ν_2 and E_1/E_2, which are a combination of four elastic constants. However, further studies using complex potentials by Dunders [27,81] indicated that λ actually depends only on two

non-dimensional combinations of the four elastic constants, which are called composite parameters and conventionally denoted as α and β [81]:

$$\alpha = \frac{\Gamma(k_1+1) - (k_2+1)}{\Gamma(k_1+1) + (k_2+1)} \tag{2.52}$$

and

$$\beta = \frac{\Gamma(k_1-1) - (k_2-1)}{\Gamma(k_1+1) + (k_2+1)} \tag{2.53}$$

where k_1 and k_2 have been defined in equations (2.19-2.20); Γ is the ratio of the shear modulus of material 2 to material 1 and can be computed by

$$\Gamma = \frac{E_2(1+\nu_1)}{E_1(1+\nu_2)} = \frac{G_1}{G_2} \tag{2.54}$$

where G_1 and G_2 are the material shear moduli respectively.

The selection of the composite parameters is not unique; however, this pair has been recognized as being the most appropriate for the analysis of plane problems [14,15,25,81]. Consequently, a transcendental equation for λ can be found to be of the following form:

$$\lambda = \lambda(\alpha, \beta, \theta_1, \theta_2) \tag{2.55}$$

If it is assumed that the values of the elastic properties are limited to the range of:

$$0 \le \Gamma \le \infty \tag{2.56}$$

and

$$0 \le \nu_1, \nu_2 \le 0.5 \tag{2.57}$$

then, from the relationships of (2.19-2.20) and (2.52-2.53), it is found that the values of α and β fall into the parallelogram:

$$-1 \le \alpha \le 1 \quad and \quad \frac{\alpha-1}{4} \le \beta \le \frac{\alpha+1}{4} \tag{2.58}$$

Bogy [14] and other researchers [6,12,16,82] used these two parameters to describe λ's behavior in the parallelogram. An example of this is shown in Fig. 2.13.

2.4.1.5. Special Cases

In addition to the general case discussed in the previous section, there are special cases which can be further simplified and therefore easily solved. Two examples, an elastic-rigid bimaterial wedge that resembles an elastic strip bonded to a rigid substrate and an interface crack which is the case when the biomaterial re-entrant angle is zero, are reviewed in the following sub-sections.

2.4.1.5.1. A Rigid-Elastic Model

When one of the two materials in Fig. 2.12 is rigid, the singular stress behavior at the wedge corner is much simpler. This case is often encountered in practical engineering practices. For instance, when an adhesive joint comprised of metal (steel or aluminum) adherends and an epoxy adhesive layer is loaded by external forces, the interfaces between the adherends and adhesive resemble such a case. This case has been widely studied [8-10,28-30].

If we assume that material 2 is rigid in Fig. 2.12 and $\theta_1=90°$, equation (2.22) or (2.31) can be simplified as

$$4k_1\cos^2\left[\frac{\pi}{2}(\lambda-2)\right]-4(\lambda-1)^2+(1+k_1)^2=0 \tag{2.59}$$

where k_1 has been defined in equation (2.19-2.20).

From equation (2.59), the eigenvalues λ can be easily calculated by numerical method.

From another point of view, this problem is a special notch problem with one of its sides fixed. The solutions of notch tip stress singularities in this case have been obtained by Williams [34] and can also be found in [35-37]. The eigenvalue function given in [34] is identical to equation (2.59). Vasilopoulos [37] suggested an algorithm for the eigenvalue problem solutions.

Reedy [8-9] proposed a formula for calculating stress intensity factor (called free-edge stress intensity factor in the original papers) for butt adhesive joints:

$$Q=\sigma^* h^{\lambda} A(\nu) \qquad (2.60)$$

where Q is the stress intensity factor, σ^* is the characteristic stress, 2h is the layer thickness, and $A(\nu)$ is a function defined by loading (tension, shear, or temperature) cases and Poisson's ratios, which were tabulated and plotted for different loading conditions and Poisson's ratios in the original presentations. After an FEM analysis was conducted, it was concluded that this formula worked well [49].

2.4.1.5.2. Singular Stress Field at an Interfacial Crack Tip

An interfacial crack is a special case of $\theta_1=\pi$ and $\theta_2=-\pi$ in Fig. 2.12, where equation (2.22) has been drastically simplified and can be found to be of the following form [6]:

$$\lambda_n=n-\frac{1}{2}+i\frac{1}{2\pi}\ln\frac{1+\beta}{1-\beta} \quad and \quad \lambda_n'=n \qquad (2.61)$$

where n=1,2,3,...; i is the imaginary unit and β is given by equation (2.53), which depends on the elastic constants. (λ_n' represent rigid body translation or rotation and will

not be discussed here.) It is obvious that the singularity is described by λ_1 with the real part $Re(\lambda_1)=1/2$ and the imaginary part depending on β. This stress field oscillates when r approaches the crack tip, which creates an additional stress field overlapping the $\sigma_{ij} \sim 1/\sqrt{r}$ field, but not the simple $\sigma_{ij} \sim 1/\sqrt{r}$ stress field in a homogeneous medium, which is well known [44-45]. Moreover, the oscillatory term in the displacements leads to a non-realistic crack opening and to an inter-penetration of the crack surfaces. Different approaches have been suggested to address this problem [6,46-48].

2.4.2. Numerical Analysis

Numerical analysis is a powerful tool for studying the mechanical behavior of bimaterial wedges. The most popular and effective methods in numerical analysis are the Finite Element Method (FEM) and the Finite Element Iterative Method (FEIM). They are reviewed in the following sections from the viewpoint of their ability to extract the singular power and to simulate singular behavior in both elastic and elasto-plastic bimaterial wedges.

2.4.2.1. Finite Element Approach

The most popular numerical method used for studying the singular stress problems at a bimaterial corner is the FEM. Some of these studies are presented in references [6-11,18-23,28-33,49,61,64,66,73,91]. Application of FEM analysis means that no special requirements are needed for the boundary conditions, and that various geometries and dimensions can be treated. If attention is paid to the fineness of the meshes around wedge corners, both the singular powers and the absolute values of the stress intensity factors can be calculated by using the following *log-log* formula [49]:

$$\log(\sigma_{ij}) = \log(Q) + \log(f_{ij}(\theta)) - \lambda \log(r) \qquad (2.62)$$

Equation (2.62) can be obtained by taking logarithmic operations on both sides of equation (1.1). However, since the FEM is usually based upon assumptions for displacements and/or stresses that are defined in terms of polynomial functions over finite elements, it will be impossible to obtain an exact representation of the behavior of the singular stress region no matter how fine the mesh is. To overcome this difficulty, several researchers have suggested special element techniques in the singular fields [18-22,27,31,32,42,46,49-55,72-74].

Walsh [19] suggested a special FEM element for the computation of stress intensity factors. The special element consists of two regions. The stress and displacement distribution in the inner region is defined in terms of the singular stress field associated with the singular domain. The outer region of the special element contains conventional finite elements that are constrained to satisfy certain equilibrium and compatibility criteria on the interface between the two regions. Examples in reference [19] showed that this method is efficient and valid. Tracey and Cook [31] constructed a three-node triangular displacement element having $r^{1-\lambda}$ interpolation functions. This element can incorporate the designed singular behavior and conform with standard (linear) elements on the exterior edge, but it does not contain constant strain fields and hence cannot pass a patch test. Akin [50] proposed an element family that can incorporate the existing isoparametric codes with minimal efforts. These elements conform with the standard isoparametric elements, but they do not contain linear fields either and are difficult to integrate accurately. Because of the shortcomings of the above-proposed special elements, Stern [51] constructed families of two- and three- dimensional finite elements to model fields with singular derivatives. The elements are complete over linear fields, conform with regular elements, and are easy to program. In summary, it can be stated that all of the above efforts are aimed at constructing elements with embedded singularities. Therefore, these techniques cannot be used for general FEM codes; in addition, the singular power λ has to be known *a priori* for an embedded singularity FEM program to be written.

Szabo [22] developed guidelines for prior design of meshes and procedures for post-solution testing in order to obtain an exact solution. Spilker and Chou [18] invented a special purpose, hybrid-stress, multi-layer finite element to satisfy the traction-free-edge conditions for solving a symmetric cross-ply laminate under uniform plane strain.

In crack tip problems, by observing that singular power is always 1/2 and the characteristics of the quadratic shape functions, Henshell and Shaw [52] and Barsoum [53] discovered that by moving the mid-node of the standard isoparametric elements to the quarter position from the standpoint of the crack tip, an exact 1/2 singular field could be achieved. This method is quite simple and can be readily used with any general FEM codes. It is shown [54] that the strain components vary as $1/\sqrt{r}$ along the sides of the quadrilateral but not in the interior. The triangular element exhibits the requisite singularity along the boundary and in the interior, that is, the strains vary as

$$\epsilon \sim r^{-\frac{1}{2}},\ r^{-1} \tag{2.63}$$

and several computations showed that this method is very efficient for calculating stress intensity factors [52-55]. Unfortunately, this method is valid only for $\lambda = 1/2$ type of singularities and not for other cases.

Whitecomb *et al.* [32] studied the reliability of FEM for calculating the singular stress field, using it to compute the stress and displacement distributions of discontinuous stress distribution bending problems and 45°/45° 4-ply composite laminates. They found that the FEM yielded accurate solutions everywhere except in a region involving the two elements closest to the stress discontinuity or singularity. They concluded that the displacement-formulated FEM appears to be a highly accurate technique for calculating inter-laminar stresses in composite laminates, which implies that FEM is effective in computing singular stress fields.

However, the use of singularity-embedded elements to solve interfacial singular stress problems was not encountered in the literature search. This may be due to the fact

that the singular power of an arbitrary bimaterial wedge cannot be known *a priori*, therefore, a proper singularity-embedded FEM program is impossible.

2.4.2.2. Finite Element Iterative Analysis

For a fairly accurate computation of the singular power of an elastic interface corner using equation (2.62) to be achieved, the numerical results from the FEM must be very accurate. This is not a simple requirement. Moreover, this method will fail when the singular power is complex. To overcome this constraint, Barsoum [20,21,42,46] invented the FEIM to accomplish this task in the case of separable singular stress fields.

The FEIM relies on the use of general purpose FEM codes to penetrate deep into the singular stress field as the iterations on a circular mesh proceed. A typical FEIM mesh representation is shown in Fig. 2.14. Assuming that the finite element equation of the linear elastic problem in Fig. 2.12 can be written as [20-21,72-74]

$$[K]\begin{Bmatrix} u_0 \\ u_{R_i} \\ u_{R_{in}} \\ u_{R_{out}} \end{Bmatrix} = \{0\} \qquad (2.64)$$

where K is the global stiffness matrix and u_0 is the displacement of the origin of the singularity, namely the interface corner for a bimaterial wedge; u_{Rin} is the displacement at the inner ring; u_{Rout} is the displacement at the outer ring (the boundary condition); and u_{Ri} is the displacements of the remaining degrees of freedom. With some matrix manipulation, the following relationship can be obtained [27]:

$$\{u_{R_{in}}\}=[T]\{U_{R_{out}}\} \qquad (2.65)$$

where T is called the transfer matrix, *i.e.*, at the *m*th iteration,

$$\{u_{R_{in}}^{m}\}=[T]\{U_{R_{out}}^{m}\} \tag{2.66}$$

and

$$\{u_{R_{out}}^{m+1}\}=\Lambda_m\{u_{R_{in}}^{m}-u_0^{m}\} \tag{2.67}$$

where Λ_m is a scalar multiplier for normalizing the vector u_{Rin}. Using the Rayleigh quotient argument [27], at convergence, it is found that

$$\Lambda_m \rightarrow \Lambda \ as \ m \rightarrow \infty \tag{2.68}$$

where Λ is the first dominant eigenvalue of the matrix [T]. It is shown that for the case of a power singularity Λ, Λ has the following form:

$$\Lambda=\left(\frac{R_{out}}{R_{in}}\right)^{1-\lambda} \tag{2.69}$$

where λ is the power of the singular stress field. Therefore, for a self-adjoint case, the displacement u is given by

$$u=Qr^{1-\lambda}g(\theta) \tag{2.70}$$

This form is referred to as a separable function.

From equations (2.17-2.18), it can be seen that the displacement field at the vicinity of the wedge corner has the form of equation (2.70), *i.e.*, the displacement function is a separable function and the FEIM can be used to study the eigenfunctions. Barsoum applied this method in investigating crack tip stress singularities for both isotropic [83] and orthotropic materials [20,46], as well as for interfacial cracks [20,46]. Sukumar [72], Erdinc [73] and Sukumar and Kumosa [74] used this method to investigate sharp notch tip stress singularities of isotropic and orthotropic materials. The problem of interface corner stress singularities has previously been approached by this method [21,49,73].

2.4.3. Experimental Analysis

Experimental analysis of the mechanical behavior of bimaterial wedges was conducted primarily by use of adhesive joints [10,28-30,43,55,58,59,61-70] and coated plates [7,71]. Most studies have focused on the local geometrical influences on the strength of adhesive joints and evaluation of stress intensity factors. Other work can also be found in the area of energy release rate (G_I) measurement and experimental techniques.

2.4.3.1. Geometric Effects

From the analytical and numerical approaches in the previous sections, it can be seen that the singular power λ is a function of the wedge angles θ_1 and θ_2 in Fig. 2.12, *i.e.*, the local terminus geometry of an adhesive joint has a crucial influence on its strength. Adams and Harris [66] tested three different edge geometries of the overlap in single-lap joints: one with a square-edged adhesive layer, one with a fillet of adhesive, and one with an adhesive fillet plus a radiused adherend. They found that significant strength increments may be achieved in single-lap joints by filleting the adhesive at the edges of the overlap and rounding the ends of the adherends. It was also postulated that adhesive joint optimization yields a substantial decrease in the stress levels in the adhesive layer, and in many cases a much lighter joint can be obtained [56]. After performing extensive studies of single-lap, double-lap, step-lap and scarf-lap joints, Hart-Smith [38,39,57] presented some guidelines for adhesive joint design to achieve higher joint strength.

In order to obtain a more-or-less uniform shear stress distribution in the adhesive layer to make maximum use of the adhesives, one must eliminate or minimize local geometry effects. For this purpose, Weissberg and Arcan [70] proposed a versatile stiff adherend test specimen (Fig. 2.6) to induce a uniform pure shear stress state practically

free of tension and compression in the adhesive layer. They assumed that a (M_I + M_{II}) or (M_I + M_{III}) mixed-mode stress state could also be arrived at by using this method. Moreover, after the Arcan test and cone-and-plate test were analyzed using FEM in [68], it was concluded that both tests show much promise as a constant shear stress in-situ testing technique. However, after similar analysis of the Arcan test, cone-and-plate test and napkin test with various modifications to the adherend edges, it was reported that the stiff adherend specimen having rounded adherend edges provided the greatest degree of uniformity in adhesive stress under all conditions. Wycherley *et al.* [69] claimed that their Iosipescu-type specimen test was able to generate a uniform shear stress state inside the adhesive layer; however, numerical results in reference [73] imply that the shear stress in the adhesive layers is still not uniform because singular stress fields exist at the wedge corners. Following a comprehensive study of the Iosipescu test principle, Kumosa [78,79] proposed three different types of Iosipescu specimens with adhesive joints (Fig. 2.11) for pure shear and mixed mode testing of geometric effects. Efforts in this direction have already been initiated [120].

2.4.3.2. Stress Intensity Factor Evaluation

Traditionally, adhesive joints have been evaluated through strength measurements. However, difficulties arise in the strength evaluation of adhesively bonded structures because the stress and displacement fields near the bonding edge, where the delamination starts, exhibit a singularity behavior, and an accurate strength measurement cannot be made using stress values alone. Considering this point, an alternative approach is to measure the fracture toughness, *i.e.*, the stress intensity factor Q, which can characterize the singular stress field and is a material constant, similar to the crack tip problems. The idea of using stress intensity factors to evaluate adhesive joints was first introduced by Gradin [10] and subsequently modified by Gradin and Groth [28-30]. Recently, Groth and Brottare [43] applied this concept to elastic-plastic materials with small scale

yielding. The techniques used by Gradin, Groth and Brottare [28-30] to measure the stress intensity factors included both experimental and FEM analyses. In addition, a single-edge notched-beam (SENB) [61] was used to evaluate the fracture toughness of ceramic adhesive joints. Some other reports can also be found in references [64,70].

One significant difference in the measurement of stress intensity factors between an interface corner and a crack tip in an isotropic material is that the stress intensity factor at the wedge corner may be complex. In the case of complex stress intensity factors, pseudocaustics can be employed for the evaluation. It has been reported that this method is very simple, accurate and versatile [75].

2.4.3.3. Other Comments

In addition to the measurement of stress intensity factors, the energy release rate G_I was also evaluated by several authors [40,58,63,70]. Specially, Kinloch and Shaw [63] used contour-double-cantilever-beam adhesive joint specimen (Fig. 2.15) to conduct their test and concluded that the adhesive bond thickness, the width of the joint, the test rate and test temperature had a great influence on G_{Ic}(joint).

Also, some adhesive thickness-effect oriented experiments were done by other researchers [58,61,62,65]. These results indicated that the strength of the adhesive joint increases as its thickness decreases. Anderson *et al.* [65] attributed this phenomenon to the fact that when the adhesive layer is thin enough, the singular stress field will be smaller than a critical value and hence will not affect the strength.

Davidson [75] presented an *in-situ* method for examining the failure of interfaces in composites. This method can be expected to be used to verify numerical calculations as it is able to experimentally determine the strains in the vicinity of an interface crack tip. Nevertheless, more investigation is needed to fully understand the procedure.

2.5. Plastic Zone Evaluation at an Interface Corner

Whenever elasto-plastic materials are introduced into a bimaterial wedge, a plastic zone will appear. In this case, it is of great interest to determine the size of the plastic zone, and if possible, to apply the elastic solution to the plastic case.

2.5.1. Analytical Approach

Groth and Brottare [43] researched a simple case. The sample they studied is shown in Fig. 2.16. The adhesive is assumed to be elastic-perfectly plastic and the adherend to be rigid. A first rough estimation of the plastic zone size may be obtained by assuming a stress (and strain) field in the vicinity of the bimaterial wedge in the surface along y-direction having the following form:

$$\sigma_y = Q_y \left(\frac{r}{h}\right)^{-\lambda} \qquad (2.71)$$

where Q_y is defined as a singular intensity factor and h is the reference length.

As the material begins to yield when $\sigma_y = \sigma_s$, the plastic zone size, r_s, may be derived from

$$\frac{r_s}{h} = \left(\frac{Q_y}{\sigma_s}\right)^{\frac{1}{\lambda}} \qquad (2.72)$$

This case is illustrated in Fig. 2.17, where stresses exceeding σ_s are simply ignored by this approximation.

From the case investigated, Groth and Brottare concluded that equation (2.72) gives a good approximation of the maximum plastic zone size.

2.5.2. Finite Element Analysis

Generally speaking, numerical methods are always the first choice for nonlinear analysis because of their versatility in dealing with both geometrical and material non-linearities. Other than Groth and Brottare [43], who have tried to estimate the size of the plastic zone, no investigations have dealt with non-linear analysis of interfacial plastic zone using numerical methods. Further studies are required in this area.

2.5.3. Finite Element Iterative Analysis

As described in Section 2.4.2.2., the FEIM was originally developed for evaluating singular stress fields in elastic media [20-21,83-85]. Subsequently, it was extended to nonlinear problems so that the interfacial crack tip stress singularities could be evaluated successfully [86-87], where Barsoum showed that for perfectly elasto-plastic materials, the displacement inside the plastic zone followed zero singularity and the strains in this zone had 1/r singularity. However, no report has been made in the application of FEIM to general elasto-plastic (power law hardening, Osgood hardening or even double linear hardening materials) interface problems.

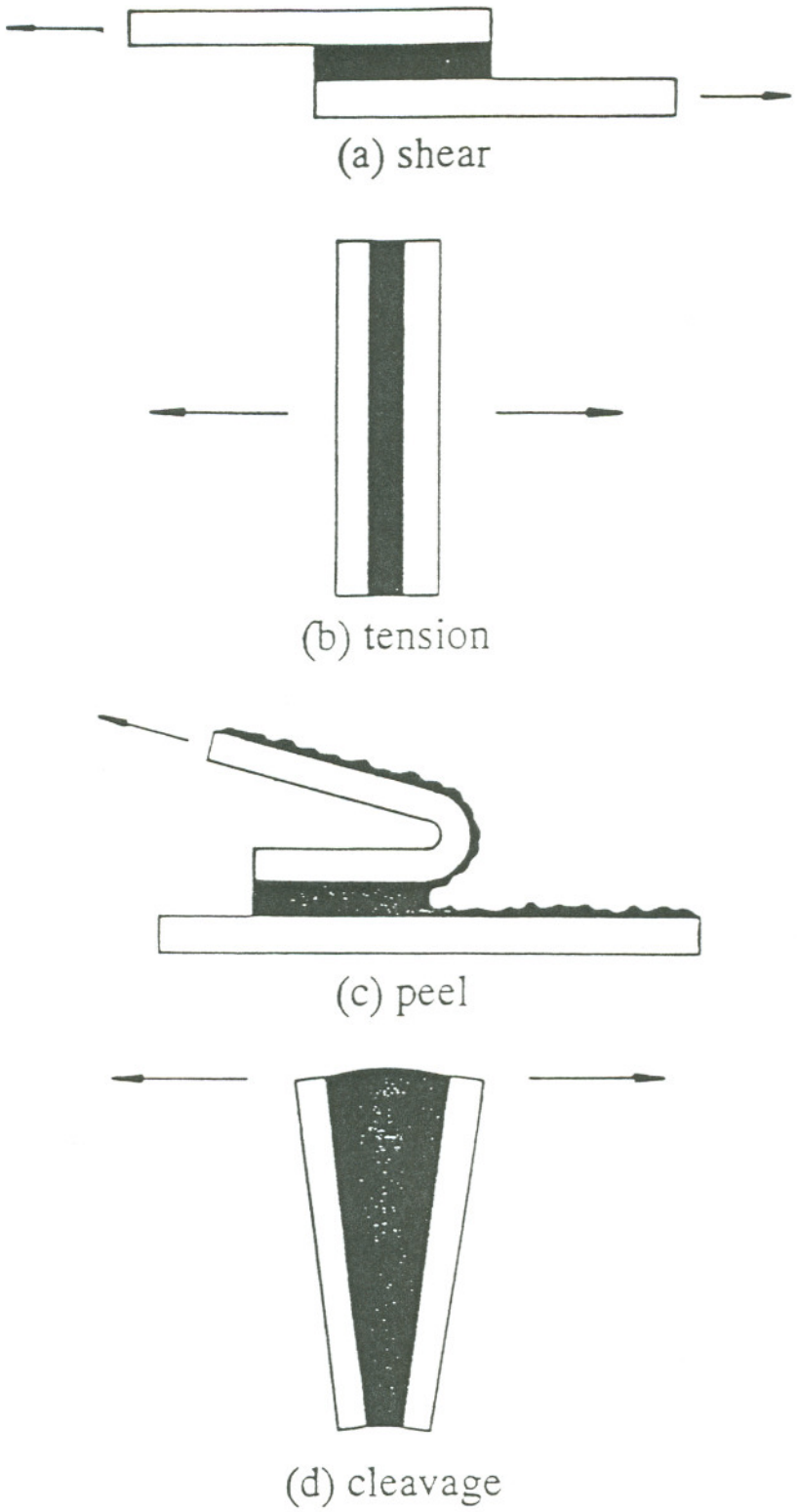

Fig. 2.1 The four important joint deformations [95].

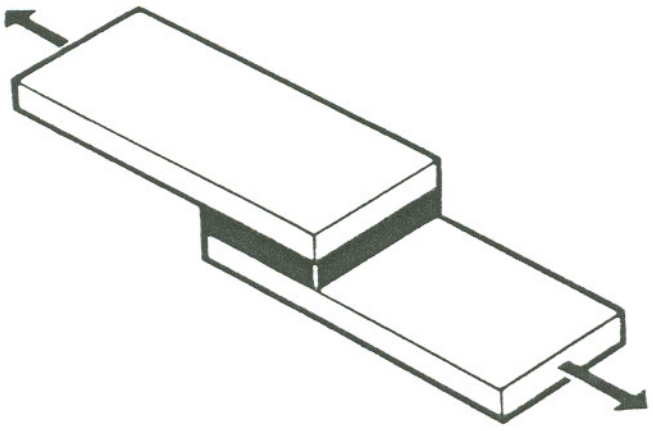

(a) single lap

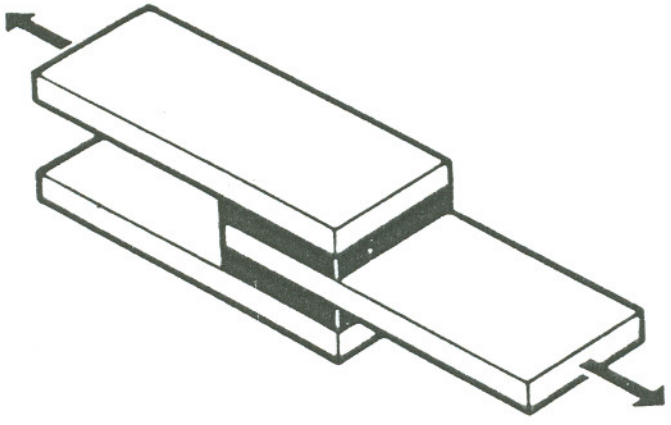

(b) double lap

Fig. 2.2 Single lap and double joints [95].

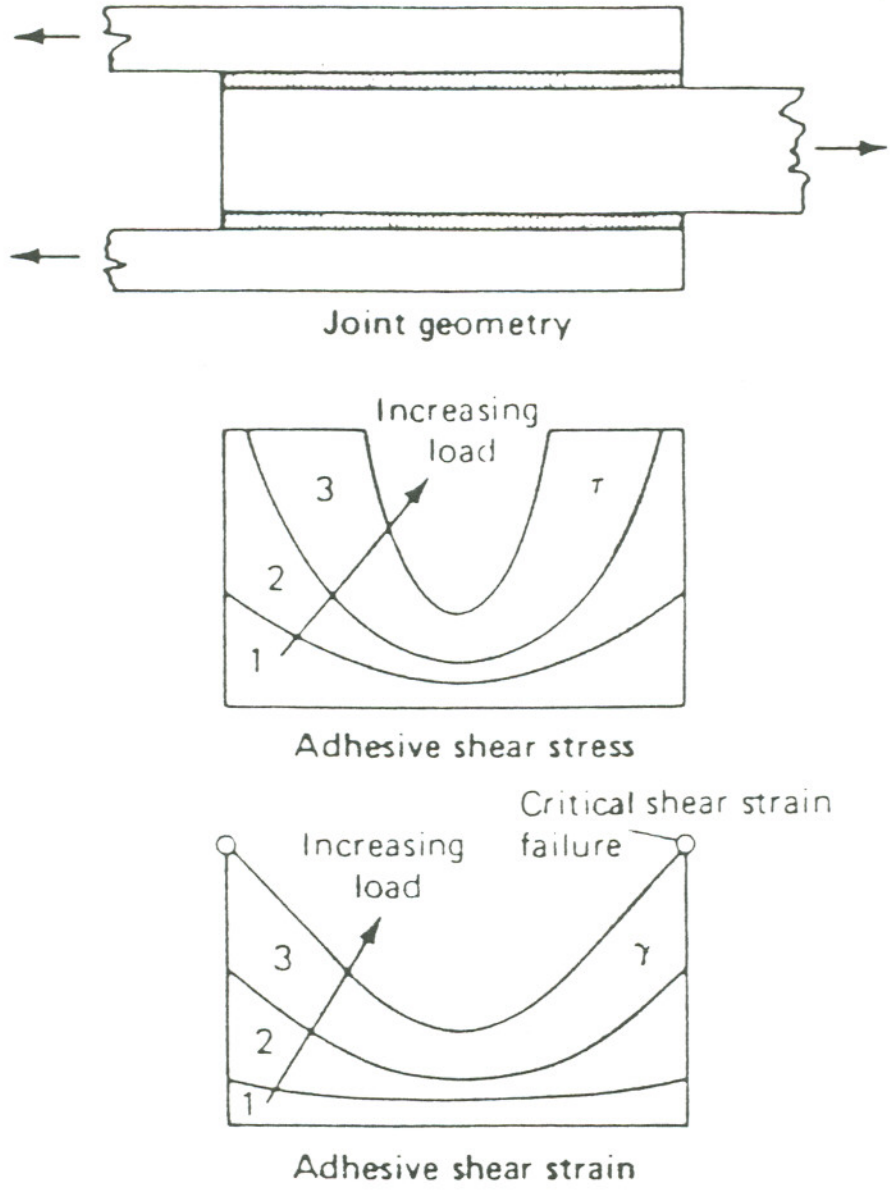

Fig. 2.3 Non-uniform shear stress distribution in a double lap joint [39,57].

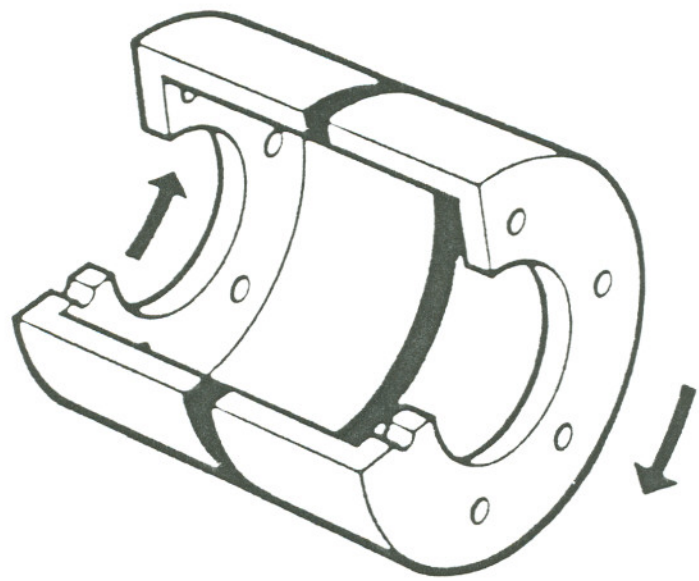

Fig. 2.4 Napkin ring test specimen [95].

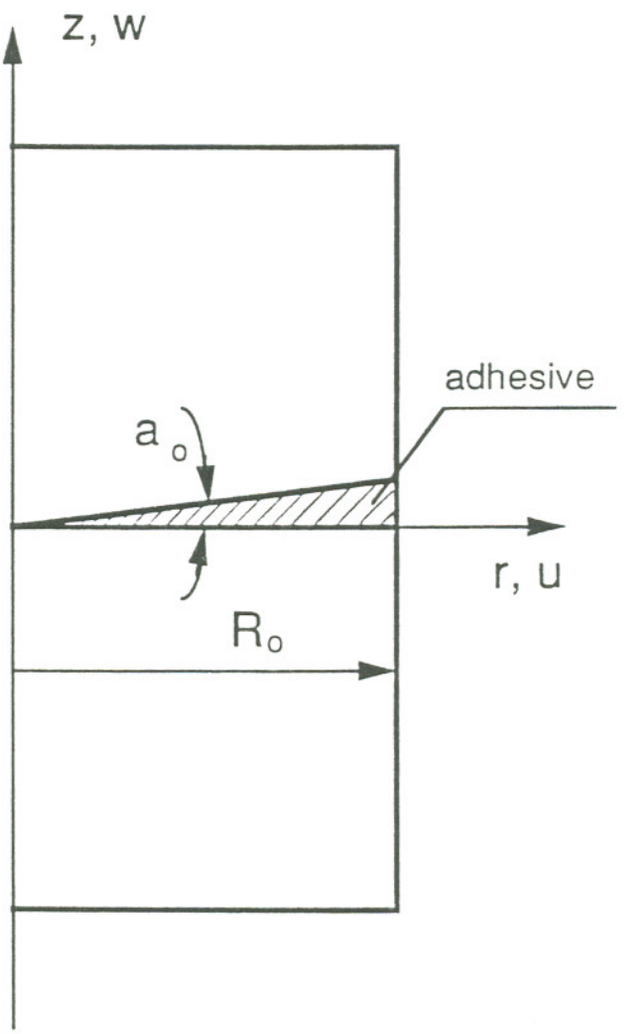

Fig. 2.5 Cone and plate specimen.

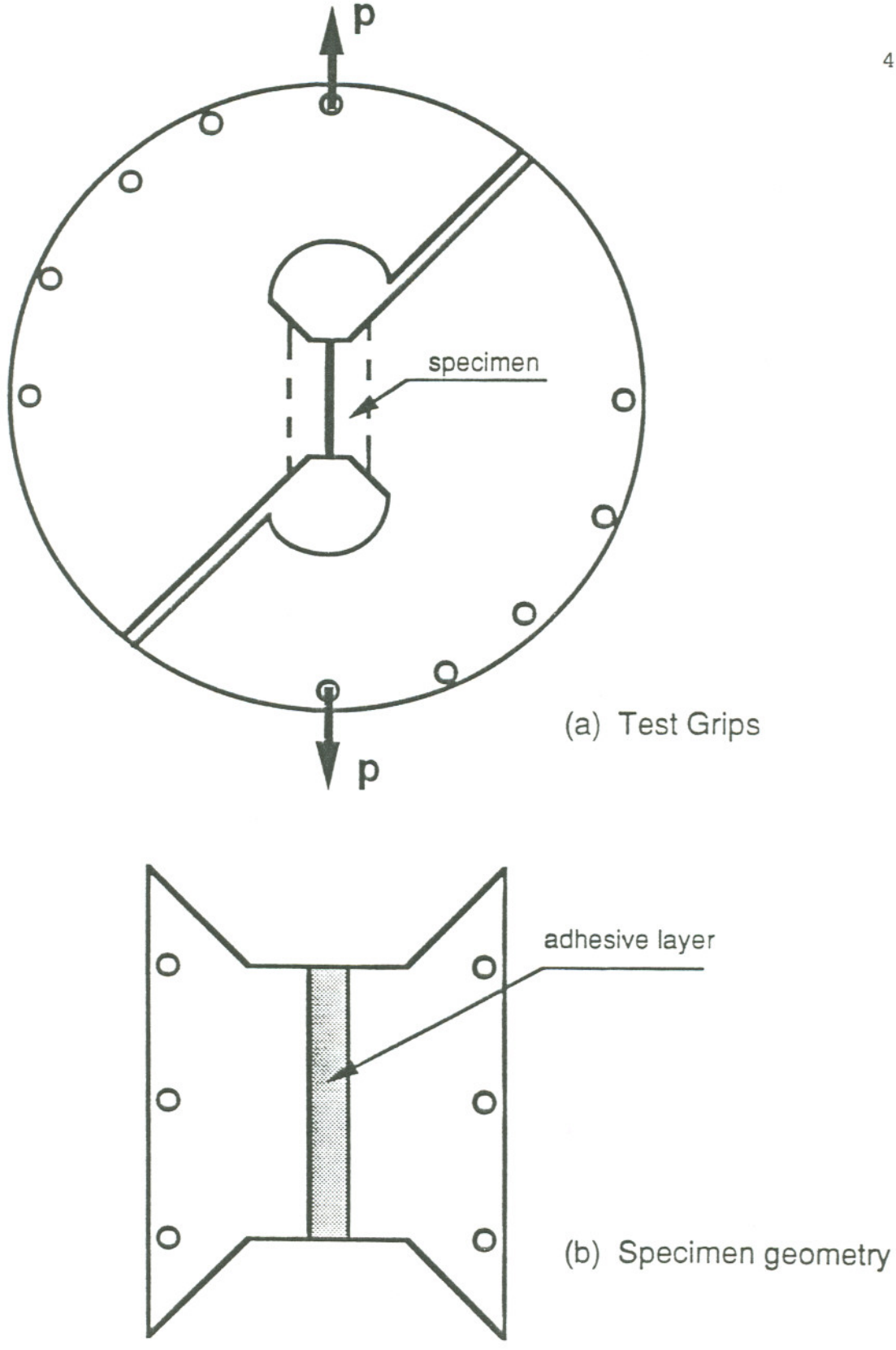

Fig. 2.6 Arcan test grips and specimen geometry.

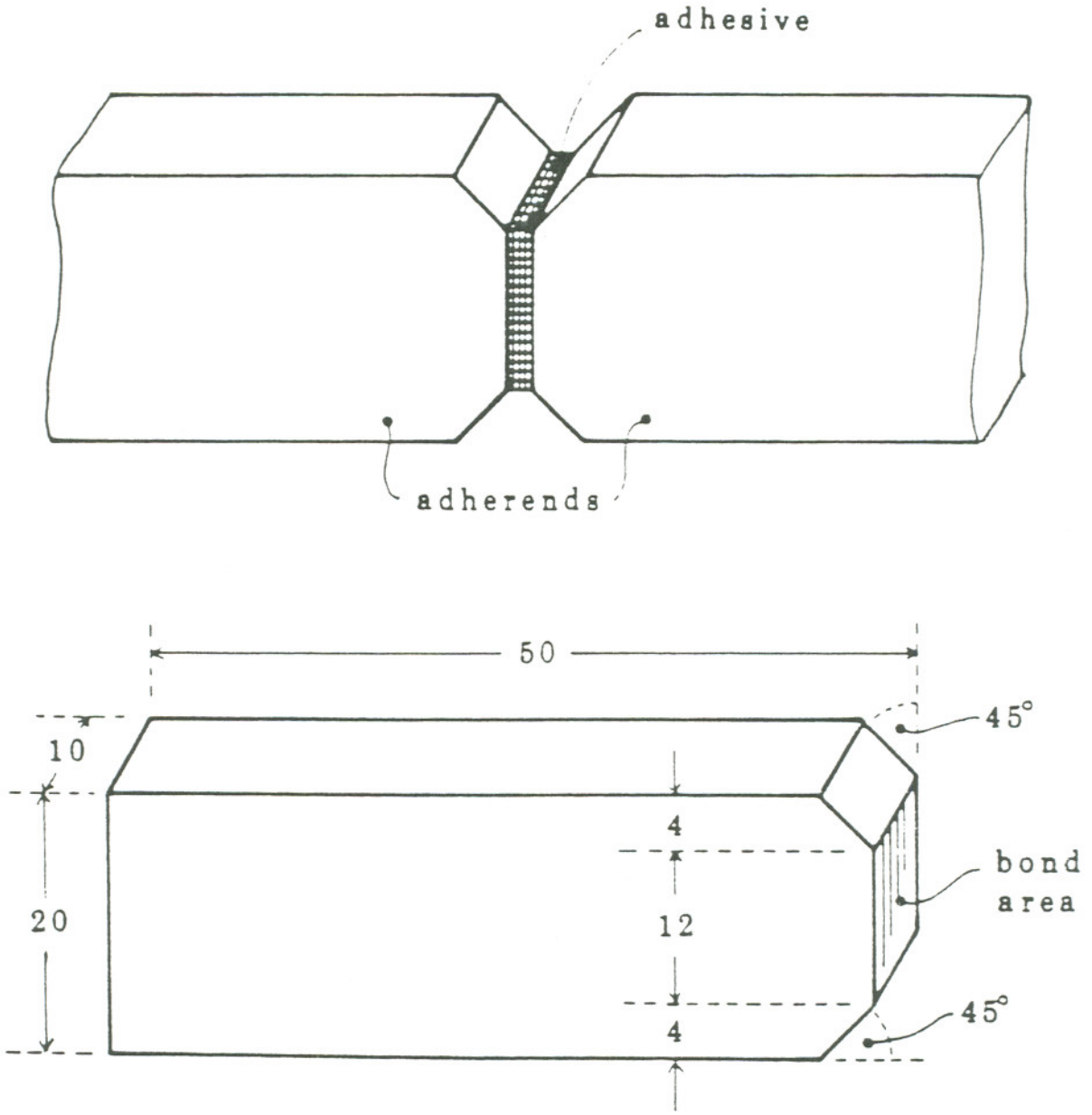

Fig. 2.7 Iosipescu-type specimen for adhesive shear testing [69].

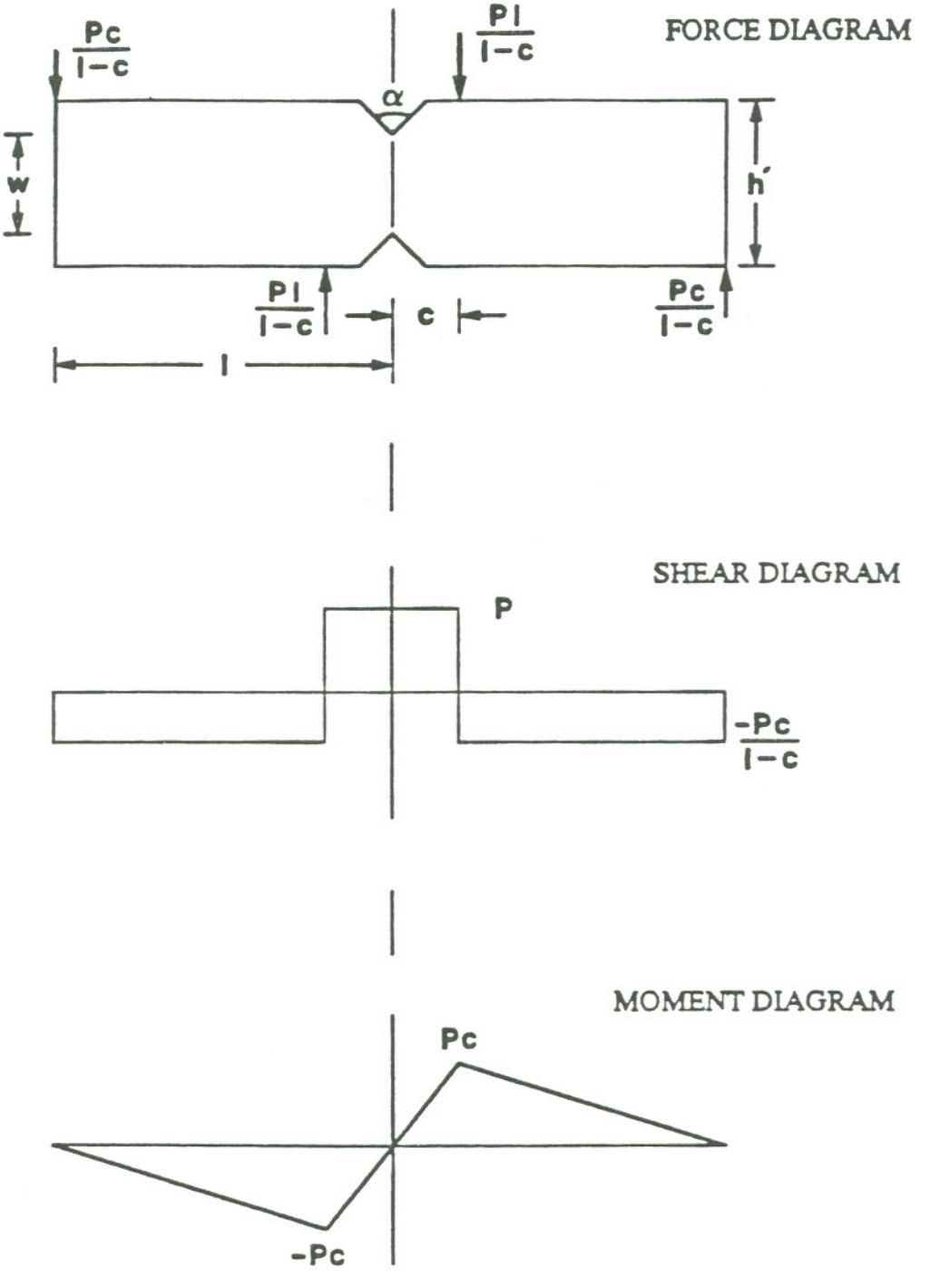

Fig. 2.8 Force,shear, and moment diagrams of the Iosipescu shear test [72].

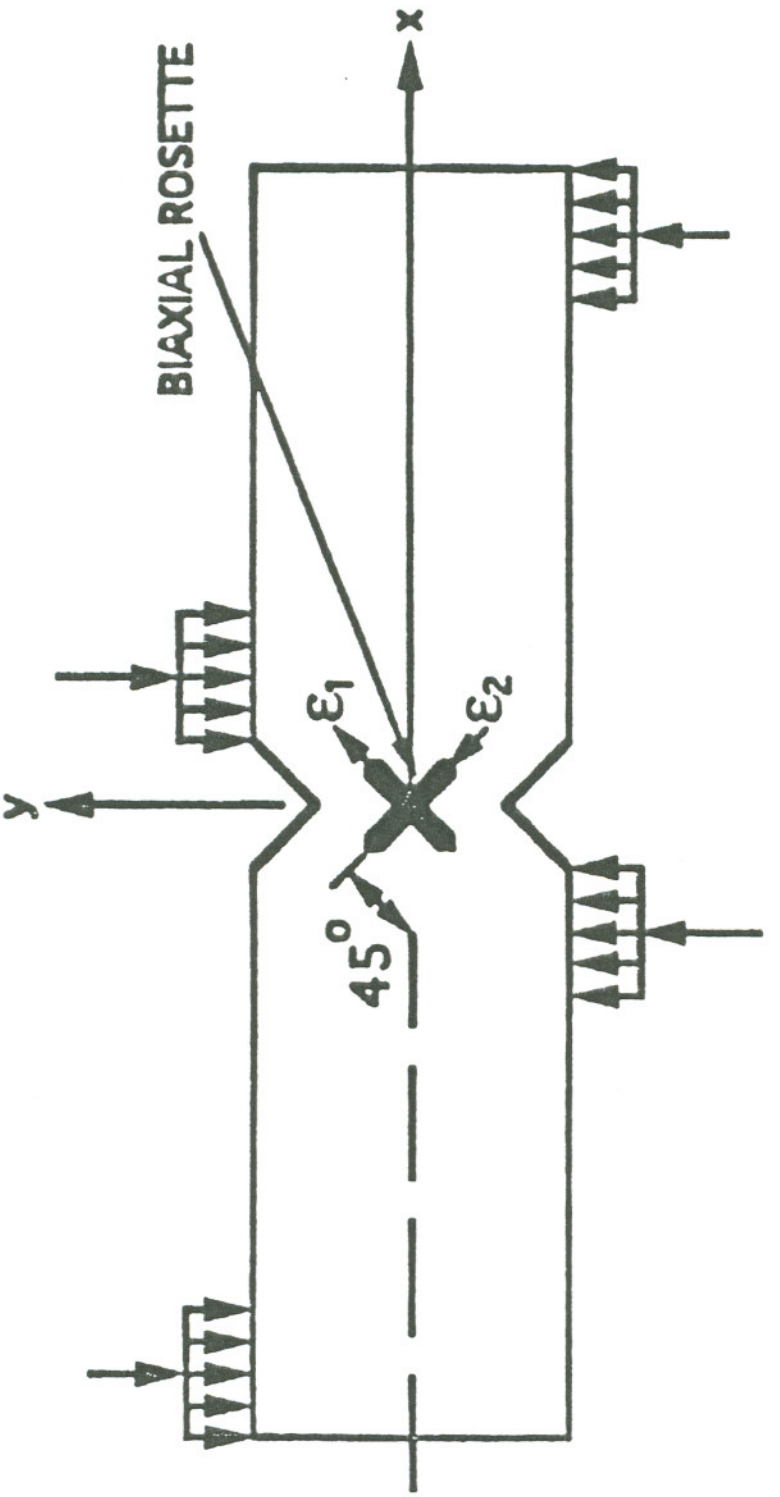

Fig. 2.9 Iosipescu shear test loading configuration [72].

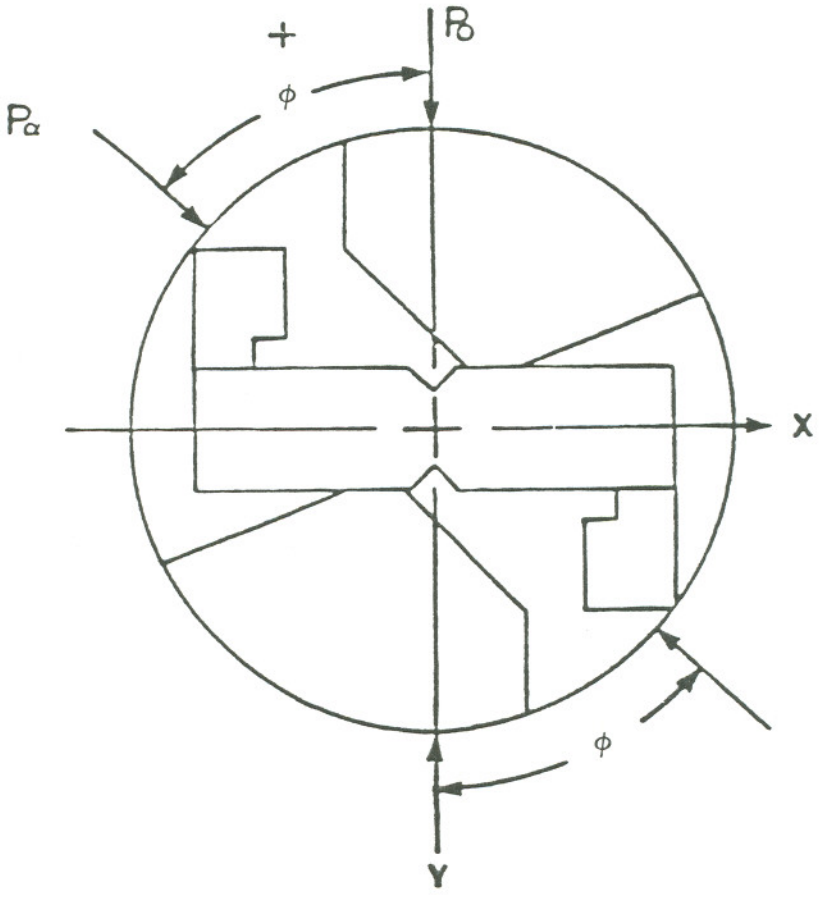

a) loading diagram

Fig. 2.10 Biaxial Iosipescu test [79,91].

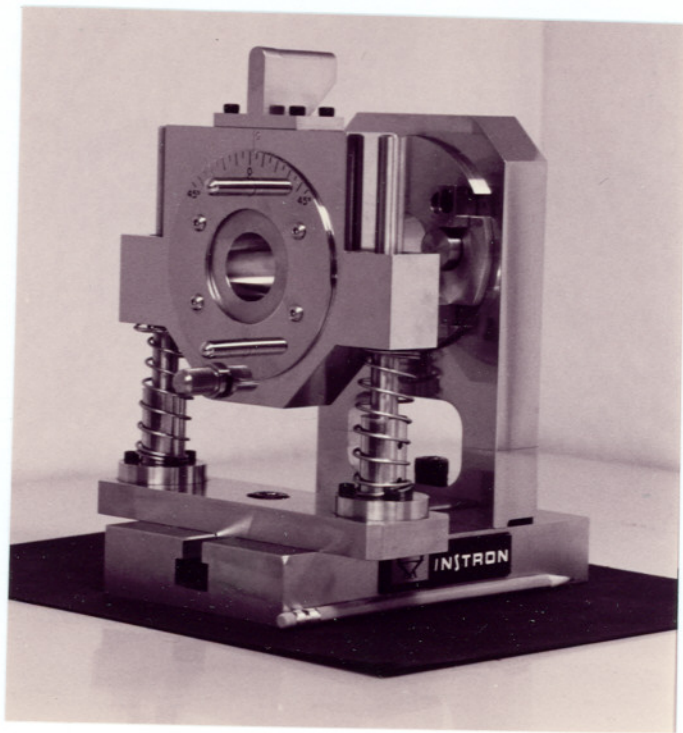

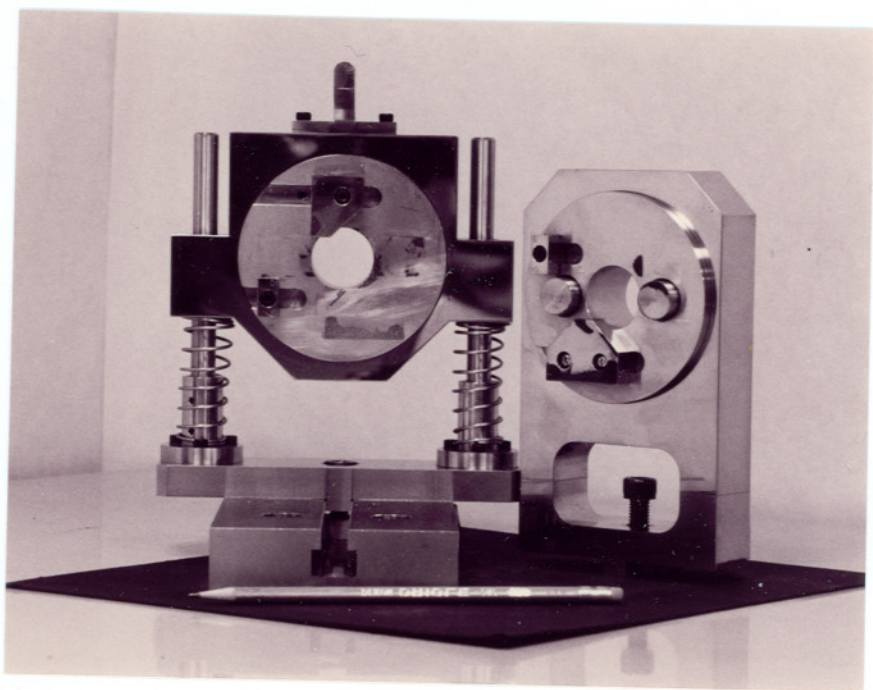

b) test fixture

Fig. 2.10 (continued).

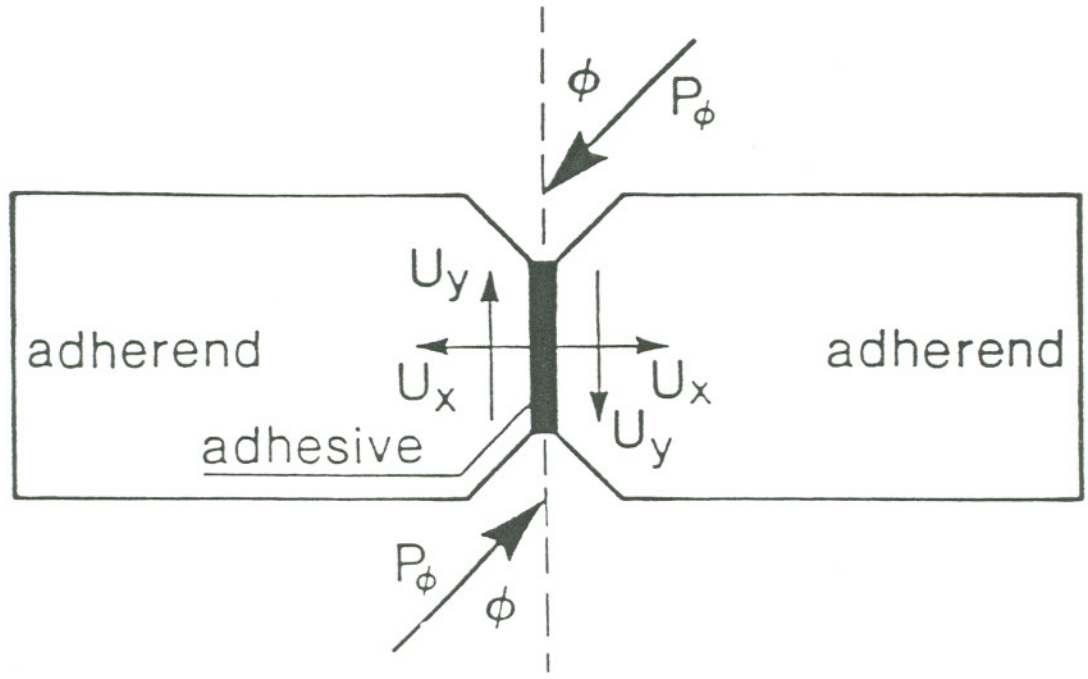

(a) mixed mode loading

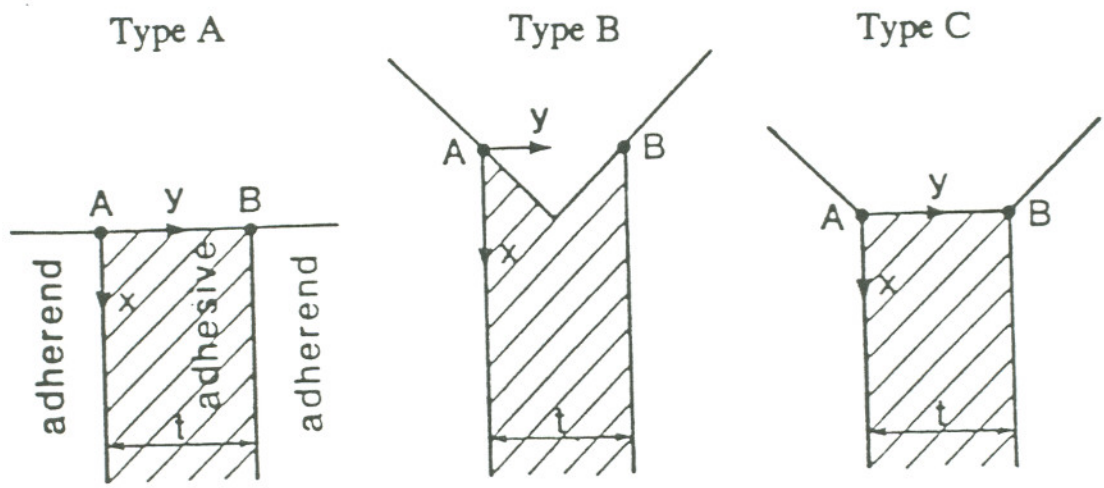

(b) notch tip geometry

Fig. 2.11 Adhesive joint Iosipescu specimen [78,79].

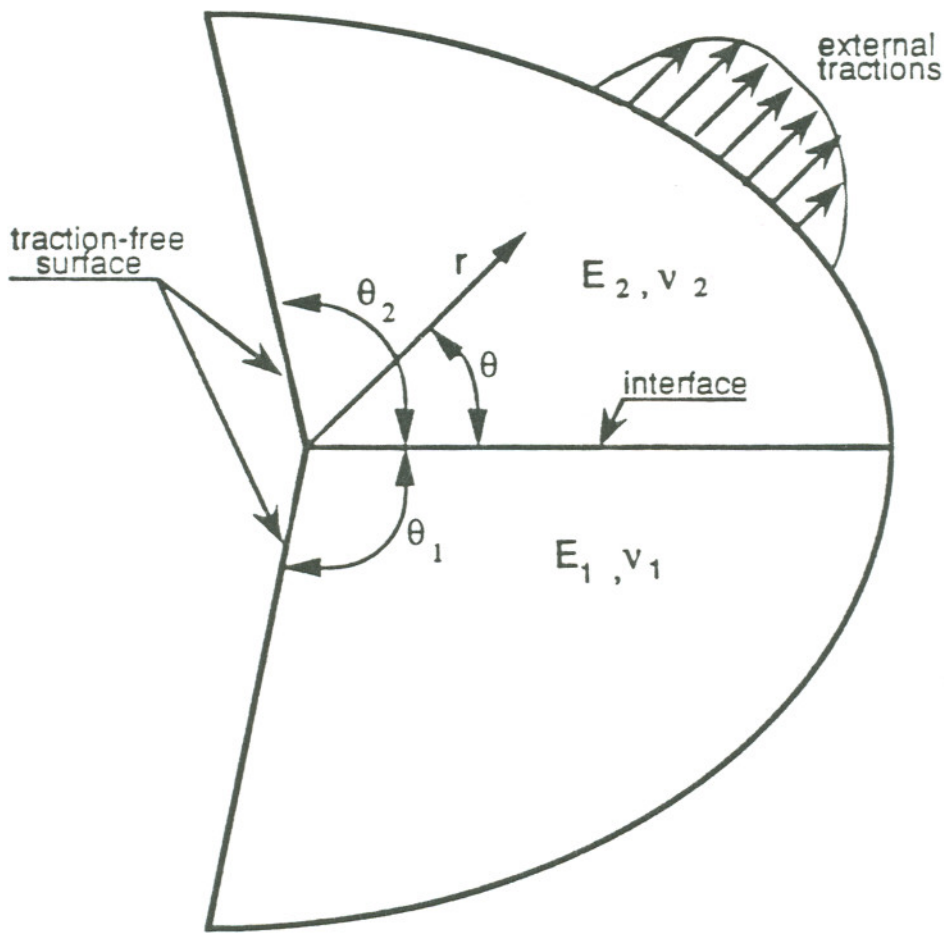

Fig. 2.12 Schematic of a bimaterial wedge.

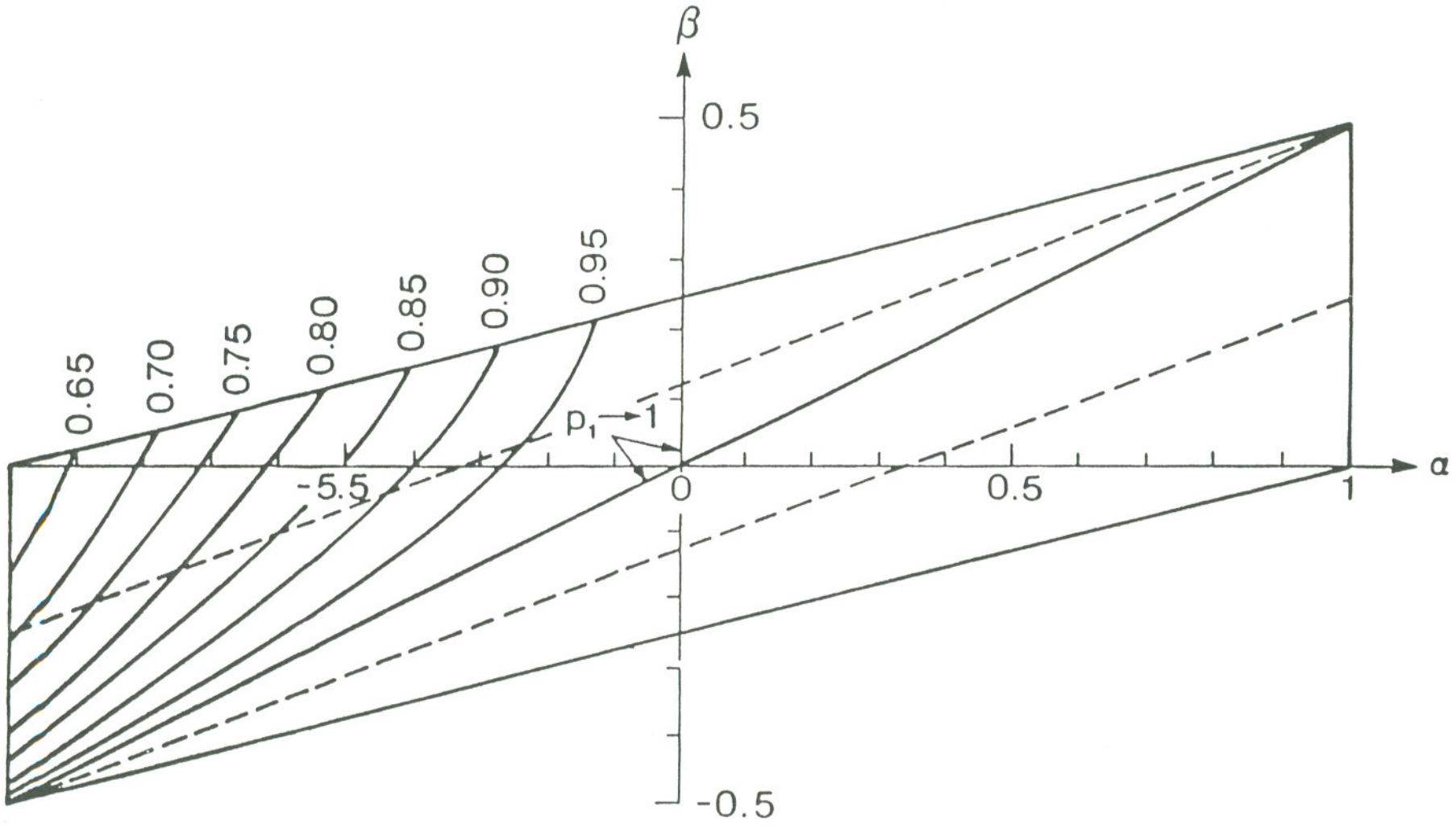

Fig. 2.13 Parallelogram of $\theta_1=-\theta_2=90°$, $\lambda=p_1$ [14].

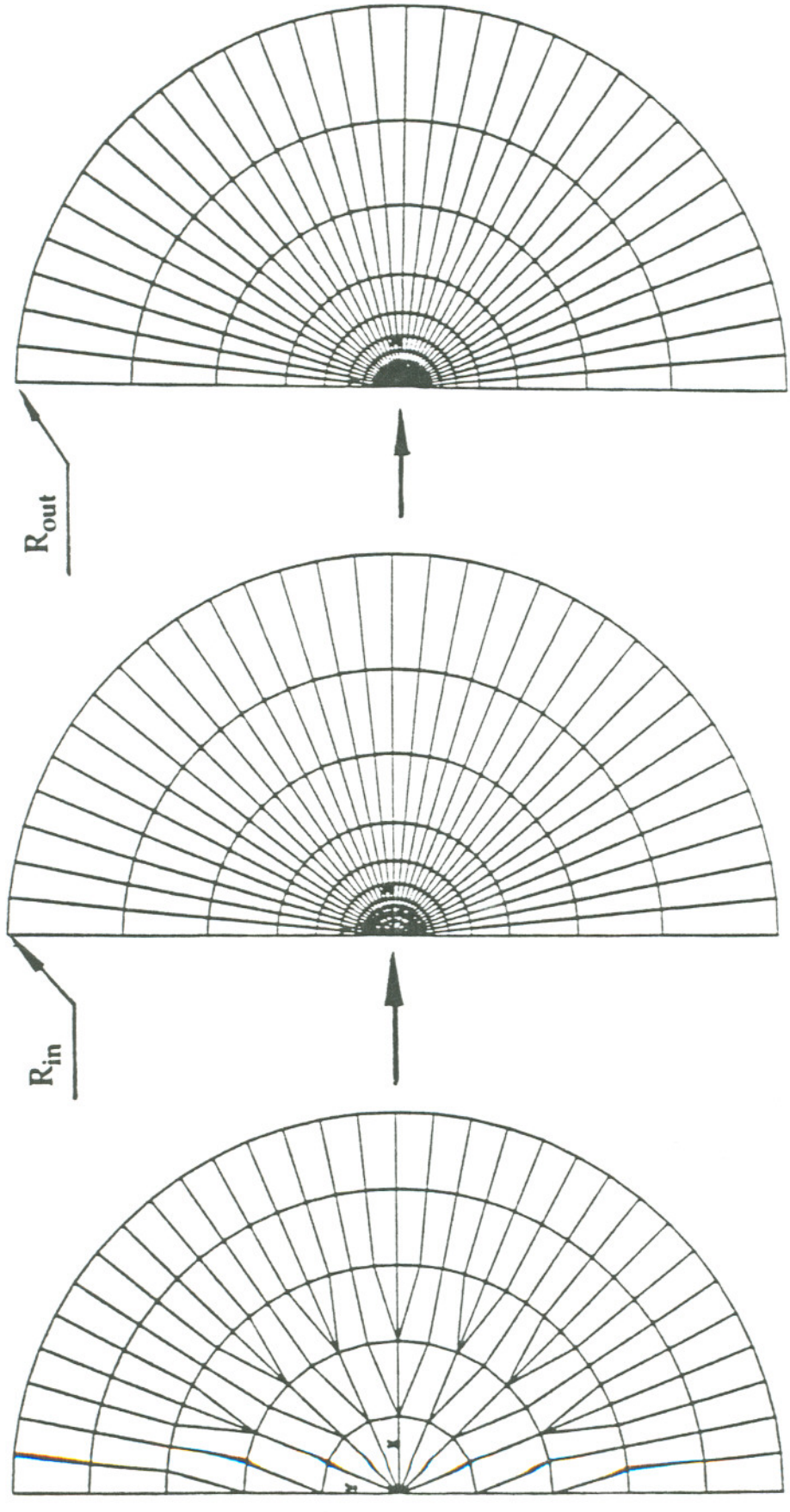

Fig. 2.14 FEIM mesh.

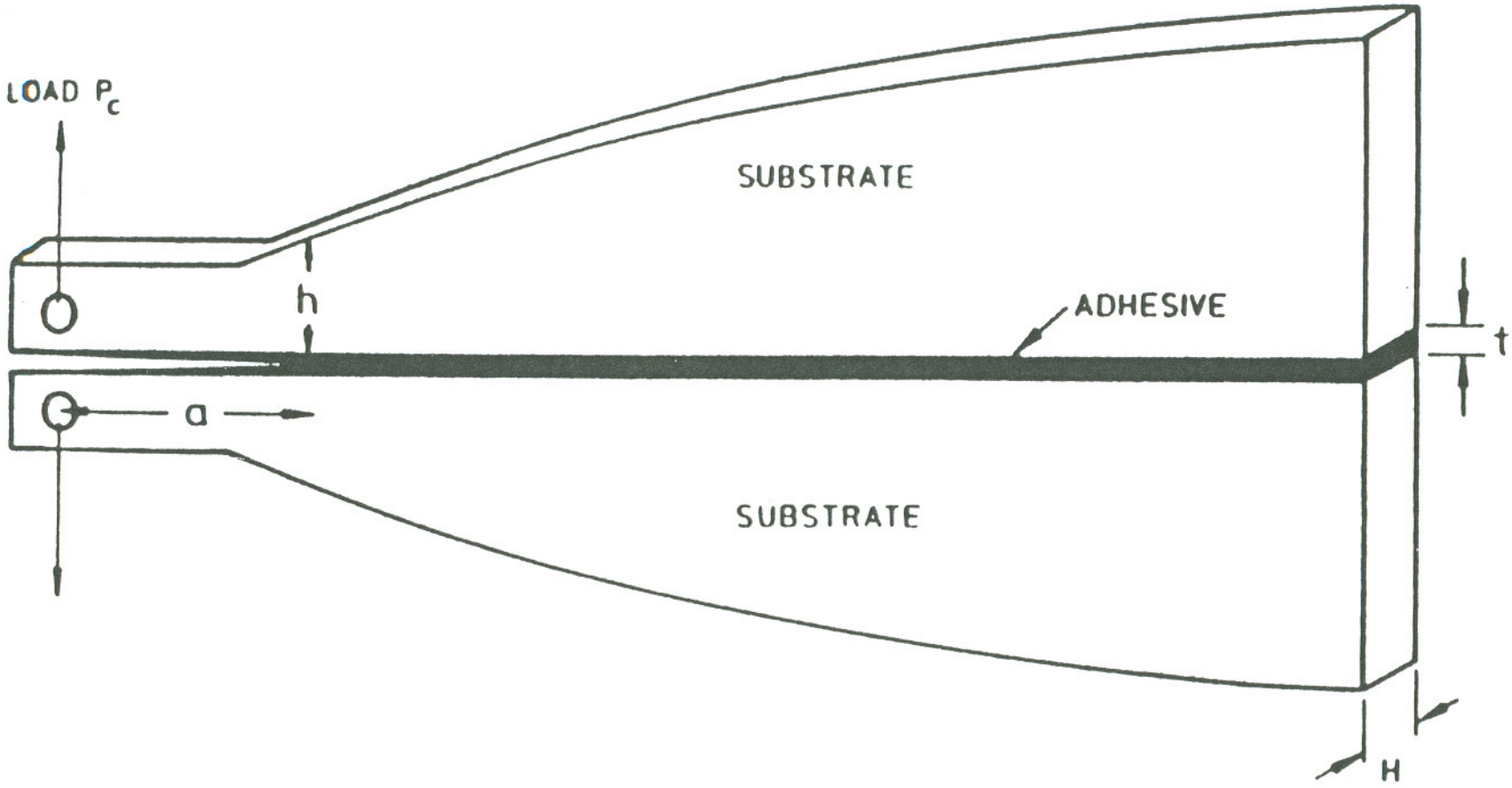

Fig. 2.15 Contour-double-cantilever-beam adhesive joint specimen [63].

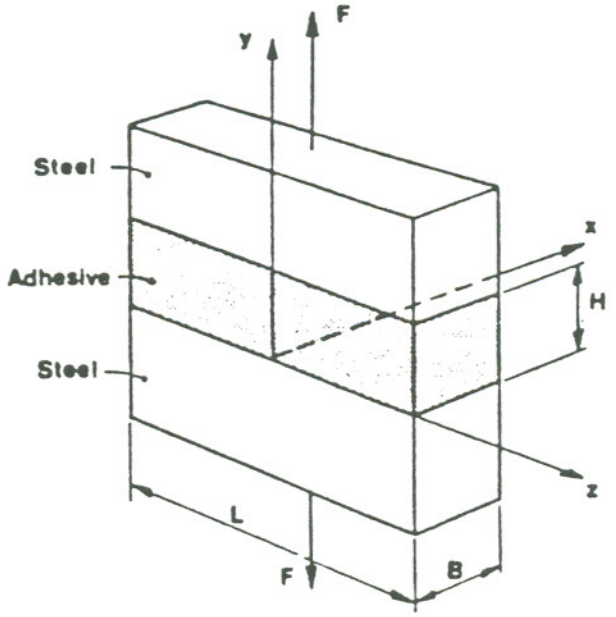

Fig. 2.16 Butt joint geometry [43].

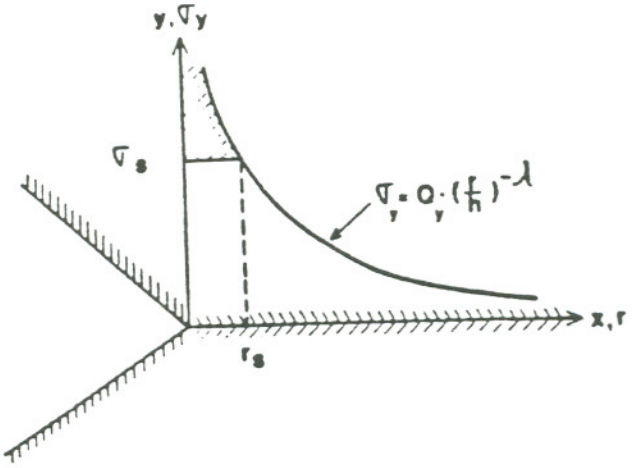

Fig. 2.17 Normal stress along the interface and approximation of plastic zone [43].

CHAPTER 3
PROCEDURES AND RESULTS

3.1. Global Stress Analysis of Adhesive Joints

Knowledge of stress distributions within an adhesive joint is critical to understanding mechanical behaviors of joints. In particular, the location of the maximum stress concentration, the degree of non-uniformity, and the peel-stress allotment should be adequately characterized. For the joints employed in this investigation, an analytical approach was used within the framework of static linear elasticity. In addition, the finite element scheme, a proven, reliable, and accurate method for stress analysis, was used to re-analyze the stresses of the joints. This numerical solutions also provided an estimate of the validity of the analytical results. Furthermore, an experimental study was performed in order to evaluate the mechanical strengths of adhesive joints.

3.1.1. Shear Lag Analysis

Shear lag analysis is a closed-form method based on linear elasticity with some assumptions to make a theoretical procedure possible and simple. It was first introduced by Cox [112] to predict paper strengths and later developed to determine stress distribution inside a composite fiber [113]. In 1971, Hart-Smith used it to compute stresses inside adhesive layers of single-lap and double lap joints [38-40]. More citations on shear lag analysis method can be found in references [38-40,112,113].

3.1.1.1. Link-Joint Model

A link-joint model, an adhesive joint used primarily as a link rather as a loading joint, is shown in Fig. 3.1 with the assumption that a uniform external load σ_0 is applied parallel to the adhesive layer (y-direction). A Cartesian coordinate system is selected to aid the analysis with its center in the axis-symmetric point of the adhesive layer (Fig. 3.1). The adhesive layer is assumed to be linear elastic, to have a Young's Modulus E_s and Poisson's ratio ν_s, and possess a dimension of t in the x-direction (width), l in the y-direction (length) and a unit thickness. The mechanical properties of the adherend are E_r and ν_r, representing the Young's modulus and Poisson's ration correspondingly.

Similar to the assumptions by Cox [112] for calculating the stress distribution inside a single fiber embedded in a matrix, the following conditions are assumed for studying the stresses inside the adhesive layer:

1) The bonding between the adhesive layer and the adherend is perfect.
2) There is no load on all the surfaces of the adhesive layer except the bonding interfaces.
3) The deformation of the adhesive layer is small, *viz.*, small deformation static elastic theory is applicable.
4) The thickness of the adhesive layer, t, is very small relative to the adherend dimension.
5) There is no change of stresses inside the adhesive layer along the x-direction, that is, stresses are uniformly distributed along the x-direction for any fixed y-coordinate values.

Provided that there is a general strain ϵ along the y-direction in the adherend, at a point with the load transferred from the adherend to the adhesive layer may be decided thus,

$$\frac{dF}{dy}=H(u_s-u_r) \tag{3.1}$$

where

F = load in the adhesive layer

H = positive constant (defined later)

u_s = y-direction displacement in the adhesive layer if adhesive is present

u_r = y-direction displacement at the same point if adhesive is absent

When equation (3.1) is differentiated with respect to y, the following is obtained:

$$\frac{d^2F}{dy^2}=H(\frac{du_s}{dy}-\frac{du_r}{dy}) \tag{3.2}$$

From the definition of strain in small deformation elastic theory, we know that

du_s/dy = strain in the adhesive layer

du_r/dy = strain in the adherend = ϵ

The strain in the adhesive layer is due to the transfer of load because the adhesive and adherend have different physical properties. To express this strain in terms of load, the differences in moduli between the adhesive layer and adherend should be taken into account. Let

$$E_{diff}=E_r-E_s \tag{3.3}$$

then

$$\frac{du_s}{dy}=\frac{F}{AE_{diff}} \tag{3.4}$$

where A is the cross-sectional area of the adhesive layer. Substituting equation (3.4) into equation (3.2)

$$\frac{d^2F}{dy^2}=H(\frac{F}{AE_{diff}}-\epsilon) \tag{3.5}$$

The characteristic equation for the above equation is

$$\xi^2-\beta^2=0 \tag{3.6}$$

where

$$\beta=\sqrt{\frac{H}{AE_{diff}}} \tag{3.7}$$

and ξ is the eigenvalue of equation (3.5) with the following values:

$$\xi=\pm\beta \tag{3.8}$$

Equation (3.5) is a non-homogeneous second order differential equation [116]. To obtain a general solution for this equation, one needs first to determine the general solution for its corresponding homogeneous equation:

$$\frac{d^2F}{dy^2}-\beta^2F=0 \tag{3.9}$$

and a special solution for equation (3.5).

With the eigenvalue solutions in equation (3.8), it can be immediately determined that a general solution for equation (3.9) can be written as

$$F_{ho}=Pe^{-\beta y}+Re^{\beta y} \tag{3.10}$$

where P and R are constants.

A special solution to equation (3.5) can be obtained by inspection:

$$F_{sp}=AE_{diff}\epsilon \tag{3.11}$$

Therefore, by summing equations (3.10) and (3.11), the general solution for equation (3.5) is

$$F=F_{ho}+F_{sp}=Pe^{-\beta y}+Re^{\beta y}+AE_{diff}\epsilon \tag{3.12}$$

Taking into account the boundary conditions:

$$F=0 \quad at \ y=\pm\frac{l}{2} \tag{3.13}$$

and substituting them into equation (3.12), one finds the constants P and R to be

$$P=R=-\frac{2AE_{diff}\epsilon}{\cosh(\frac{1}{2}l\beta)} \tag{3.14}$$

Consequently, the y-direction stress distribution inside the adhesive layer is

$$\sigma_y=E_{diff}\epsilon\left[1-\frac{\cosh(\beta y)}{\cosh(\frac{1}{2}l\beta)}\right] \tag{3.15}$$

The variation of the shear stress τ_{xy} along the adherend-adhesive interface is obtained by considering the equilibrium of the forces acting on an element of the adhesive layer as shown in Fig. 3.2

$$dF=2\tau_{xy}dy \tag{3.16}$$

therefore

$$\begin{aligned}\tau_{xy}&=\frac{1}{2}\frac{dF}{dy}\\&=-\frac{\beta E_{diff}\epsilon}{2}\frac{\sinh(\beta y)}{\cosh(\frac{1}{2}l\beta)}\end{aligned} \tag{3.17}$$

From Fig. 3.1, it can be seen that the strain ϵ in the adherend is generated by the applied load σ_o, then:

$$\sigma_o=E_r\epsilon \tag{3.18}$$

Substituting equation (3.18) into equations (3.15) and (3.17), the stress distributions inside the adhesive layer are

$$\sigma_y=\sigma_o\left(1-\frac{E_s}{E_r}\right)\left[1-\frac{\cosh(\beta y)}{\cosh(\frac{1}{2}l\beta)}\right] \tag{3.19}$$

$$\tau_{xy}=-\frac{\beta\sigma_o}{2}\left(1-\frac{E_s}{E_r}\right)\frac{\sinh(\beta y)}{\cosh(\frac{1}{2}l\beta)} \tag{3.20}$$

For two-dimensional problems of this type, H can be defined as [113]

$$H=\frac{G_s}{\ln(w/t)} \tag{3.21}$$

where

G_s = shear modulus of the adhesive

w = total length of the joint (x-direction)

t = width of the adhesive layer

A schematic of the stress distributions is plotted in Fig. 3.3, with the following properties:

l=10 mm, w=20 mm, t=1.0 mm,

E_s=2000 MPa, ν_s=0.35, E_h=73000 MPa, ν_h=0.30

therefore

G=740.74074 MPa, H=247.26533, β=0.059014

If the adhesive is elasto-plastic, there will be plateaus on the stress curves in Fig. 3.3 when σ_y or/and τ_{xy} exceed their yield limits (yielding strength). Such an example was shown by Hart-Smith [57].

3.1.1.2. Butt-Joint Model

Adhesive joints are rarely used as demonstrated in Fig. 3.1. Rather, a frequent joint type is butt joint (Fig. 3.4). If the adherends are adequately long compared with the adhesive layer width, the stress distributions inside the adhesive layer still can be approximately described by equation (3.19) and (3.20) by substituting σ_0 with $(-\nu\sigma_0)$, that is, the y-direction strain is produced due to the Poisson's ratio effect. The stresses are

$$\sigma_y = -\nu\sigma_o\left(1-\frac{E_s}{E_r}\right)\left[1-\frac{\cosh(\beta y)}{\cosh(\frac{1}{2}l\beta)}\right] \tag{3.22}$$

$$\tau_{xy} = \frac{\nu\beta\sigma_o}{2}\left(1-\frac{E_s}{E_r}\right)\frac{\sinh(\beta y)}{\cosh(\frac{1}{2}l\beta)} \tag{3.23}$$

The relative stress distributions remain the same as in Fig. 3.3 if the signs are not considered. For butt joint, however, the most important stress component, the peel stress σ_x, cannot be predicted using this method. A more sophisticated scheme or numerical methods is or are necessary to conduct this calculation.

3.1.2. Airy Stress Function

An Airy stress function approach to solve stress distributions inside adhesive layers of adhesive joint Iosipescu specimens (see Fig. 2.11) is attempted in this section.

A generic configuration for the analysis of stress distributions in an adhesive layer is shown in Fig. 3.5, a portion cut from within the inner loading points of Fig. 2.11a. The layer width t is assumed to be very thin. The force loads F_x and F_y, and moment load M, can be referred from Figs. 2.8 and 2.11, where the moment will be zero along the y-axis (*i.e.*, x=0). The convention for the geometric and mechanical properties is assumed to be the same as in Fig. 3.1.

The major difference between the joints in Figs. 3.4 (or 3.1) and 3.5 is that the adhesive layers experience different deformation. The dominating deformation in Fig. 3.4

is tensile while it is shear in Fig. 3.5. As a result, the approach to simulate the mechanical behavior inside the adhesive joint will be different. Since there is no moment load along the y-axis, it is legitimate to assume that the shear stress distribution inside the adhesive layer will take the form:

$$\tau_{xy}=\frac{F_y}{l}+\frac{dg(x)}{dx}\frac{df(y)}{dy} \tag{3.24}$$

where

F_y = the force component in the y-direction (Fig. 3.5)

l = the adhesive layer length (Fig. 3.5)

g(x) and f(y): functions to be determined

In order to guarantee the shear forces being in equilibrium inside the adhesive layer, that is

$$\int_{-\frac{l}{2}}^{\frac{l}{2}} \tau_{xy}dy=F_y \tag{3.25}$$

f(y) has to be an even function.

If we denote a stress function for the adhesive layer as ψ, as in Section 2.4.1.1, but using a Cartesian coordinate system, stress components will have the following expressions:

$$\sigma_x=\frac{\partial^2\psi}{\partial y^2} \tag{3.26}$$

$$\sigma_y = \frac{\partial^2 \psi}{\partial x^2} \tag{3.27}$$

$$\tau_{xy} = -\frac{\partial^2 \psi}{\partial x \partial y} \tag{3.28}$$

Substituting equation (3.25) into (3.28) and integrating equation (3.28) in terms of x and y, one can obtain ψ:

$$\psi(x,y) = -\frac{F_y}{l} xy - f(y)g(x) + C_1(x) + C_2(y) \tag{3.29}$$

where $C_1(x)$ and $C_2(y)$ are functions to be determined. If equation (3.29) is taken into equation (3.27), σ_y can be expressed as

$$\sigma_y = -f(y)\frac{dg^2(x)}{dx^2} + \frac{dC_1^2(x)}{dx^2} \tag{3.30}$$

By considering the boundary conditions that σ_y is zero at both ends of the adhesive layer, one finds

$$-f(\frac{l}{2})\frac{dg^2(x)}{dx^2} + \frac{dC_1^2(x)}{dx^2} = 0 \tag{3.31}$$

Only $y = l/2$ is used in equation (3.31) because f(.) is an even function. After some mathematical operations, equation (3.31) is equivalent to

$$C_1(x)=D_1x+D_2+f(\frac{l}{2})g(x) \tag{3.32}$$

where D_1 and D_2 are constants. Because all of the first order exponent terms in the stress function do not contribute to the stress components [36], equation (3.29) now can be rewritten as

$$\psi(x,y)=-\frac{F_y}{l}xy+\left[f(\frac{l}{2})-f(y)\right]g(x)+C_2(y) \tag{3.33}$$

let

$$h(y)=f(\frac{l}{2})-f(y), \quad (h(\pm\frac{l}{2})=0) \tag{3.34}$$

(h(.) is also an even function) and equation (3.33) will become

$$\psi(x,y)=-\frac{F_y}{l}xy+h(y)g(x)+C_2(y) \tag{3.35}$$

According to the elastic theory, stress function ψ has to be biharmonic [equation (2.11)], that is,

$$\frac{\partial^4\psi}{\partial x^4}+2\frac{\partial^4\psi}{\partial x^2\partial y^2}+\frac{\partial^4\psi}{\partial y^4}=0 \tag{3.36}$$

Substitute equation (3.35) into (3.36)

$$h(y)\frac{dg^4(x)}{dx^4}+2\frac{dg^2(x)}{dx^2}\frac{dh^2(y)}{dy^2}+g(x)\frac{dh^4(y)}{dy^4}+\frac{dC_2^4(y)}{dy^4}=0 \tag{3.37}$$

and assume that

$$g(x)h(y)\neq 0 \tag{3.38}$$

Divide both sides of equation (3.37) by *g(x)h(y)*

$$\frac{dg^4(x)}{g(x)dx^4}+2\frac{dg^2(x)}{g(x)dx^2}\frac{dh^2(y)}{h(y)dy^2}+\frac{dh^4(y)}{h(y)dy^4}+\frac{1}{g(x)h(y)}\frac{dC_2^4(y)}{dy^4}=0 \tag{3.39}$$

Notice in the constitution of equation (3.39) that the first term is only a function of x, the third is only a function of y, and both the second and fourth terms are functions of x and y. It is therefore necessary to assure that the first and third terms cancel each other. Hence,

$$\begin{cases}\dfrac{dg^4(x)}{dx^4}=D_0\\ \dfrac{dh^4(y)}{dy^4}=-D_0\end{cases} \tag{3.40}$$

where D_0 is a constant. Solving equations (3.40) and taking into account that h(.) is an even function, we obtain

$$g(x)=\frac{D_0}{4!}x^4+D_3x^3+D_4x^2+D_5x+D_8 \tag{3.41}$$

and

$$h(y)=-\frac{D_0}{4!}y^4+D_7y^2+D_8 \tag{3.42}$$

Further substituting equations (3.41) and (3.42) into equation (3.39), we have the following equation:

$$2(\frac{D_0}{2}X^2+6D_3x+2D_4)(-\frac{D_0}{2}y^2+2D_7)+\frac{dC_2^4(y)}{dx^4}=0 \tag{3.43}$$

Similar to the principle of treating equation (3.39), it is legitimate to assume

$$(\frac{D_0}{2}X^2+6D_3x+2D_4)=constant \tag{3.44}$$

to make equation (3.43) have only one variable y left. With equation (3.44), it can be seen that

$$D_0=D_3=0 \tag{3.45}$$

therefore, equation (3.43) is simplified as

$$8D_4D_7+\frac{dC_2^4(y)}{dx^4}=0 \tag{3.46}$$

Solve equation (3.46) and omit the terms lower than order 2, and one gets

$$C_2(y)=-\frac{D_4D_7}{3}y^4+D_9y^3+D_{10}y^2 \tag{3.47}$$

where D_9 and D_{10} are constants.

With a substitution of equations (3.41), (3.42), (3.45) and (3.37) back into equation (3.35), the stress function is found to have the following form:

$$\psi = -\frac{F_y}{l}xy + (D_4x^2 + D_5x + D_6)(D_7y^2 + D_8) - \frac{D_4D_7}{3}y^4 + D_9y^3 + D_{10}y^2 \tag{3.48}$$

so the tensile stress in the y-direction, referring to equation (3.26) is

$$\sigma_x = 2D_7(D_4x^2 + D_5x + D_6) - 4D_4D_7y^2 + 6D_9y + 2D_{10} \tag{3.49}$$

By the principle of equilibrium in the x-direction, one can write

$$\begin{aligned} F_x &= \int_{-\frac{l}{2}}^{\frac{l}{2}} \sigma_x dy \\ &= 2D_7(D_4x^2 + D_5x + D_6)l - \frac{1}{3}D_4D_7l^3 + 2D_{10}l \end{aligned} \tag{3.50}$$

Since F_x is a constant whenever the external load is fixed, therefore

$$\begin{cases} D_4 = D_5 = 0 \\ D_6D_7 + D_{10} = \dfrac{F_x}{2l} \end{cases} \tag{3.51}$$

Further, via the moment equilibrium, the following relationship has to be held:

$$\begin{aligned} M &= \int_{-\frac{l}{2}}^{\frac{l}{2}} \sigma_x y dy = \int_{-\frac{l}{2}}^{\frac{l}{2}} \left(\frac{F_x}{l} + 6D_9y\right) y dy \\ &= \frac{1}{2}D_9l^3 \end{aligned} \tag{3.52}$$

where M, a function of x-ordinate, is the bending moment on the corresponding plane and can be calculated from Fig. 2.8. Consequently, D_9 can be determined:

$$D_9=\frac{2M}{l^3} \tag{3.53}$$

and one can immediately solve for the stress functions by substituting equations (3.51) and (3.53) back into equation (3.48):

$$\psi=-\frac{F_y}{l}xy+\frac{F_x}{2l}y^2+\frac{2M}{l^3}y^3 \tag{3.54}$$

so that the stress components can be computed using the following equations:

$$\begin{cases}\sigma_x=\dfrac{F_x}{l}+12\dfrac{M}{l^3}y\\ \sigma_y=0\\ \tau_{xy}=\dfrac{F_y}{l}\end{cases} \tag{3.55}$$

Assuming that an adhesive joint Iosipescu specimen (Fig. 2.11) has a $l=10$ mm adhesive layer length along the notch root axis and is under pure shear loading with P=10 N, stress distributions within the layer can be calculated using formula (3.55) and depicted in Figs. 3.9-3.11, where these closed form solutions are used to compare with the numerical results.

3.1.3. FEM Analysis

A schematic of adhesive joint Iosipescu specimens is shown in Fig. 2.11. The

adherend can be either isotropic or orthotropic. The adhesive layer thickness (t) is adjustable according to experimental purposes.

The Iosipescu method, originally designed to determine the shear properties of metals in 1967 [100], has been investigated by many researchers [101-103], then modified to measure in-plane biaxial mechanical properties of metals and composites [104-107, 110]. The latest version is the modified biaxial Iosipescu test fixture (Fig. 2.10a) developed at the University of Cambridge [107] and now being marketed by Instron Corporation. The loading diagram of the fixture is shown in Fig. 2.10b. The Iosipescu specimen can be tested on this fixture in a pure shear or in-plane biaxial mode.

Figure 3.6 is a schematic drawing of a Type A adhesive joint Iosipescu specimen. Its finite element representation is shown in Fig. 3.7, which is assumed to be under biaxial loading conditions. An examination of Fig. 3.7 reveals that if the boundary conditions are taken into account, no axial symmetry is available; therefore, a whole specimen mesh is necessary. The interface corner was very finely meshed (Fig. 3.8c) so that the complicated stress state could be adequately simulated. The external loadings were assumed to be uniformly distributed forces over the loading surfaces (Fig. 3.6), since force-couple boundary conditions were found to best approximate the experimental loading configurations [89-91]. The summation of the external loading at any individual loading location was kept the same, disregarding the loading angles, which would make the results comparable based on the same external loading magnitude. Eight-node isoparametric elements were employed. The total number of elements was 5984 and the total number of nodes 18373. All of the finite element calculations were accomplished using the software code of ANSYS, Version 4.4A [54].

The other two types of Iosipescu joint specimens were meshed and calculated similarly. All of these joint root mesh configurations are depicted in Fig. 3.8, where finer elements were employed at all the interface corners and sharp notch tips in order to capture the potential singular stress behavior at those points. The degree of freedom (DOF) or the total number of elements varies, but the schemes are identical.

Computations were carried out assuming linear elastic deformation.

Assuming that the loading angle is ϕ, the externally applied compressive load is P (Figs. 2.10a and 2.11), the distance between the inner loads is a, and the distance between the outer load is b (Fig. 3.6), the specimen width is 20 mm, the force couples P_a and P_b (Fig. 3.7) can be evaluated as follows according to the force and moment balance requirement:

$$P_a = \frac{(a+20\tan\phi)P}{a-b+40\tan\phi} \tag{3.56}$$

$$P_b = \frac{(b-20\tan\phi)P}{a-b+40\tan\phi} \tag{3.57}$$

Obviously, the force components along x- and y-directions along the adhesive center line (x=0) are

$$\begin{cases} F_y = -P\cos\phi \\ F_x = -P\sin\phi \end{cases} \tag{3.58}$$

Therefore, the nominal shear stress along the adhesive center line is

$$\tau_{xy} = -\frac{P\cos\phi}{10} \tag{3.59}$$

and the tensile stress in x-direction along this line is

$$\sigma_x = -\frac{P\sin\phi}{10} \tag{3.60}$$

The minus signs in equations (3.59) and (3.60) are used to obey the sign convention in the theory of elasticity [36]. Throughout this analysis, the externally applied compressive force is fixed at 10 N. Therefore, under pure shear loading conditions, the nominal shear stress along the adhesive center line will have the value of -1 MPa.

3.1.3.1. Geometric Effects

Three types of notch root configurations (Fig. 2.11b and 3.8) were taken into account, with an assumption that the distances along the notch root axis would retain the same value of 10 mm for all three cases. A detailed schematic drawing of the joints of Type A is shown in Fig. 3.6 with its FEM representation in Fig. 3.7. Stress distributions of shear and tensile in x- and y-directions inside the adhesive layers are depicted in Figs. 3.9, 3.10 and 3.11 for all three geometries under pure shear loading. The location labels on these three figures are interpreted as if there is a Cartesian coordinate system placed at the four-fold center of the adhesive layer for individual specimens (see Fig. 3.5).

3.1.3.2. Loading Angle Effects

When the adhesive layer was assumed to be 0.2 mm of Type A joint, the shear stress distributions along different paths are shown in Fig. 3.12 under various loading conditions. Figure 3.13 shows the tensile stresses along x-direction (σ_x) and Figure 3.14 reveals the tensile stresses along y-direction (σ_y) under those conditions.

3.1.3.3. Adhesive Thickness Effects

Shear stress distributions along different paths for external loadings in a pure shear mode are shown in Fig. 3.15 for adhesive layer thicknesses of 0.1, 0.2 and 0.5 mm; in addition, σ_x is shown in Fig. 3.16 and σ_y in Fig. 3.17.

For loading angles other than pure shear, one typical case of a=-30° loading angle (shear and tension) is presented along several paths for the three adhesive layer thicknesses. Figure 3.18 shows the shear stress distributions, Fig. 3.19 the x-direction, and Fig. 3.20 the y-direction tensile stress configurations. For a direct view of stress uniformity inside the adhesive layer, equivalent stress contours for different adhesive layer thicknesses at loading angle 30° (shear and compression) are shown in Fig. 3.21.

3.1.4. Experimental Approach

Adhesive joint specimens were made for experimental studies. All three types were considered; their photographs are shown in Figs. 3.22-3.24. A schematic of specimen of Type A is shown in Fig. 3.6 to demonstrate the specimen dimensions. The adherends are aluminum, and adhesives are 3M[1] brand brittle DP 100 and ductile DP 190 [92-94]. All tests were conducted at room temperature.

3.1.4.1. Procedure

To conduct adhesive joint Iosipescu specimen tests, three steps are necessary: adherend preparation, specimen making, and joint testing.

Adherend Preparation:

1. Machine the aluminum adherends into a shape as in Fig. 3.22-24 with a surface finish of about grade 16L.
2. Polish the to-be-glued surfaces with #C600 emery paper.
3. Rinse the adherends sufficiently in running tap water.
4. Degrease them using Acetone in a supersonic tank for 5 minutes.

---

[1] 3M is a trademark.

5. Clean them in Oakite[2] Aluminum Cleaner solution (see below) at 88±5°C for about 15 minutes.
6. Rinse them in running tap water immediately.
7. Put them in acid etch solution (see below) for 10 minutes at 65±3°C.
8. Rinse them in running tap water immediately.
9. Dry them in the air for 15 minutes.
10. Dry forcefully at 65±5°C for 10 minutes.

Oakite[2] Aluminum Cleaner Solution [115]

`Preparation:` Add total required quantity of Aluminum Cleaner 164 to half the volume of water, cold, while stirring and heat to about 82°C. Then, add the remaining half of water and adjust solution to operating temperature.

`Application:` It is normally used at 45 to 75 g/l of water in the temperature range of 52 to 82°C.

Acid Etch Solution [92-94]

Chemicals	wt%
Sodium dichromate	1
Sulfuric acid, 66°Be	9
2024-T3 aluminum (dissolved)	0.04
Tap water	24.8

Specimen Making:

1. Load the well-cleaned adherends on the Bonding Assembly[3] (Fig. 3.25) with

---

[2] Oakite is a trademark.

[3] Bonding Assembly is a jig made in OGI for making adhesive joint Iosipescu specimens.

teflon tape laid under the adherends to prevent them from being bonded to the jig.

2. Apply the appropriate adhesive to the (joint) gap.
3. Let the specimens cure at room temperature (23 ± 1°C) for 24 hours (DP 100 adhesive) or 7 days (DP 190 adhesive).
4. Modify the root geometries to the desired shape using a sharp surgical blade.
5. Polish all the surfaces with #C600 sandpaper.
6. Measure all the dimensions of a specimen. At least three points should be evaluated for each dimension and the average value is the one used as its namely measure.

Joint Testing:

1. Load the specimen on the Modified Iosipescu Fixture (Fig. 2.10) and set the loading angle as desired.
2. Connect all the sensors and recording equipment.
3. Set the loading displacement speed at 0.0025 mm/sec for rigid adhesive joints or 0.0125 mm/sec for flexible adhesive specimens.
4. Conduct the test on an Instron[4] mechanical testing machine.
5. Save the data and broken specimens for further processing and examinations.

3.1.4.2. General Observations During Testing

Typical load-displacement diagrams for adhesive joint Iosipescu specimen testing are shown in Fig. 3.26a, b and c, which are the three categories classified according to the following:

(1) The force load went up almost linearly with an increase in the displacement until the specimen was broken (Fig. 3.26a). The percentage of specimens broken

[4] Instron is a trademark.

in this manner was about 32%.

(2) The load rose almost linearly when the displacement increased until a kink point was observed (Fig. 3.26b). This kink indicates that there was an instant unloading at that moment. Afterwards, the load incremented again up to the breaking point. This category took place in about 38% of the specimens.

(3) The load ran up almost linearly when the displacement increased until a kink point was noticed; however, one or more kinks would appear as the external displacement load kept going up until the final rupture of the joint (Fig. 3.26c). About 30% of the specimens tested failed this way.

Both the first kink and the final rupture loads were recorded. These loads was used to analyze the mechanical behavior of the joints. However, for the first case, it is obvious that the first kink and the rupture loads were the same (Fig. 3.26a).

After the first kink popped up, a small crack at the notch root was initiated, most of the time at the interface corner (Figs. 3.58, 3.60 and 3.62) and sometimes at the notch sharp tip for Type B geometry (Fig. 3.59). Sudden crack propagation was found to occur with the appearance of multiple kinks. In this scenario, the crack surfaces were generally step-wise (Fig. 3.63) for rigid adhesive joints. For joints bonded by flexible adhesives, the fracture surfaces were flat from a macroscopical viewpoint (Fig. 3.65) since the failure pattern was peel-off for these types of joints. More observations and discussions on crack surfaces will be given in later sections.

3.1.4.3. Experimental Results

Results of tests for different notch root geometries and loading angles are presented in Figs. 3.27 and 3.28, in which only the rigid adhesive was used with an adhesive layer thickness being kept at 1.0 mm. Two types of adhesives, DP 100 and DP 190, were employed to conduct another set of tests so that the effects of adhesive

properties could be observed. The data obtained are plotted in Figs. 3.29 and 3.30. Thickness effect can also be considered through comparison of Figs. 3.27 to 3.30 in terms of rigid adhesive (DP 100).

3.2. Singular Stress Analysis at an Interface Corner

The stress singularity at an adhesive interface is a major problem for joint designs. In evaluating the asymptotic field for corner stress singularity, it is essential to consider various joint geometries, adhesive and adherend elastic properties, and nonlinear material effects. The asymptotic singular fields for many adhesive joint geometries are not available due to the complexity of the analytical formulations.

3.2.1. Composite Parameter Calculation Using Williams' Stress Function

In light of the literature review in Chapter 2, it can be deduced that when the geometry of a bimaterial wedge is fixed (for instance, Fig. 2.12), the singular power λ can be simplified as a function of a pair of composite parameters α and β [equation (2.55)] [27,81]; however, the parameters were obtained using complex potentials that generally are difficult to understand without a mastery of complex functions and integral transformations. In this section, the simple Williams' stress function will be used to extract these two parameters.

A bimaterial wedge with an arbitrary geometry as in Fig. 2.12 is assumed. In addition, all the geometrical and physical property conventions remain the same as in Section 2.4.1. Therefore, from equations (2.13)-(2.16), the individual stress components in the polar coordinate system can be written as

$$\begin{aligned}\sigma_{rr}=(1-\lambda)r^{-\lambda}[&(2+\lambda)\sin(\lambda\theta)A_1+\cos(\lambda\theta)A_2)\\&-(2-\lambda)(\sin((2-\lambda)\theta)A_3+\cos((2-\lambda)\theta)A_4)]\end{aligned} \tag{3.61}$$

$$\sigma_{\theta\theta}=(2-\lambda)(1-\lambda)r^{-\lambda}[(2+\lambda)\sin(\lambda\theta)A_1+\cos(\lambda\theta)A_2) +\sin((2-\lambda)\theta)A_3+\cos((2-\lambda)\theta)A_4] \tag{3.62}$$

$$\sigma_{r\theta}=(1-\lambda)r^{-\lambda}[\lambda(-\cos(\lambda\theta)A_1+\sin(\lambda\theta)A_2) +(2-\lambda)(-\cos((2-\lambda)\theta)A_3+\sin((2-\lambda)\theta)A_4)] \tag{3.63}$$

From the theory of elasticity, the relationship between displacements and strains can be written in the following form:

$$\epsilon_{rr}=\frac{\partial u_r}{\partial r} \tag{3.64}$$

$$\epsilon_{\theta\theta}=\frac{\partial u_\theta}{r\partial\theta}+\frac{u_r}{r} \tag{3.65}$$

$$\gamma_{r\theta}=\frac{\partial u_r}{r\partial\theta}+\frac{\partial u_\theta}{\partial r}-\frac{u_\theta}{r} \tag{3.66}$$

where ϵ_{rr}, $\epsilon_{\theta\theta}$ and $\gamma_{r\theta}$ denote the radial strain, circumferencial strain, and total shear strain, respectively.

In accordance with Hooke's law for a generalized plane stress case, the strains can be expressed in terms of stresses:

$$\epsilon_{rr}=\frac{1}{E}(\sigma_{rr}-\nu\sigma_{\theta\theta}) \tag{3.67}$$

$$\epsilon_{\theta\theta}=\frac{1}{E}(\sigma_{\theta\theta}-\nu\sigma_{rr}) \tag{3.68}$$

$$\gamma_{r\theta}=\frac{2(1+\nu)}{E}\sigma_{r\theta} \tag{3.69}$$

where E is the Young's modulus and ν denotes the Poisson's ratio in a generalized plane stress condition. If a plane strain condition is assumed, E and ν should be replaced by

$$E=\frac{E}{1-\nu^2} \tag{3.70}$$

and

$$\nu=\frac{\nu}{1-\nu} \tag{3.71}$$

By using equations (3.61)-(3.71) and assuming no rigid body motion, the displacement components are

$$\begin{aligned} u_r=\frac{r^{1-\lambda}}{E}&[((2+\lambda)-\nu(2-\lambda))(\sin(\lambda\theta)A_1+\cos(\lambda\theta)A_2) \\ &-(2-\lambda)(1+\nu)(\sin((2-\lambda)\theta)A_3+\cos((2-\lambda)\theta)A_4)] \end{aligned} \tag{3.72}$$

and

$$\begin{aligned} u_\theta=-\frac{r^{1-\lambda}}{E}&[(\nu\lambda+(\lambda-4))(\cos(\lambda\theta)A_1-\sin(\lambda\theta)A_2) \\ &+(2-\lambda)(1+\nu)(\cos((2-\lambda)\theta)A_3-\sin((2-\lambda)\theta)A_4)] \end{aligned} \tag{3.73}$$

In addition, when all the stress expressions [equations (3.61-3.63)] and displacement components [equations (3.72) and (3.73)] are substituted into the boundary conditions in equations (2.2)-(2.9), eight linear equations are obtained:

$$\begin{aligned}&\sin(\lambda\theta_1)A_1^{(1)}+\cos(\lambda\theta_1)A_2^{(1)}\\&+\sin(2-\lambda)\theta_1)A_3^{(1)}+\cos((2-\lambda)\theta_1)A_4^{(1)}=0\end{aligned} \tag{3.74}$$

$$\begin{aligned}&\sin(\lambda\theta_2)A_1^{(2)}+\cos(\lambda\theta_2)A_2^{(2)}\\&+\sin(2-\lambda)\theta_2)A_3^{(2)}+\cos((2-\lambda)\theta_2)A_4^{(2)}=0\end{aligned} \tag{3.75}$$

$$\begin{aligned}&-\lambda\cos(\lambda\theta_1)A_1^{(1)}+\lambda\sin(\lambda\theta_1)A_2^{(1)}\\&-(2-\lambda)\cos(2-\lambda)\theta_1)A_3^{(1)}+(2-\lambda)\sin((2-\lambda)\theta_1)A_4^{(1)}=0\end{aligned} \tag{3.76}$$

$$\begin{aligned}&-\lambda\cos(\lambda\theta_2)A_1^{(2)}+\lambda\sin(\lambda\theta_2)A_2^{(2)}\\&-(2-\lambda)\cos(2-\lambda)\theta_2)A_3^{(2)}+(2-\lambda)\sin((2-\lambda)\theta_2)A_4^{(2)}=0\end{aligned} \tag{3.77}$$

$$A_2^{(1)}+A_4^{(1)}-A_2^{(2)}-A_4^{(2)}=0 \tag{3.78}$$

$$\lambda A_1^{(1)}+(2-\lambda)A_3^{(1)}-\lambda A_1^{(2)}-(2-\lambda)A_3^{(2)}=0 \tag{3.79}$$

$$\Gamma(\lambda+k_1-1)A_2^{(1)}+\Gamma(\lambda-2)A_4^{(1)}-(\lambda+k_2-1)A_2^{(2)}-(\lambda-2)A_4^{(2)}=0 \tag{3.80}$$

$$\Gamma(\lambda-k_1-1)A_1^{(1)}-\Gamma(\lambda-2)A_3^{(1)}-(\lambda-k_2-1)A_1^{(2)}+(\lambda-2)A_3^{(2)}=0 \tag{3.81}$$

where k_1 and k_2 are defined as in equations (2.19) and (2.20), and Γ by equation (2.54).

With an algebraic manipulation of equations (3.77) and (3.80), it is found that

$$\begin{aligned}&((\Gamma(k_1+1)+k_2+1)-(k_2+1)\\&+(\Gamma-1)(\lambda-2))A_2^{(1)}+(\Gamma-1)(\lambda-2)A_4^{(1)}-(k_2+1)A_2^{(2)}=0\end{aligned} \tag{3.82}$$

while using equations (3.78) and (3.81), one obtains

$$\begin{aligned}&((-\Gamma(k_1+1)+k_2+1)+(k_2+1)\\&+(\Gamma-1)\lambda)A_1^{(1)}-(\Gamma-1)(\lambda-2)A_3^{(1)}+(k_2+1)A_1^{(2)}=0\end{aligned} \tag{3.83}$$

A close inspection reveals that if two composite parameters α and β are defined as in equations (2.52) and (2.53), then equations (3.82) and (3.83) can be rewritten as:

$$(1+\alpha+(\alpha-\beta)(\lambda-2))A_2^{(1)}+(\alpha-\beta)(\lambda-2)A_4^{(1)}-(1-\alpha)A_2^{(2)}=0 \tag{3.84}$$

and

$$(-1-\alpha+(\alpha-\beta)\lambda)A_1^{(1)}-(\alpha-\beta)(\lambda-2)A_3^{(1)}+(1-\alpha)A_1^{(2)}=0 \tag{3.85}$$

The composite parameters α and β were first introduced by Dunders [27]. In this section, the parameters were determined by the direct application of Williams' Airy stress function. It should be noted that only two independent composite parameters (such as α and β) can exist. However, the choice of these two parameters is not unique; any two independent parameters (which would be functions of Γ, k_1 and k_2) can be selected depending upon convenience for the application being considered. In this case, the two parameters [α and β in equations (2.52) and (2.53)] have been widely recognized as the most appropriate for the analysis of two-dimensional interface problems [81].

3.2.2. FEM Approach

3.2.2.1. Stress Concentration Observation

To obtain preliminary knowledge about a problem, it is often necessary to begin studying a problem from one of its simplest forms. A rectangular plate comprised of two different linear-elastic materials, shown in Fig. 3.31, was employed to conduct an initial macro-scale analysis of the asymptotic stress field. The plate had a length of 40 mm and a width of 20 mm. The interface between Point A and Point B was at an angle of $\alpha=45°$. The properties for Material 1 were: Young's modulus E_1 = 10000 MPa and Poisson's ratio $\nu_1=0.3$. For Material 2, Young's modulus E_2 was 1000 MPa, and Poisson's ratio ν_2 took the value 0.35. Plane strain loading condition with evenly distributed tensile stresses (20 N/mm^2) on both ends DC and EF (Fig. 3.31) was assumed. Eight-node quadrilateral and six-node triangular isoparametric elements were used with isotropic elastic properties. The finite element model is illustrated in Fig. 3.32, which was meshed with relatively small elements at the interface corners. Seven rings of elements surrounded each corner. The mesh consisted a total of 522 elements and 1646 nodes. The computation was carried out via FEM software code ANSYS 4.4A [54].

The deformed structure superimposed with its original contour is shown in Fig. 3.33. This figure clearly shows that Material 1 tends to elongate less when compared to the lower softer material (Material 2). In addition, the von Mises equivalent stress [see equation (3.89)] distribution is presented in Fig. 3.34. Maximum stress concentration can be found at wedge corner A. It is surprising, however, that the minimum value of the equivalent stress exists at another interface corner, point B. This may imply that no stress singularity takes place at this corner for the current material combination and structural geometry. This is a very important observation: if a bimaterial interface can be such designed that no singularity exists at its interface corner, this bimaterial wedge will surely have the highest strength; therefore, a micro-scale study is conducted in a later

section to reveal the truth.

3.2.2.2. Asymptotic Field at Interface Corners

A linear elastic, two-dimensional finite element analysis of an adhesive butt joint, shown in Fig. 3.35, was conducted to investigate the eigenfunctions around an interface corner. This joint was assumed to be made of a layer of softer adhesive and two stiffer adherends, as may be the case for an adhesively bonded steel or aluminum joint, and to be subjected to traverse tension loading, which was a prescribed uniform displacement on the adherends along the y-direction to induce a nominal strain 0.0001 inside the adhesive layer. No load was applied along the x-direction. The width of the joint analyzed was 400 mm with the thickness 2t ranging from 0.1 to 200 mm. A state of plane strain was assumed in the analysis.

Given the four-fold symmetry of the model, only one quarter of the joint was discretized (Fig. 3.36) using two-dimensional six-node triangular and eight-node quadrilateral isoparametric plane strain elements. It can been seen from Fig. 3.36 that a very fine mesh was used in the vicinity of interface corner in order to capture the singular stress fields in this area. The finite element code ANSYS Version 4.4A [54] was employed in this analysis.

As a matter of convenience, equations (3.61)-(3.63) may be expressed in the following form [same as equation (1.1)] [8,9,49]:

$$\sigma_{ij}=Qr^{-\lambda}f_{ij}(\theta) \tag{3.86}$$

where Q, in analogy with the K-parameter used in linear elastic fracture mechanics, is defined as the stress intensity factor and $f_{ij}(\theta)$ is a bounded function that defines the trigonometric component of equations (3.61)-(3.63). With a combination of Q and $f_{ij}(\theta)$ as $Q_{ij}(\theta)$, equation (3.86) can be written as:

$$\sigma_{ij}=Q_{ij}(\theta)r^{-\lambda} \tag{3.87}$$

where $Q_{ij}(\theta)$ is defined as the **radial stress intensity factor**. Taking logarithmic operations on both sides, equation (3.87) becomes

$$\log\sigma_{ij}=\log Q_{ij}(\theta)-\lambda \log r \tag{3.88}$$

Figure 3.37 shows a plot of $\log(\sigma_e)$ versus $\log(r)$ for varying thicknesses of the adhesive layer at the interface ($\theta = 0°$), where σ_e is the equivalent stress (as defined by von Mises [36])

$$2\sigma_e^2=(\sigma_1-\sigma_2)^2+(\sigma_2-\sigma_3)^2+(\sigma_3-\sigma_1)^2 \tag{3.89}$$

where σ_1, σ_2 and σ_3 are the principal stresses. Equivalent stress σ_e can be obtained from the finite element analysis. The parameters $Q_e(\theta)$ and λ can be easily obtained from the curves presented in Fig. 3.37, since, as can be seen from equation (3.87), λ is the slope of the lines and $Q_e(\theta)$ is the value of σ_e for r equal to 1.

From Fig. 3.37, it is seen that when r goes to zero, the equivalent stress σ_e increases exponentially, except when r is too small as in this case the shape functions used to form the finite element code are unable to accurately describe these exponential changes. Taking these facts and the observations in Section 3.2.2.1 into account, it is obvious that around the interface corner there exists a singular stress field (asymptotic field).

The normalized angular displacement eigenfunction distributions, u_x and u_y inside the asymptotic field, are shown in Figs. 3.38a and b correspondingly at the radii of 0.1 and 1.0 mm. These FEM-based eigenfunctions will be used to compare with those from analytical and FEIM approaches in later sections, and hence to find out the advantages and disadvantages of individual schemes.

3.2.2.3. Computation of λ and Q Using log-log Approach

Assuming the principle in Fig. 3.37, a $\log\sigma_e$-$\log r$ plot was used to extract the numerically computed singular powers and the radial stress intensity factors defined by equation (3.87). Substituting the subscript *ij* with *e* (equivalent) in both equations (3.87) and (3.88), we obtain

$$\sigma_e = Q_e(\theta) r^{-\lambda} \tag{3.90}$$

where $Q_e(\theta)$ denotes the equivalent radial stress intensity factor, and

$$\log\sigma_e = \log Q_e(\theta) - \lambda \log r \tag{3.91}$$

Consequently, with the results of the finite element calculation of an adhesive joint, it is easy to extract the singular power λ and the radial equivalent stress intensity factor $Q_e(\theta)$ of this joint by using equation (3.91). To ensure high accuracy levels, a linearized least square fitting method was employed in this study.

Table 3.1 Comparison of analytical and numerical singular powers and normalized radial equivalent stress intensity factors (ν=0.3, t=10 mm)

E (MPa)	θ	0°	18°	36°	54°	72°	90°
analytical solution	λ	.28882	.28882	.28882	.28882	.28882	.28882
	$Q_e^*(\theta)$[5]	1.0000	1.1346	1.2572	1.3283	1.3283	1.2555
300	λ	.28939	.28960	.28838	.28877	.29000	.29065
	$Q_e(\theta)$	.10245	.11620	.12963	.13672	.13596	.12825
	$Q_e^*(\theta)$	1.0000	1.1342	1.2654	1.3345	1.3271	1.2519
2632	λ	.28919	.28960	.28925	.28927	.28927	.29336
	$Q_e(\theta)$	.89960	1.0195	1.1320	1.1960	1.1928	1.1485
	$Q_e^*(\theta)$	1.0000	1.1338	1.2583	1.3295	1.3132	1.2767
21000	λ	.28931	.28929	.28905	.28910	.28938	.29372
	$Q_e(\theta)$	1.0151	1.1963	1.3429	1.4124	1.3808	1.2843
	$Q_e^*(\theta)$	1.0000	1.1785	1.3229	1.3914	1.3602	1.2651

[5] $Q_e^*(\theta)$ is the normalized value with respect to its zero degree angle, that is, $Q_e^*(\theta)=Q_e(\theta)/Q_e(0)$.

Table 3.2 Comparison of analytical and numerical singular powers and normalized radial equivalent stress intensity factors (ν=0.3, E=2632 MPa)

t (mm)	θ	0°	18°	36°	54°	72°	90°
analytical solution	λ	.28882	.28882	.28882	.28882	.28882	.28882
	$Q_e^*(\theta)$	1.0000	1.1346	1.2572	1.3283	1.3283	1.2555
50	λ	.28903	.28932	.28894	.28889	.28925	.28906
	$Q_e(\theta)$	1.4319	1.6325	1.8030	1.9058	1.9011	1.8007
	$Q_e^*(\theta)$	1.0000	1.1401	1.2592	1.3310	1.3277	1.2576
10	λ	.28919	.28960	.28925	.28927	.28927	.29336
	$Q_e(\theta)$	.89960	1.0195	1.1320	1.1960	1.1928	1.1485
	$Q_e^*(\theta)$	1.0000	1.1338	1.2583	1.3295	1.3132	1.2767
1.0	λ	.28952	.28899	.28935	.28946	.29409	.29994
	$Q_e(\theta)$	.46159	.52493	.58102	.61384	.59929	.55149
	$Q_e^*(\theta)$	1.0000	1.1372	1.2587	1.3299	1.2983	1.1948
0.1	λ	.28898	.28870	.28838	.29374	.30575	.32070
	$Q_e(\theta)$	.23830	.27097	.29950	.30541	.28442	.24762
	$Q_e^*(\theta)$	1.0000	1.1371	1.2568	1.2816	1.1935	1.0391

The FEM model used for this purpose is the same as in Fig. 3.35; however, both adherends are assumed to be rigid ($E_{adherend}=\infty$) with a external prescribed y-direction uniform displacement to generate a nominal strain of 0.0003 inside the adhesive layer. Only one quarter of the adhesive layer is necessary to be discretized (Fig. 3.39) for the entire computations because of the four-fold symmetry. The adhesive layer thickness, Young's modulus, and Poisson's ratio were treated as the independent variables. For different cases, the numerical results of λ and $Q_e(\theta)$ are listed in Tables 3.1, 3.2, 3.3 and 3.4 respectively, where the analytical data were obtained via equation (2.59) with the Newton-Raphson method [49,117], and the normalized equivalent radial stress intensity factor is labeled as $Q_e^*(\theta)$ through normalizing $Q_e(\theta)$ with respect to its value at zero degree angle, $Q_e(0)$.

Table 3.3 Comparison of analytical and numerical singular powers and normalized radial equivalent stress intensity factors (ν=0.26, t=10 mm)

E (MPa)	θ	0°	18°	36°	54°	72°	90°
analytical solution	λ	.26184	.26184	.26184	.26184	.26184	.26184
	$Q_o^*(\theta)$	1.0000	1.1050	1.2099	1.2774	1.2872	1.2348
2632	λ	.26232	.26249	.26234	.26235	.26318	.26374
	$Q_o(\theta)$	.84150	.92964	1.0194	1.0765	1.0814	1.0354
	$Q_o^*(\theta)$	1.0000	1.1048	1.2115	1.2792	1.2851	1.2304

Table 3.4 Comparison of analytical and numerical singular powers and normalized radial equivalent stress intensity factors (ν=0.35, t=10 mm)

E (MPa)	θ	0°	18°	36°	54°	72°	90°
analytical solution	λ	.32030	.32030	.32030	.32030	.32030	.32030
	$Q_o^*(\theta)$	1.0000	1.1730	1.3135	1.3826	1.3639	1.2600
2632	λ	.32185	.32086	.32048	.32077	.32271	.32164
	$Q_o(\theta)$	1.0151	1.1963	1.3429	1.4124	1.3808	1.2843
	$Q_o^*(\theta)$	1.0000	1.1785	1.3229	1.3914	1.3602	1.2651

3.2.2.4. Free Edge Stress Intensity Factor

A free edge stress intensity factor calculation formula, based on dimensional analysis, was proposed by Reedy [8-9]. When the ratio of the adhesive length to its thickness is greater than 20, $Q_y(0)$, defined as the free edge stress intensity factor, can be evaluated by the following equation [8-9]:

$$Q_y(0)=\sigma^*(2t)^{\lambda}A(\nu) \tag{3.92}$$

where 2t is the adhesive layer thickness, σ^* is defined as the characteristic stress at the center of the adhesive in the x-direction ($\sigma^* = \sigma_x$ at the center), and $A(\nu)$ is a function

of ν and loading conditions, whose values for different ν in pure tension and pure shear loading conditions have been characterized by Reedy [8-9].

For a plane strain case, σ^* is

$$\sigma^* = \frac{\nu E}{(1+\nu)(1-2\nu)} \epsilon_n \tag{3.93}$$

where ϵ_n is the nominal strain at the center of the adhesive [8-9].

Table 3.5 Numerical and predicted free edge stress intensity factors

ν	E	λ	t	σ^*	A(ν)	$Q_y^{(R)\#}$	$Q_y^{(N)\#}$	error
.26	2632	.2618	10	.3394	1.736	1.077	1.056	1.9%
.30	300	.2888	10	.05192	1.32	.1333	.1326	.5%
.30	2632	.2888	10	.4555	1.32	1.169	1.159	.9%
.30	21000	.2888	10	3.635	1.32	9.329	9.279	.5%
.30	2632	.2888	50	.4555	1.32	1.861	1.851	.5%
.30	2632	.2888	1	.4555	1.32	.6013	.5883	2%
.35	2632	.3203	10	.6823	.948	1.352	1.342	.7%

#: $Q_y^{(R)}$ by Ready's formula; $Q_y^{(N)}$ via numerical methods.

For a validation of equation (3.92), the free edge stress intensity factors, for several different cases under the loading condition of a nominal strain $\epsilon_n = 0.0003$, were evaluated using equation (3.90) and compared with the results predicted by equation (3.92). All data are listed in Table 3.5.

3.2.2.5. Singular Zone Evaluation

A stress field is said to be singular if the stress distribution obeys the following rule:

$$\sigma_{ij} \sim r^{-\lambda} \tag{3.94}$$

From the previous analytical and FEM analyses (Section 3.2.2.1 and 3.2.2.2), it is clear that the stress field near the bimaterial corner is singular. The singular power describes the strength of the singular field, and the stress intensity factor indicates the magnitude of this field. However, the geometry of the singular zone, inside which the stresses obey relation (3.94), remains unknown from the aforementioned analyses. Therefore, a new method for evaluating the geometry of a singular stress zone is necessary.

It is clear that the true stresses within a finite bimaterial wedge (except a very localized area near the singular point) can be always obtained numerically. If it is assumed that the stress distribution inside this wedge can be globally described by the singular stress formula of equation (3.87), the assumed stress distribution should be identical to the true stress distribution in the close vicinity of the singular stress point located at the bimaterial wedge corner. However, at points away from the wedge corner, the assumed stresses will diverge from the true stresses, since the singular zone is only localized at the corner (see Fig. 3.37). A measure of the degree of divergence can be defined as

$$\gamma_\sigma = \left| \frac{\sigma_{true} - \sigma_{assumed}}{\sigma_{true}} \right| x100 \tag{3.95}$$

where the sub-index σ implies that the degree of divergence is obtained based on the stress field.

In this study, it was assumed that a point was said to be within the singular zone if γ_σ at this point was less than 1.0; otherwise, this point was outside the singular zone.

In order that singular stress zone geometries could be investigated from another point of view, the displacement fields were also employed to calculate the degree of divergence, which was defined as

$$\gamma_u = \left| \frac{u_{true} - u_{assumed}}{u_{true}} \right| x100 \qquad (3.96)$$

and the criterion for singular zone determination based on displacement fields was selected as 1.0 as well.

The singular stress zone geometries, extracted using different parameters under various conditions, are shown in Fig. 3.40.

3.2.3. FEIM Scheme

From the FEM results in Table 3.2, it was found that when the adhesive layer thickness (2t) was adequately small, the finite element solutions near the free surface were not acceptable either because the singular zone seemed to be very localized or the element sizes at the interface corner were too coarse to determine the singular power λ correctly (see Table 3.2). As a matter of fact, even if t is larger, the FEM solutions near the wedge corner are not accurate either because of the incapability of the polynomial shape function to approximate the steeply changing stress field (see Fig. 3.37). Therefore, the FEIM suggested by Barsoum [83-87] was used to calculate λ under different material combinations and wedge geometries.

3.2.3.1. An Isotropic Elastic-Rigid Bimaterial Wedge

An isotropic elastic-rigid bimaterial wedge was considered with all conventions being the same as in Fig. 3.35, but with rigid adherends ($E_{adherend} = \infty$). Without losing generality, only one of the four bimaterial wedges in Fig. 3.35 will be considered in this section. Thus, the geometry of interest looks like an elastic adhesive layer bonded to a rigid substrate.

The basic requirement in applying the FEIM is that the displacements within the singular field can be written as

$$u_i = Q r^{1-\lambda} g_i(\theta) \tag{3.97}$$

that is, this is a separable function [83-87,118]. Therefore, the ratio between the displacements at an outer ring of r_{out} and those at an inner ring of radius r_{in} along any ray has the form of

$$\frac{u_i^{(out)}}{u_i^{(in)}} = \left(\frac{r_{out}}{r_{in}}\right)^{1-\lambda} \tag{3.98}$$

By studying equation (3.98), it is obvious that inside the singular stress zone, the ratio of any two displacements along any ray is only a function of the two radii and the singular power λ, but is not a function of the ray angle θ. With this observation, the singular power can be computed by going through the following procedures. First, the region of interest, taking into account quarter symmetry, Fig. 3.35 (assuming rigid adherends) is analyzed by the FEM with a relatively coarse discretization as shown in Fig. 3.39. Then, a subarea of interest is re-meshed with rings and rays as shown in Fig. 3.41. The global displacement field, computed by the FEM on the outline of the subarea, is prescribed on the out-most ring to serve as the new boundary conditions for this sub-domain, and a new iterative computation for this area is carried out using the FEM. The singular power of this iteration can subsequently be obtained using equation (3.88) or (3.91). The termination of the iterative procedure is controlled by a relative convergence criterion, which is defined as

$$\chi = \frac{\lambda_{i+1} - \lambda_i}{\lambda_{i+1}} \times 100 < const \tag{3.99}$$

where *const* is a constant being determined by desiring a light or tight criterion. It is chosen as 0.001% throughout this presentation unless otherwise specified.

If the first iterative solution is unable to meet the convergence criterion in equation (3.99), it implies that the subarea is not entirely inside the singular field. Therefore, further calculations need to be carried out through a scaling of the displacements on the inner ring with an appropriate factor [20,21,42,46,49,83-87], then imposing them on the outer ring as the rebuilding boundary conditions, re-computing this sub-domain using the FEM, extracting the new iterative singular power, and checking whether the accuracy level is adequate. If not, with repeating the above procedure, the singular zone may always be deeply approached, and the correct singular power may therefore be computed. The FEIM analysis in this section was conducted using the mesh shown in Fig. 3.41, where R_{out} =0.1 mm, R_{in} =0.001 mm. By denoting the original whole structural analysis as the zero*th* iteration and the subsequent iterations as 1,2,3,..., the singular power at the free surface obtained by the FEIM for the case t=1.0 mm in (Table 3.2) is shown in Table 3.6.

Another computation was also carried out for an arbitrarily prescribed displacement field imposed on the outer ring of Fig. 3.41. The result, listed in Table 3.7, shows that during the third iteration the computed λ was accurate to the fourth significant digit.

Table 3.6 Number of iterations and singular power λ at the free surface (ν=0.30)

number of iteration	λ
1	.29214
2	.28866
3	.28869
4	.28869

Table 3.7 Number of iterations and singular power λ for a arbitrary loading condition (ν=0.30)

number of iteration	λ
1	.18733
2	.28985
3	.28869
4	.28869

3.2.3.2. An Isotropic Orthogonal Elastic Bimaterial Wedge

A more complicated case, an orthogonal elastic bimaterial wedge made from two isotropic materials, was studied in this section to compare with previous FEM results for similar geometries. A portion of Fig. 3.36, one bimaterial interface wedge corner from the four corners in Fig. 3.35, was subtracted to conduct these computations.

The FEIM representation, similar to that in Fig. 2.14 but with different DOF (degree of freedom), consists of 69 rings. The ratio of the radius of the outer ring R_{out} to that of the inner ring R_{in} was 10. It was found that if the inner ring was too close to the singular point, it was difficult to achieve convergence. The scaling factor [49,118] used was 3.5. An equivalent stress field was employed to compute the singular power. The convergence criterion used in this analysis was determined as the relative difference between the singular powers obtained in two successive iterations [equation (3.99)]. The entire analysis was performed using the macro capabilities of ANSYS 4.4A [54].

The normalized displacement eigenfunctions computed via FEIM with the same material combinations as in Fig. 3.35 are plotted in Figs. 3.38a and b in comparison with the functions from analytical analysis or FEM approach. Singular power dependence on the ratio of Young's moduli is shown in Fig. 3.42. In addition, the dependence on the Poisson's ratios is depicted in Fig. 3.43. The composite parameters, which are very significant for studying bimaterial interface problems, are employed so that their

relationship with the eigenvalue under orthogonal bimaterial wedge condition can be studied. The results are listed in Table 3.8 and illustrated in Fig. 3.44 as well.

3.2.3.3. An Isotropic Skewed Elastic Bimaterial Wedge

As studied in Section 3.2.1.1 with the FEM, it was noted that stress concentration only emerged at wedge corner A but not wedge corner B in Fig. 3.33, that is, the bimaterial wedge stress singularity for a skewed interface could be avoided if the skewed interface angle and material combinations met special conditions. In order that the general governing law can be discovered, a schematic drawing of the mathematical model of a bimaterial wedge with a skewed interface is shown in Fig. 3.45 where the interface is assumed to be straight and perfectly bonded. Both materials involved are isotropic and linear elastic with the assumption of plane strain loading condition. In addition, surface CAD in Fig. 3.45, where CA and AD are presumed co-planar, is traction free. The external loadings are prescribed on the rest of the boundaries and are generally of mixed mode characteristics.

Various skewed interface angles and mechanical properties were assigned to the bimaterial wedge in Fig. 3.45 for an investigation of the geometrical and physical influences on the interfacial stress singularities. Namely, the skewed interface angle were taken from 11.25° to 168.75° in the step of 11.25°; the ratio of Young's moduli E_1/E_2 was varied from two to infinity; the Poisson's ratio of Material 2 (ν_2) was chosen at 0.275, 0.30, 0.35 and 0.40; and the Poisson's ratio of Material 1 (ν_1) was fixed at 0.30 to simulate metallic materials such as steel and aluminum alloys. The step interval of the interface angle was selected as 11.25° because in ANSYS [54] the tolerable minimum angle for triangle elements, used to generate the mesh around the wedge corners, was about 10.5°. Moreover the FEIM, a simple and accurate tool for studying asymptotic stress fields [42,46,49,72], was employed to conduct the calculation via the ANSYS program design language (APDL) [54].

Table 3.8 Singular power distribution at α=-0.5

β	k_1	k_2	ν_1	ν_2	Γ	E_2/E_1	λ_n	λ_t
-.375	1.00	3.0000	.500	.0000000	.6666667	.4444444	-.2458	-.2499
-.375	1.50	3.6154	.375	-.1538462	.6153846	.3786982	-	-.2499
-.375	2.00	4.1429	.250	-.2857144	.5714286	.3265306	-	-.2499
-.375	2.50	4.6000	.125	-.4000000	.5333333	.2844444	-	-.2499
-.375	3.00	5.0000	.000	-.5000000	.5000000	.2500000	-	-.2499
-.350	1.00	2.7500	.500	.0625000	.6250000	.4427083	-.1432	-.1433
-.350	1.50	3.2857	.375	-.0714285	.5714285	.3858998	-	-.1433
-.350	2.00	3.7368	.250	-.1842105	.5263158	.3434903	-	-.1433
-.350	2.50	4.1220	.125	-.2804878	.4878049	.3119836	-	-.1433
-.350	3.00	4.4545	.000	-.3636363	.4545454	.2892562	-	-.1433
-.300	1.00	2.3333	.500	.1666666	.5555556	.4320988	-.5579e-1	-.5585e-1
-.300	1.50	2.7500	.375	.0625000	.5000000	.3863636	-.5579e-1	-.5585e-1
-.300	2.00	3.0909	.250	-.0227273	.4545455	.3553719	-	-.5585e-1
-.300	2.50	3.3750	.125	-.0937500	.4166667	.3356481	-	-.5585e-1
-.300	3.00	3.6154	.000	-.1538461	.3846154	.3254438	-	-.5585e-1
-.250	1.00	2.0000	.500	.2500000	.5000000	.4166667	.3160e-5	0
-.250	1.50	2.3333	.375	.1666667	.4444444	.3771044	.1587e-6	0
-.250	2.00	2.6000	.250	.1000000	.4000000	.3520000	.0000	0
-.250	2.50	2.8182	.125	.0454545	.3636364	.3379247	.1773e-6	0
-.250	3.00	3.0000	.000	.0000000	.3333333	.3333333	.2378e-5	0
-.200	1.00	1.7273	.500	.3181818	.4545455	.3994491	.4197e-1	.4201e-1
-.200	1.50	2.0000	.375	.2500000	.4000000	.3636364	.4197e-1	.4201e-1
-.200	2.00	2.2143	.250	.1964285	.3571429	.3418367	.4197e-1	.4201e-1
-.200	2.50	2.3871	.125	.1532258	.3225806	.3306741	.4197e-1	.4201e-1
-.200	3.00	2.5294	.000	.1176470	.2941177	.3287197	.4197e-1	.4201e-1
-.150	1.00	1.5000	.500	.3750000	.4166667	.3819444	.7554e-1	.7562e-1
-.150	1.50	1.7273	.375	.3181818	.3636364	.3486101	.7554e-1	.7562e-1
-.150	2.00	1.9032	.250	.2741936	.3225806	.3288241	.7554e-1	.7562e-1
-.150	2.50	2.0435	.125	.2391304	.2898551	.3192607	.7554e-1	.7562e-1
-.150	3.00	2.1579	.000	.2105263	.2631579	.3185596	.7554e-1	.7562e-1

-.100	1.00	1.3077	.500	.4230769	.3846154	.3648915	.1033	.1034
-.100	1.50	1.5000	.375	.3750000	.3333333	.3333333	.1033	.1034
-.100	2.00	1.6471	.250	.3382353	.2941177	.3148789	.1033	.1034
-.100	2.50	1.7632	.125	.3092105	.2631579	.3062481	.1033	.1034
-.100	3.00	1.8571	.000	.2857143	.2380952	.3061225	.1033	.1034
-.050	1.00	1.1429	.500	.4642857	.3571429	.3486395	.1267	.1268
-.050	1.50	1.3077	.375	.4230769	.3076923	.3184508	.1267	.1268
-.050	2.00	1.4324	.250	.3918919	.2702703	.3009496	.1267	.1268
-.050	2.50	1.5301	.125	.3674699	.2409639	.2928985	.1267	.1268
-.050	3.00	1.6087	.000	.3478261	.2173913	.2930057	.1267	.1268
.000	1.00	1.0000	.500	.5000000	.3333333	.3333333	.1466	.1468
.000	1.50	1.1429	.375	.4642857	.2857143	.3042672	.1466	.1468
.000	2.00	1.2500	.250	.4375000	.2500000	.2875000	.1466	.1468
.000	2.50	1.3333	.125	.4166667	.222222	.2798354	.1466	.1468
.000	3.00	1.4000	.000	.4000000	.2000000	.2800000	.1466	.1468
.050	1.00	.8750	.500	.5312500	.3125000	.3190104	-	.1641
.050	1.50	1.0000	.375	.5000000	.2666667	.2909091	.1639	.1641
.050	2.00	1.0930	.250	.4767442	.2325581	.2747431	.1639	.1641
.050	2.50	1.1649	.125	.4587629	.2061856	.2673536	.1639	.1641
.050	3.00	1.2222	.000	.4444445	.1851852	.2674897	.1639	.1641
.100	1.00	.7647	.500	.5588235	.2941177	.3056517	-	.1791
.100	1.50	.8750	.375	.5312500	.2500000	.2784091	-	.1791
.100	2.00	.9565	.250	.5108696	.2173913	.2627599	-	.1791
.100	2.50	1.0192	.125	.4951923	.1923077	.2555884	.1788	.1791
.100	3.00	1.0690	.000	.4827587	.1724138	.2556480	.1788	.1791
.125	1.00	.7143	.500	.5714285	.2857143	.2993197	-	.1858
.125	1.50	.8182	.375	.5454545	.2424242	.2724768	-	.1858
.125	2.00	.8947	.250	.5263158	.2105263	.2570637	-	.1858
.125	2.50	.9535	.125	.5116279	.1860465	.2499850	-	.1858
.125	3.00	1.0000	.000	.5000000	.1666667	.2500000	.1856	.1858

λ_n was obtained by the FEIM scheme and λ_t by the analytical approach.

Table 3.9 Stress singularity distribution
(ν_1=0.30 and ν_2=0.35)

α (°)	Singular Power (λ)				
	E_1/E_2=2	E_1/E_2=10	E_1/E_2=30	E_1/E_2=70	E_1/E_2=∞
11.25	.087	.309	.389	.417	*
22.50	.109	.289	.333	.344	*
33.75	.086	.213	.231	*	.425
45.00	.034	.094	*	.258	.428
56.25	.000	.047	.254	.341	.418
67.50	.000	.169	.304	.354	.396
78.75	.003	.220	.309	.340	.365
90.00	.049	.227	.286	.306	.320
101.25	.070	.200	.238	.250	.257
112.50	.063	.139	.159	.165	.169
123.75	.027	.035	.037	.038	.045
126.00	0	0	0	0	.004
135.00	0	0	0	0	0
146.25	0	0	0	0	0
157.50	0	0	0	0	0
168.75	0	0	0	0	0

* Convergence was not observed.

The fan-shaped mesh configuration used in this study for the FEIM processes is depicted in Fig. 3.46. It is comprised of 320 six-node triangular and eight-node quadrilateral plane strain isoparametric elements and 1001 nodes. No singularity-embedded element was used because the singular power was not known *a priori*. For all analyses, only one physical mesh (Fig. 3.46) was generated and used because any specific skewed interface could be obtained by assigning the mechanical properties of the two materials to the corresponding elements through selecting the appropriate ray, emanating from the bimaterial wedge corner, as the dividing line, which subsequently became the interface desired. For a different skewed interface angle, one

only needed to use the ray at this angle as the separating line, and to assign the elements' properties with the same procedure.

Table 3.10 Stress singularity distribution
($E_1/E_2=30$ and $\nu_1=0.30$)

α (°)	Singular Power (λ)			
	$\nu_2=.275$	$\nu_2=.30$	$\nu_2=.35$	$\nu_2=.40$
11.25	.394	.393	.389	.385
22.50	.340	.338	.333	.327
33.75	.236	.235	.231	.223
45.00	*	*	*	*
56.25	.185	.216	.254	.280
67.50	.259	.275	.304	.328
78.75	.265	.280	.309	.335
90.00	.240	.256	.286	.314
101.25	.187	.204	.238	.270
112.50	.102	.121	.159	.196
123.75	0	0	.037	.081
126.00	0	0	0	0
135.00	0	0	0	0
146.25	0	0	0	0
157.50	0	0	0	0
168.75	0	0	0	0

* Convergence was not observed.

The stress singularities were evaluated through consideration of u_y displacements using a linearized least square fitting method. The convergence was assumed when the relative error between the singular powers of two consecutive iterations was less than 0.1% [equation (3.99)]. When the Poisson's ratios of Material 1 (ν_1) and Material 2 (ν_2) were held at 0.30 and 0.35 respectively, the stress singularities are listed in Table 3.9 for various skewed interface angles and different ratios of Young's moduli (E_1/E_2).

Similarly, with E_1/E_2 being kept at 30 and ν_1 being fixed at 0.30, the values of the singular powers are presented in Table 3.10, where the skewed interface angles and the Poisson's ratio of Material 2 (ν_2) were treated as the changing parameters.

The data listed in both tables were the averaged values of λ evaluated along three different rays emanating from the wedge corner. The rays were defined on both free surfaces AC and AD, and along ray AB at an angle 45° (Fig. 3.45). It was not necessary to redefine these rays for different skewed interface angles since it is well known that, from analytical and numerical [46,118] analyses, the stress singularities are the same in both materials at the wedge corner. The value of λ in the two tables was rounded off to three digits after the decimal point. The average number of iterations for convergence under mixed loadings was obtained after six to seven iterations. However, convergence could not be observed for certain skewed angles when the ratio of Young's moduli (E_1/E_2) was greater or equal to about 30 (Table 3.9).

The relationship between the stress singularities and the ratios of Young's moduli is depicted in Fig. 3.47 for the whole range of skewed interface angles and with the Poisson's ratios of Material 1 (ν_1) and Material 2 (ν_2) being held at 0.3 and 0.35 correspondingly. Further, the effects of Poisson's ratio of Material 2 (ν_2) on the stress intensities, at different skewed angles, is shown in Fig. 3.48, when E_1/E_2 was equal to 30, and ν_1 was kept at 0.3. The shaded areas in Figs. 3.47 and 3.48 represented the places where convergence for real solutions could not be achieved. A typical non-convergent iteration procedure is presented in Fig. 3.57, where it is evident that the solution became worse as the number of iterations increased.

3.2.3.4. An Orthotropic Orthogonal Elastic Bimaterial Wedge

In composite applications, materials are anisotropic *per se*. Therefore, the understanding of mechanical behavior of anisotropic bimaterial wedges is of significance. In this section, efforts will be concentrated on the asymptotic fields of an

orthogonal bimaterial wedge comprised of isotropic and orthotropic materials.

For convenience in describing the orthotropic material properties, a new parameter, orthotropic ratio, is denoted as ω and defined as

$$\varpi = \frac{E_{11}}{E_{22}} \tag{3.100}$$

Table 3.11 Singular power dependence on orthotropic ratio
($E^{(1)}_{11}=E^{(1)}_{22}=3000$ MPa, $\nu^{(1)}_{12}=0.35$ and $\nu^{(2)}_{12}=0.25$)

$\omega^{(2)}$	Singular Power λ					
	$E^{(2)}_{22}=5.0e2$	$E^{(2)}_{22}=1.5e3$	$E^{(2)}_{22}=3.0e3$	$E^{(2)}_{22}=5.0e3$	$E^{(2)}_{22}=1.0e4$	$E^{(2)}_{22}=2.0e4$
0.07	.2831	.1774	.08696	.02546	.002147	.07106
0.10	.2258	.1349	.05541	.006364	.002655	.07260
0.20	.1722	.07833	.01162	-.01009	.02706	.1074
0.40	.1434	.04256	-.006223	-.0002065	.06346	.1462
0.60	.1332	.02873	-.007425	.01265	.08590	.1671
1.00	.1250	.01680	-.002369	.03252	.1132	.1904
1.50	.1209	.01053	.005137	.04955	.1332	.2026
2.00	.1186	.007230	.01167	.06174	.1463	.2161
3.00	(.1158)	(.003969)	(.02193)	(.07854)	(.1631)	(.2284)
5.00	(.1120)	(.001113)	(.03570)	(.09848)	(.1815)	(.2411)
7.50	(.1080)	(-.0005245)	(.04672)	(.1130)	(.1940)	(.2494)
10.0	(.1046)	(-.001492)	(.05440)	(.1225)	(.2018)	(.2545)
14.0	(.09976)	(-.002507)	(.06309)	(.1329)	(.2100)	(.2597)

(.): Materials used were physically impossible.

The model employed here is similar in shape to that in Fig. 3.45, with a fixed value of $\alpha=90°$ to make the wedge orthogonal. The FEM mesh is also similar to Fig. 3.46. Material 1 is assumed to be isotropic with Young's modulus 3000 MPa and Poisson's ratio 0.35 to simulate an adhesive. Material 2 has an orthotropic characteristic

with a fixed Poisson's ratio $\nu^{(2)}_{12}$[6] of 0.35 and varying Young's modulus. This model should be able to reveal the asymptotic field of an adhesive joint made of orthotropic materials. The effects of orthotropic ratio of Material 2 on the eigenvalues are depicted in Table 3.11. To show the changing trend visually, Fig. 3.49 illustrates part of the data in Table 3.11. In addition, the dependence of singular powers on Poisson's ratio of Material 2 is represented jointly by Table 3.12 and Fig. 3.50.

Table 3.12 Singular power dependence on Poisson's ratio
($E^{(1)}_{11}=E^{(1)}_{22}=3000$ MPa and $\nu^{(1)}_{12}=0.35$)

$\nu^{(2)}_{12}$	Singular Power λ						
	$E^{(2)}_{11}=1e4$ $E^{(2)}_{22}=1e4$ $\omega^{(2)}=1$	$E^{(2)}_{11}=2e4$ $E^{(2)}_{22}=4e3$ $\omega^{(2)}=5$	$E^{(2)}_{11}=4e3$ $E^{(2)}_{22}=2e4$ $\omega^{(2)}=.2$	$E^{(2)}_{11}=5e4$ $E^{(2)}_{22}=1e4$ $\omega^{(2)}=5$	$E^{(2)}_{11}=1e4$ $E^{(2)}_{22}=5e4$ $\omega^{(2)}=.2$	$E^{(2)}_{11}=1.4e5$ $E^{(2)}_{22}=1e4$ $\omega^{(2)}=14$	$E^{(2)}_{11}=1e4$ $E^{(2)}_{22}=1.4e5$ $\omega^{(2)}=1/14$
.00001	.1246	.1017	.1017	.1991	.1191	.2297	.2297
0.05	.1220	.09583	.1010	.1955	.1988	(.2258)	.2302
0.10	.1196	.08978	.1012	.1920	.1993	(.2219)	.2324
0.15	.1174	(.08349)	.1023	(.1885)	.2006	(.2179)	.2367
0.20	.1153	(.07680)	.1043	(.1850)	.2028	(.2140)	.2442
0.25	.1132	(.06978)	.1074	(.1815)	.2061	(.2100)	.2603
0.30	.1110	(.06210)	.1117	(.1779)	.2109	*	*
0.35	.1087	(.05363)	.1182	(.1744)	.2177	*	*
0.37	-	(.04997)	.1218	(.1730)	.2214	*	*
0.40	.1062	*	*	*	*	*	*
0.45	.1033	*	*	*	*	*	*
.49999	.09973	*	*	*	*	*	*

-: Not calculated; *: Convergence was not reached; (.): Materials used were physically impossible.

[6] The superscript (2) denotes Material 2, and the subscript 12 indicates orientation of the parameters and corresponds to xy in a Cartesian system. This notation will be employed through this presentation unless specified otherwise.

It should be pointed out that, in a generalized two-dimensional situation, the mechanical properties for orthotropic materials have to meet a special condition [3,5]:

$$E_{11}\nu_{12}=E_{22}\nu_{21} \tag{3.101}$$

Therefore, whenever three of the four parameters in equation (3.101) are fixed, the fourth is defined by this relation.

By substituting equation (3.100) into (3.101), the following can be obtained:

$$\nu_{21}=\omega\nu_{12} \tag{3.102}$$

Taking column 2 in Table 3.12 as an example, $\omega=5$, physically ν_{12} cannot exceed 0.1 because the maximum value ν_{21} being able to hold is 0.5. However, numerically or artificially, ν_{12} can have a higher value than 0.1. From the point of pure academic interest, values of ν_{12} greater than 0.1 were considered, but the resultant data were parenthesized in Tables 3.11 and 3.12 to distinguish them from those whose material properties had physical backgrounds.

3.2.3.5. Singular Zone Evaluation

In Section 3.2.2.5, the singular stress zone was investigated using the FEM. However, it was stated in Section 3.2.2.3 that the evaluation of the singular power and the stress intensity factor for very small thicknesses of the adhesive layer was fairly inaccurate when the conventional FEM was used. Therefore, as an alternative approach, the singular stress zone was semi-quantitatively evaluated in this section by applying the FEIM.

The specimen geometry was kept the same as shown in Fig. 3.35 with t=0.25 mm. The singular stress zones were assumed to be quarter circles in both materials and are represented by their radii r_{Q1} and r_{Q2} as shown in Fig. 3.51. The procedure

employed to evaluate the radii of the singular zones was as follows:

(1) Conduct a whole structural finite element analysis.
(2) Design an FEIM mesh similar to the one shown in Fig. 2.14 with $R_{out}=0.1$ mm and $R_{in}=0.01$ mm using six-node isoparametric triangular and eight-node isoparametric quadrilateral elements with an assumption of plane strain deformation.
(3) Begin the FEIM routine (see Section 3.2.3.1).
(4) If the convergence criterion, defined in equation (3.99), is satisfied, it can be assumed that the singular stress zone is reached.

The dependence of the singular stress zone on the ratio of Young's moduli is shown in Fig. 3.52 for the case $\nu_1=0.3$ and $\nu_2=0.35$. The singular stress zone size as a function of the Poisson's ratios of the two materials is presented in Fig. 3.53.

3.2.3.6. FEIM Convergence Rate Dependence on Material Properties

In this study, the criterion of convergence required that χ in equation (3.99) be less than or equal to 0.001%[7]. This ensures a match to the fourth significant digit of two successive iterative solutions. Fig. 3.54 shows a relationship between the value of the singular power and the corresponding numbers of iteration for this case. Clearly, preliminary iterations produced significantly different values of λ along the three different rays presented in Fig. 3.54. However, as the procedure continued, the value of λ along all directions converged to the fourth significant digit. In order that the effects of material properties on the convergence rate could be observed, two more studies, convergence rate dependence on the Young's modulus ratio and the values of Poisson's ratio, were

[7] unless specified otherwise.

conducted. The results are presented in Figs. 3.55 and 3.56.

In special circumstances, convergence may not be attained with the present scheme. The reason is speculated to be either that the eigenvalue is too small for the employed numerical method or that it is complex. For the latter case, a special evaluation scheme must be employed [84]. A typical non-convergence procedure is shown in Fig. 3.57, which came from the skewed interface bimaterial wedge studies in section 3.2.3.3. The eigenvalue was believed to be complex in this particular situation [119,120].

3.2.4. Experimental Analysis

Theoretical prediction from analytical and numerical analysis suggests that crack initiation point should be located at the interface wedge corners or sharp notch tips because stresses are mathematically singular at these points. Mechanical tests (Section 3.1.3) have provided such an observation from a more or less macro-scale standing point. Investigations from a micro-scale point of view should be carried out to reveal more details of the crack initiation and propagation driving forces. Under such a motivation, examinations of the fracture surfaces of broken specimen from the Iosipescu tests were performed with an optical microscope and scanning electronic microscope (SEM).

3.2.4.1. Procedure

After the mechanical tests were completed, the two parts of each broken specimen were paired and photographed under an optical microscope to identify the failure path. Then, the broken surfaces were coated with Au-Pt by way of spray coating equipment to ensure conductivity of the fractured adhesive surfaces. The prepared specimens were thereafter examined using a Zeiss DSM 960 digital scanning electronic microscope (SEM). Areas of interest on the fractured surfaces were photographed for future analyses.

3.2.4.2. Observations

Generally, fracture paths for rigid adhesive joints varied from zig-zag routines to a peel-off pattern (separation along the adhesive-adherend interface). The zig-zag paths occurred more often than peel-off. Typical zig-zag failure patterns are shown in Figs. 3.58-3.60 for geometry Type A, B and C respectively. A typical peel-off fracture specimen is depicted in Fig. 3.61. All of these failures were initiated at the vicinity of singular stress points, *viz.*, interface wedge corners (all joint types) or sharp notch tips (Type B only).

For Type A adhesive joint Iosipescu specimens made of flexible adhesive, only the peel-off pattern was observed.

When a crack started from an interface wedge corner, there were two possibilities for the propagation route, namely, through the adhesive layer (zig-zag) or straight along the interface (peel-off). For the first case, after a crack emerged at one notch root, it began to advance along the interface for some distance, then deviated into the adhesive layer, propagated to the other interface, and finally went along this interface all the way to the other notch root to separate the two adherends (Figs. 3.59-3.60). In the second case, the crack started, developed, and failed only at one interface (Fig. 3.61).

If a crack initiated at the notch tip, which was only possible for Type B joint specimen, the separation process would always be as following:

> starting at a notch tip → propagating to one interface with a inclined angle with respect to the notch root axis → advancing to the interface wedge corner on the other notch root → having totally damaged this joint.

The fracture route was a zig-zag path. No fracture path encompassed only within the adhesive layer has ever been observed.

A typical zig-zag cracked joint was examined using the SEM. The two portions

are shown in Fig. 3.62. It seemed that the crack started at the left-top corner of the left part in Fig. 3.62 (or the right-top corner of the right portion). It went into the specimen along the interface for a small distance, then changed the crack route into the adhesive layer till reached the other interface, and finally advanced all the way along the latter interface to fail. The right portion was extensively examined. All photos are presented in Figs. 3.63a--f, where the crack initiation, propagation, step-wise surface profiles, secondary cracks, and delamination surfaces were depicted. The left part of Fig. 3.62 was also inspected and is illustrated in Figs. 3.64a and b to aid the understanding of the formation of the fractured surfaces.

The peel-off fractured surfaces for rigid adhesive joints can be readily seen from Figs. 3.62-3.64. A typical peel-off surface for a flexible adhesive joint is shown in Fig. 3.65.

3.3. Plastic Zone Evaluation

An elastic-perfectly plastic model, shown in Fig. 3.66, was used for the analysis, and small displacement theory was employed. The loading condition was a prescribed displacement field, and the dimensions of the model were the same as in the elastic case, Fig. 3.35. However, in order to have a bigger plastic zone for easier visualization and better accuracy, the adhesive layer was assumed to be 50 mm thick and in a plane strain condition for the FEM analysis.

3.3.1. First Analytical Approach

In a polar coordinate system, it is known that the equivalent stress at a point of radius r and angle θ may be calculated using equation (3.91). For a fixed angle θ, the relationship between the stress and radius r is graphically represented in Fig. 3.67a. By denoting the yield strength of the adhesive σ_y, the boundary between the elastic and

plastic zone can be found by comparing the equivalent stress σ_e and yield strength σ_y, where the equivalent stress is defined in equation (3.89). If it is assumed that the plastic zone radius r_P is the point where σ_e equals σ_y (see Fig. 3.67a), r_P can be obtained from the following relationship:

$$\sigma_y=\sigma_e=Q_e r_P^{-\lambda} \tag{3.103}$$

that is,

$$r_P=\delta=\left(\frac{Q_e}{\sigma_y}\right)^{\frac{1}{\lambda}} \tag{3.104}$$

3.3.2. Second Analytical Approach

It is evident that the plastic zone size in Fig. 3.67a, estimated using equation (3.104), is conservative when it is noted that the area above σ_y (Fig. 3.67a) was neglected. Therefore, an improved interface plastic zone geometry evaluation, similar to that for cracks by Irwin [44], was derived as follows. First, the stress-distance curve in Fig. 3.67a was translated to the right direction by a distance of η (Fig. 3.67b), that is, the plastic zone radius (r_P) increment was also equal to η. In order to satisfy the force balance requirement, the two shadowed areas in Fig. 3.67b should be equal to each other. The following equation was therefore obtained:

$$\eta\sigma_y=\int_0^{\delta}(Q_e r^{-\lambda}-\sigma_y)dr \tag{3.105}$$

with which η can be obtained, and thus the total r_P is

$$r_P=\delta+\eta=\frac{1}{1-\lambda}\left(\frac{Q_e}{\sigma_y}\right)^{\frac{1}{\lambda}} \tag{3.106}$$

By use of equations (3.104) and (3.106), and the linear elastic analysis data in Table 3.1, the theoretical plastic zones at the interface corner were computed and plotted in Fig. 3.68 in a loading condition resulting in a nominal strain $\varepsilon_n=0.0003$.

3.3.3. Numerical Scheme

Numerically, the plastic zone at the interface corner can be computed by the FEM. With a plot of the equivalent stress contours of a bimaterial wedge from the FEM results, the plastic zone at the wedge corner can easily be represented. This technique was used in the present study. The numerical results under the loading condition of $\varepsilon_n=0.0003$ are shown in Fig. 3.68.

Let r_{Pmax} be the maximum radius of the plastic zone and θ_{Pmax} be the angle between the interface and r_{Pmax}. The variations of θ_{Pmax} with ε_n and r_{Pmax} with ε_n were plotted in Fig. 3.69 and Fig. 3.70 respectively, where the analytical data was obtained from equation (3.106) and the numerical data from the FEM calculations.

3.3.4. Interactions of Plastic and Singular Zones

Whenever non-linear materials exhibiting elasto-plastic behavior are introduced at a bimaterial wedge, the material at the wedge corner will yield, that is, a plastic zone will emerge. Theoretically, at this stage, no singular stress zone exists at all around this corner as the stresses are bounded. However, a singular stress zone can be extensively defined at the wedge corner as an area inside which all stresses obey relation (3.94). Therefore, by computing the singular power λ distribution along a ray from the

numerical data, it is possible to determine whether there exists a singular stress zone and how big it is. Fig. 3.71 shows the singular power distribution along the ray $\theta=36°$ for elastic and plastic cases at $\epsilon_n=0.00025$. In addition, the entire area has been divided into four zones (Fig. 3.71) according to the value of λ. Fig. 3.72 shows the λ distributions along the ray $\theta=36°$ for different loads, and Fig. 3.73 shows the distribution along different rays at $\epsilon_n=0.0003$. Further, the relationship between r_Q and r_P along the ray $\theta=36°$ is shown in Fig. 3.74.

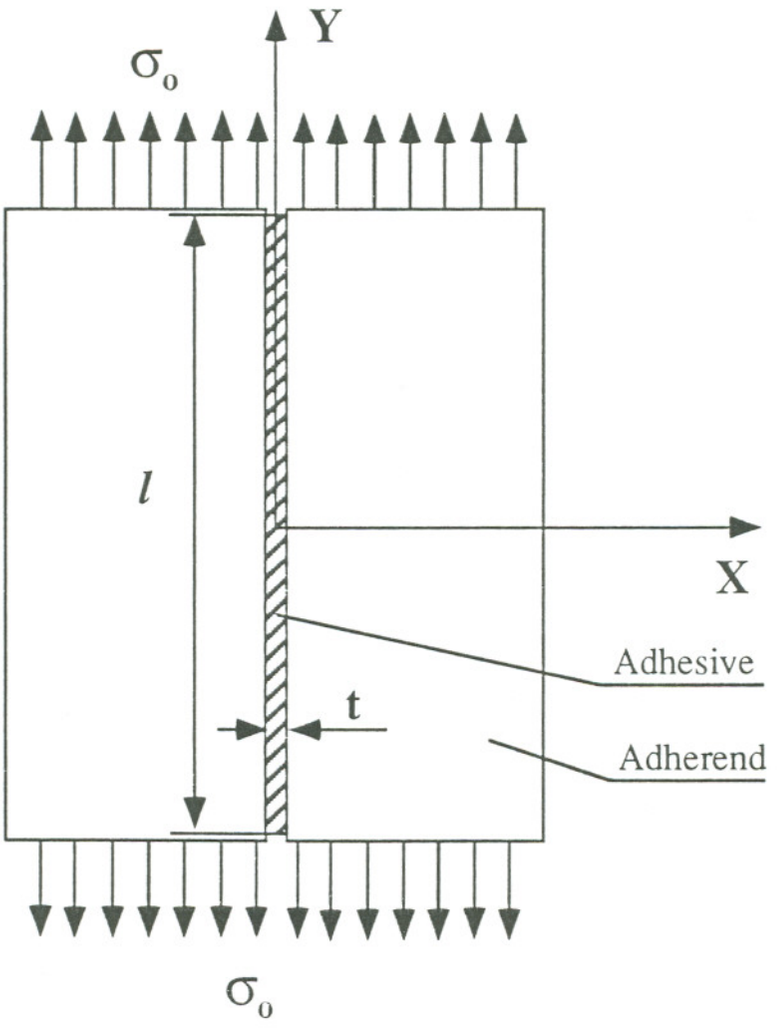

Fig. 3.1 A link-joint model.

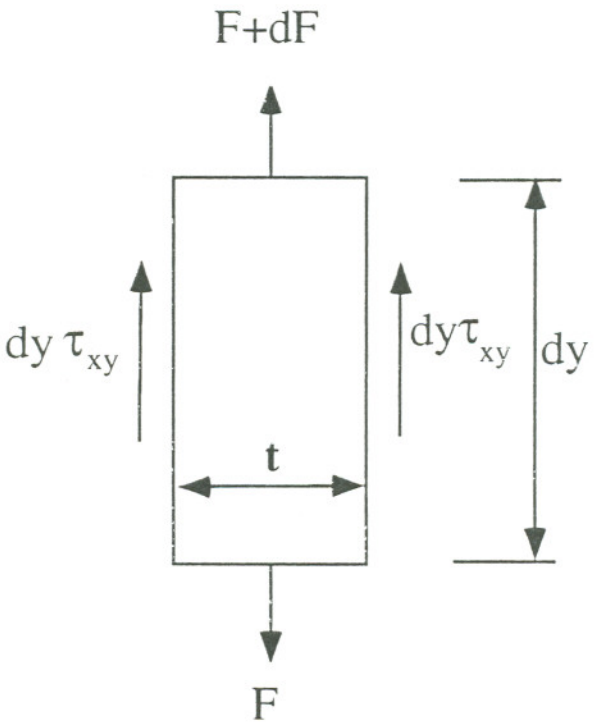

Fig. 3.2 An element of adhesive layer.

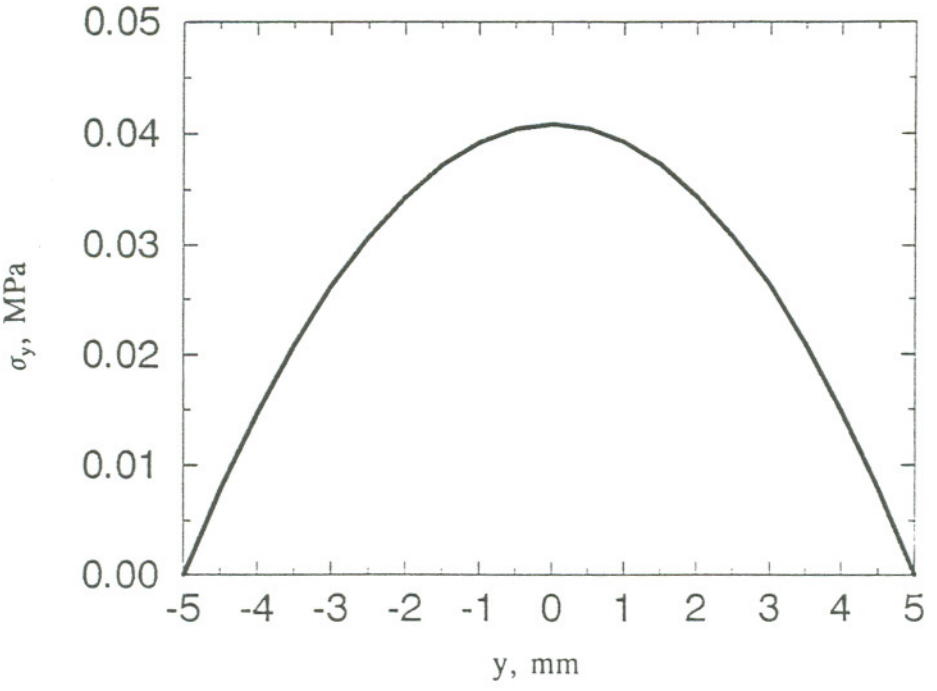

a) tensile stress

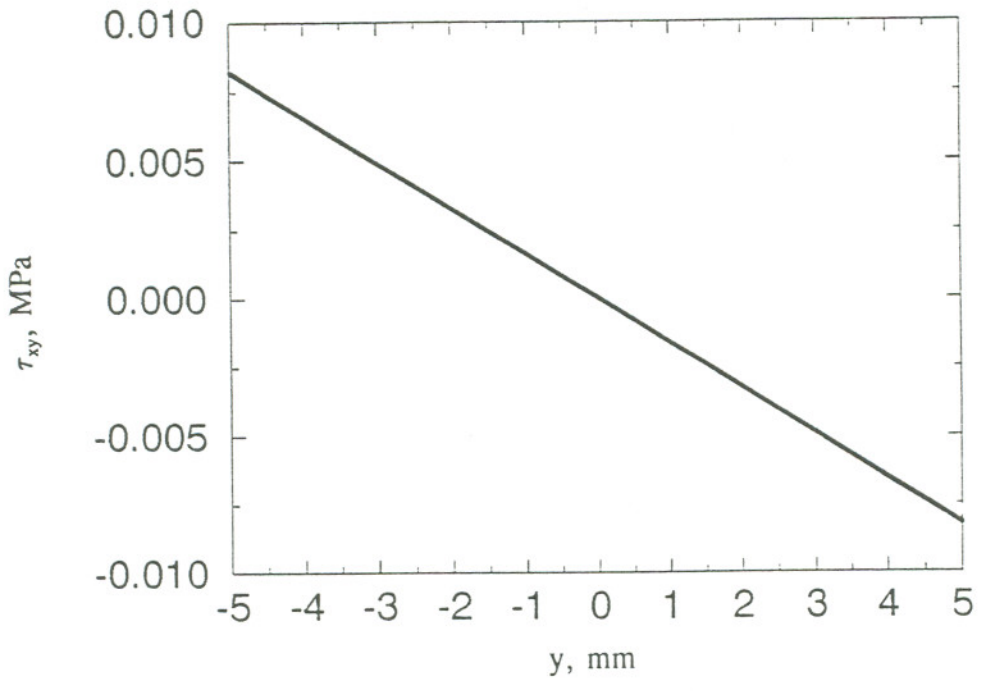

b) shear stress

Fig. 3.3 Stress distribution inside the adhesive layer of a link joint.

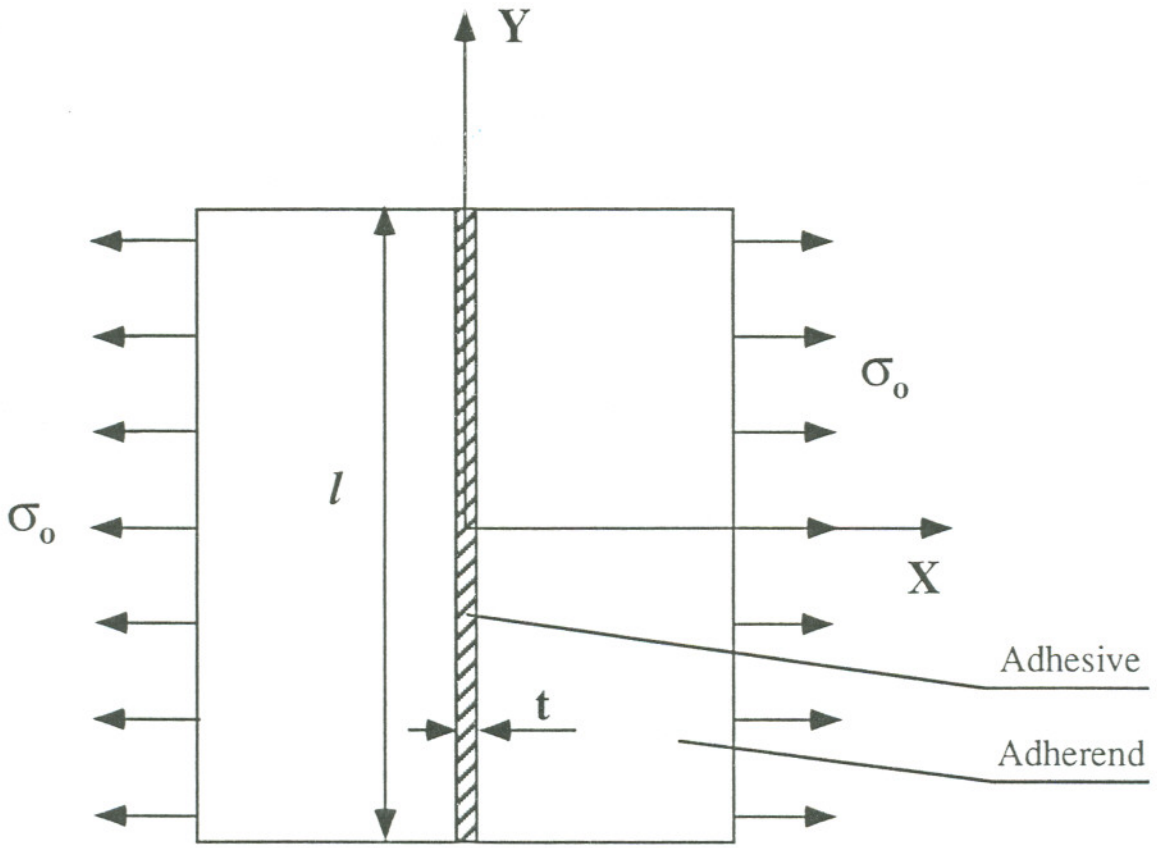

Fig. 3.4 A butt-joint model.

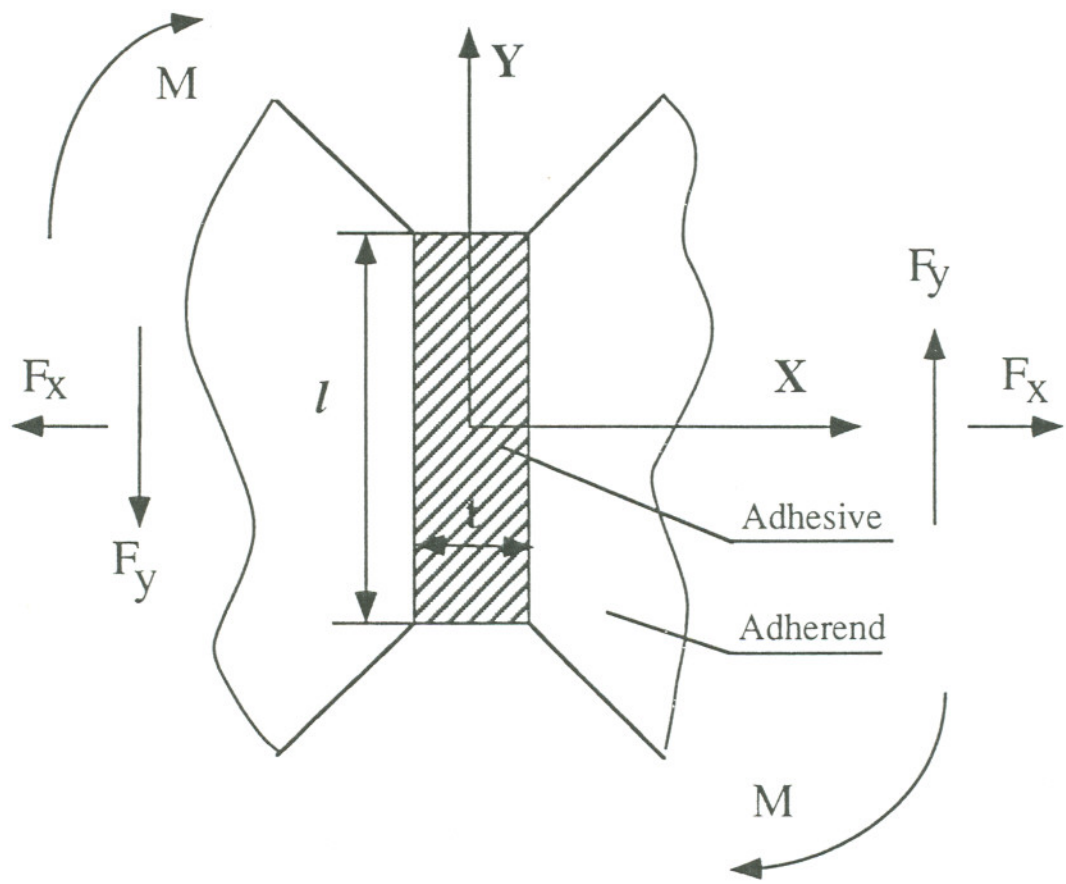

Fig. 3.5 Schematic of portion of Type C adhesive joint Iosipescu specimen.

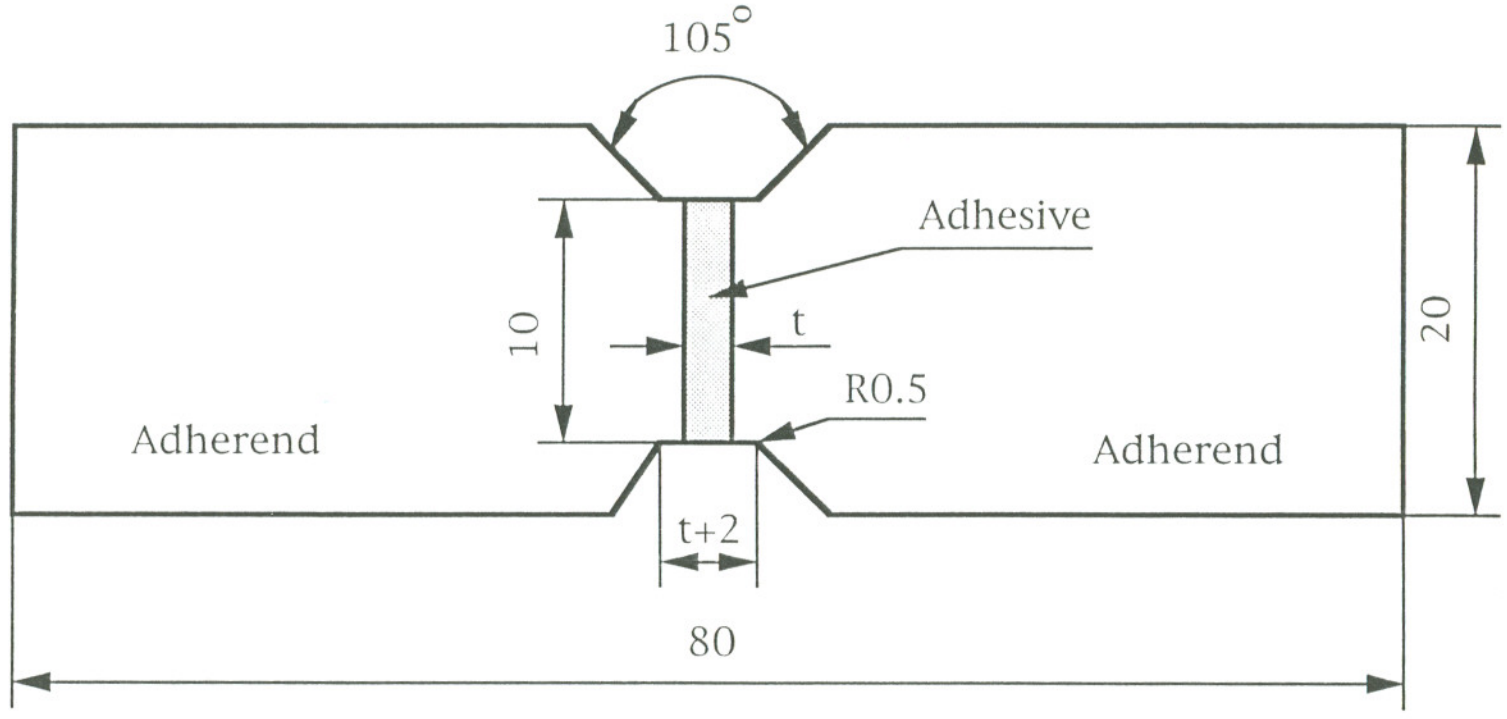

Fig. 3.6 Schematic of Type A adhesive joint Iosipescu specimen.

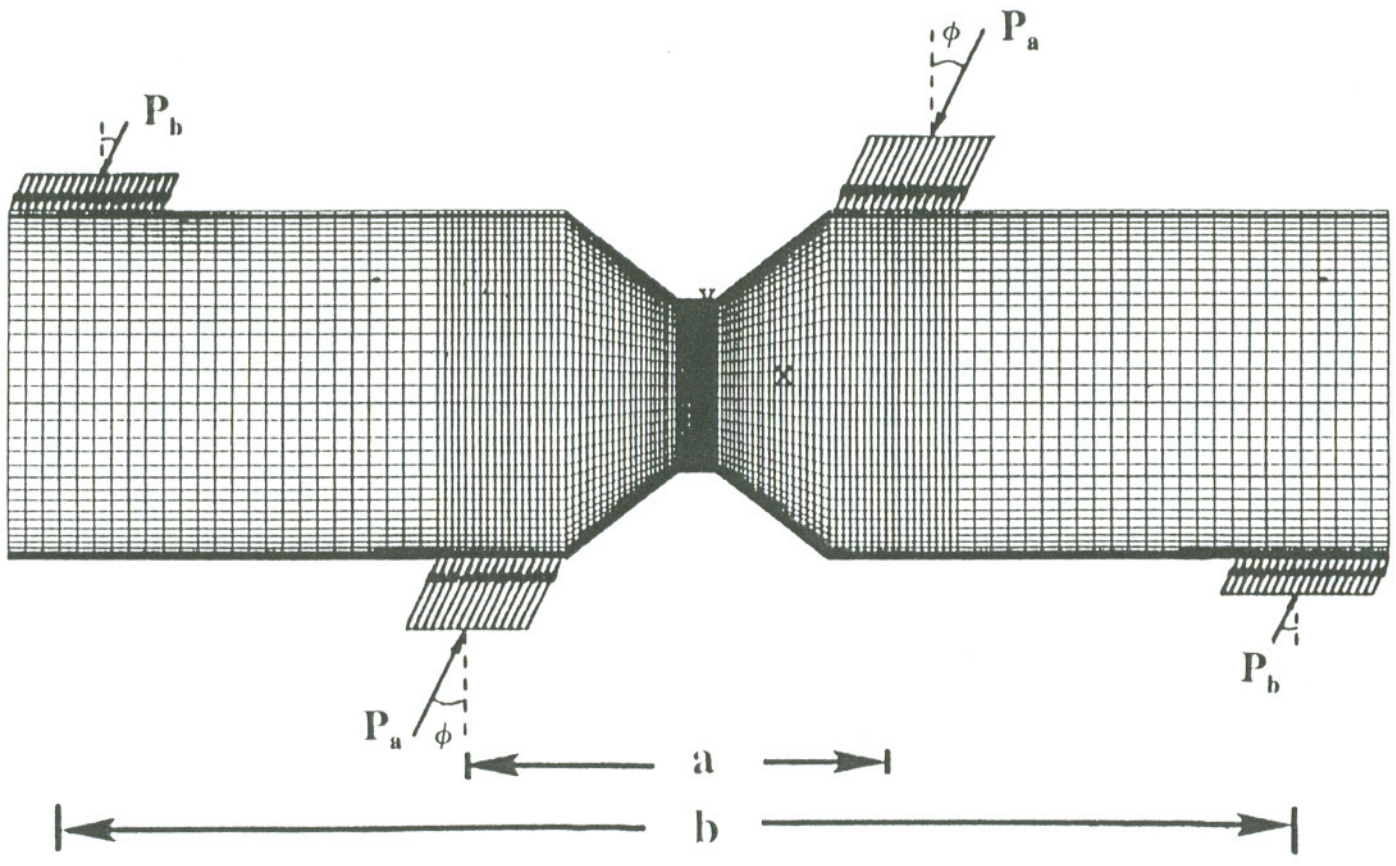

Fig. 3.7 FEM representation of Type A adhesive joint Iosipescu specimen under biaxial loading conditions.

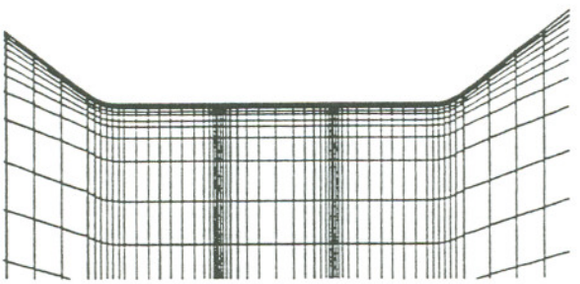

a) Type A

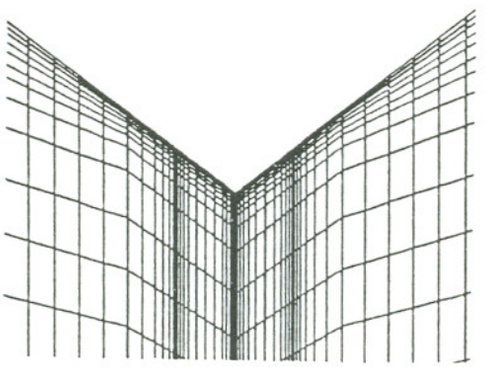

b) Type B

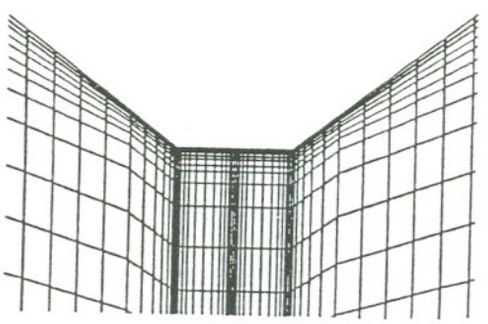

c) Type C

Fig. 3.8 Mesh configurations of different types of joint root geometries.

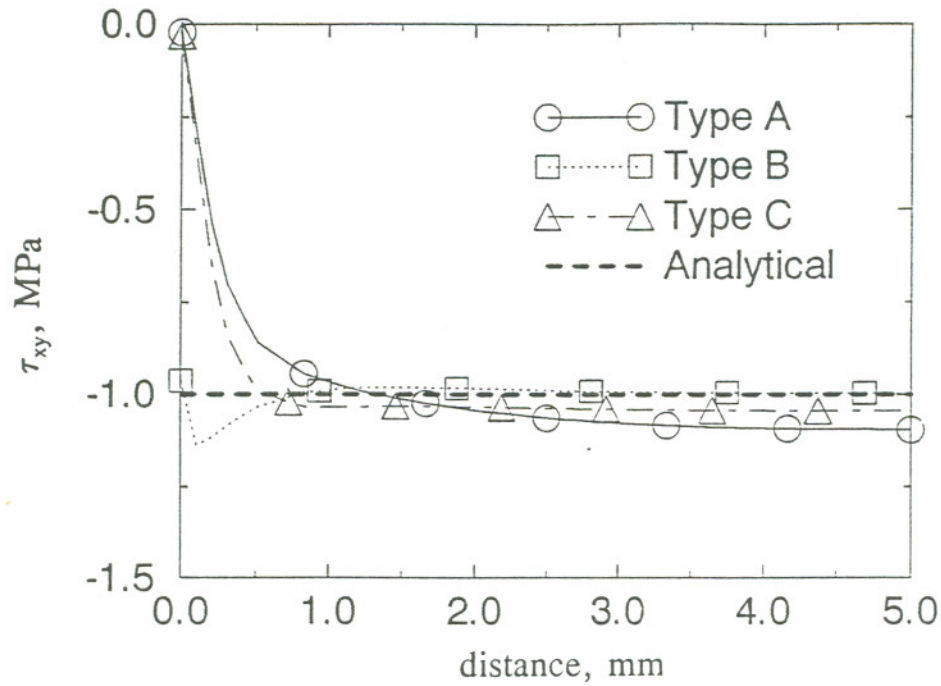

a) along the notch root axis (x=0)

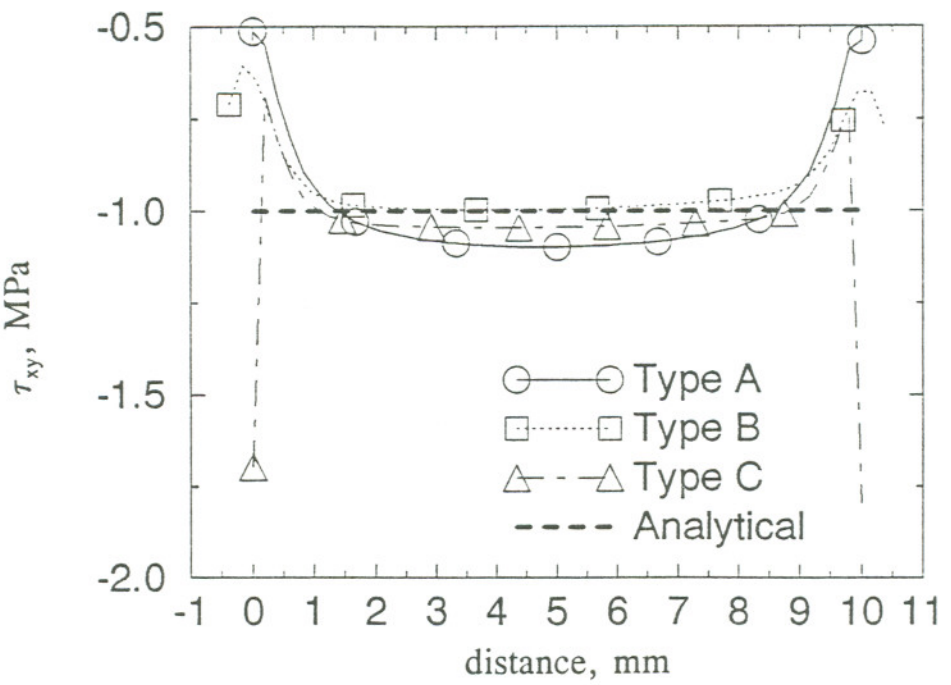

b) along the adhesive-adherend interface (x=0.5)

Fig. 3.9 Shear stress distributions for different specimens under pure shear loading condition (ϕ=0°, t=1.0 mm).

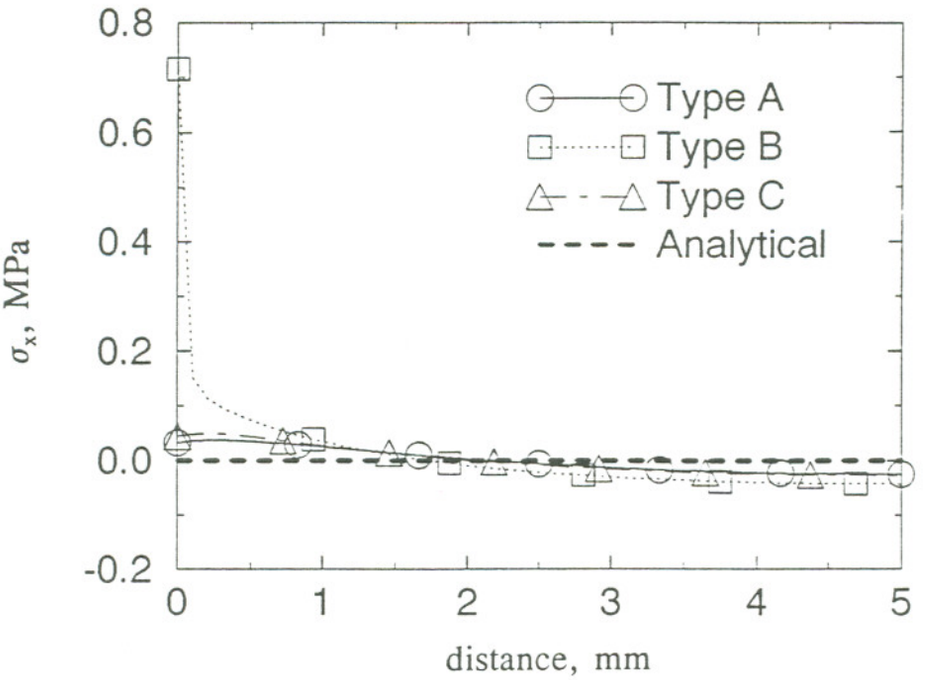

a) along the notch root axis (x=0)

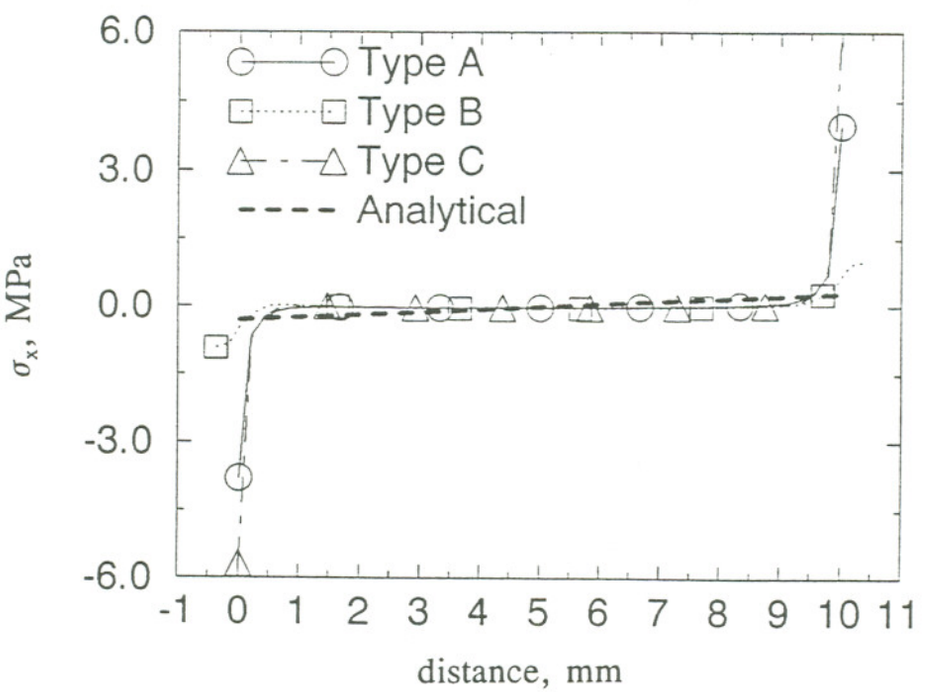

b) along the adhesive-adherend interface (x=0.5)

Fig. 3.10 Normal stress distributions for different specimens under pure shear loading condition (ϕ=0°, t=1.0 mm).

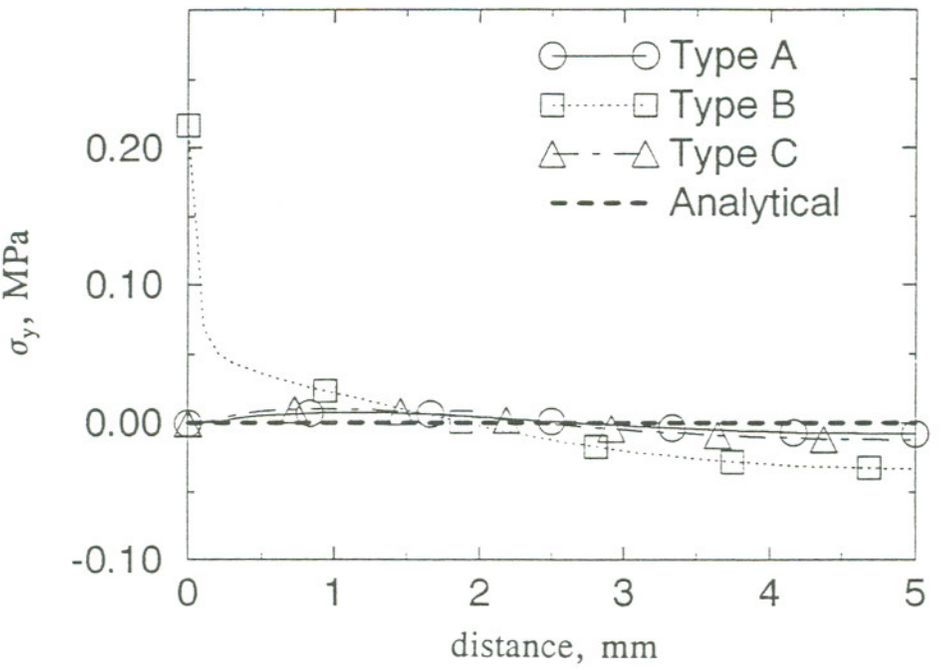

a) along the notch root axis (x=0)

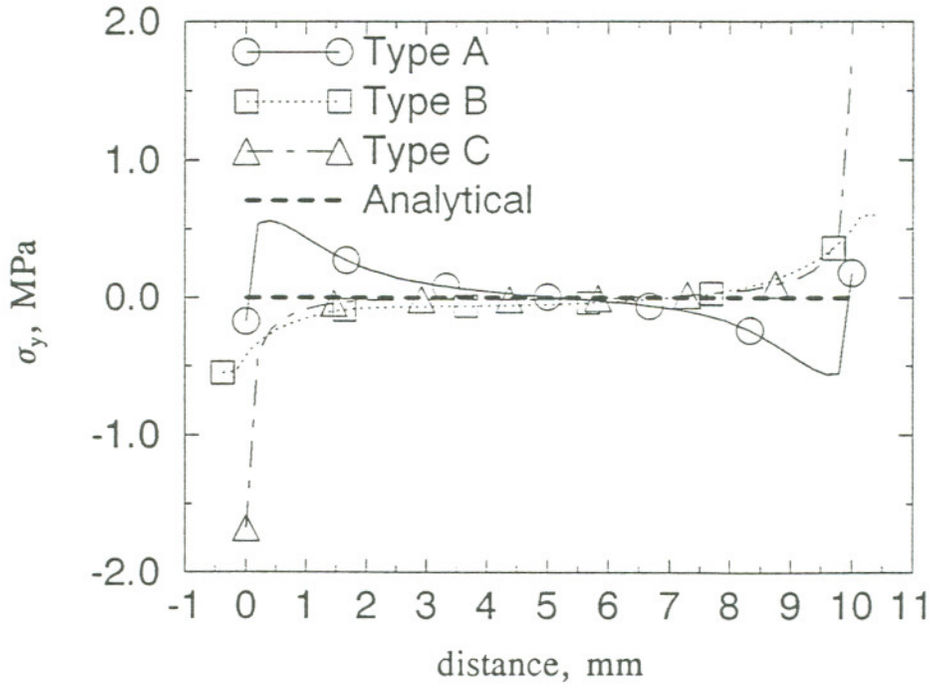

b) along the adhesive-adherend interface (x=0.5)

Fig. 3.11 Normal stress distributions for different specimens under pure shear loading condition (ϕ=0°, t=1.0 mm).

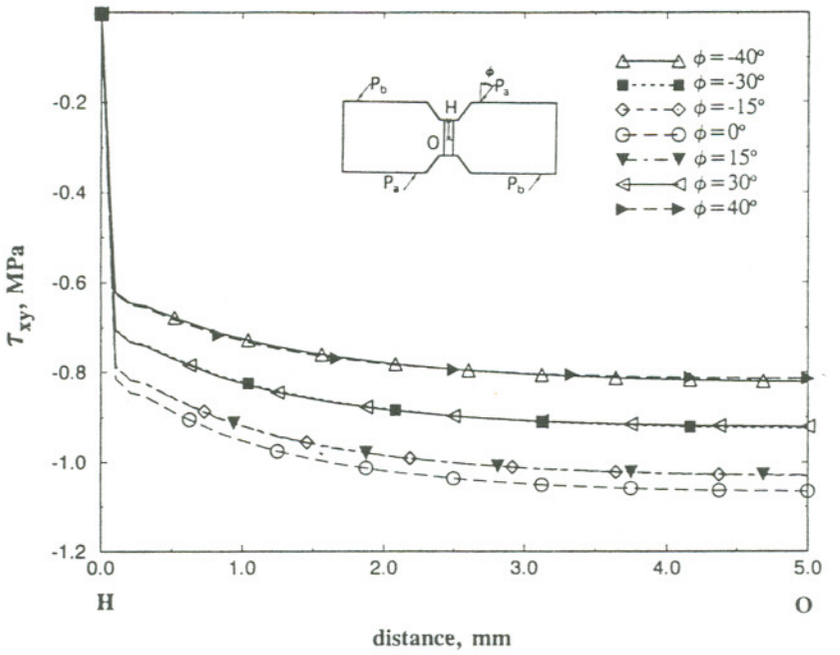

a) along the notch root axis (x=0)

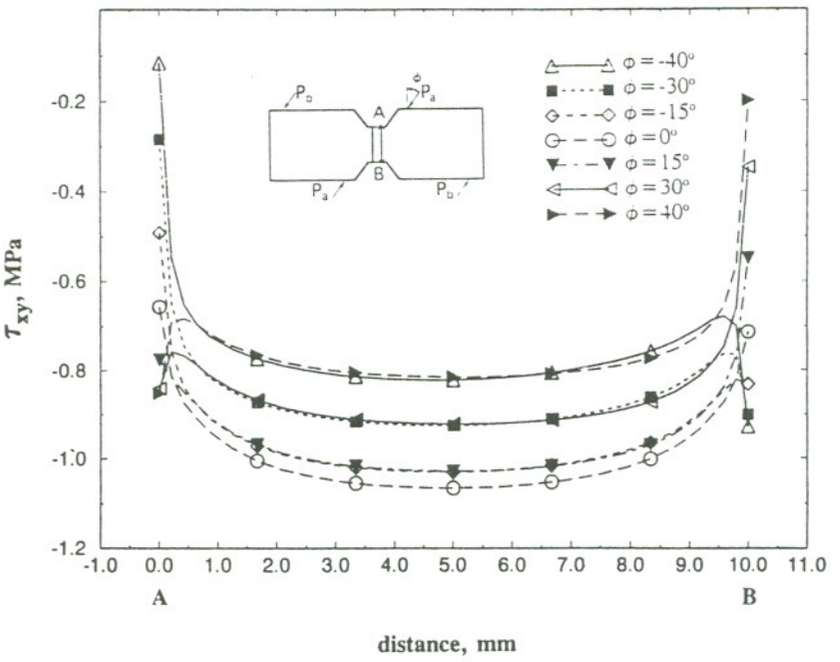

b) along the adhesive-adherend interface (x=0.5)

Fig. 3.12 Shear stress distributions for Type A specimen under various loading conditions (ϕ=0°, t=1.0 mm).

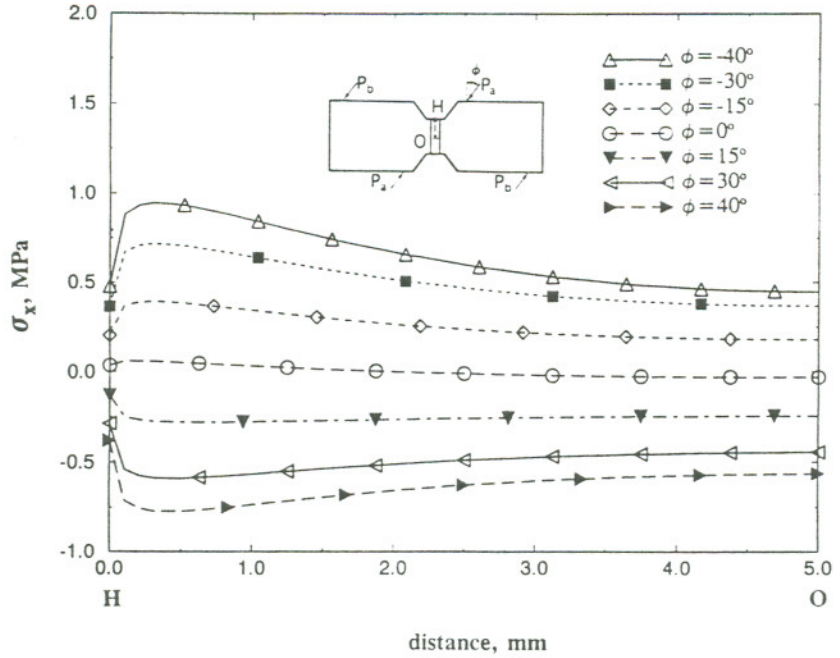

a) along the notch root axis (x=0)

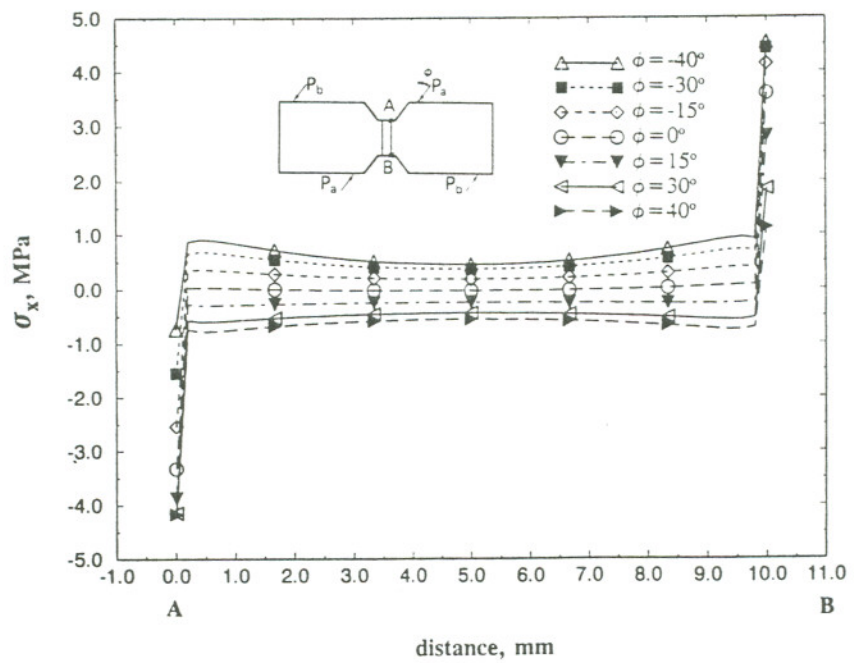

b) along the adhesive-adherend interface (x=0.5)

Fig. 3.13 Normal stress distributions for Type A specimen under various loading conditions (t=1.0 mm).

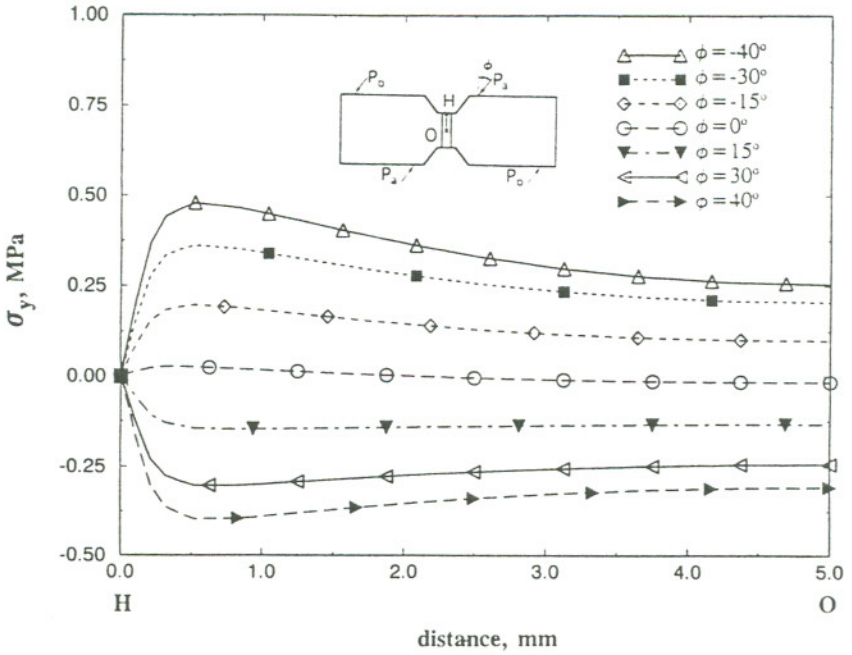

a) along the notch root axis (x=0)

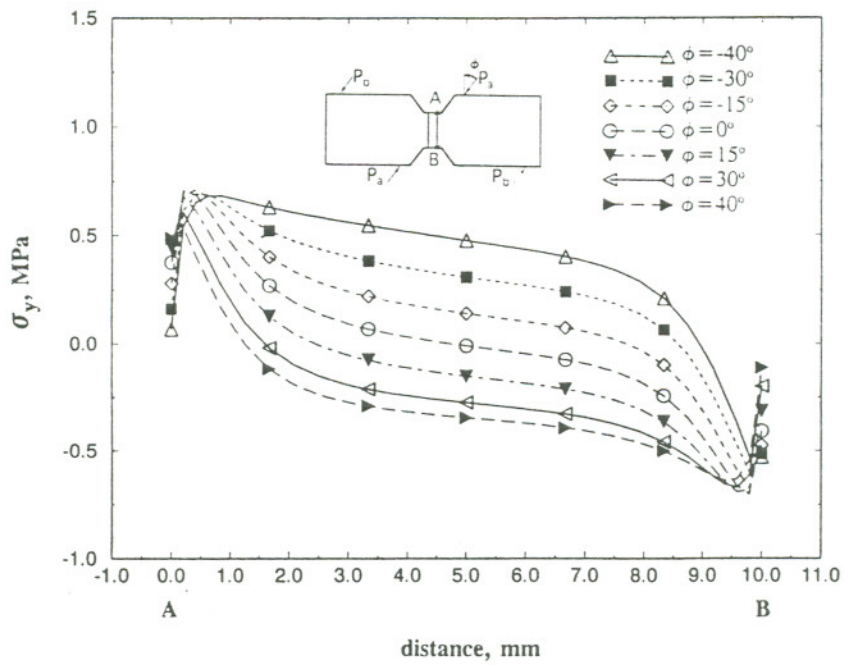

b) along the adhesive-adherend interface (x=0.5)

Fig. 3.14 Normal stress distributions for Type A specimen under various loading conditions (t=1.0 mm).

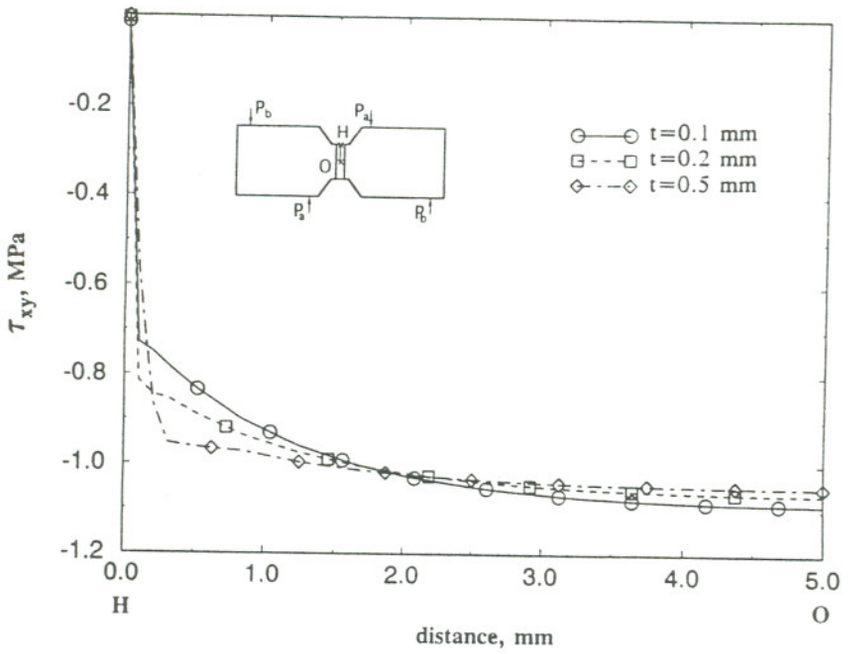

a) along the notch root axis (x=0)

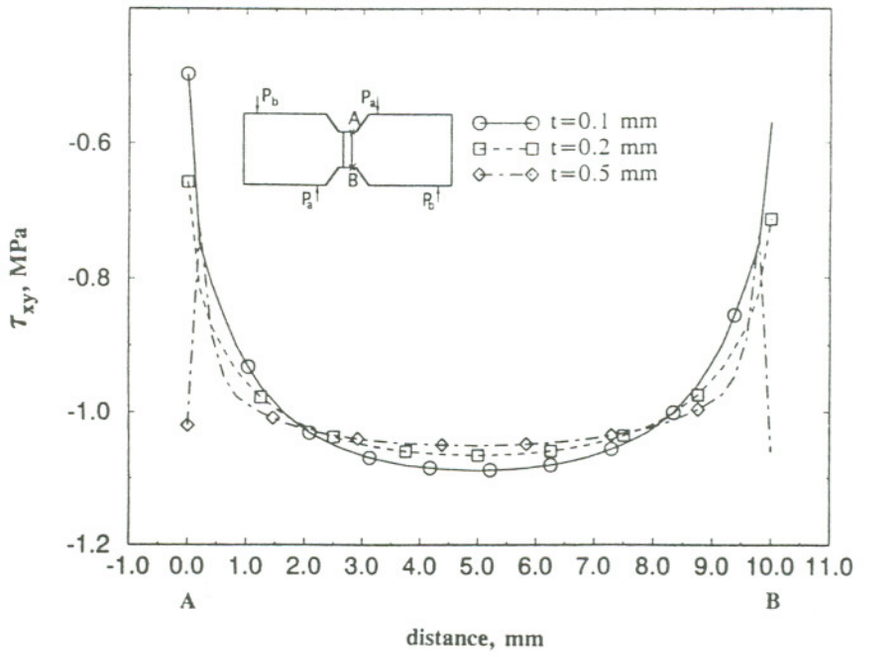

b) along the adhesive-adherend interface (x=t/2)

Fig. 3.15 Shear stress distributions for Type A specimen with different adhesive layer thicknesses under pure shear loading condition (ϕ=0°).

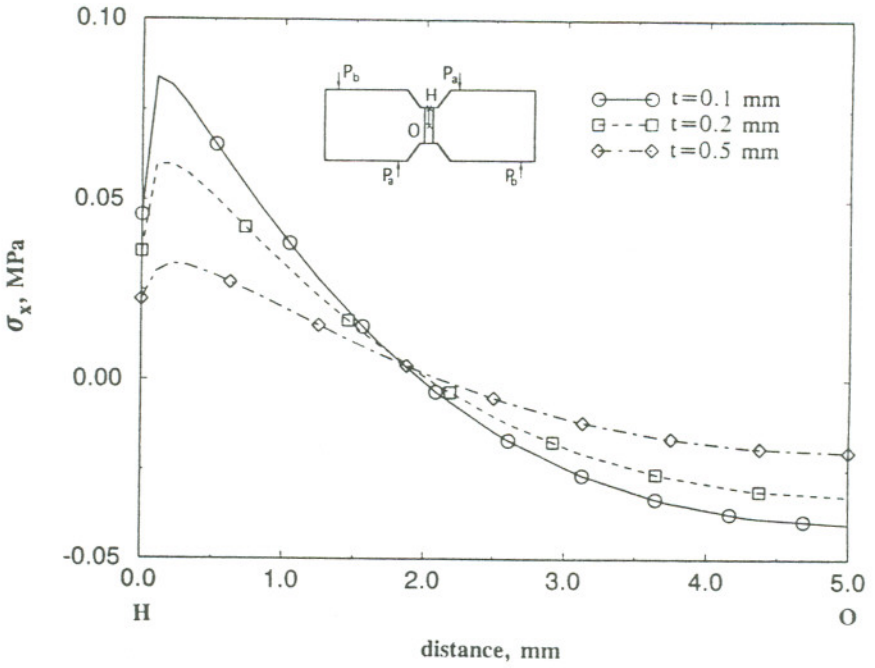

a) along the notch root axis (x=0)

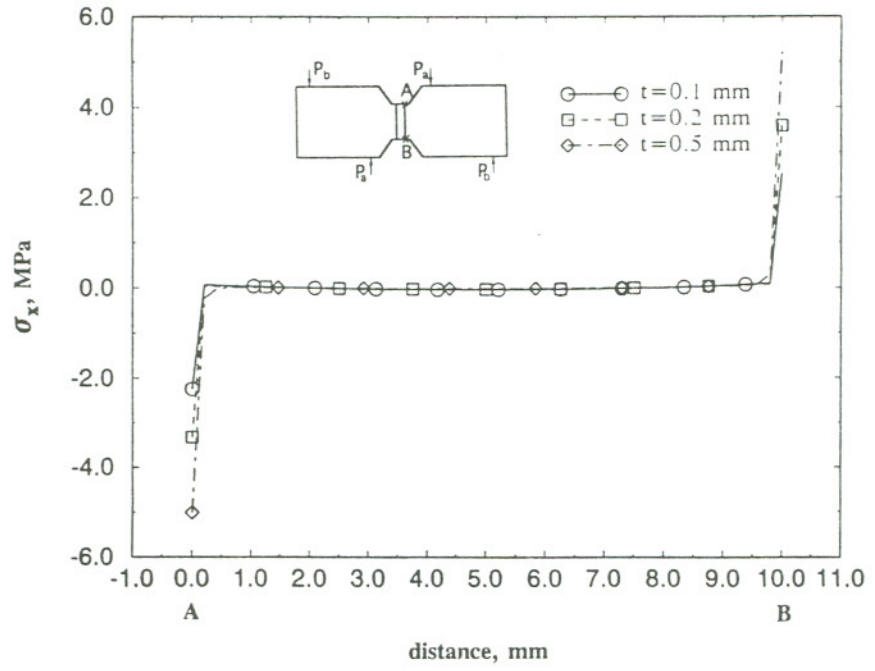

b) along the adhesive-adherend interface (x=t/2)

Fig. 3.16 Normal stress distributions for Type A specimen with different adhesive layer thicknesses under pure shear loading condition (ϕ=0°).

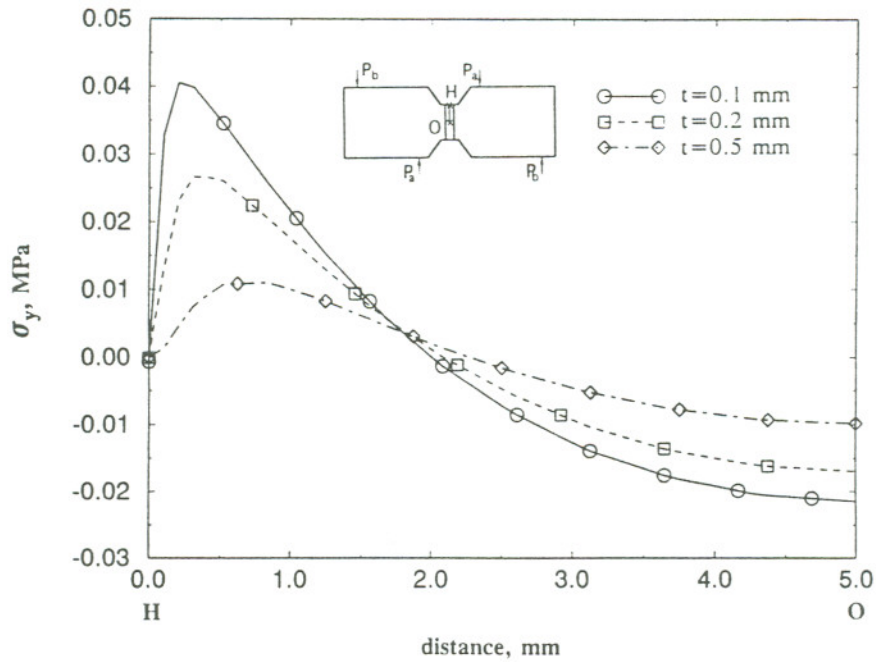

a) along the notch root axis (x=0)

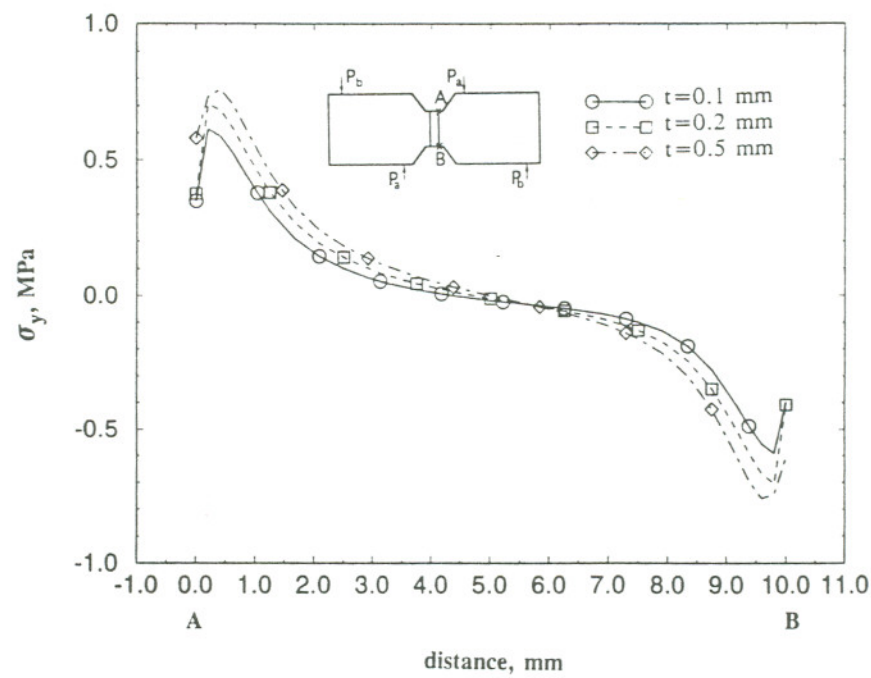

b) along the adhesive-adherend interface (x=t/2)

Fig. 3.17 Normal stress distributions for Type A specimen with different adhesive layer thicknesses under pure shear loading condition (ϕ=0°).

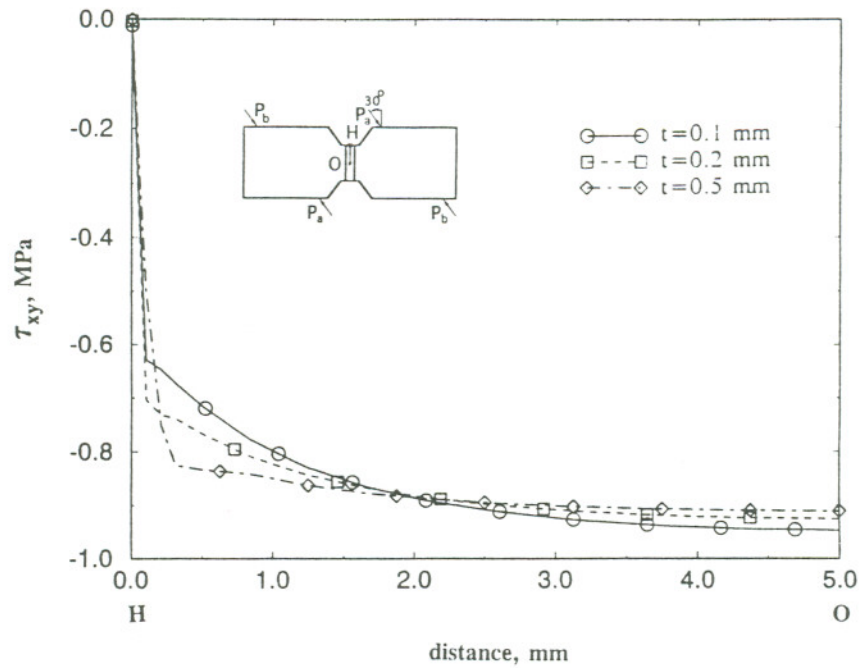

a) along the notch root axis (x=0)

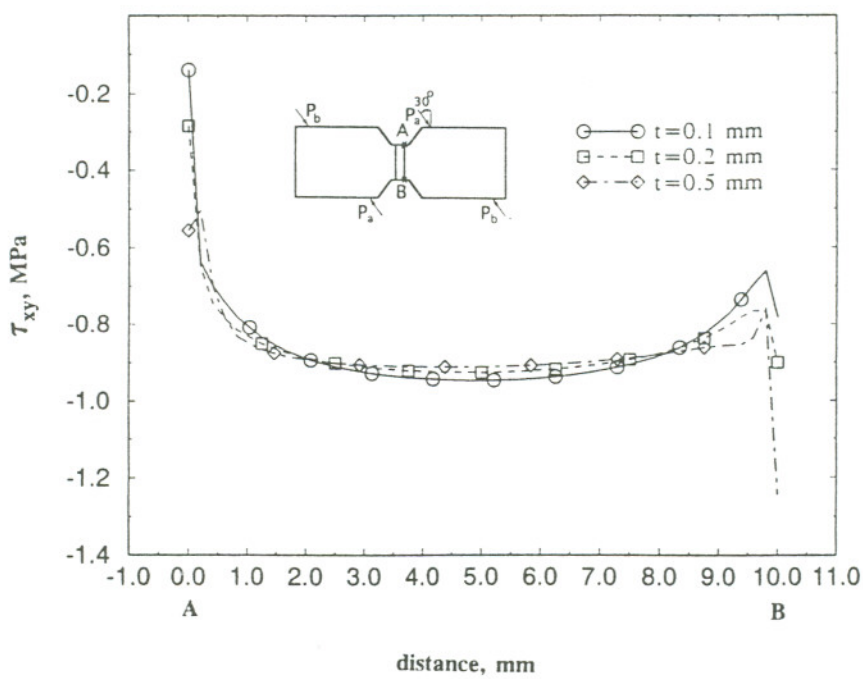

b) along the adhesive-adherend interface (x=t/2)

Fig. 3.18 Shear stress distributions for Type A specimen with different adhesive layer thicknesses under tension-compression loading condition (ϕ=-30°).

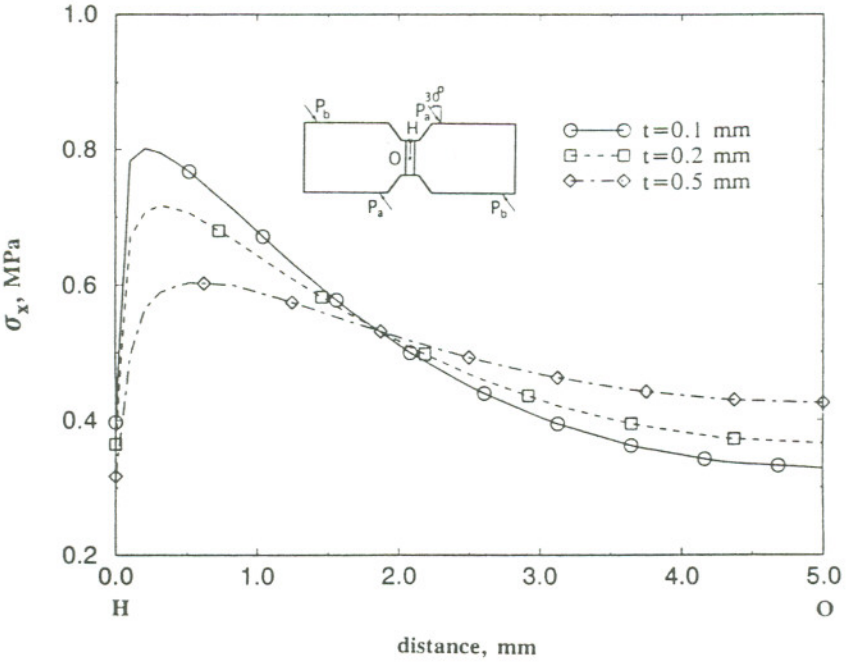

a) along the notch root axis (x=0)

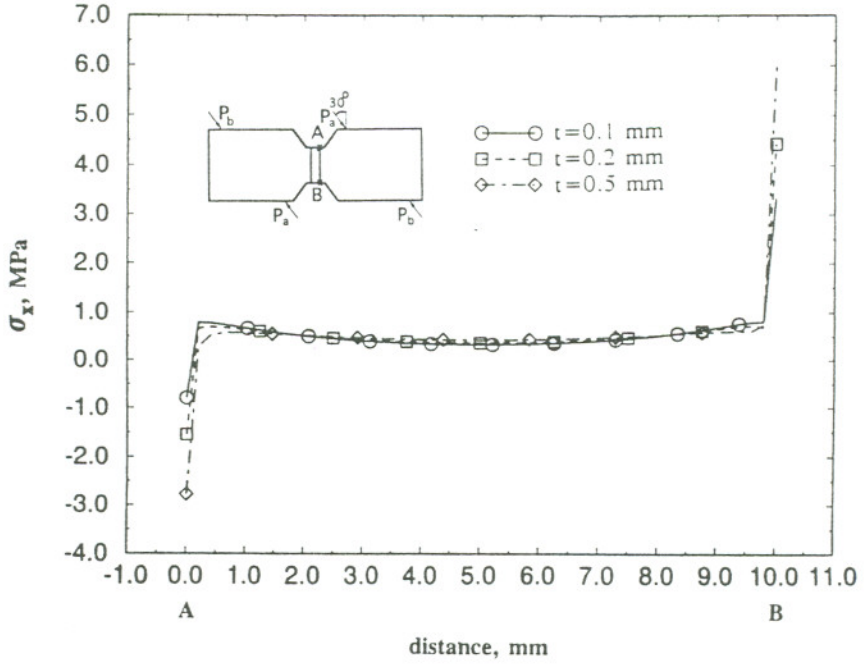

b) along the adhesive-adherend interface (x=t/2)

Fig. 3.19 Normal stress distributions for Type A specimen with different adhesive layer thicknesses under tension-compression loading condition (ϕ=-30°).

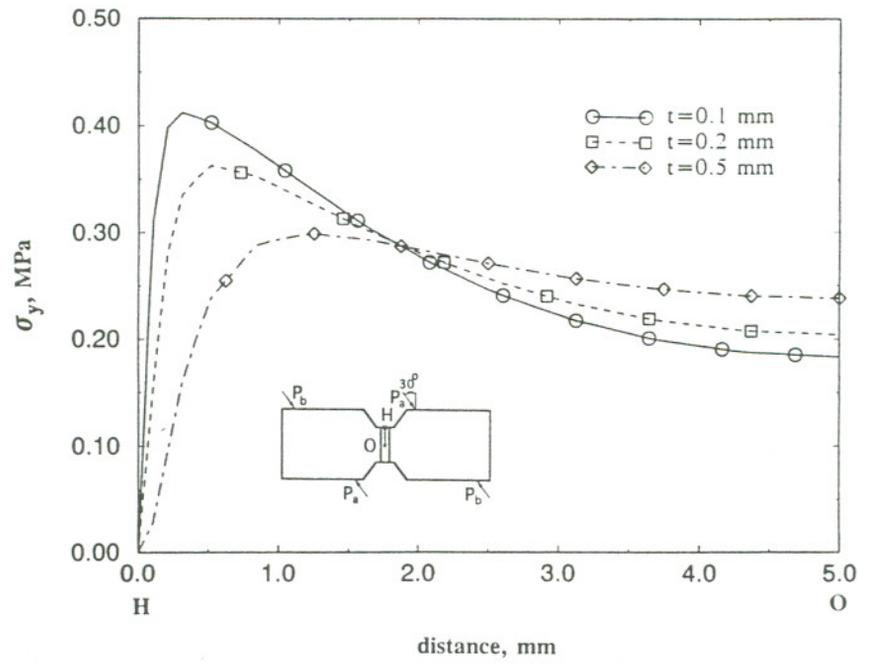

a) along the notch root axis (x=0)

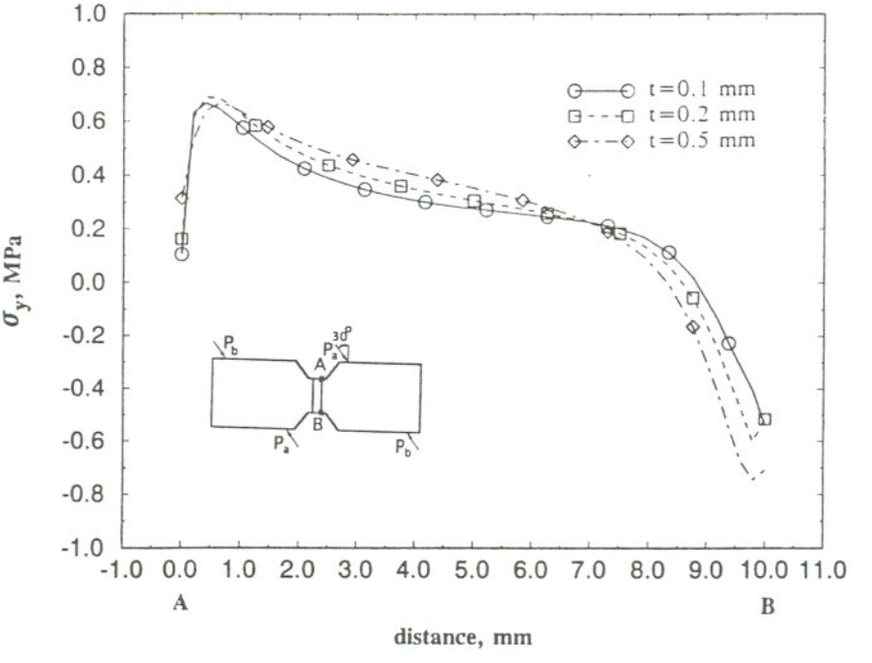

b) along the adhesive-adherend interface (x=t/2)

Fig. 3.20 Normal stress distributions for Type A specimen with different adhesive layer thicknesses under tension-compression loading condition (ϕ=-30°).

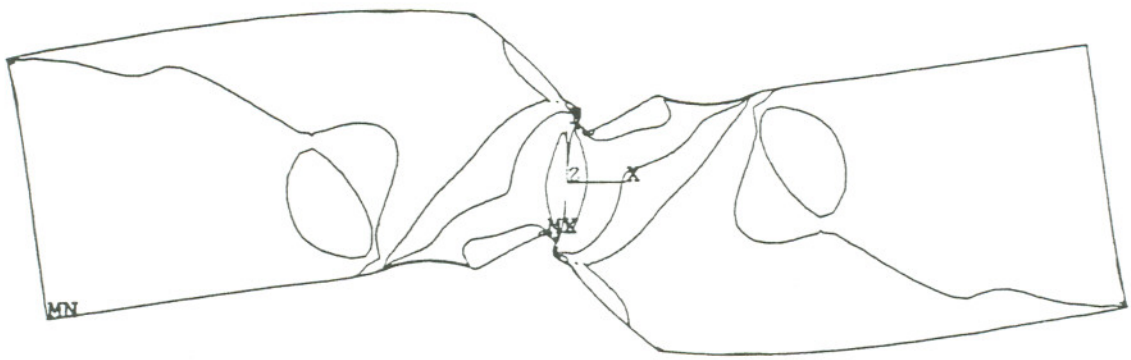

a) t=0.1 mm

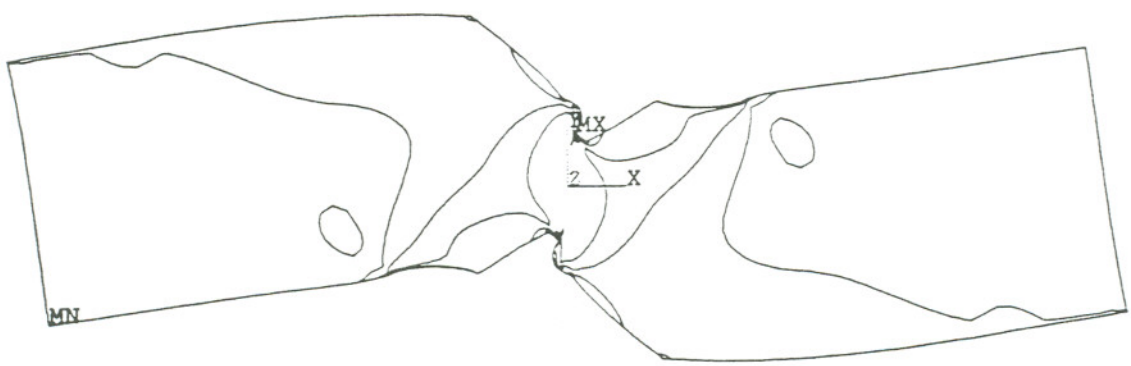

b) t=0.2 mm

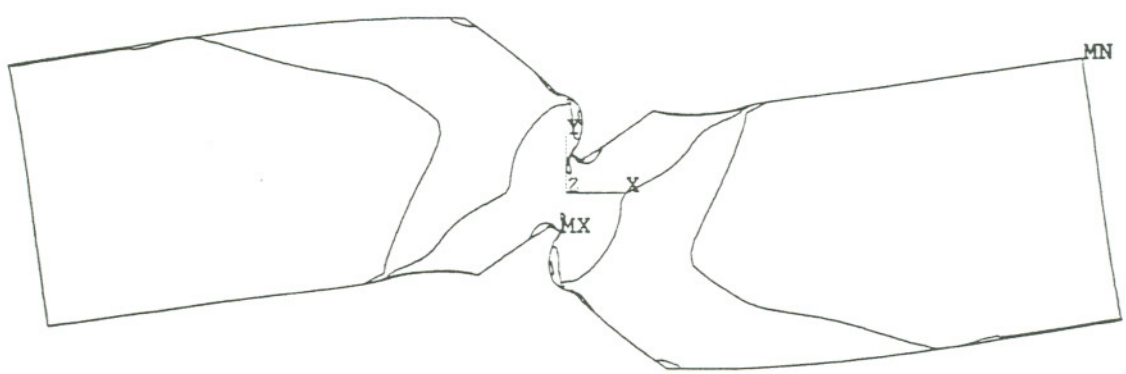

c) t=0.5 mm

Fig. 3.21 Equivalent stress contours for Type A specimen with different adhesive layer thicknesses under tension-compression loading condition (ϕ=-30°).

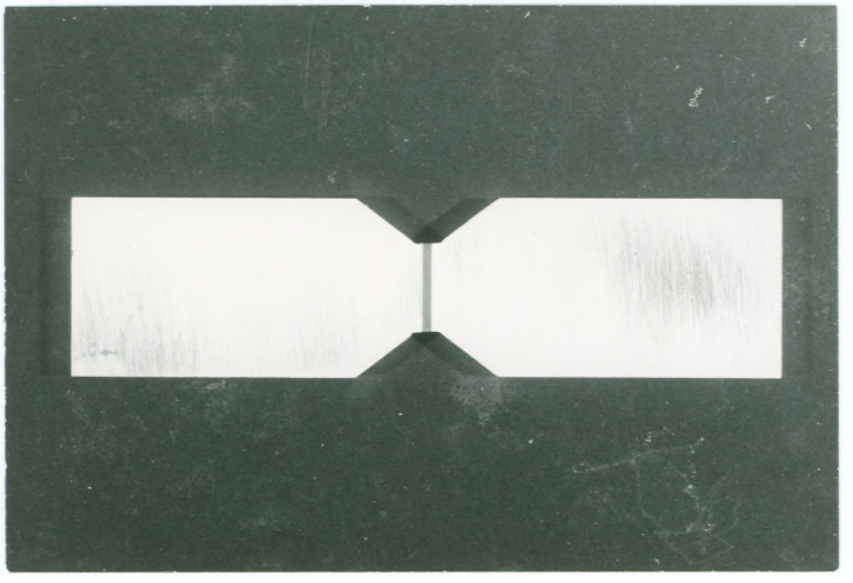

a) specimen overview

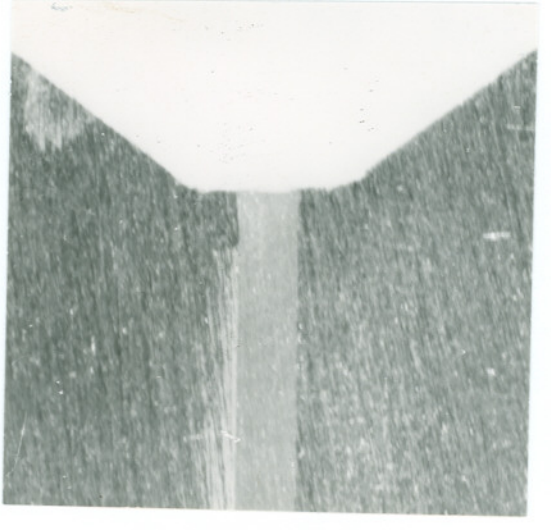

b) notch root geometry

Fig. 3.22 Adhesive joint Iosipescu specimen (Type A, t=1.0 mm).

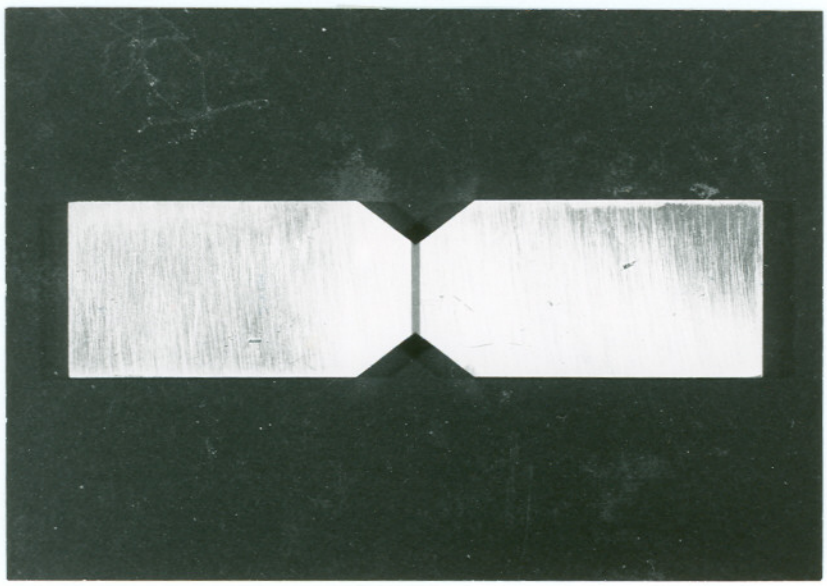

a) specimen overview

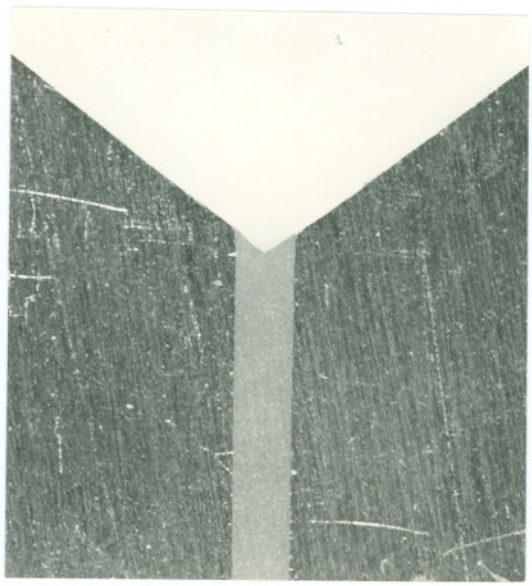

b) notch root geometry

Fig. 3.23 Adhesive joint Iosipescu specimen (Type B, t=1.0 mm).

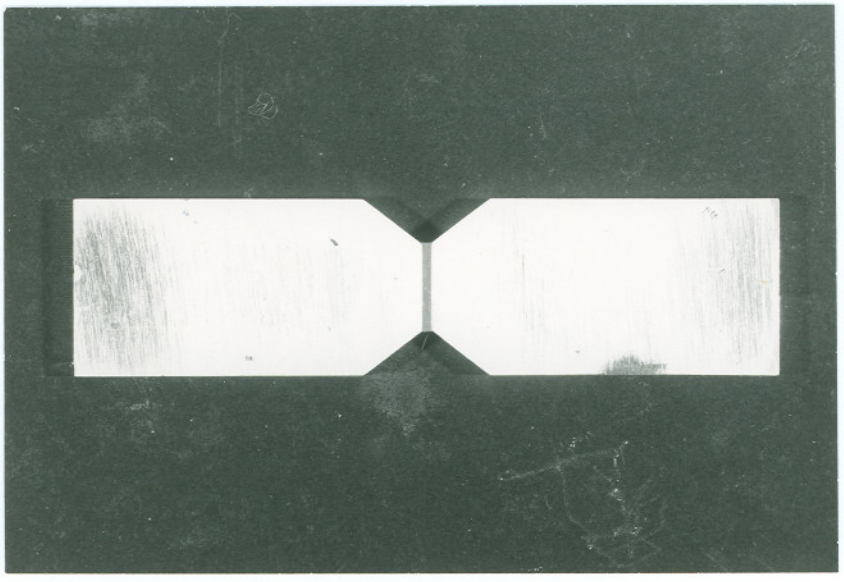

a) specimen overview

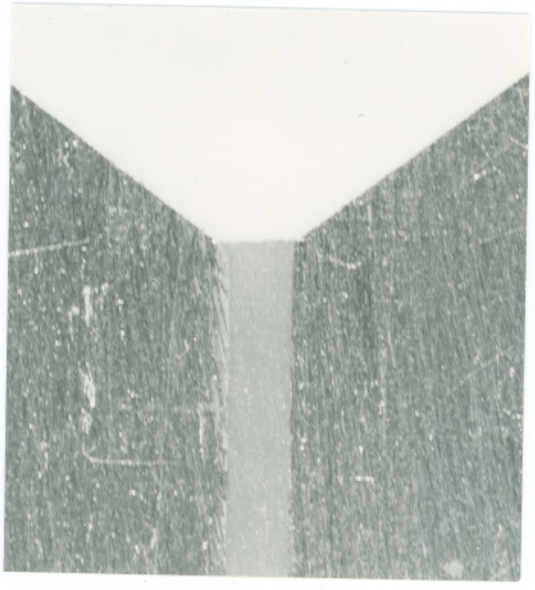

b) notch root geometry

Fig. 3.24 Adhesive joint Iosipescu specimen (Type C, t=1.0 mm).

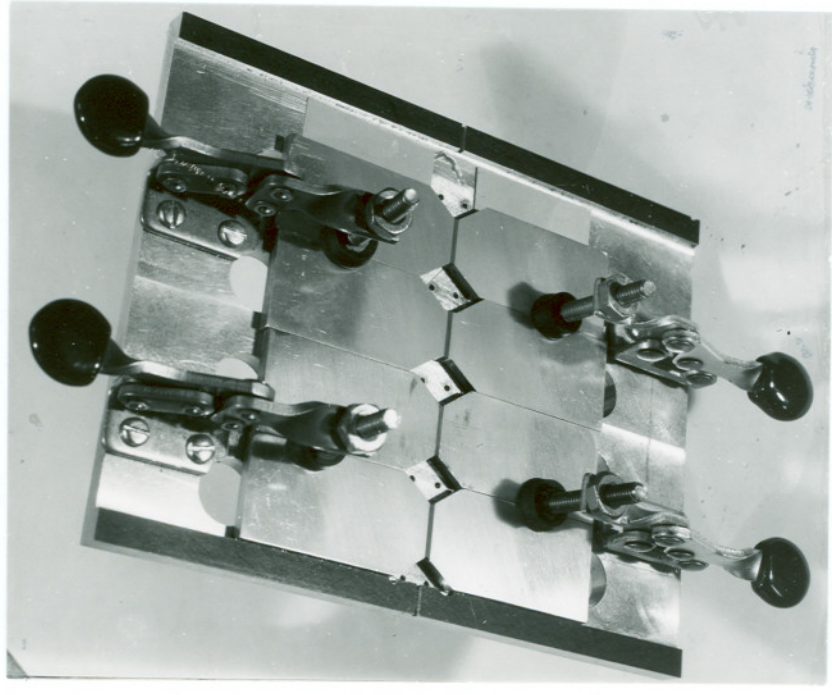

Fig. 3.25 Bonding assembly for making adhesive joint Iosipescu specimen.

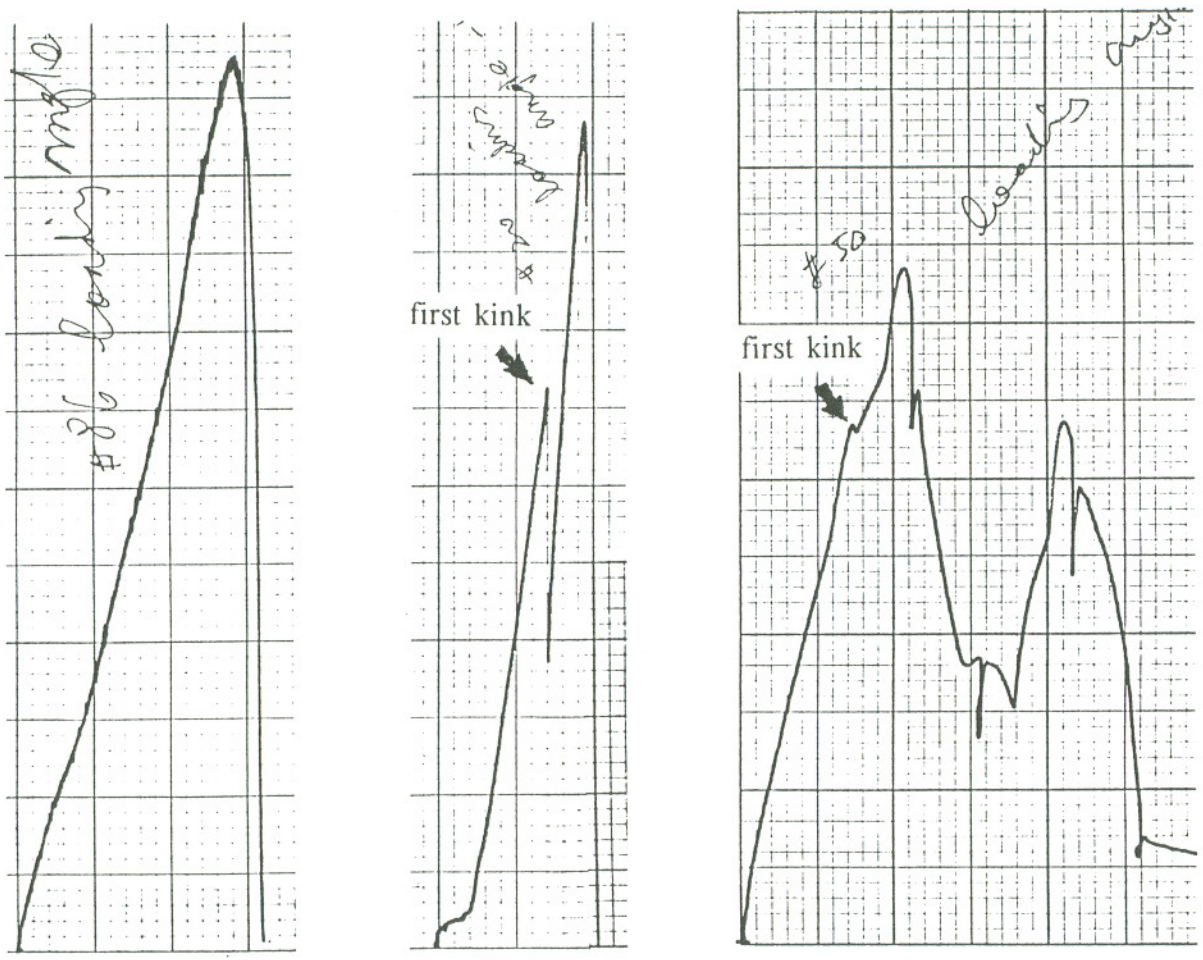

a) without kink b) with one kink c) with multi-kinks

Fig. 3.26 Typical load-displacement diagrams (vertical: force load; horizontal: displacement).

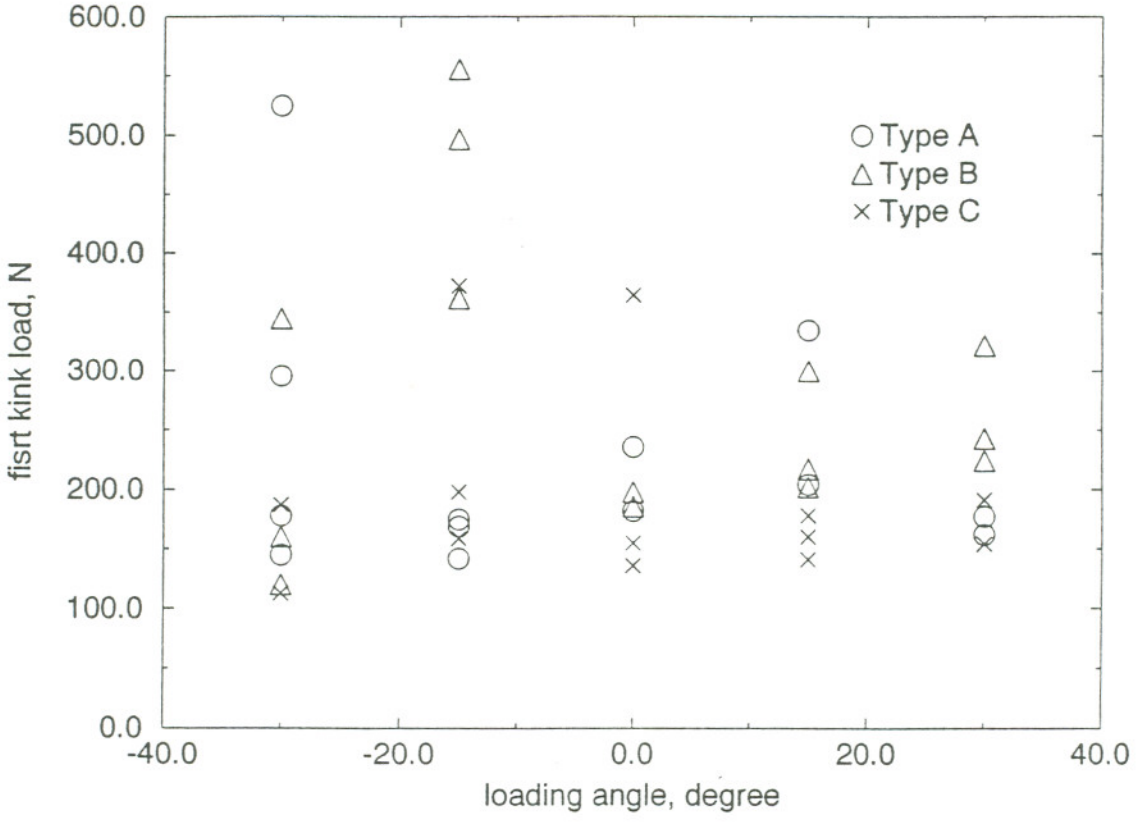

Fig. 3.27 First kink loads for different specimens (rigid adhesive, t=1.0 mm).

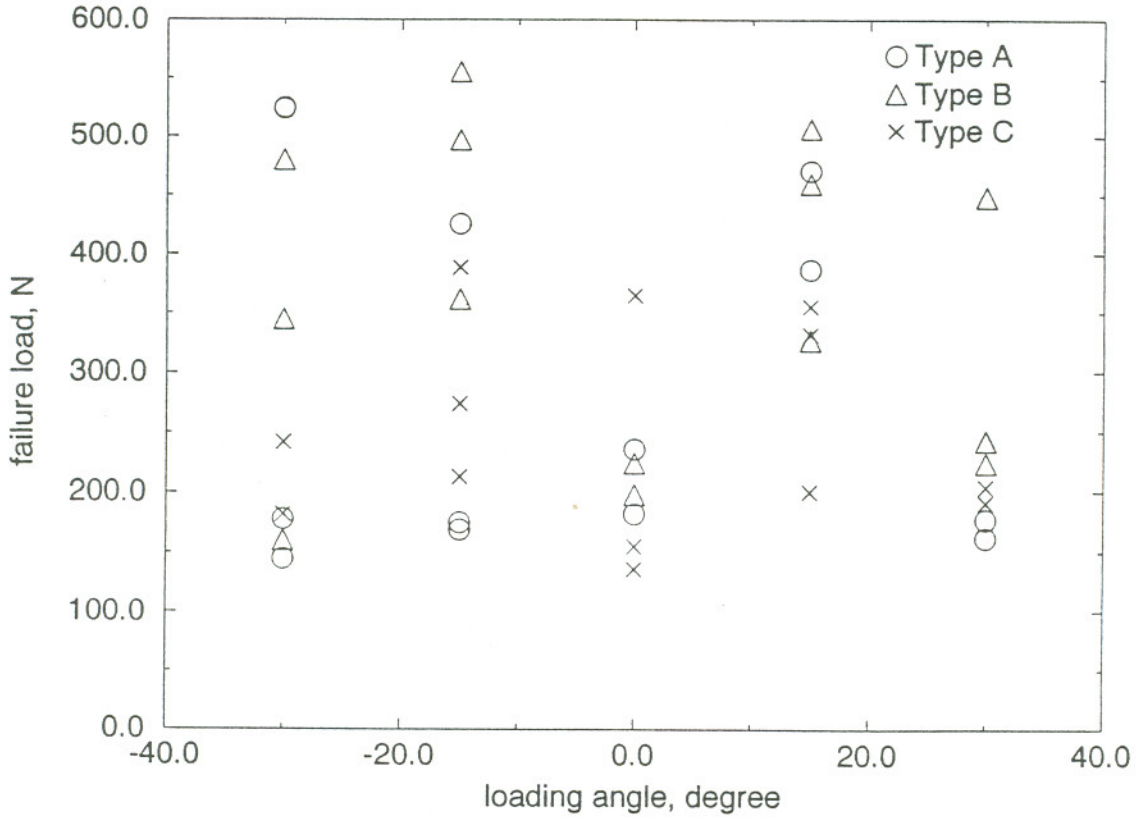

Fig. 3.28 Rupture loads for different specimens (rigid adhesive, t=1.0 mm).

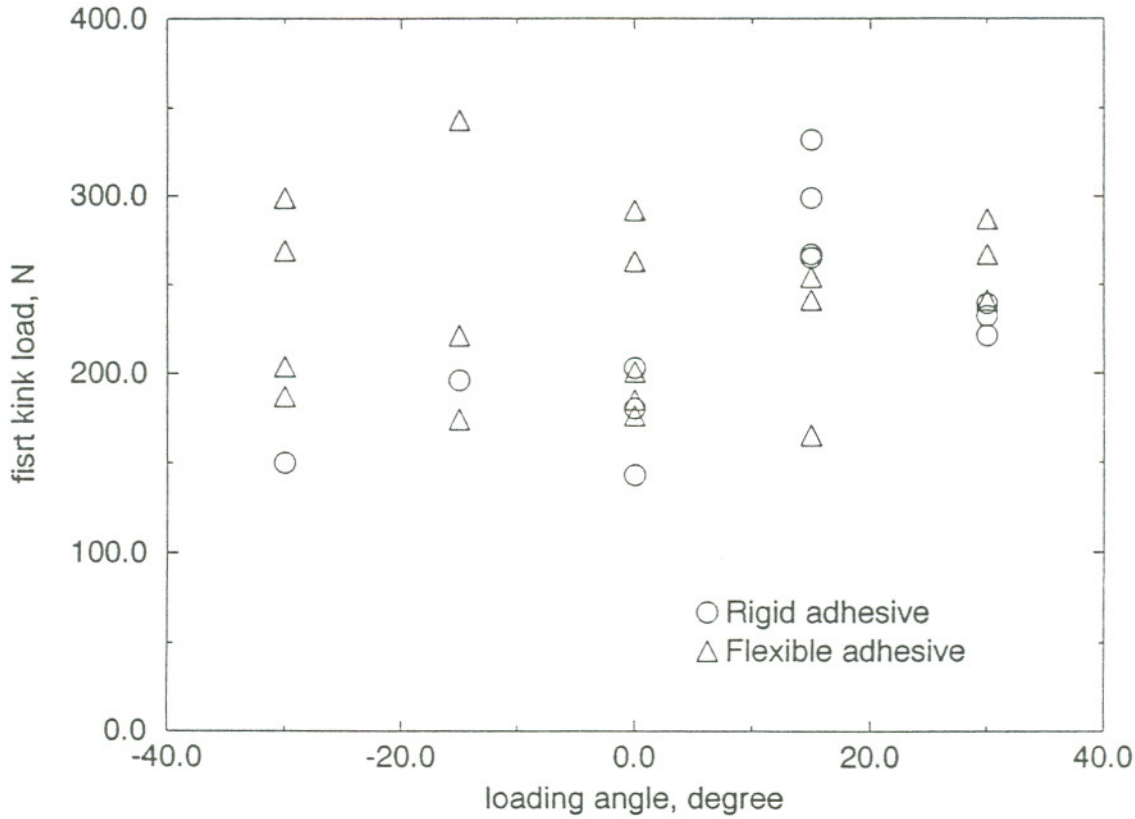

Fig. 3.29 First kink loads for different adhesives (Type A, t=0.2 mm).

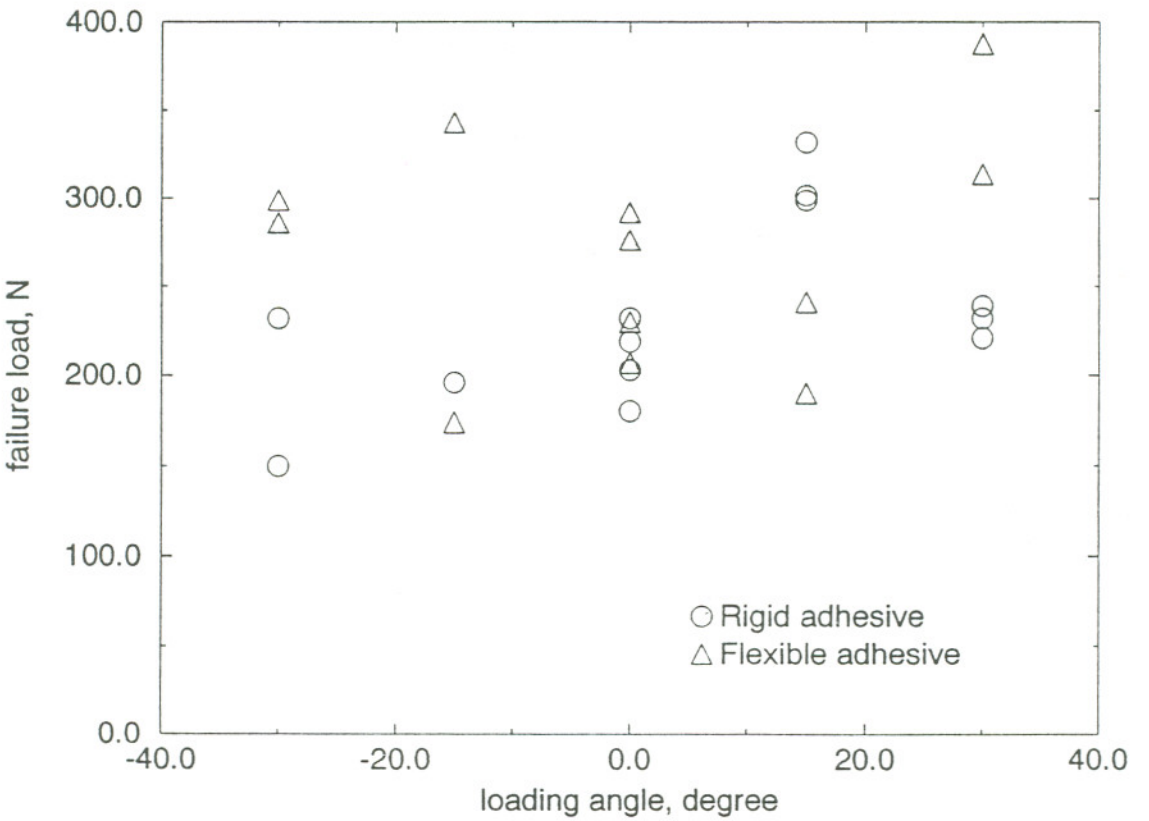

Fig. 3.30 Rupture loads for different adhesives (Type A, t=0.2 mm).

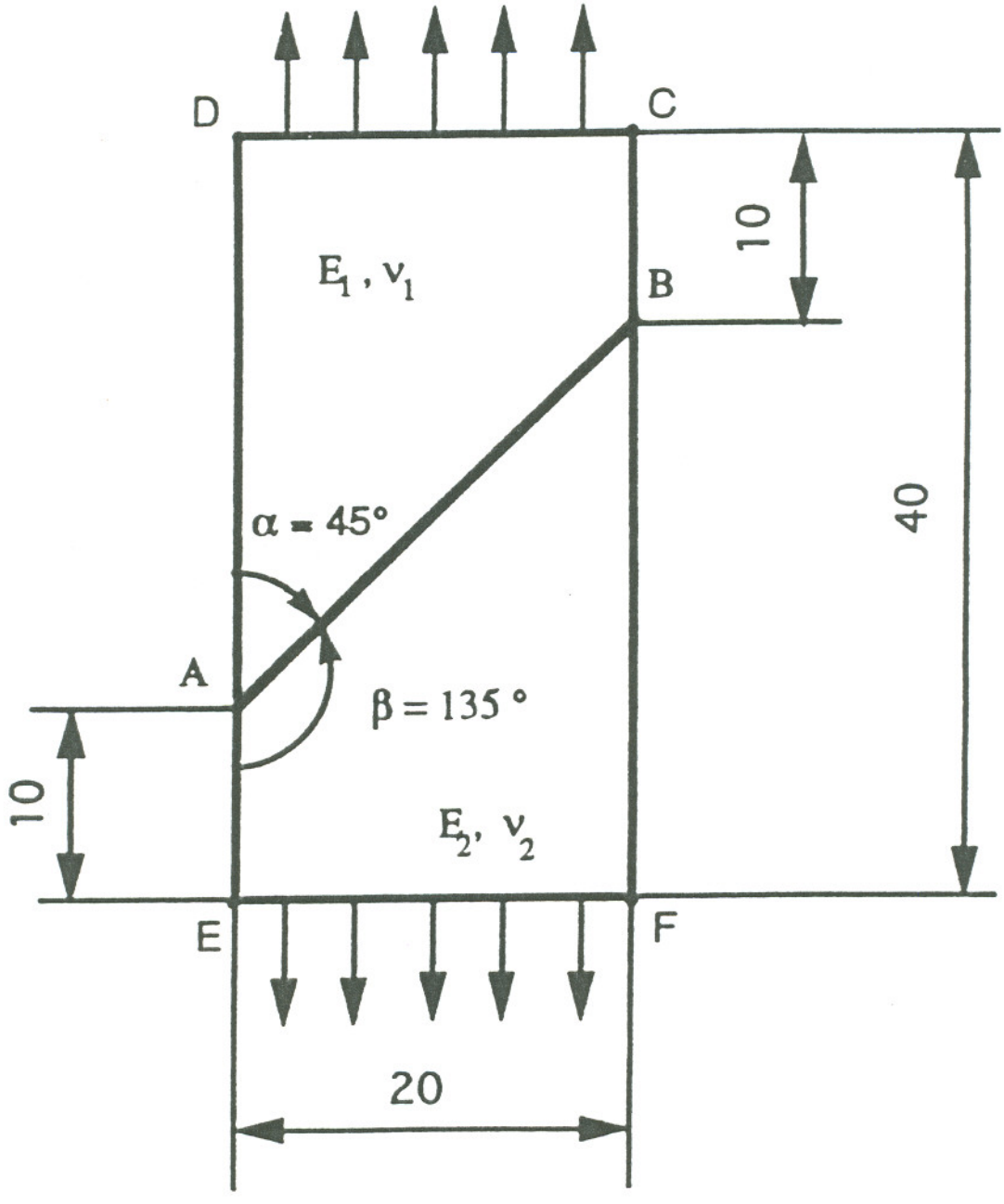

Fig. 3.31 A rectangle with a skewed interface.

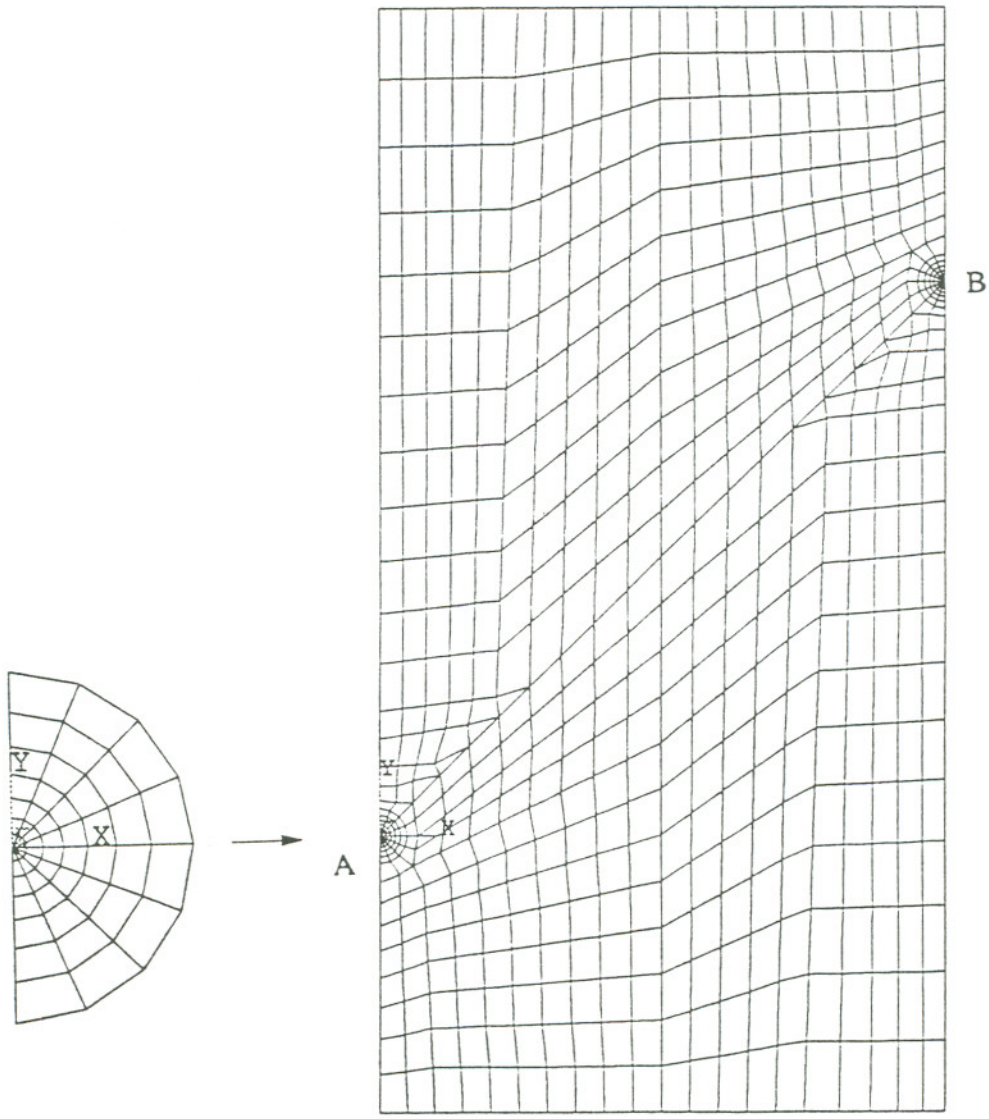

Fig. 3.32 FEM representation of figure 3.31.

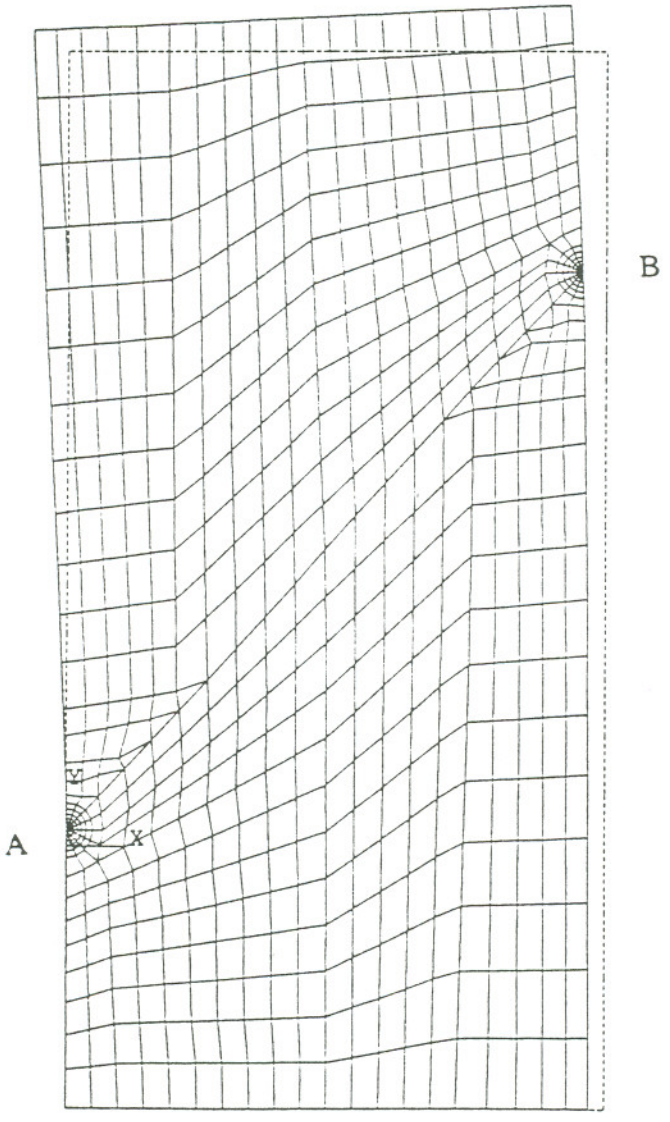

Fig. 3.33 Deformed structure superimposed on its original outline (dashed line).

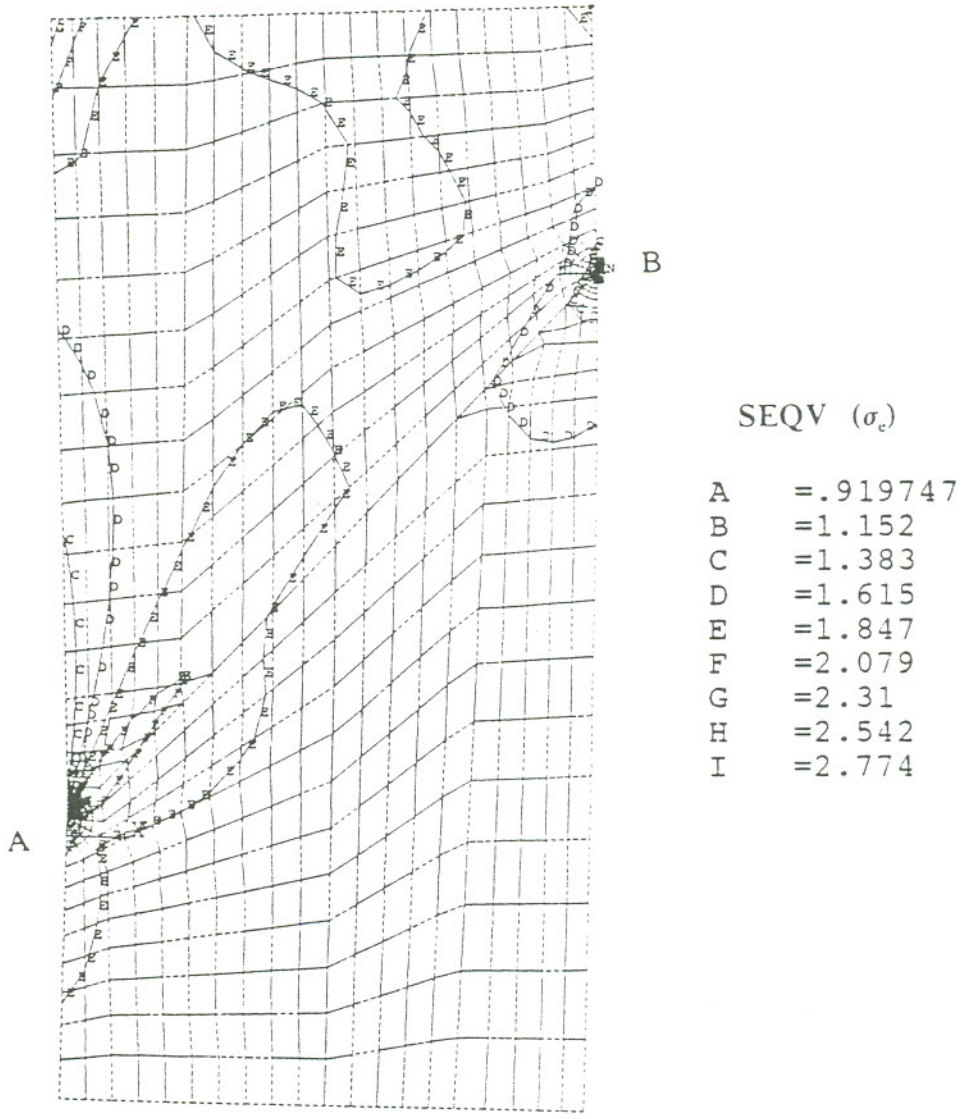

Fig. 3.34 Equivalent stress contour.

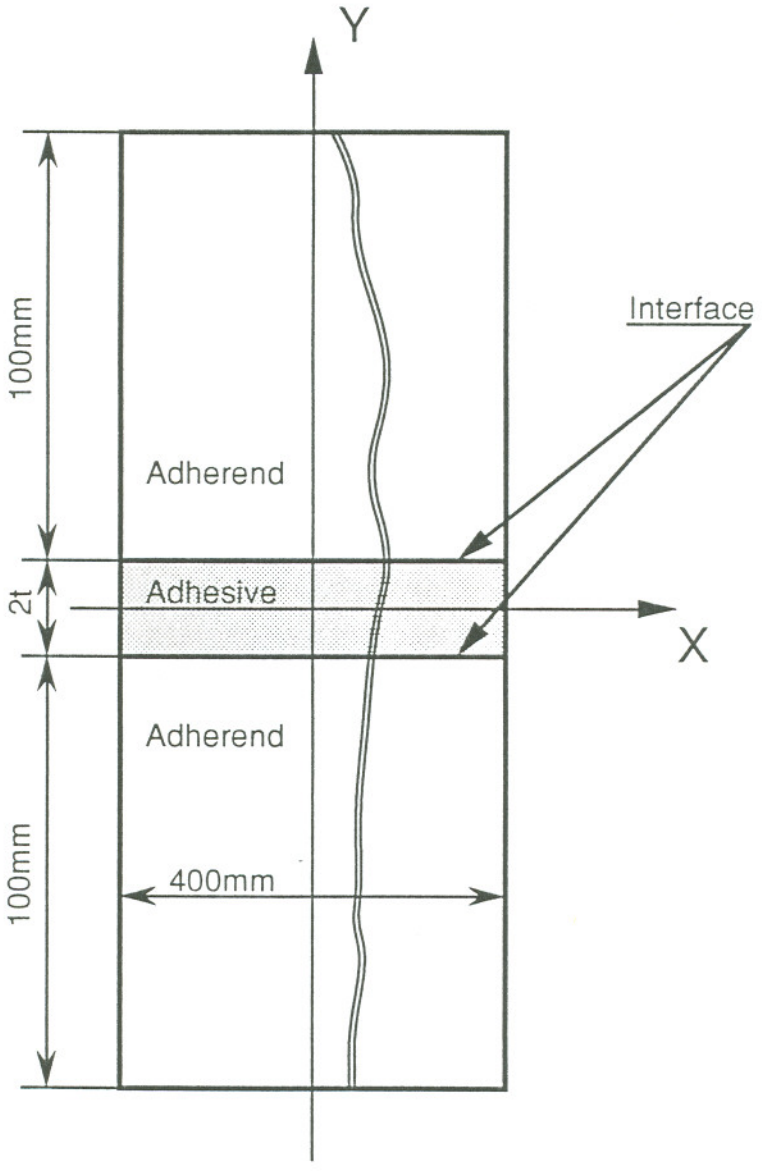

Fig. 3.35 Schematic of adhesive butt joint geometry

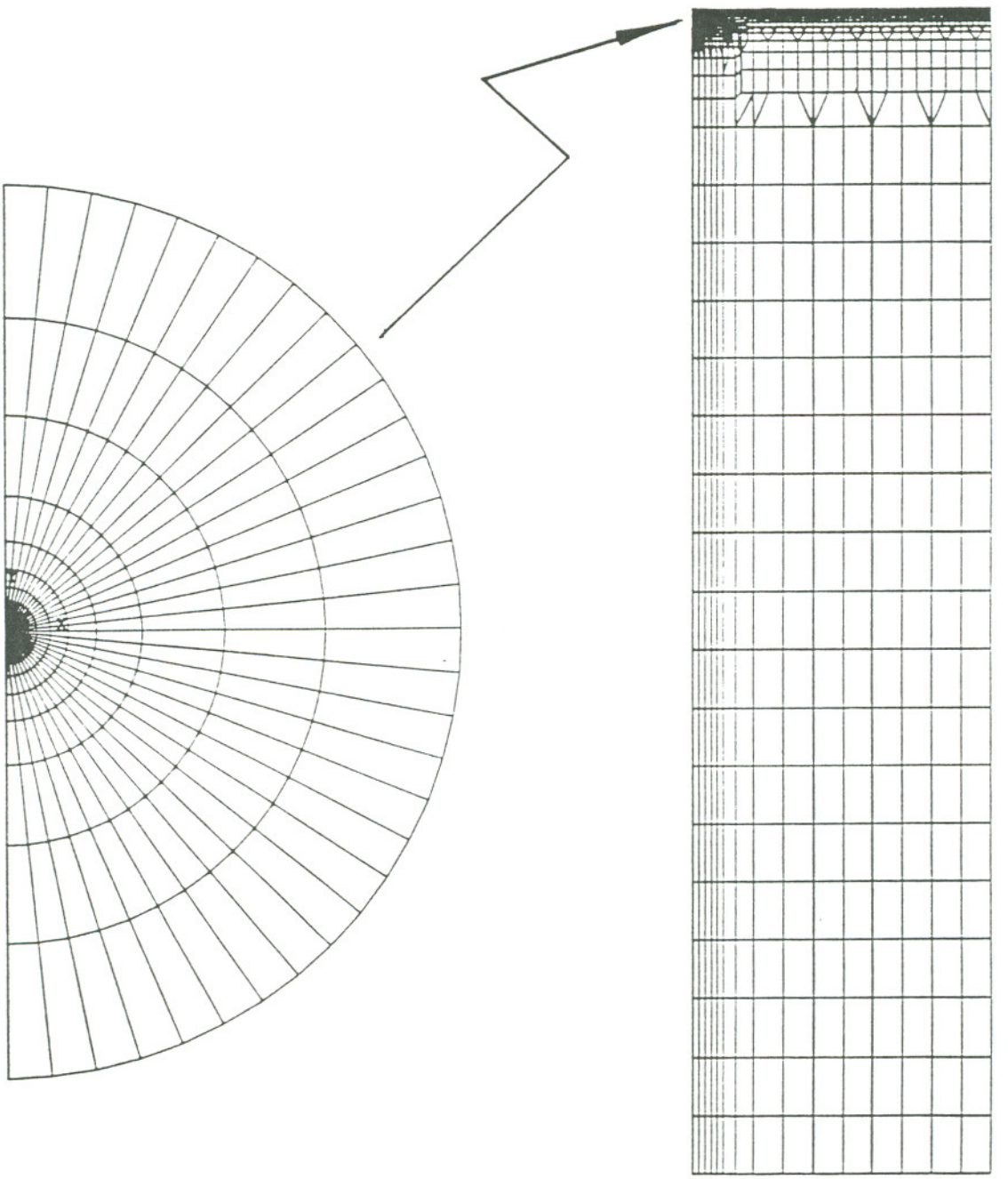

Fig. 3.36 Finite element representation of a butt joint.

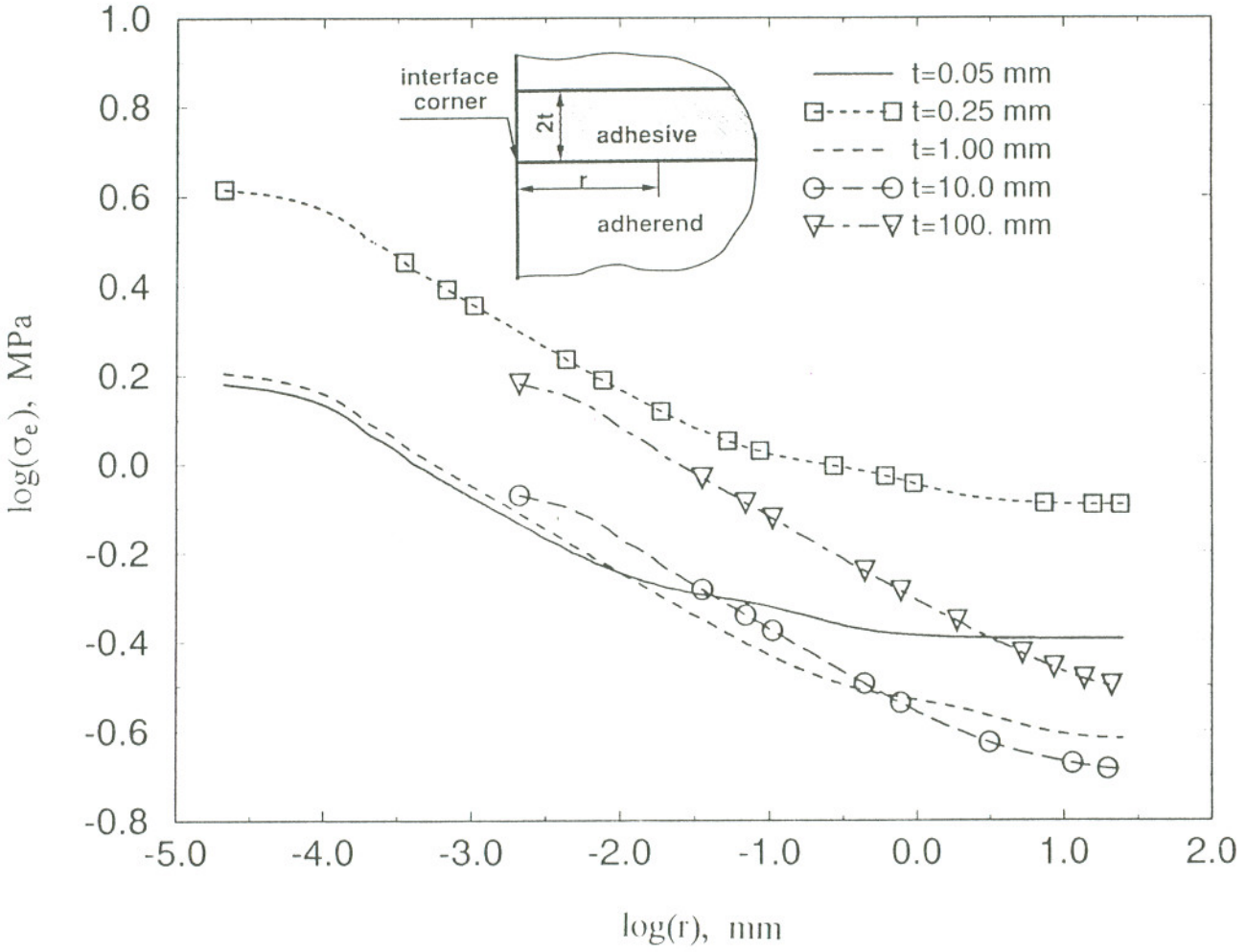

Fig. 3.37 Equivalent stress distributions along bimaterial interface corners (E_1=21000 MPa, E_2=3000 MPa, ν_1=0.30 and ν_2=0.35).

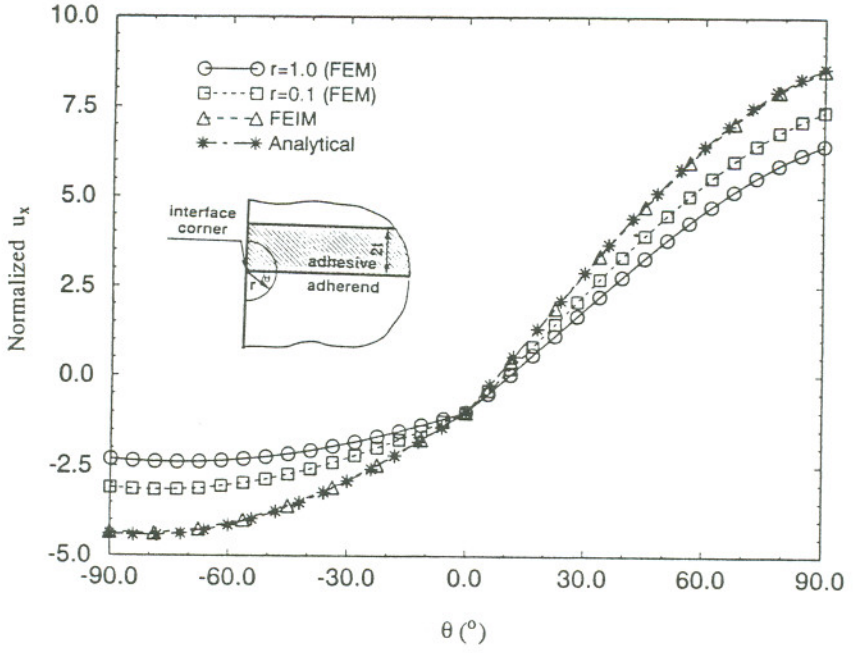

a) x-direction

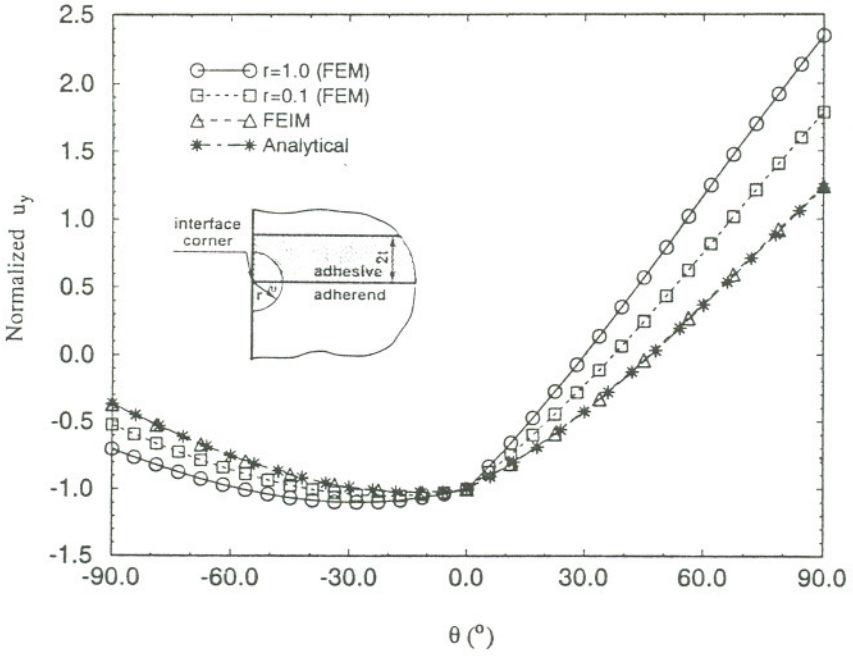

b) y-direction

Fig. 3.38 Normalized displacement eigenfunctions
(E_1=21000 MPa, E_2=3000 MPa, ν_1=0.30 and ν_2=0.35).

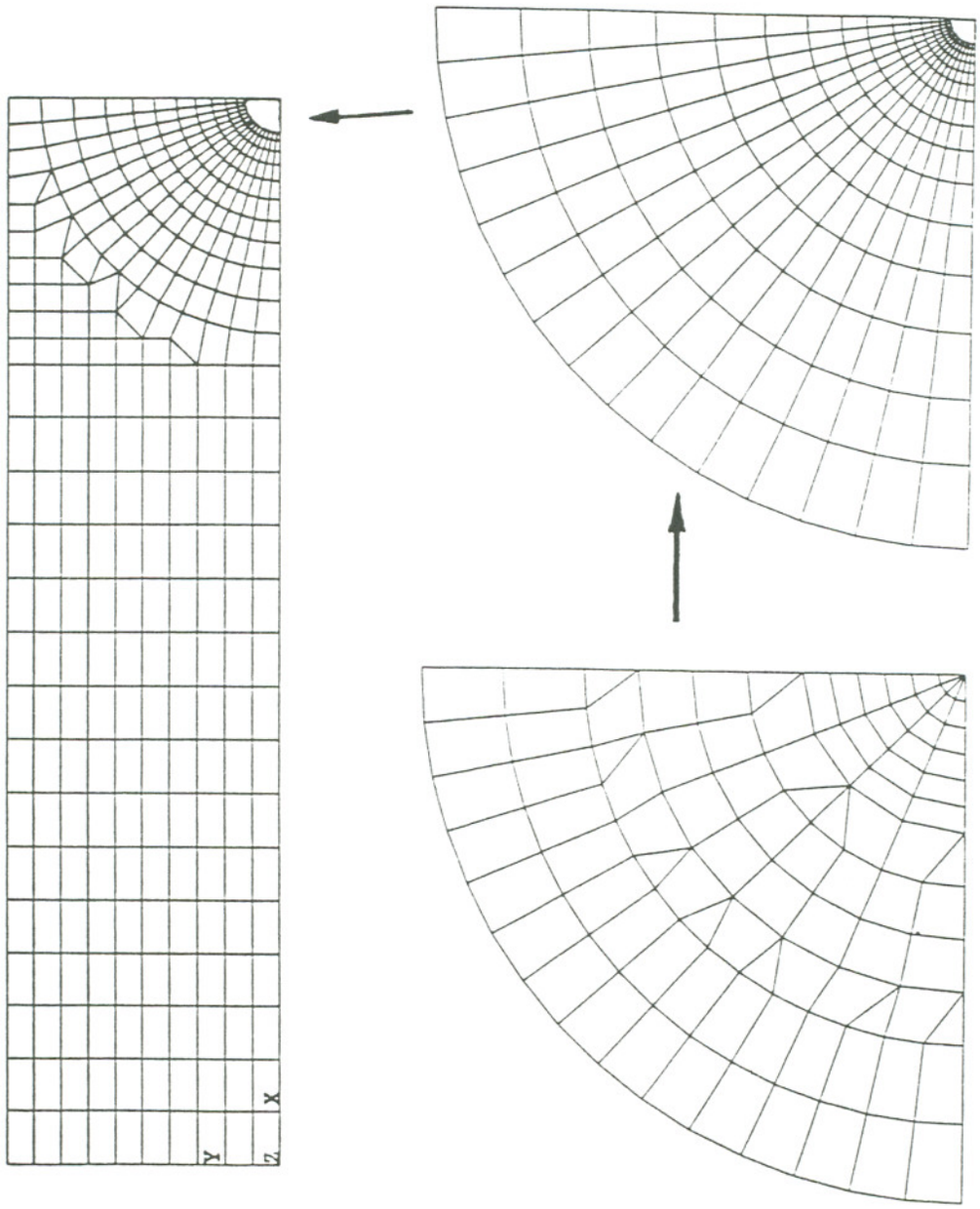

Fig. 3.39 Finite element representation of a butt joint made of elastic adhesive and rigid adherends (resembling an elastic layer bonded to a rigid substrate).

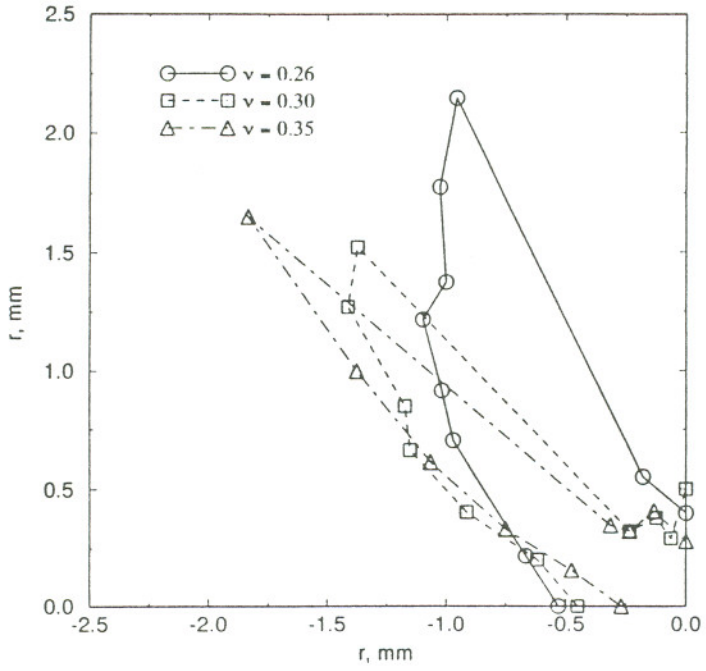

a) E=2632 MPa, t=10 mm

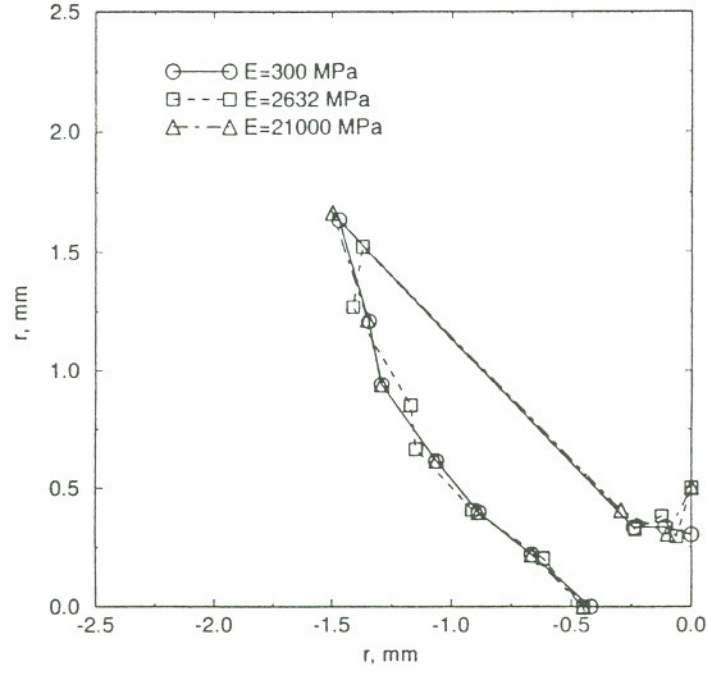

b) ν=0.30, t=10 mm

Fig. 3.40 Stress singular zone geometry at bimaterial wedge corners of figure 3.39.

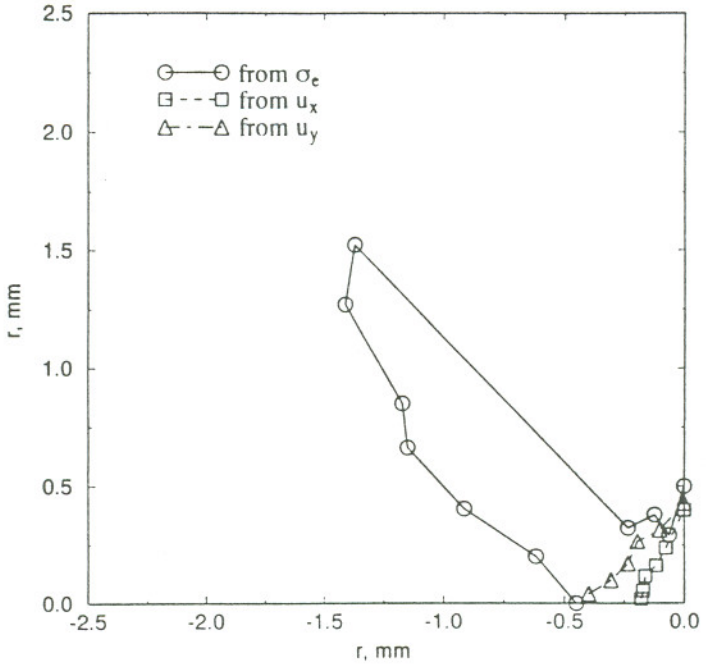

c) E=2632 MPa, ν=0.30, t=10 mm

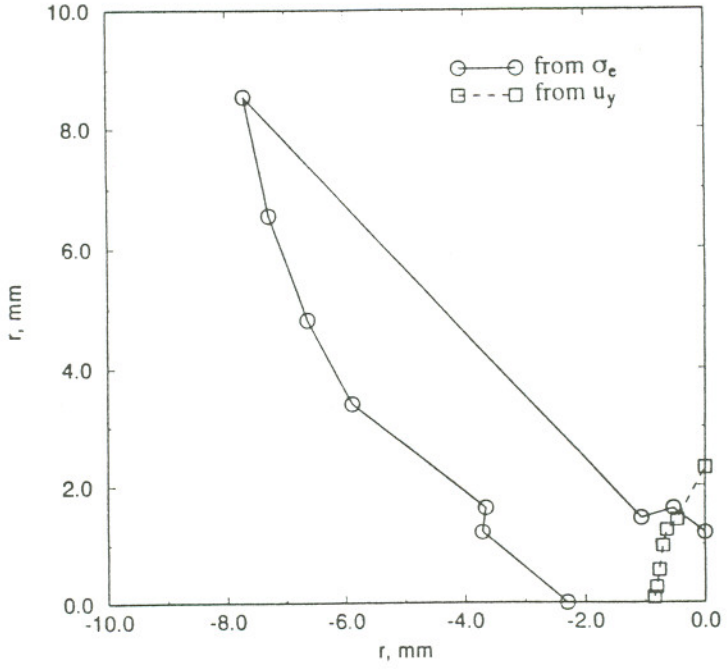

d) E=2632 MPa, ν=0.30, t=50 mm

Fig. 3.40 (continued).

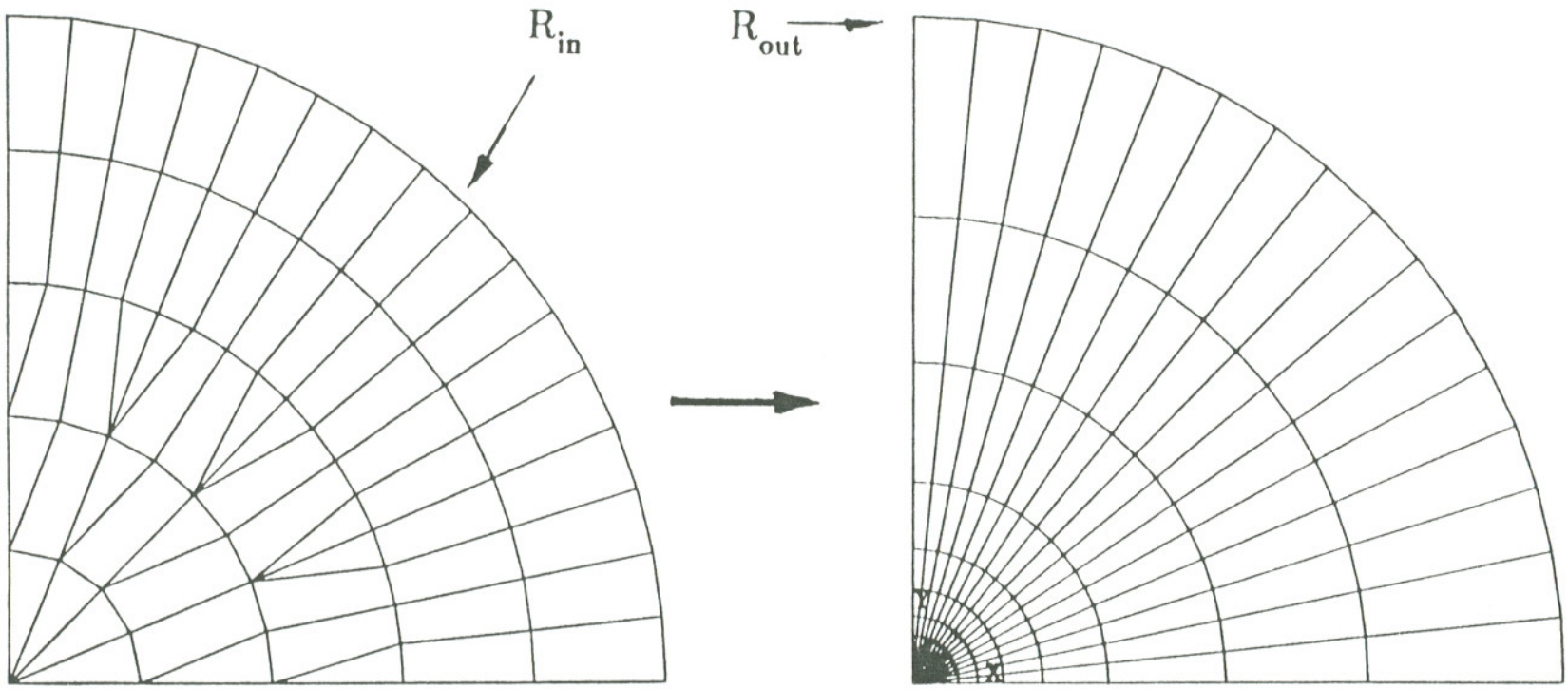

Fig. 3.41 FEIM mesh for an elastic strip bonded on a rigid substrate.

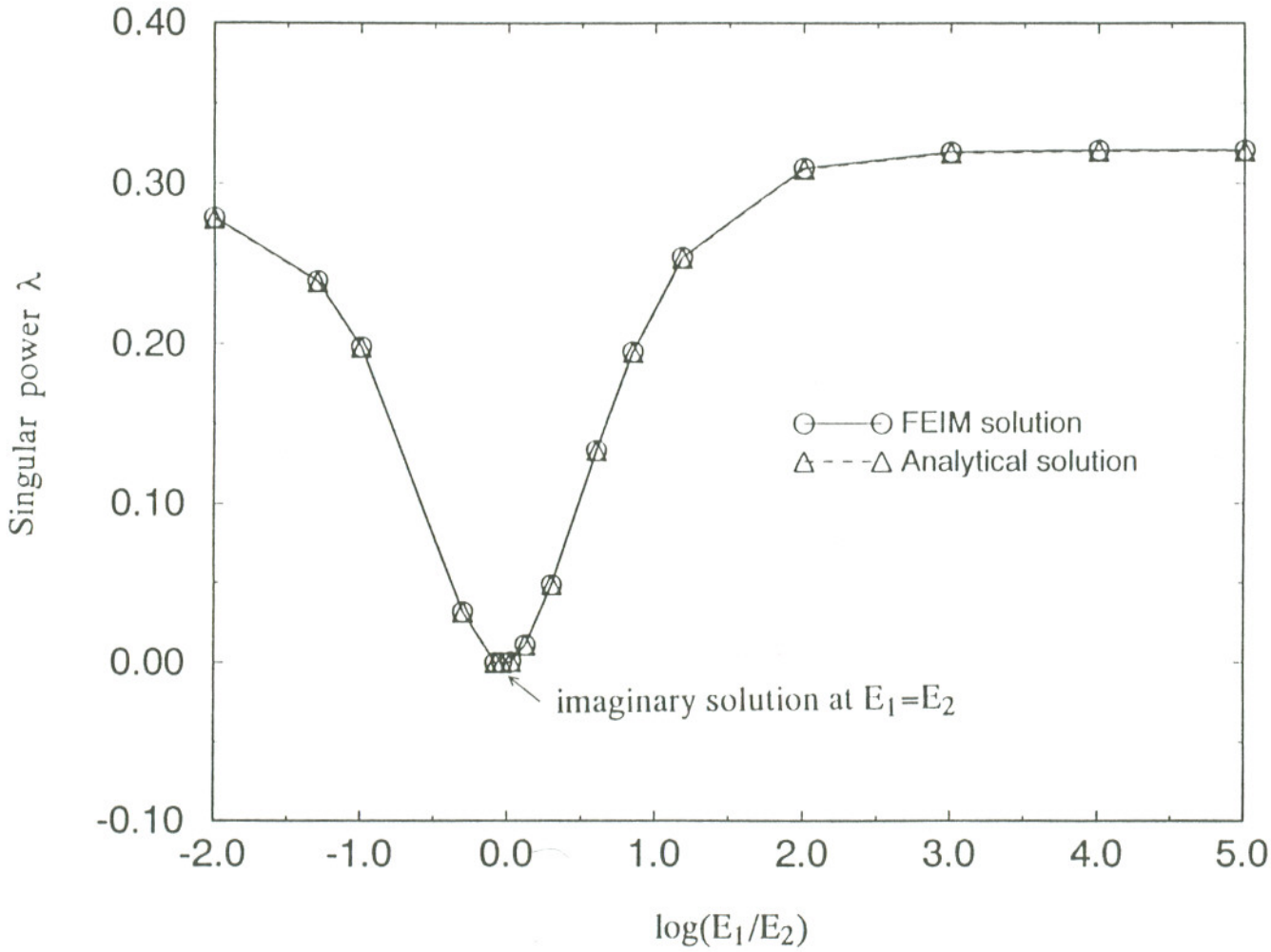

Fig. 3.42 Singular power λ dependence on E_1/E_2
(E_2=3000 MPa, ν_1=0.3, ν_2=0.35, t=0.25 mm).

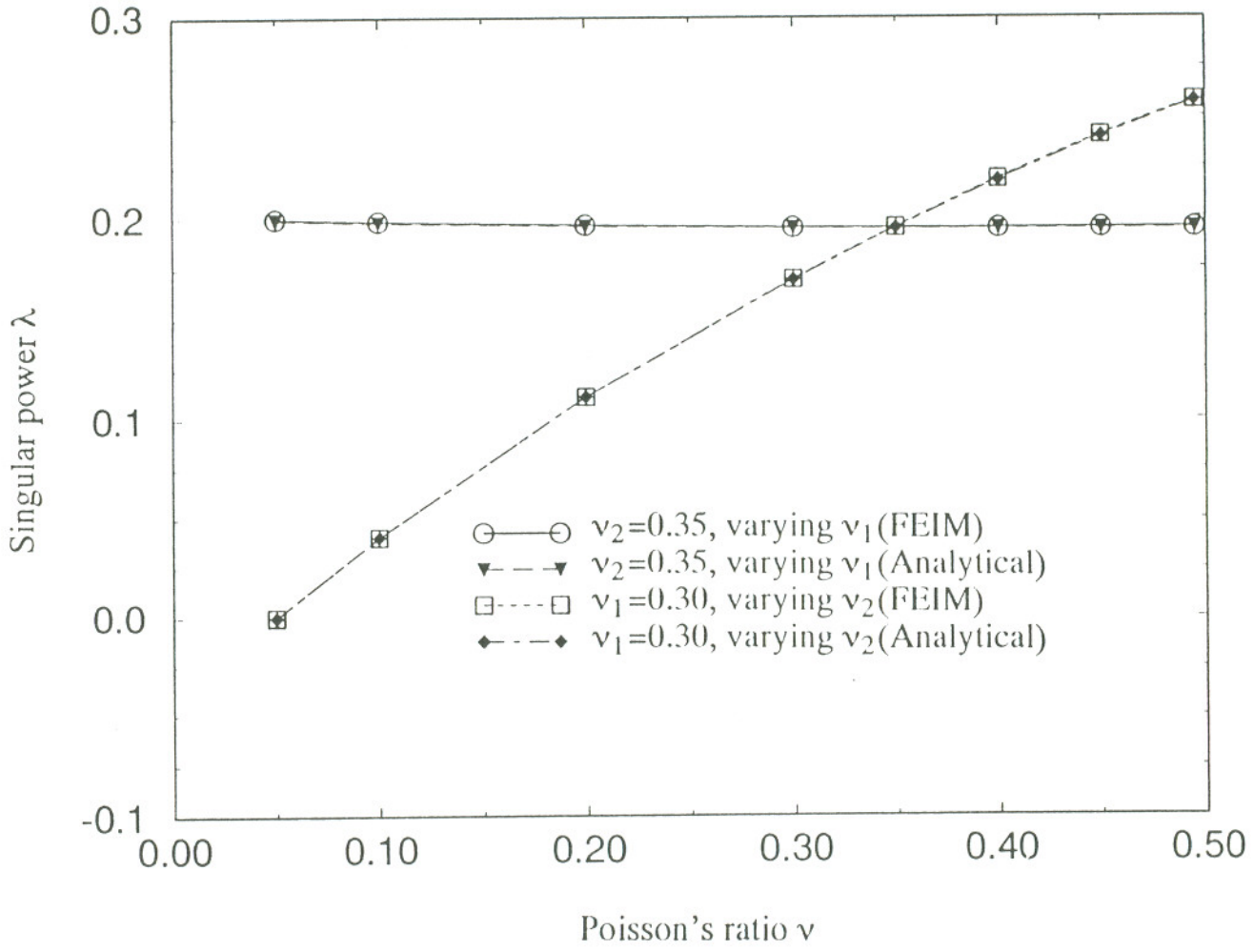

Fig. 3.43 Singular power λ dependence on Poisson's ratios (E_1=210000 MPa, E_2=3000 MPa, t=0.25 mm).

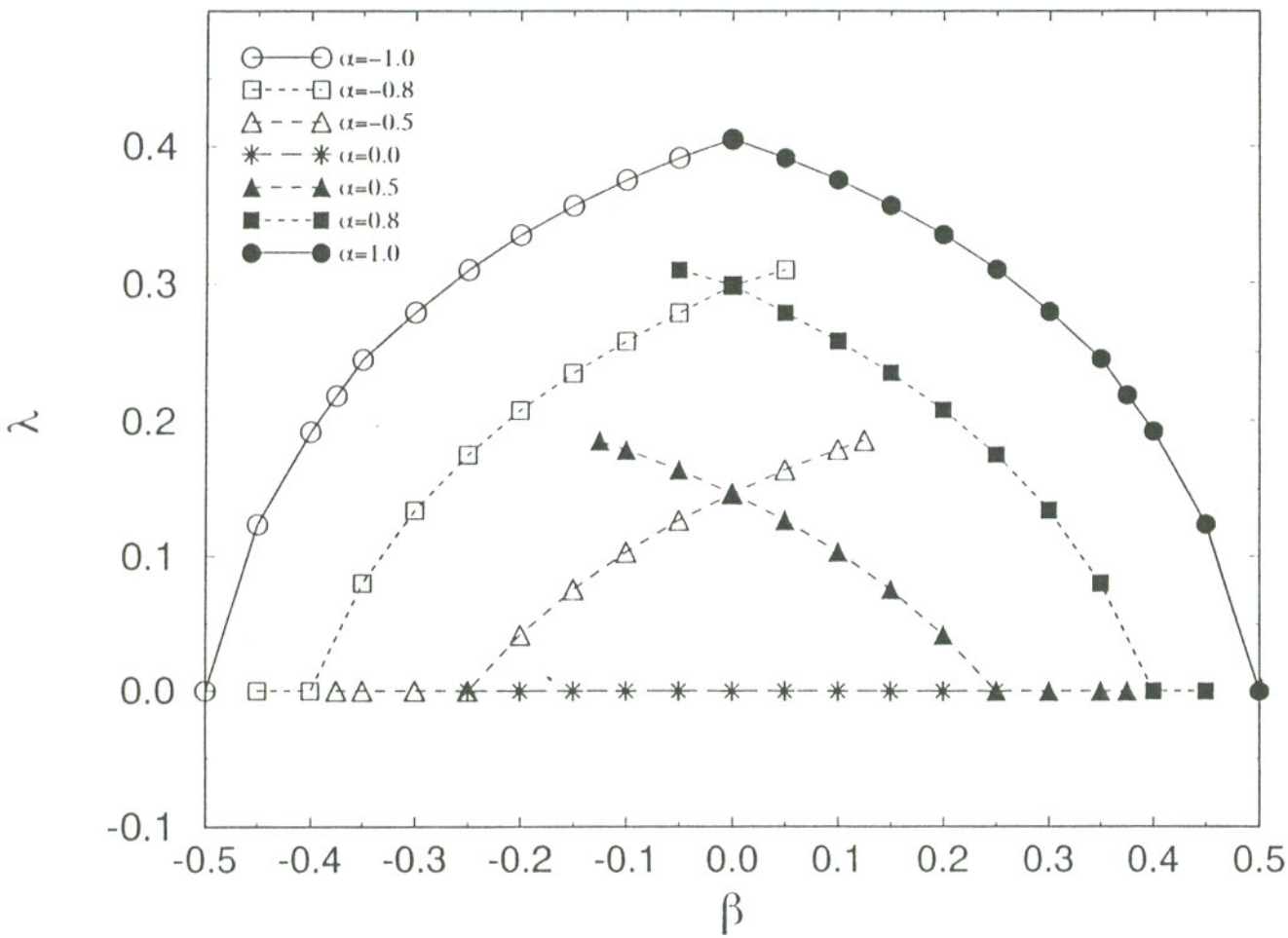

Fig. 3.44 Singular power λ dependence on composite parameters.

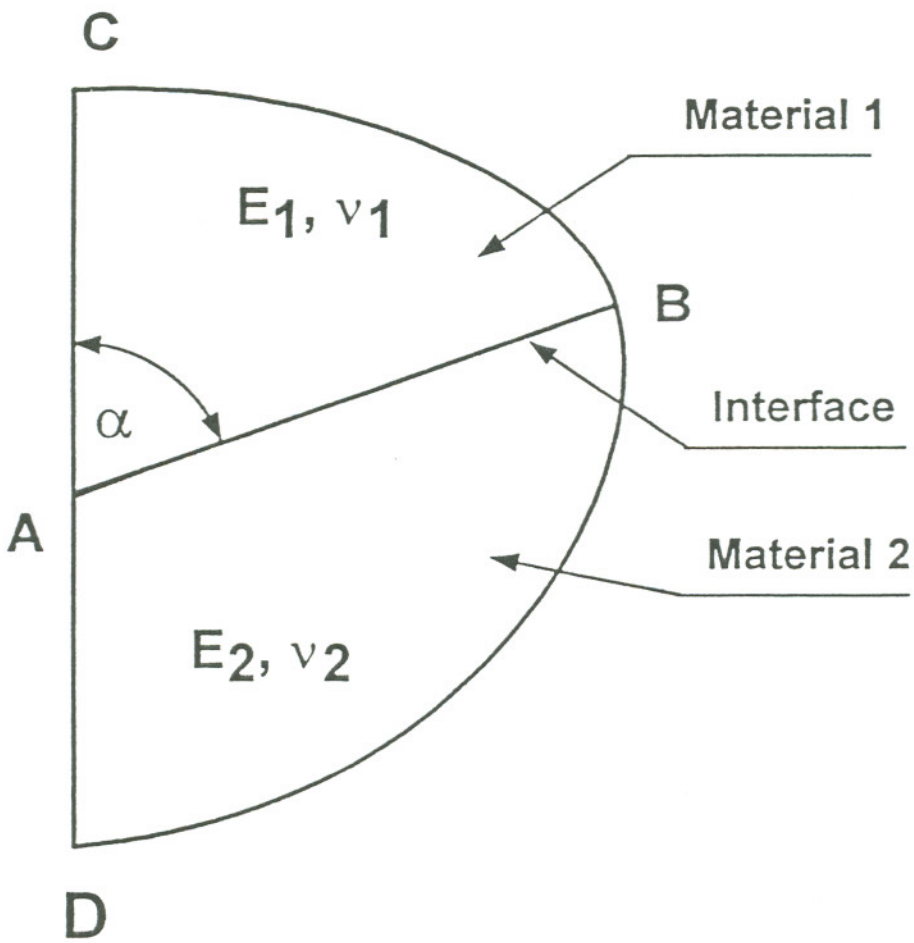

Fig. 3.45 Schematic of a bimaterial wedge with a skewed interface.

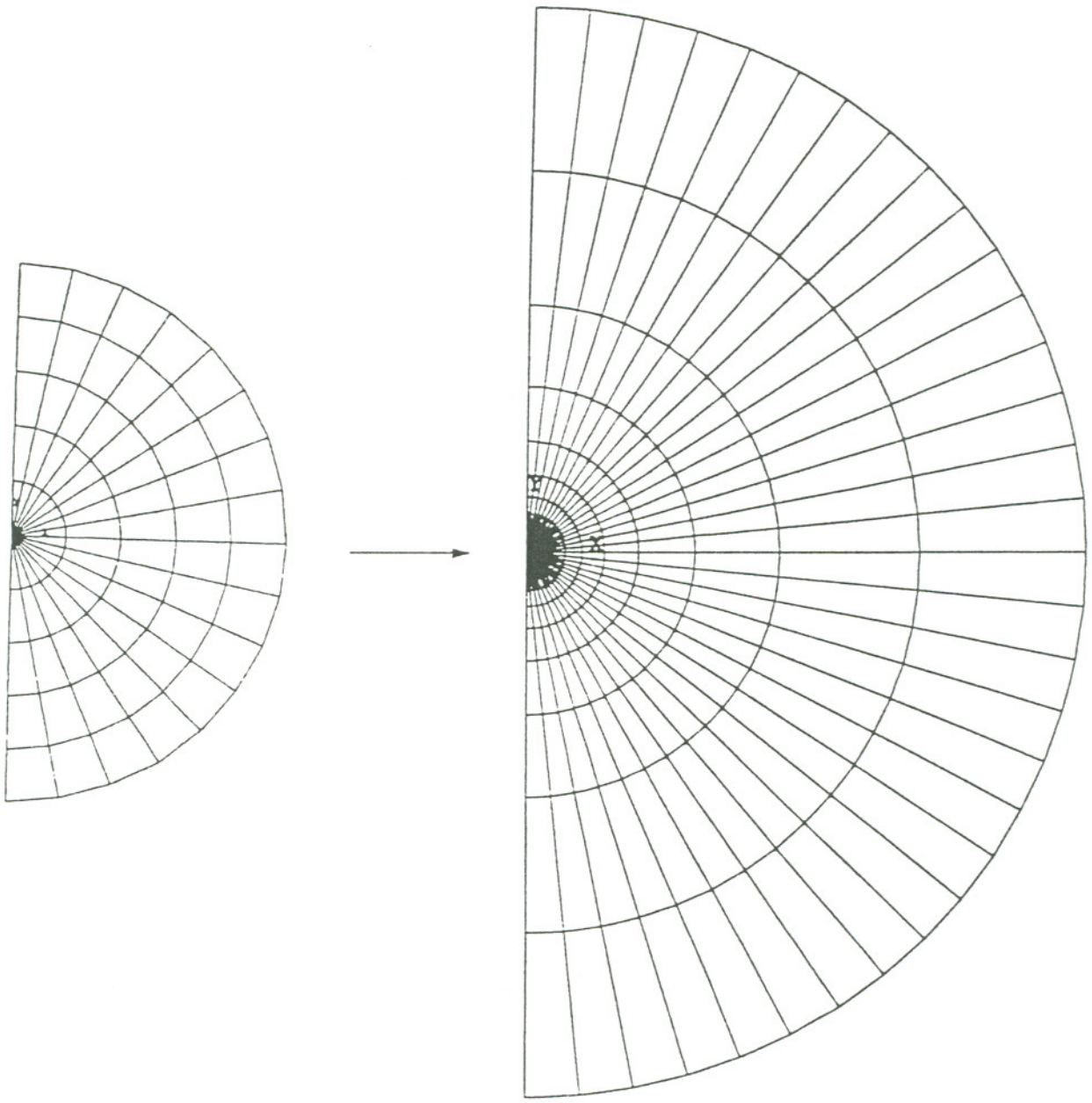

Fig. 3.46 FEIM representation for a skewed interface wedge corner.

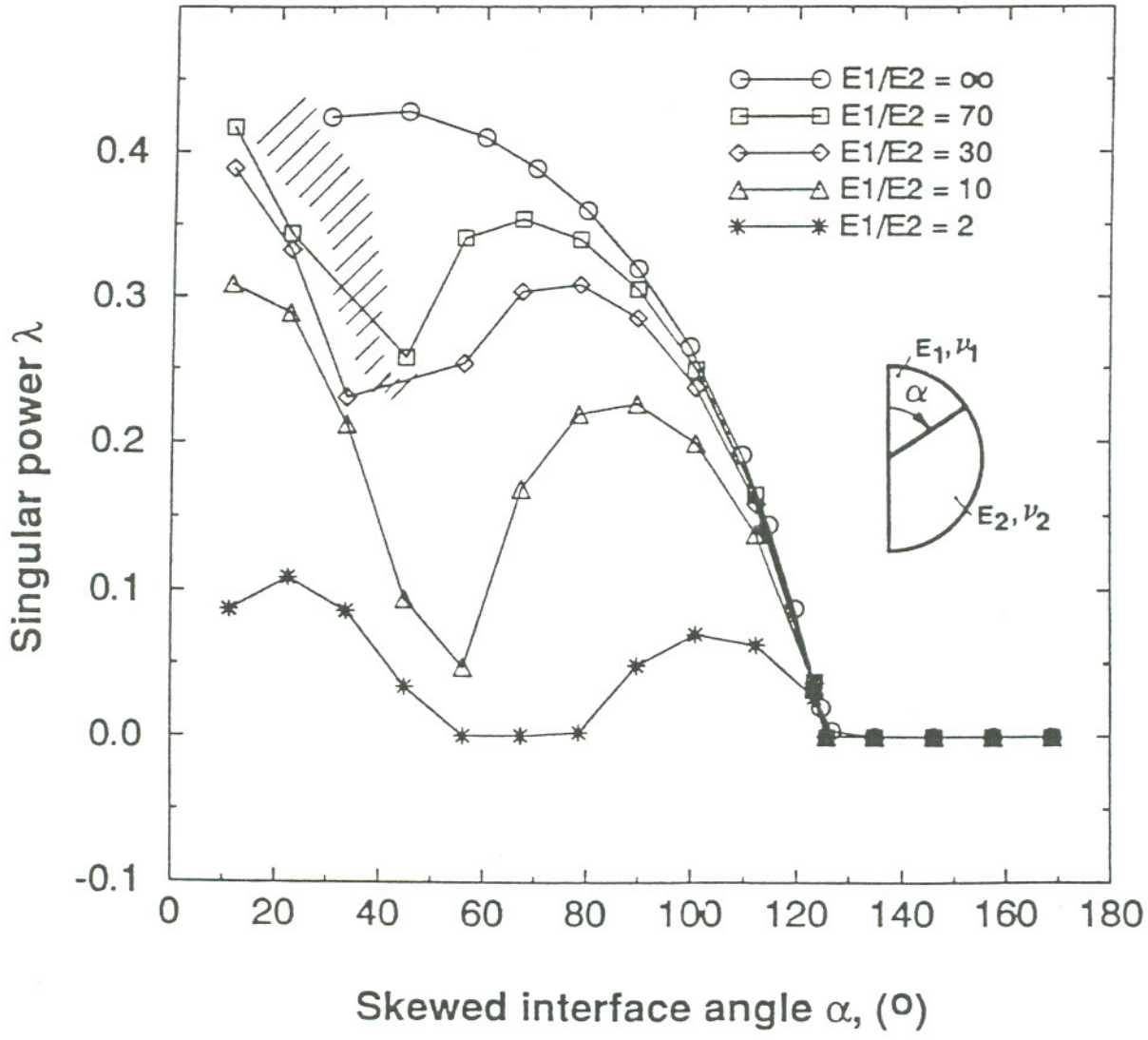

Fig. 3.47 Singular power λ dependence on skewed interface angle α with varying Young's modulus ratio E_1/E_2 ($\nu_1=0.3$, $\nu_2=0.35$).

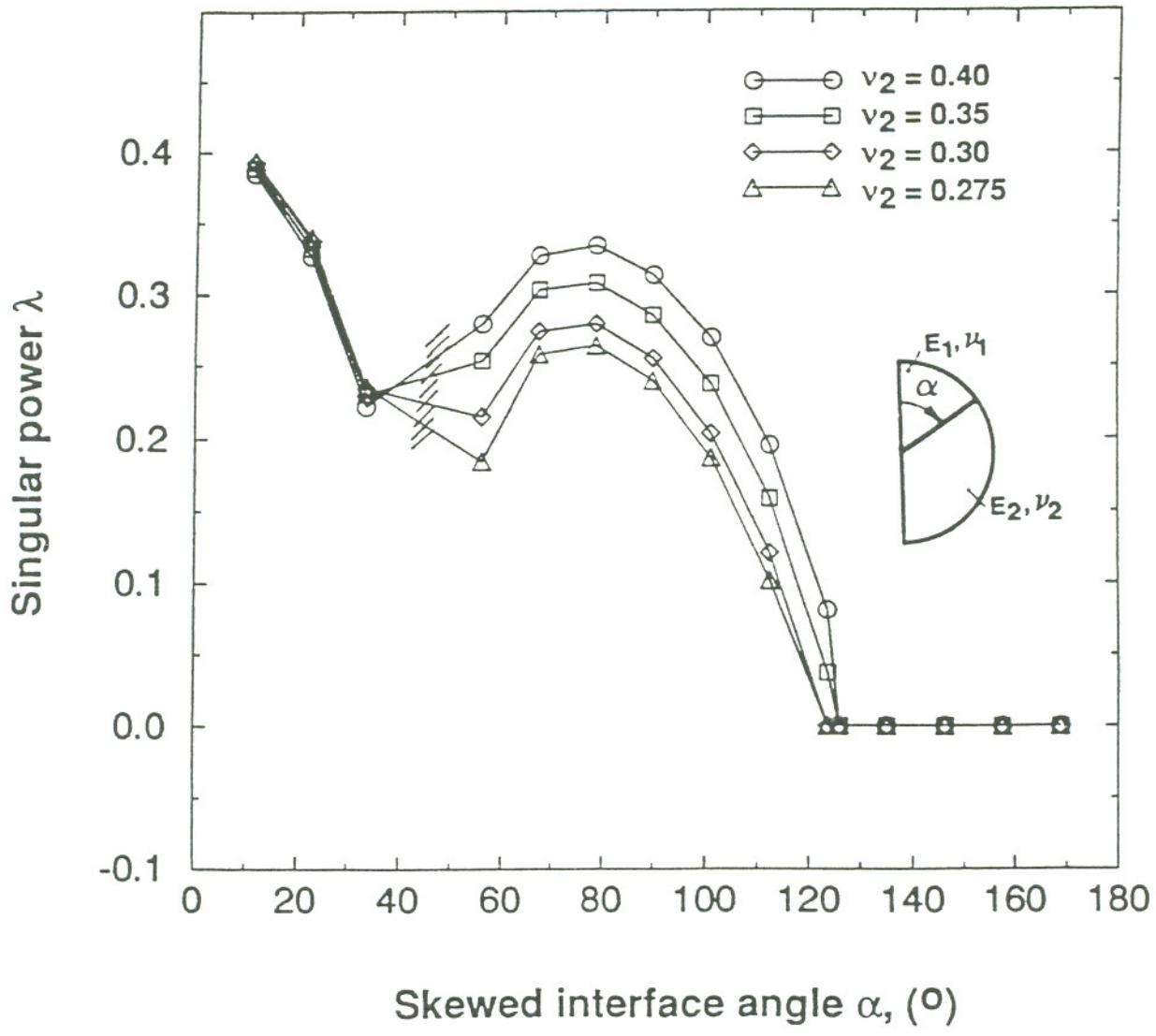

Fig. 3.48 Singular power λ dependence on skewed interface angle α with varying Poisson's ratio of Material 2 (the adherend, $E_1/E_2=30$, $\nu_1=0.3$).

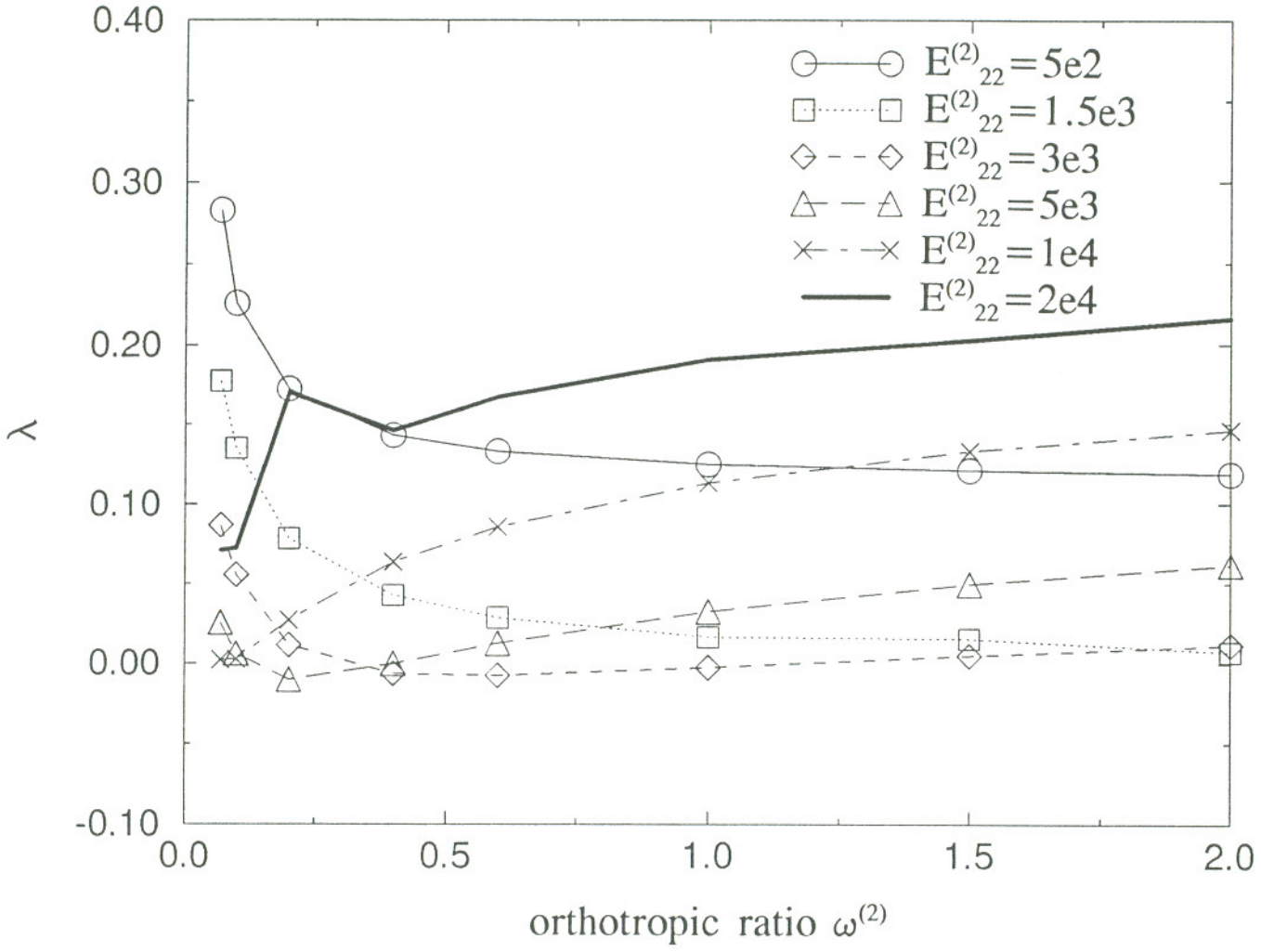

Fig. 3.49 Singularity distribution vs. orthotropic ratio of material 2 ($E^{(1)}_{12}=E^{(1)}_{21}=3000$ MPa, $\nu^{(1)}_{12}=0.35$, $\nu^{(2)}_{12}=0.35$).

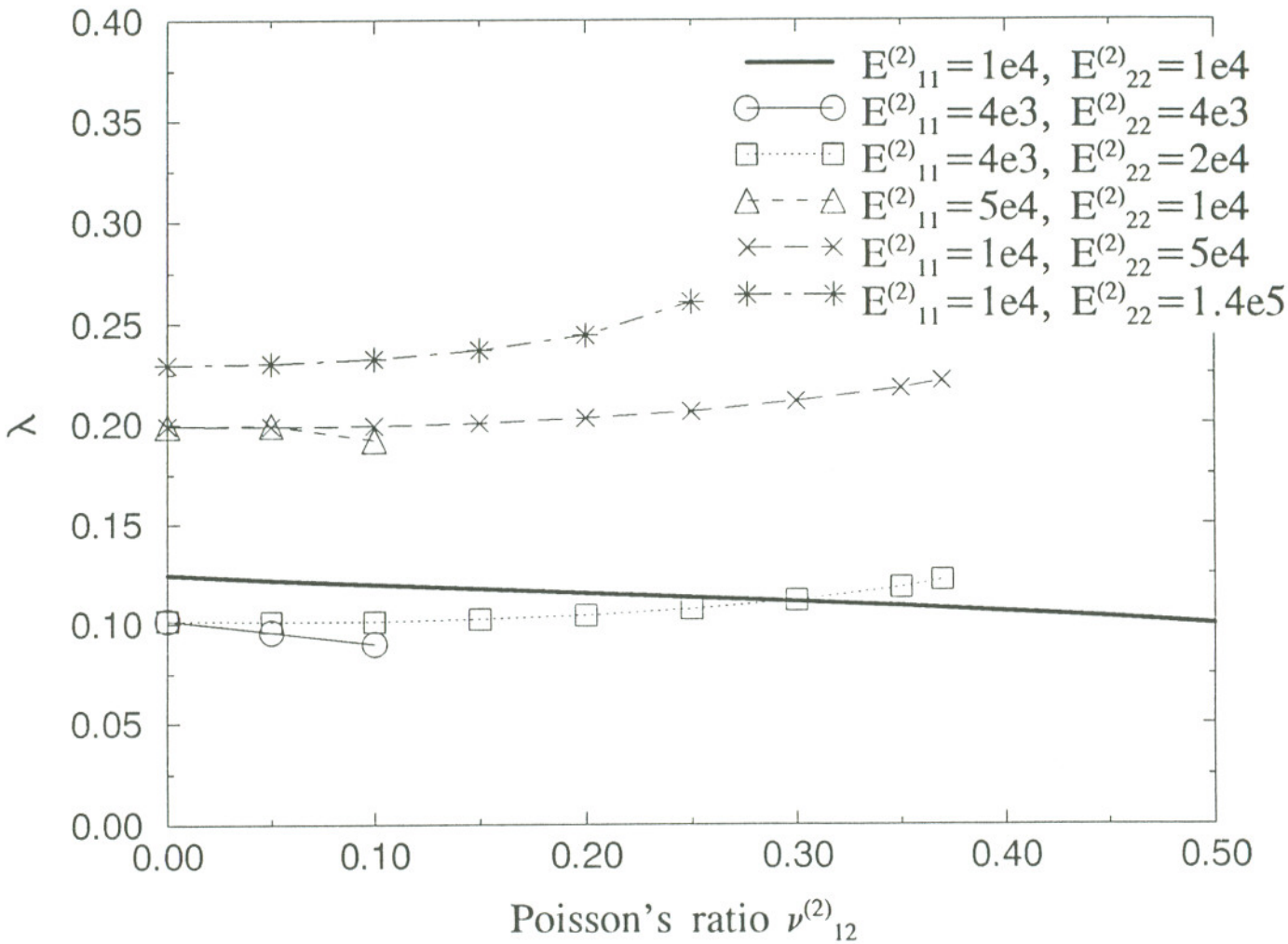

Fig. 3.50 Singularity distribution vs. Poisson's ratio of material 2 ($E^{(1)}_{12}=E^{(1)}_{21}=3000$ MPa, $\nu^{(1)}_{12}=0.35$).

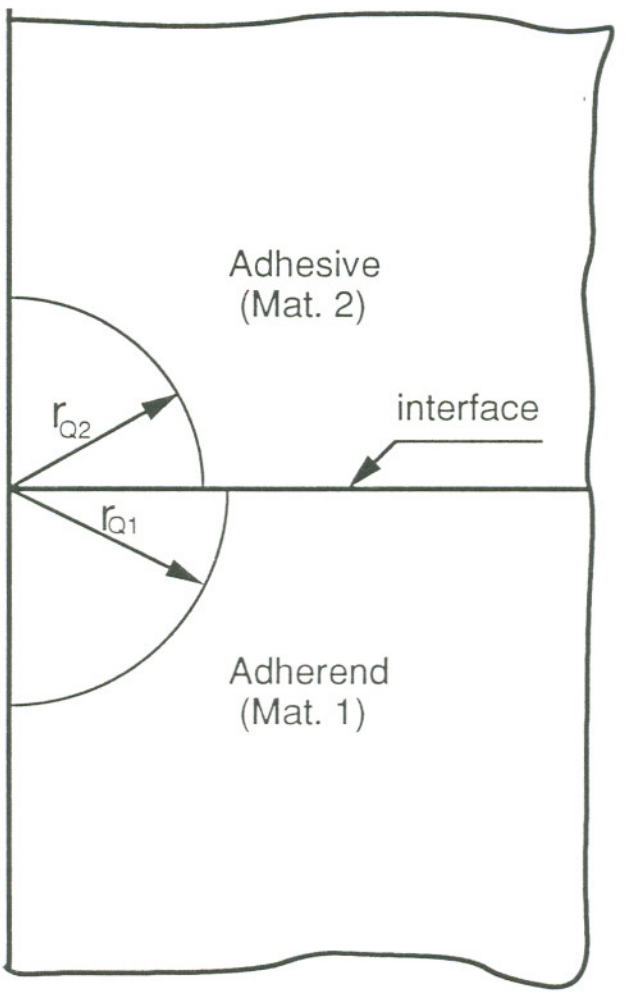

Fig. 3.51 Schematic drawing of singular stress zones

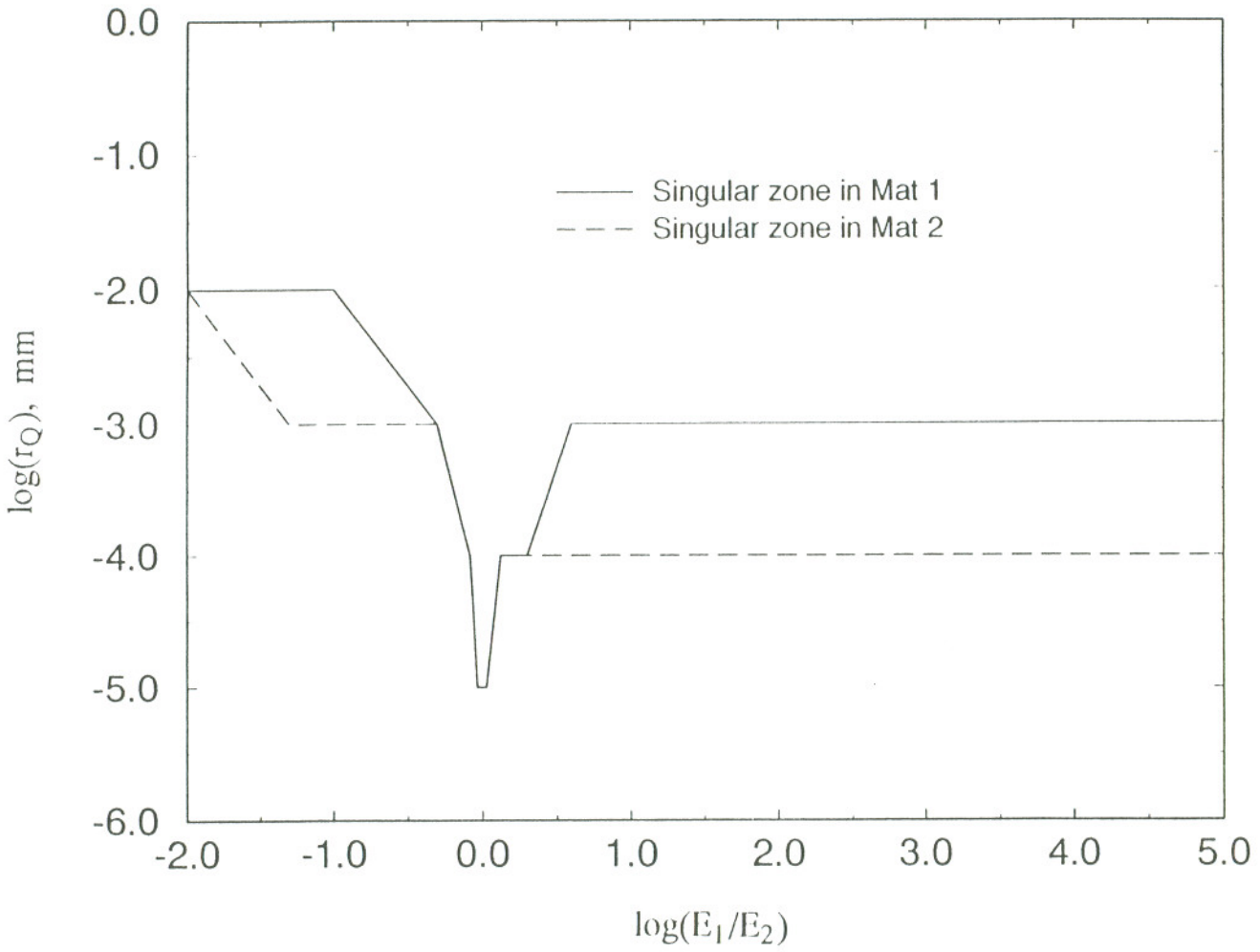

Fig. 3.52 Stress singular zone dependence on E_1/E_2 (E_2=3000 MPa, ν_1=0.3, ν_2=0.35, t=0.25 mm).

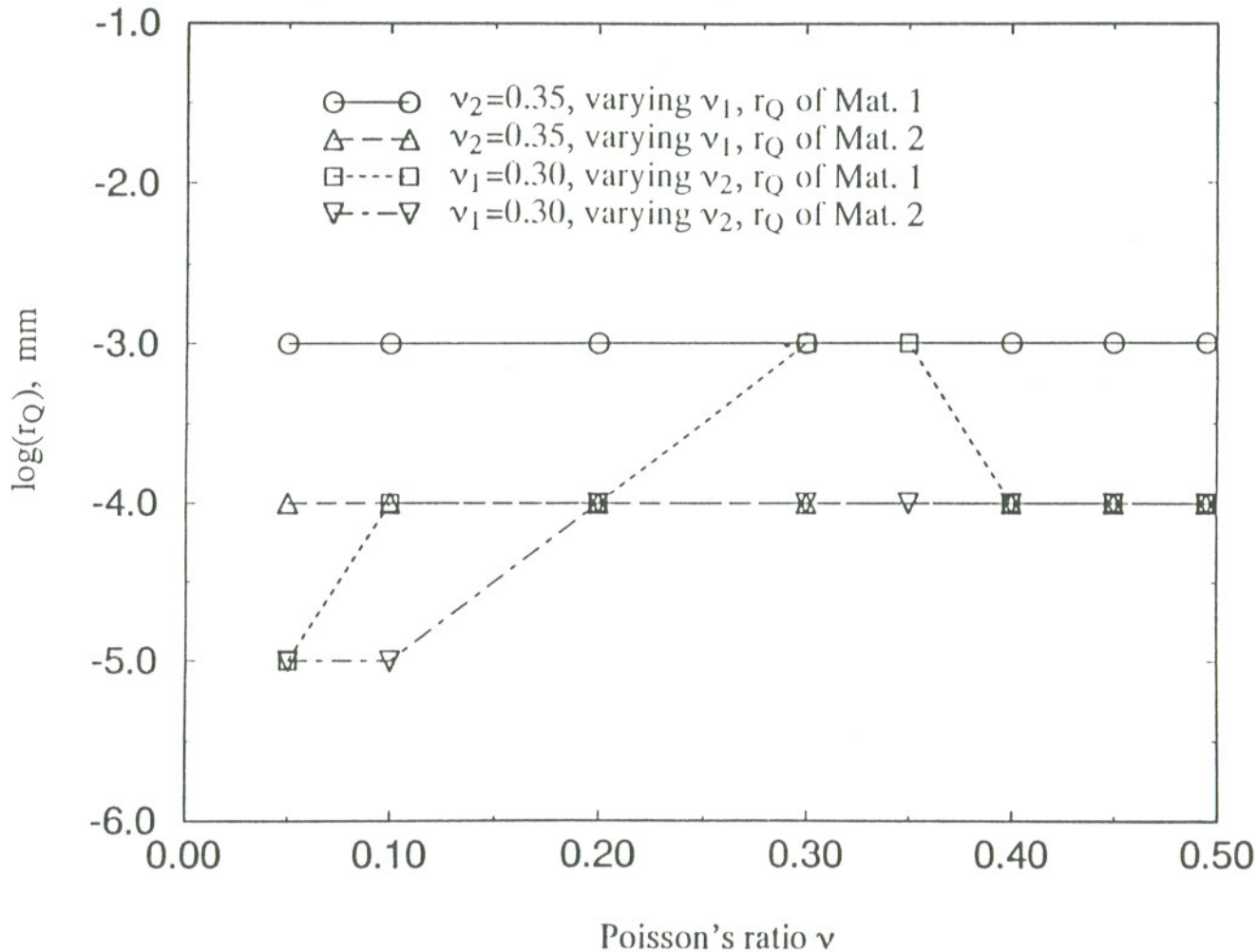

Fig. 3.53 Stress singular zone dependence on Poisson's ratios (E_1=21000 MPa, E_2=3000 MPa, t=0.25 mm).

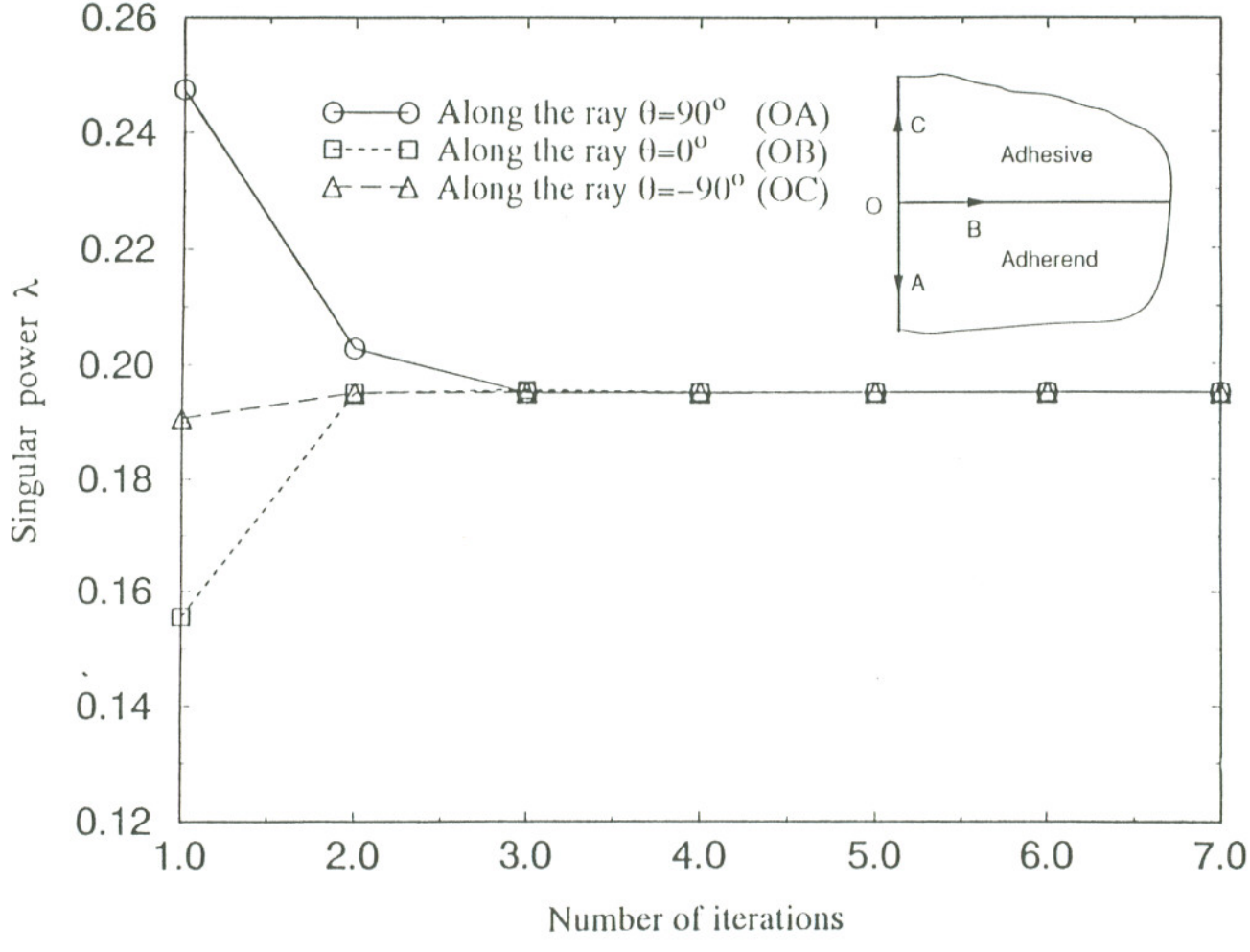

Fig. 3.54 FEIM convergence rate for a bimaterial wedge from figure 3.35 (E_1=21000 MPa, E_2=3000 MPa, ν_1=0.3, ν_2=0.35, t=0.25 mm).

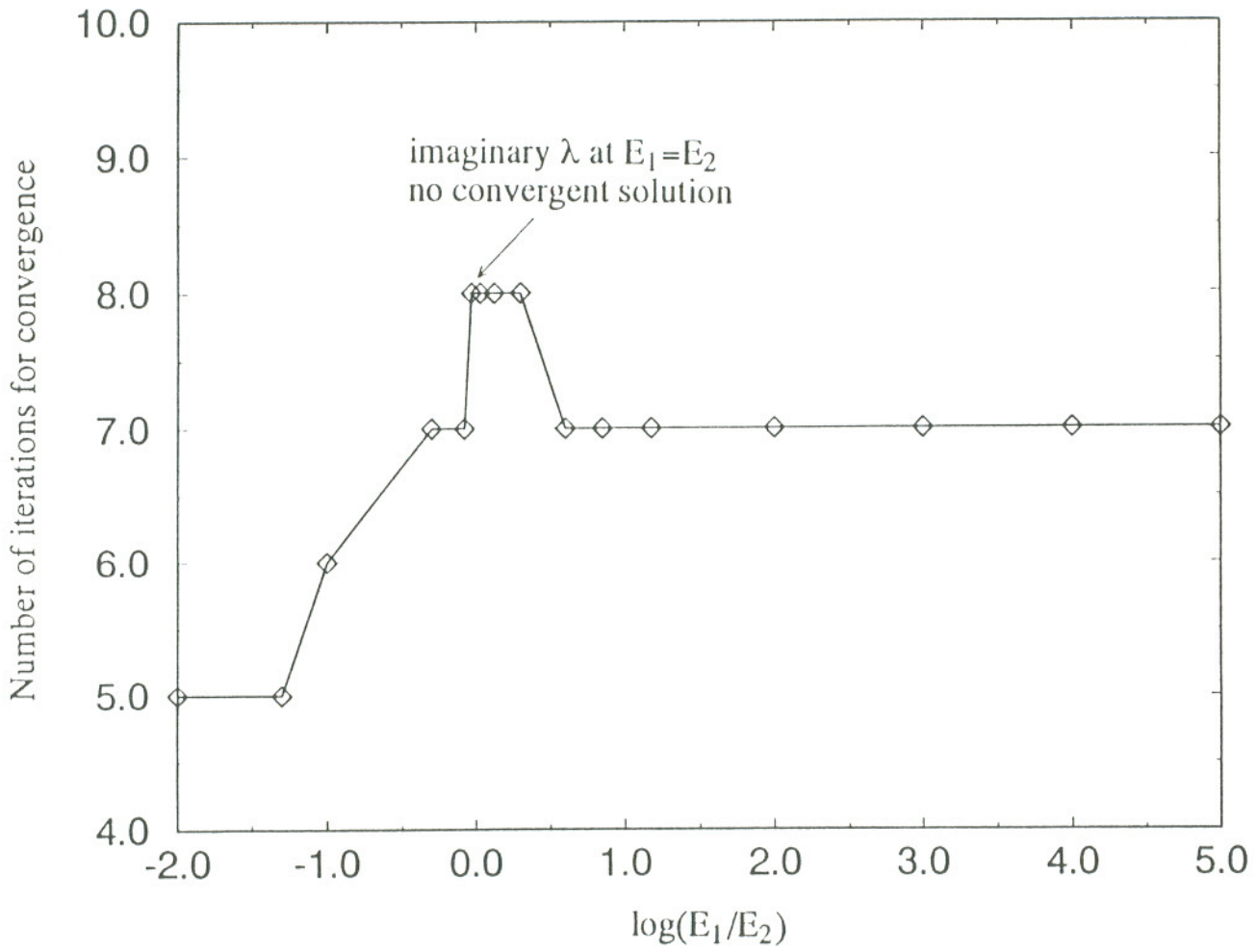

Fig. 3.55 FEIM convergence rate dependence on E_1/E_2 (E_2=3000 MPa, ν_1=0.3, ν_2=0.35, t=0.25 mm).

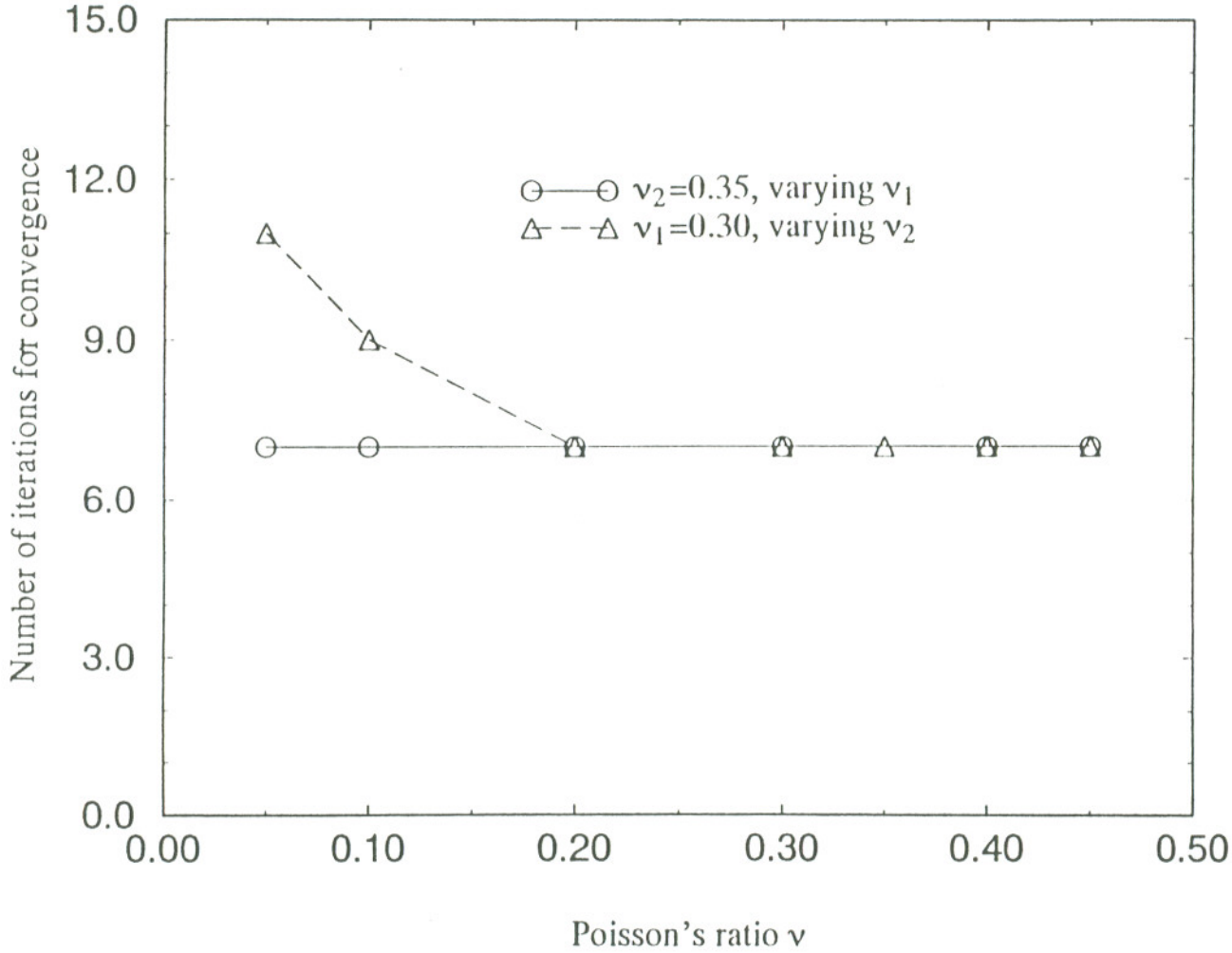

Fig. 3.56 FEIM convergence rate dependence on Poisson's ratios (E_1=21000 MPa, E_2=3000 MPa, t=0.25 mm).

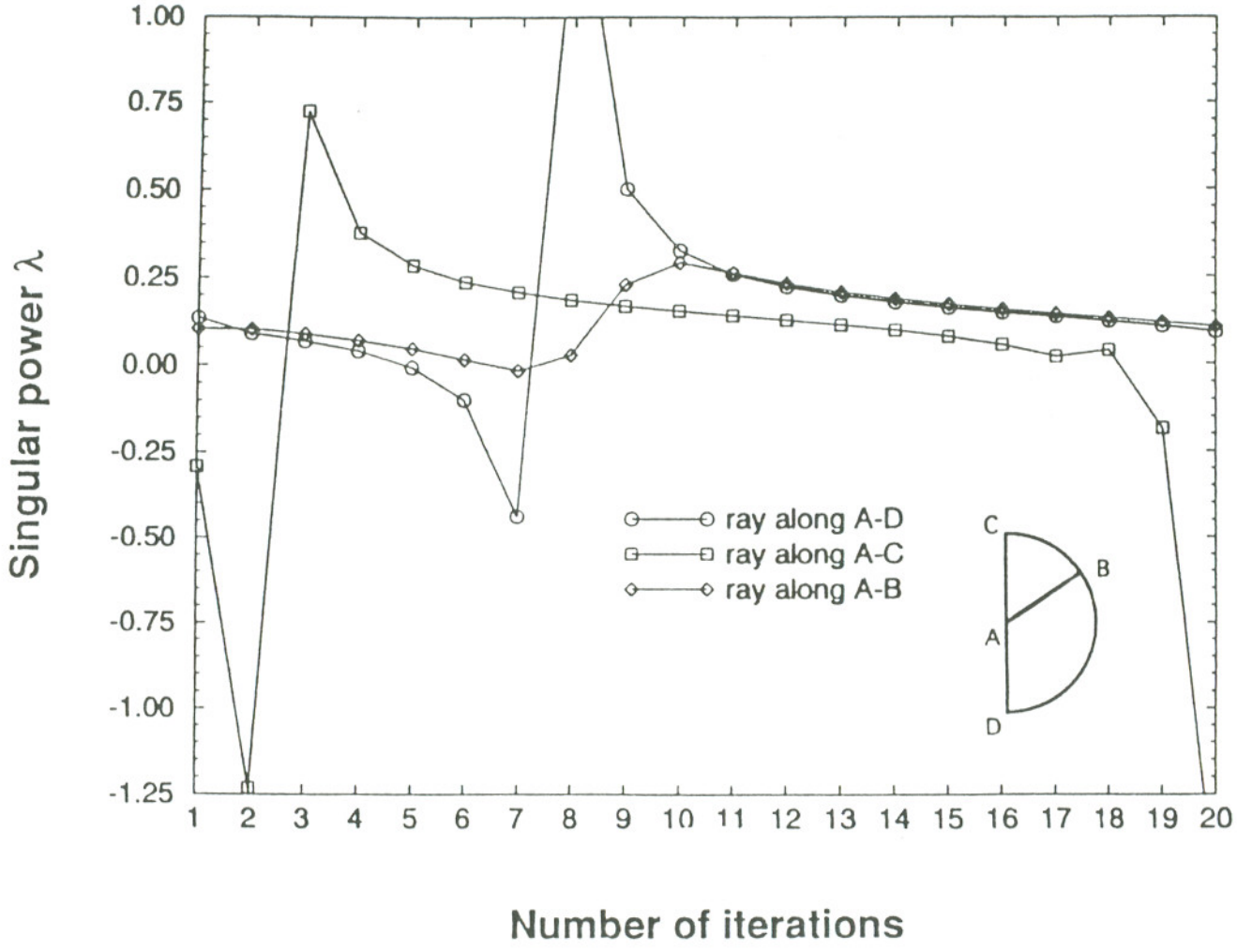

Fig. 3.57 Typical non-convergence representation for a skewed interface bimaterial wedge ($E_1/E_2=30$, $\nu_1=0.3$, $\nu_2=0.40$, $\alpha=40^o$).

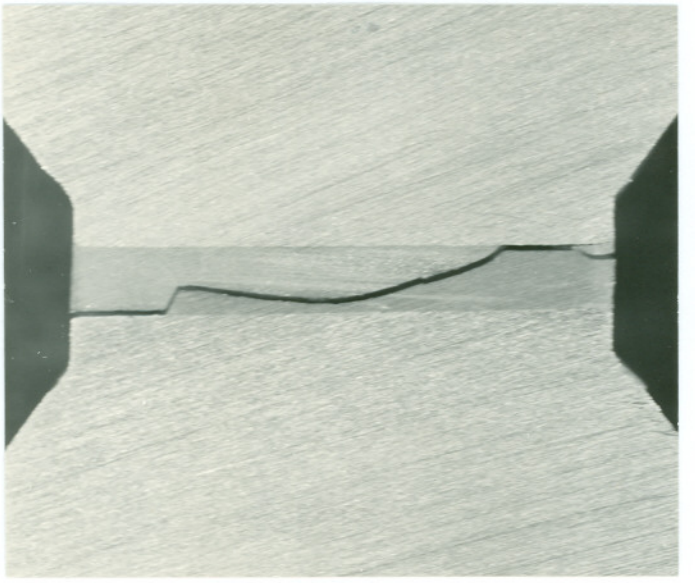

Fig. 3.58 Zig-zag crack path (rigid adhesive, t=1.0 mm, ϕ=15°).

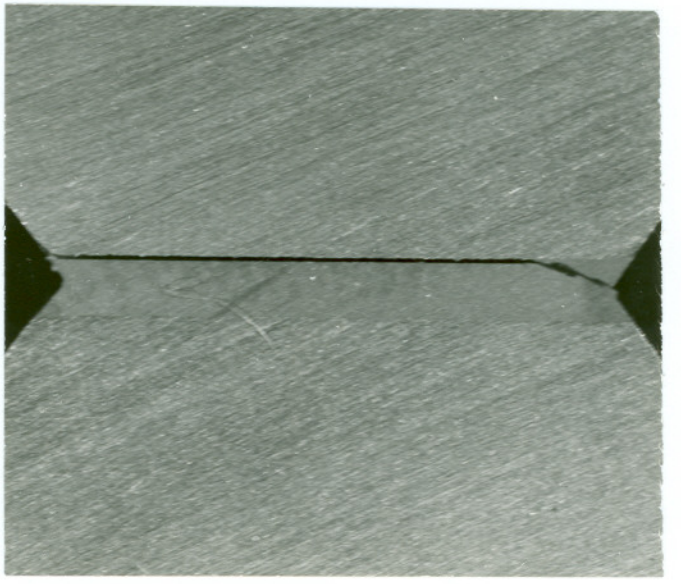

Fig. 3.59 Zig-zag crack path (rigid adhesive, t=1.0 mm, ϕ=-30°).

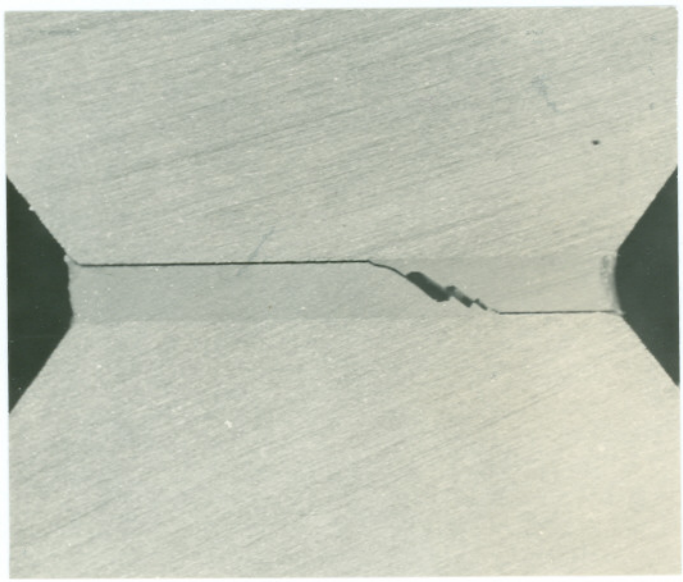

Fig. 3.60 Zig-zag crack path (rigid adhesive, t=1.0 mm, ϕ=-30°).

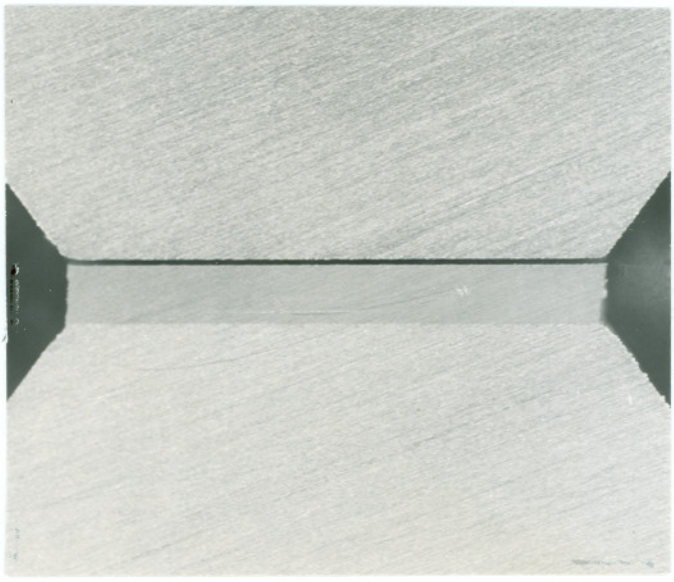

Fig. 3.61 Peel-off crack path (rigid adhesive, t=1.0 mm, ϕ=30°).

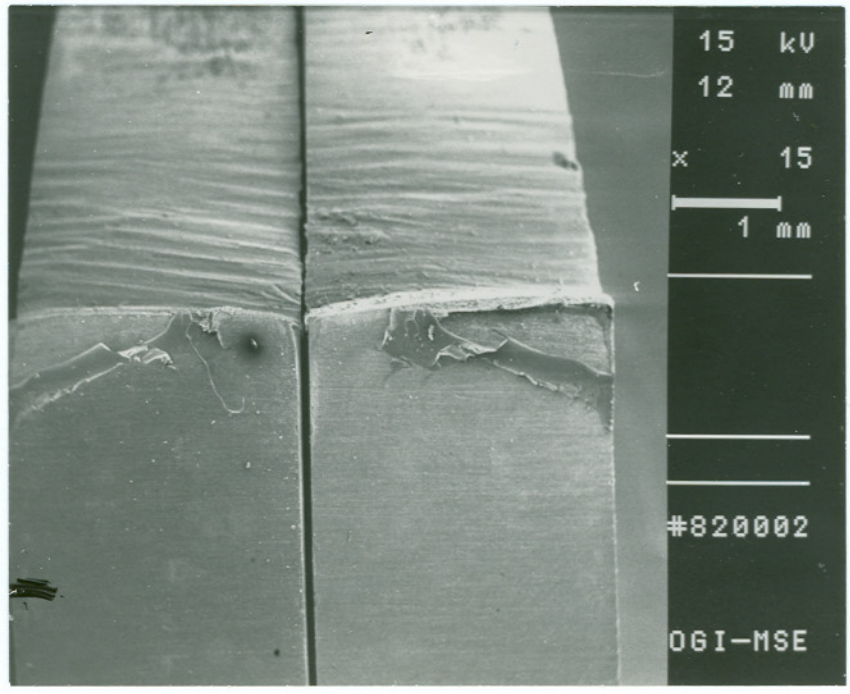

Fig. 3.62 Fracture surface profile (rigid adhesive, t=0.2 mm, ϕ=15°).

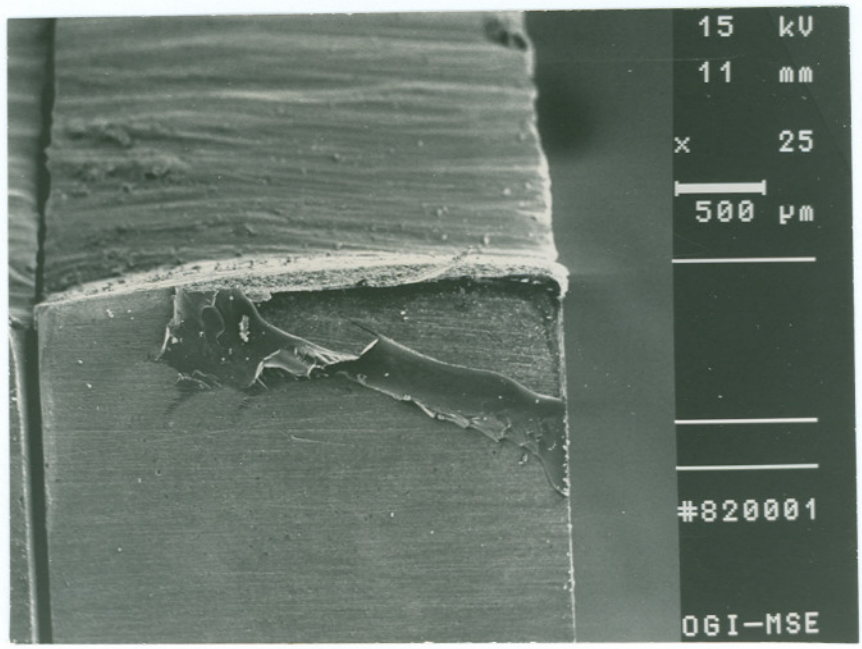

a) crack initiation corner

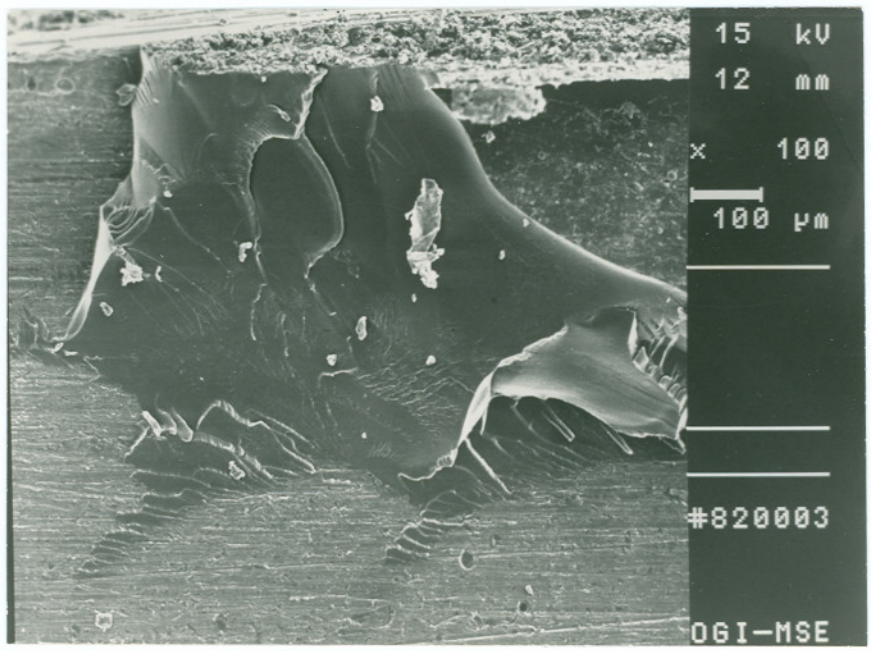

b) adhesion between adhesive (glossy surface) and adherend (scratched surface)

Fig. 3.63 Fracture surface profile (rigid adhesive, t=0.2 mm, ϕ=15°).

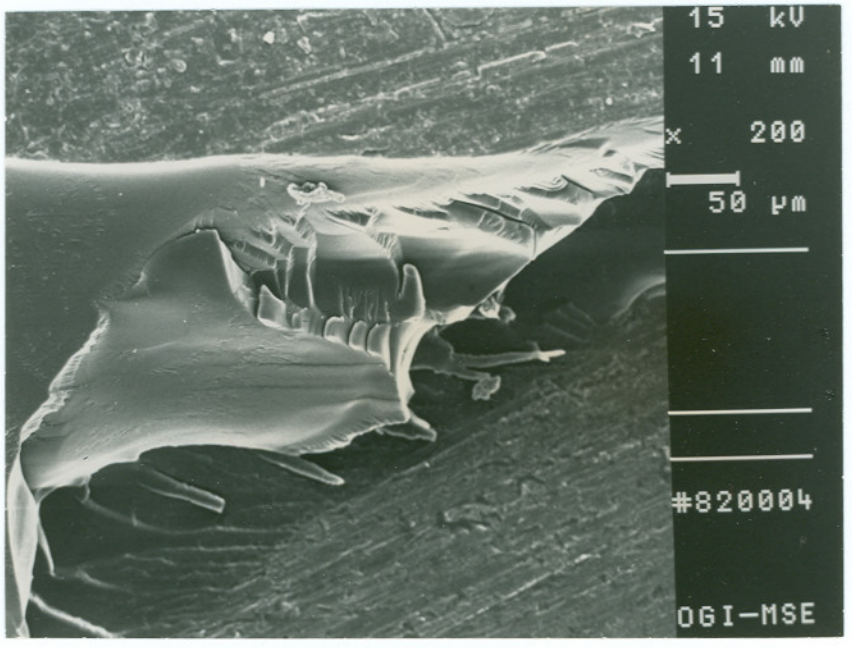

c) ragged fracture surface and secondary cracks

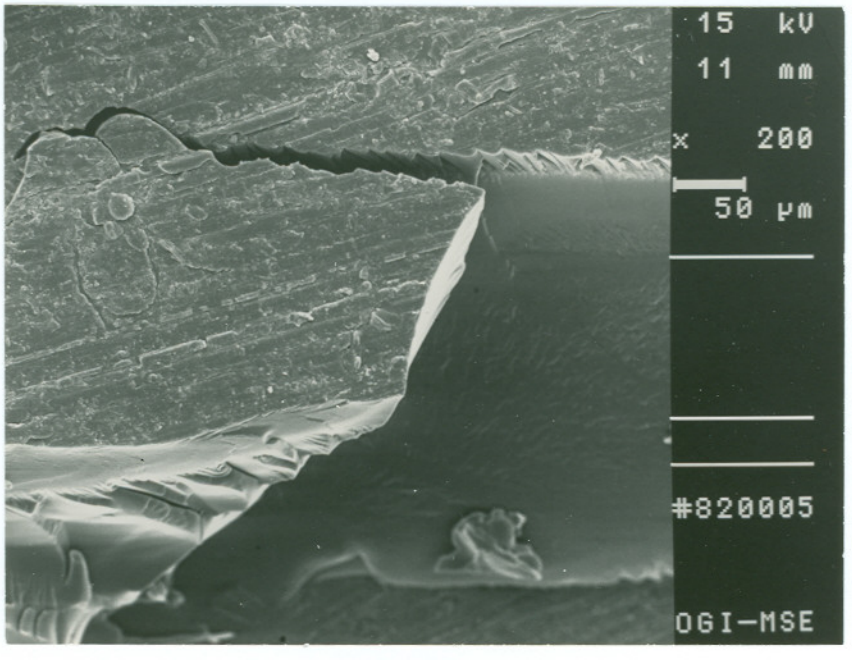

d) secondary cracks

Fig. 3.63 (continued).

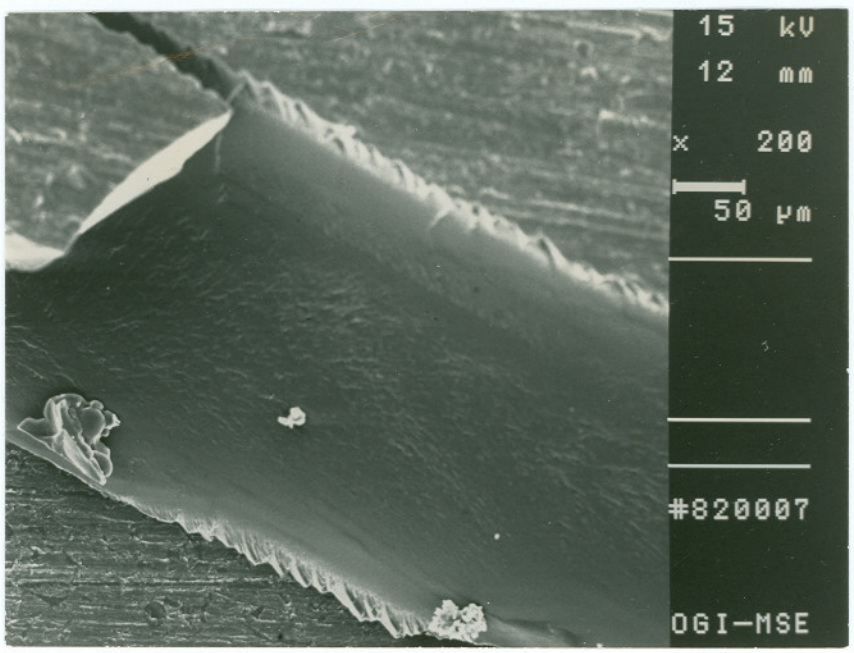

e) step-wise surfaces near the interfaces

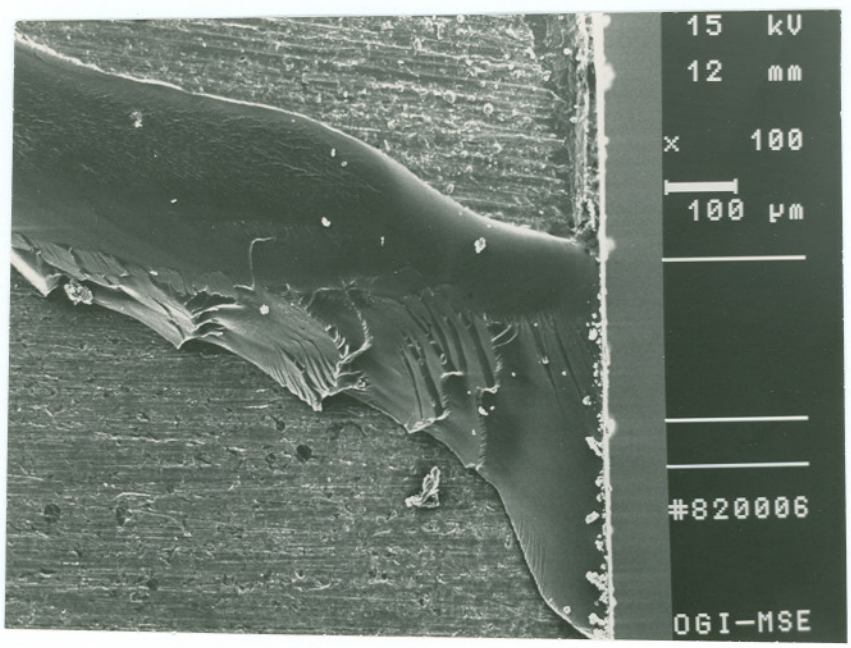

f) step-wise fracture surfaces

Fig. 3.63 (continued).

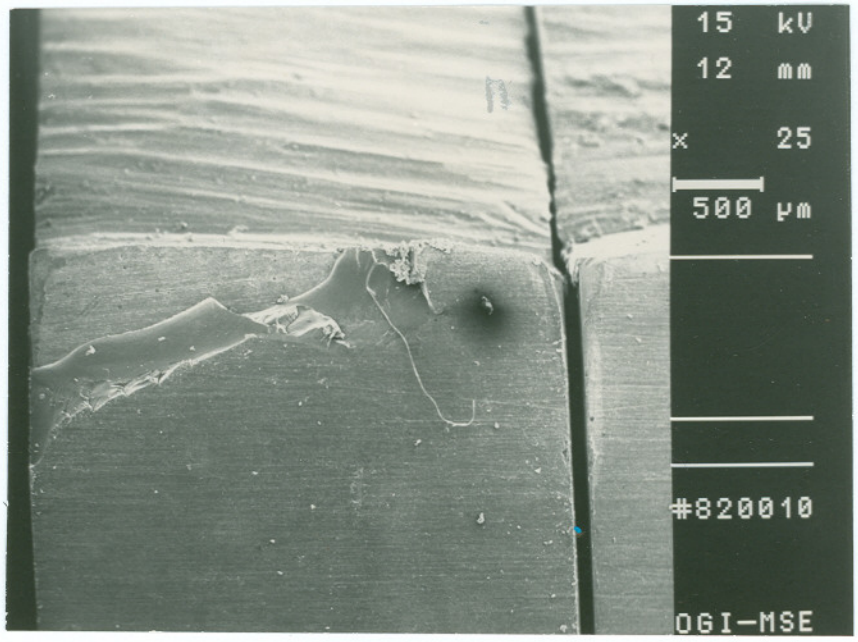

a) crack initiation corner

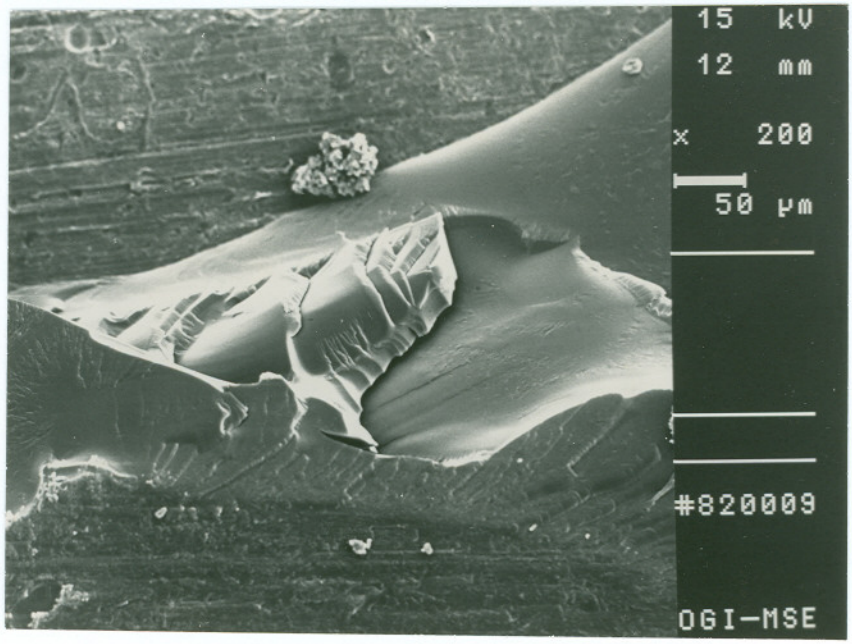

b) step-wise surfaces and secondary cracks

Fig. 3.64 Fracture surface profile (rigid adhesive, t=0.2 mm, ϕ=15°).

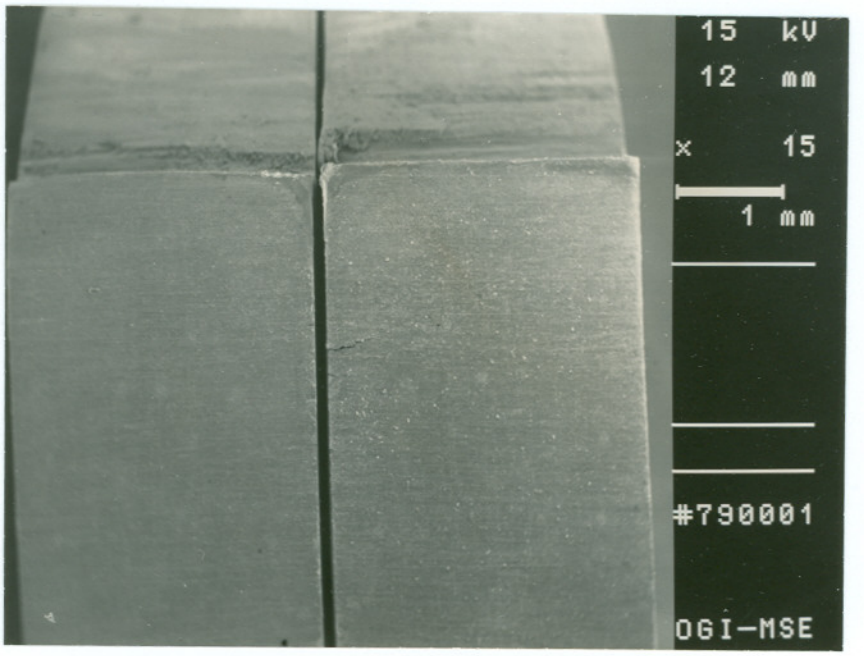

a) crack initiation corner and delamination surface

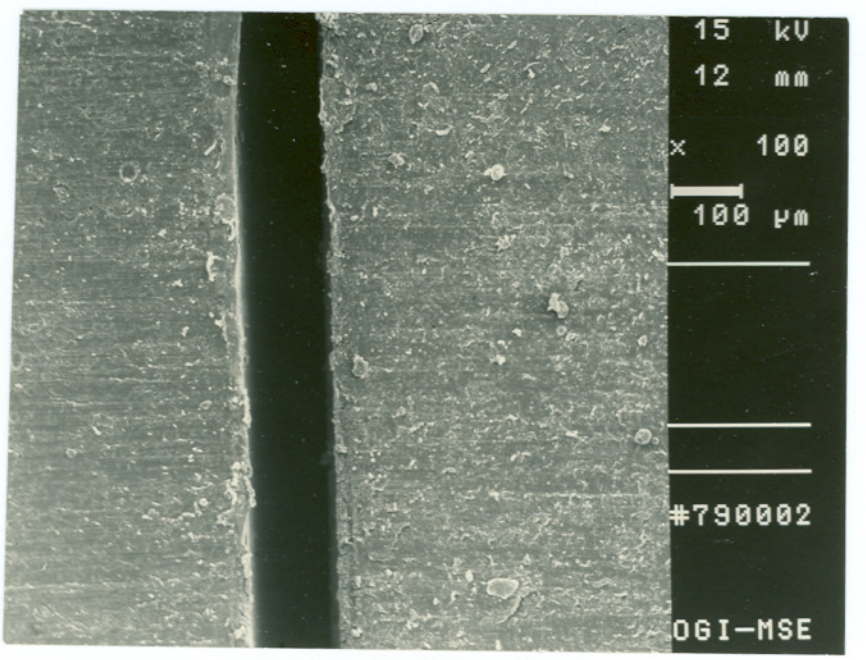

b) delamination surface

Fig. 3.65 Fracture surface profile (flexible adhesive, t=0.2 mm, ϕ=-15°, right: Aluminum surface; left: Adhesive surface).

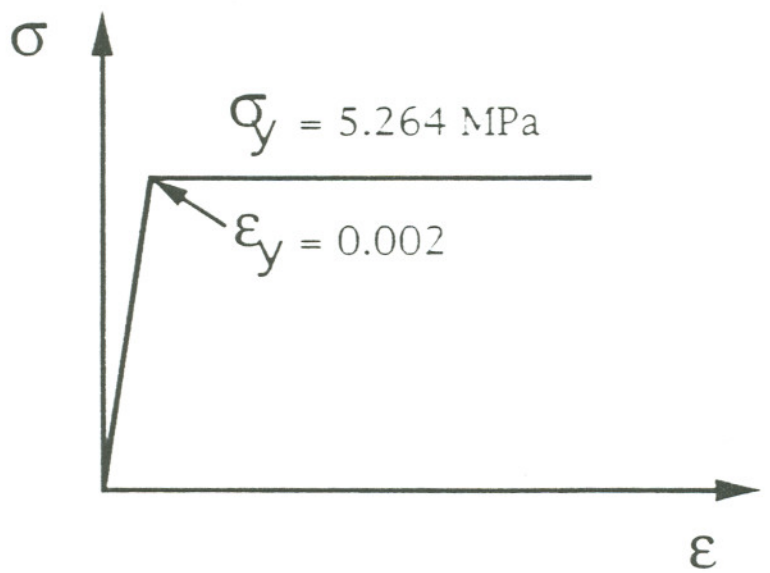

Fig. 3.66 Elastic-perfectly plastic model.

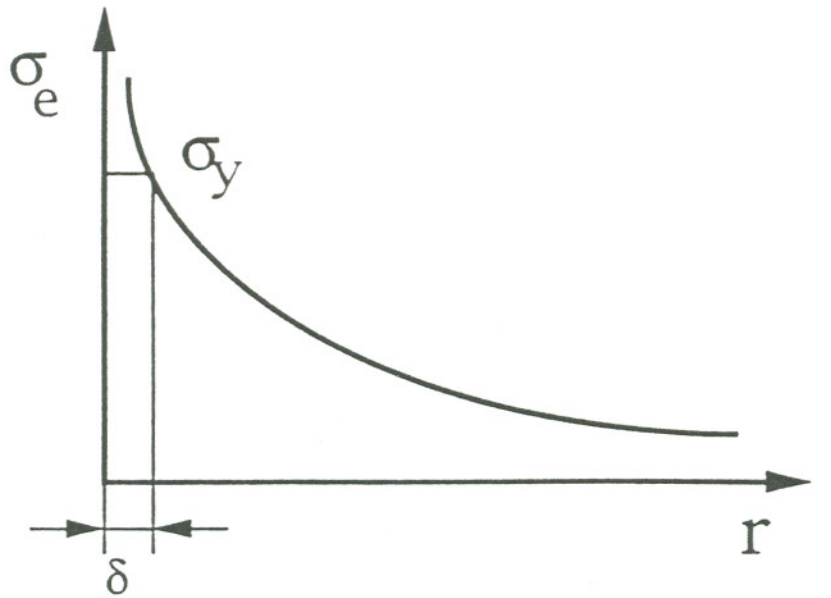

(a) First estimation

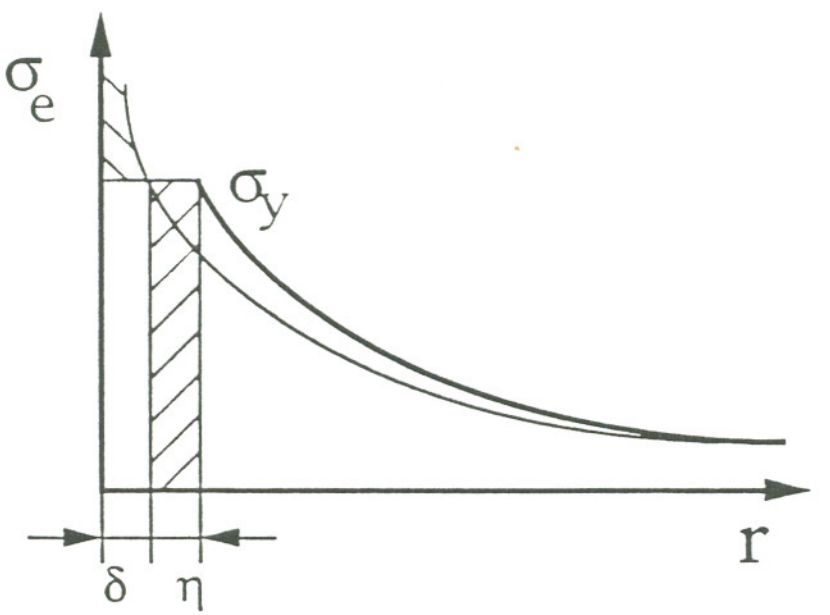

(b) Second estimation

Fig. 3.67 Plastic zone estimation.

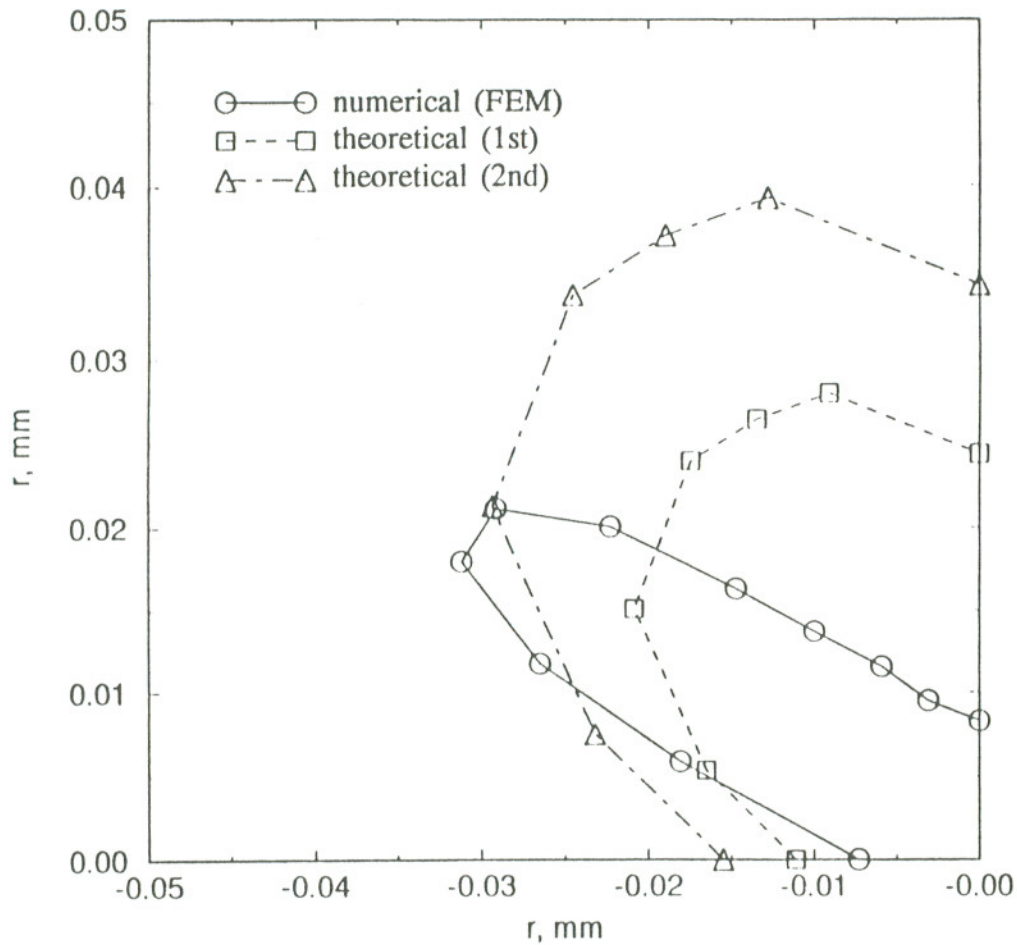

Fig. 3.68 Plastic zones (E=2632 MPa, ϵ_n=0.0003, t=50 mm, ν=0.35).

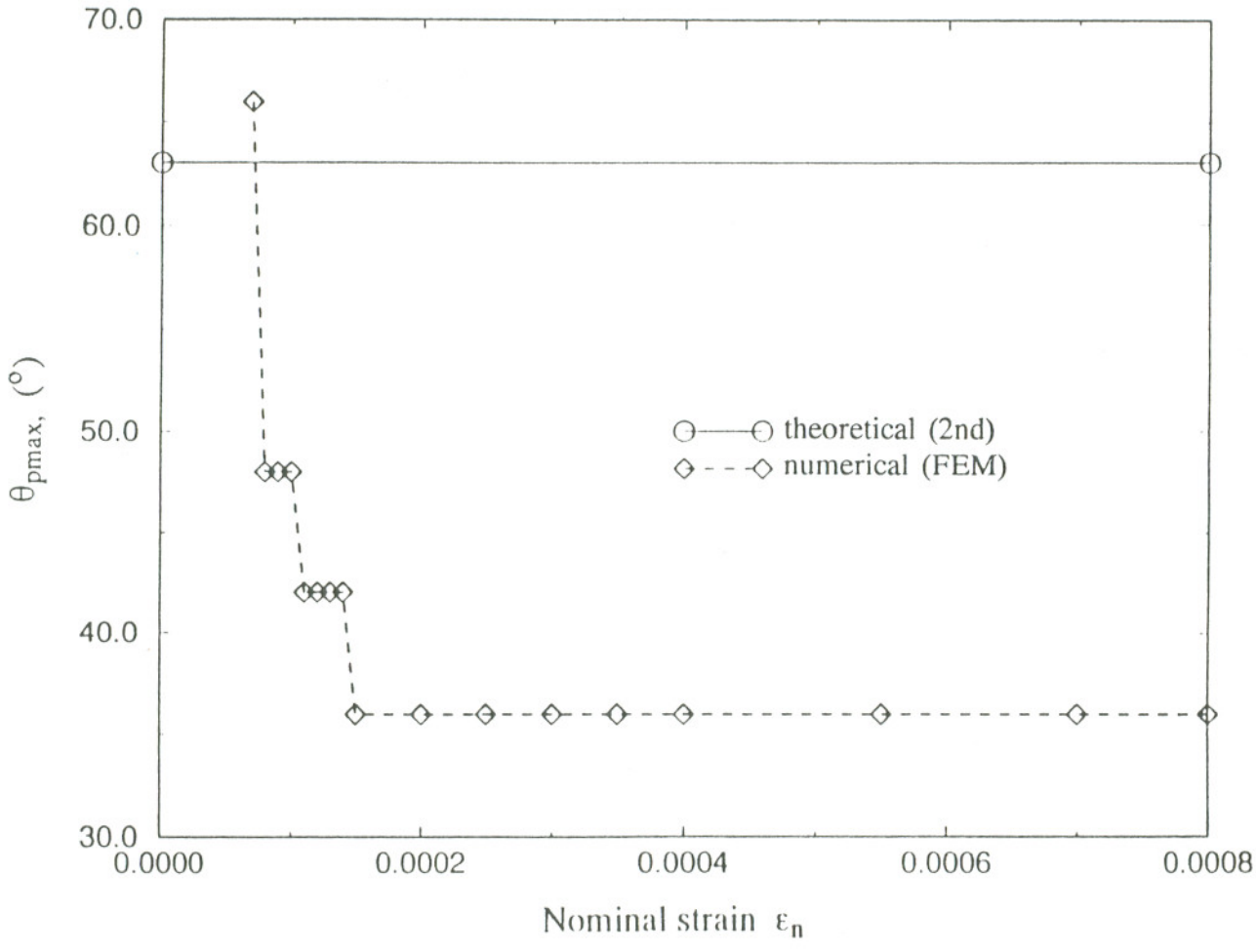

Fig. 3.69 θ_{Pmax} vs. ϵ_n (E=2632 MPa, t=50 mm, ν=0.35).

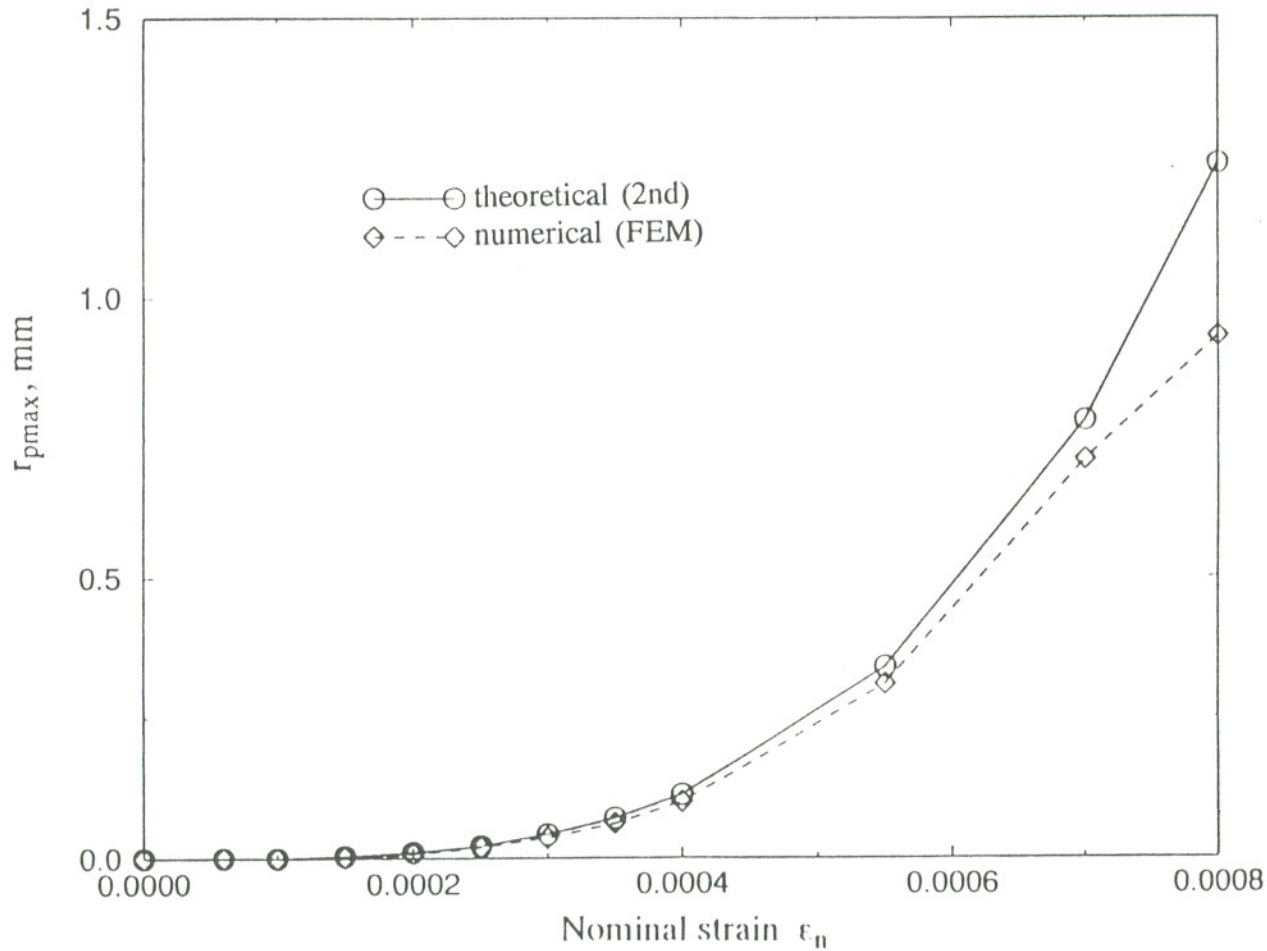

Fig. 3.70 r_{Pmax} vs. ϵ_n (E=2632 MPa, t=50 mm, ν=0.35).

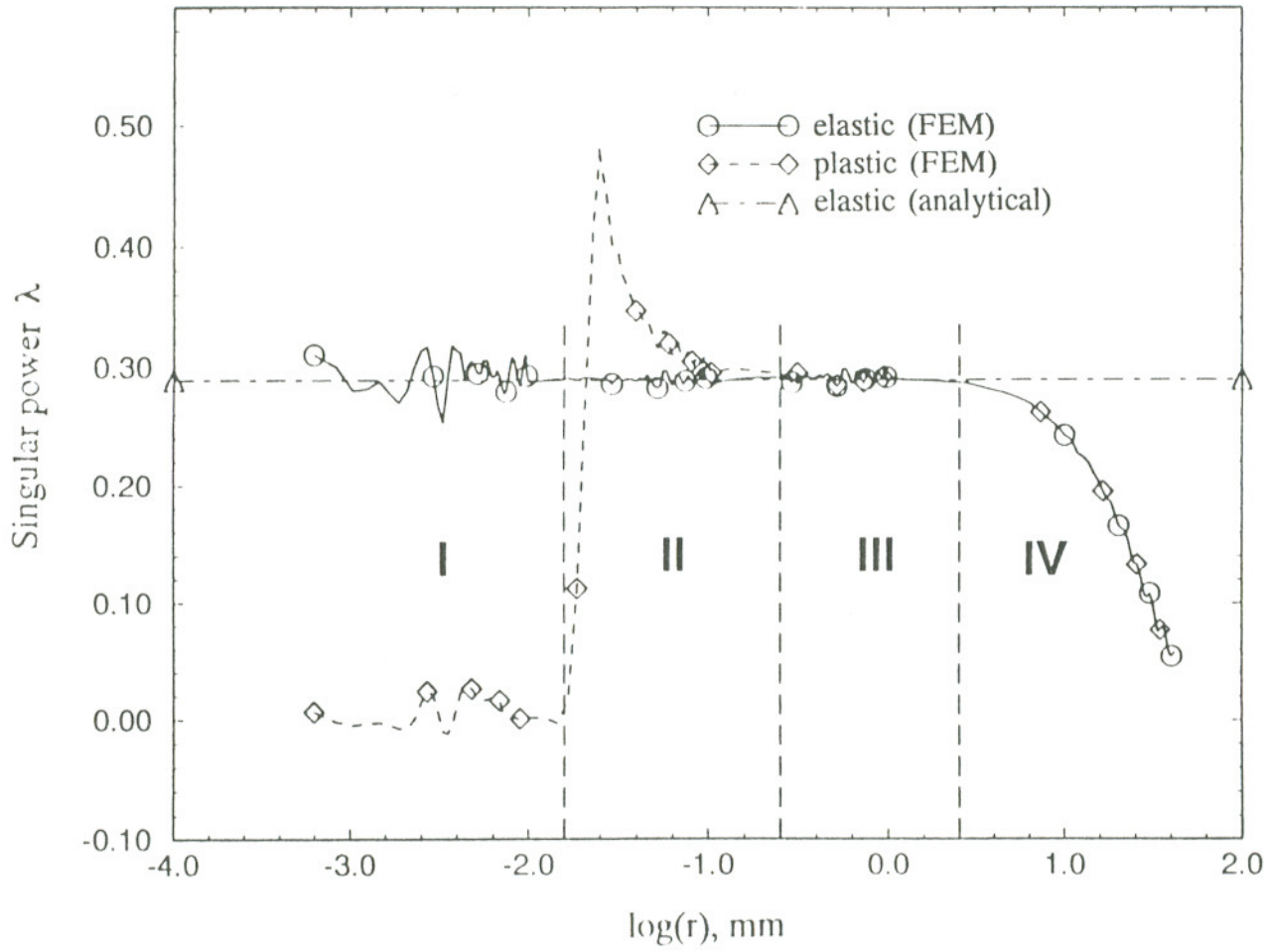

Fig. 2.71 λ distribution along 36° ray
(E=2632 MPa, ϵ_n=0.00025, t=50 mm, ν=0.35).

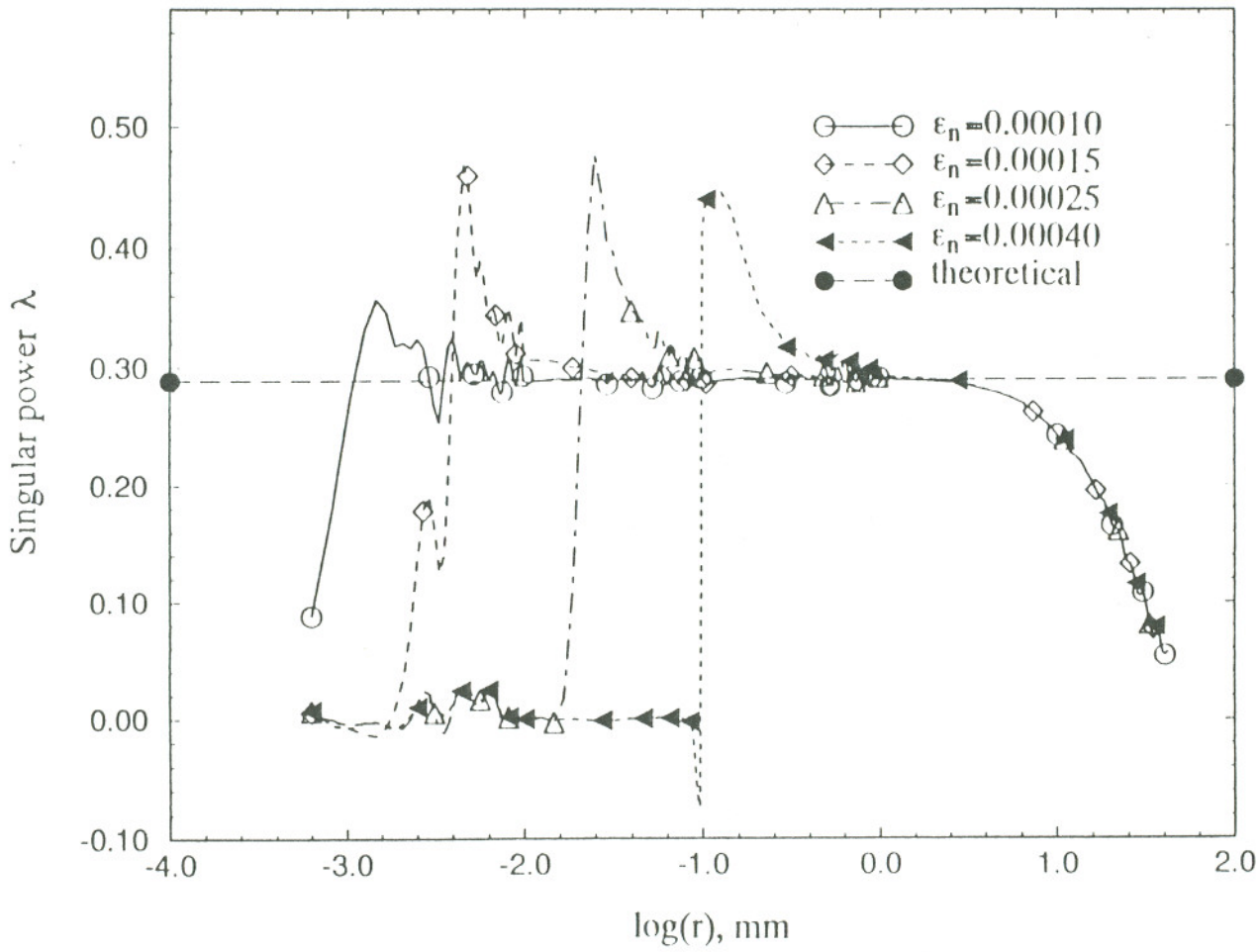

Fig. 3.72 λ distribution vs. ϵ_n along 36° ray
(E=2632 MPa, t=50 mm, ν=0.35).

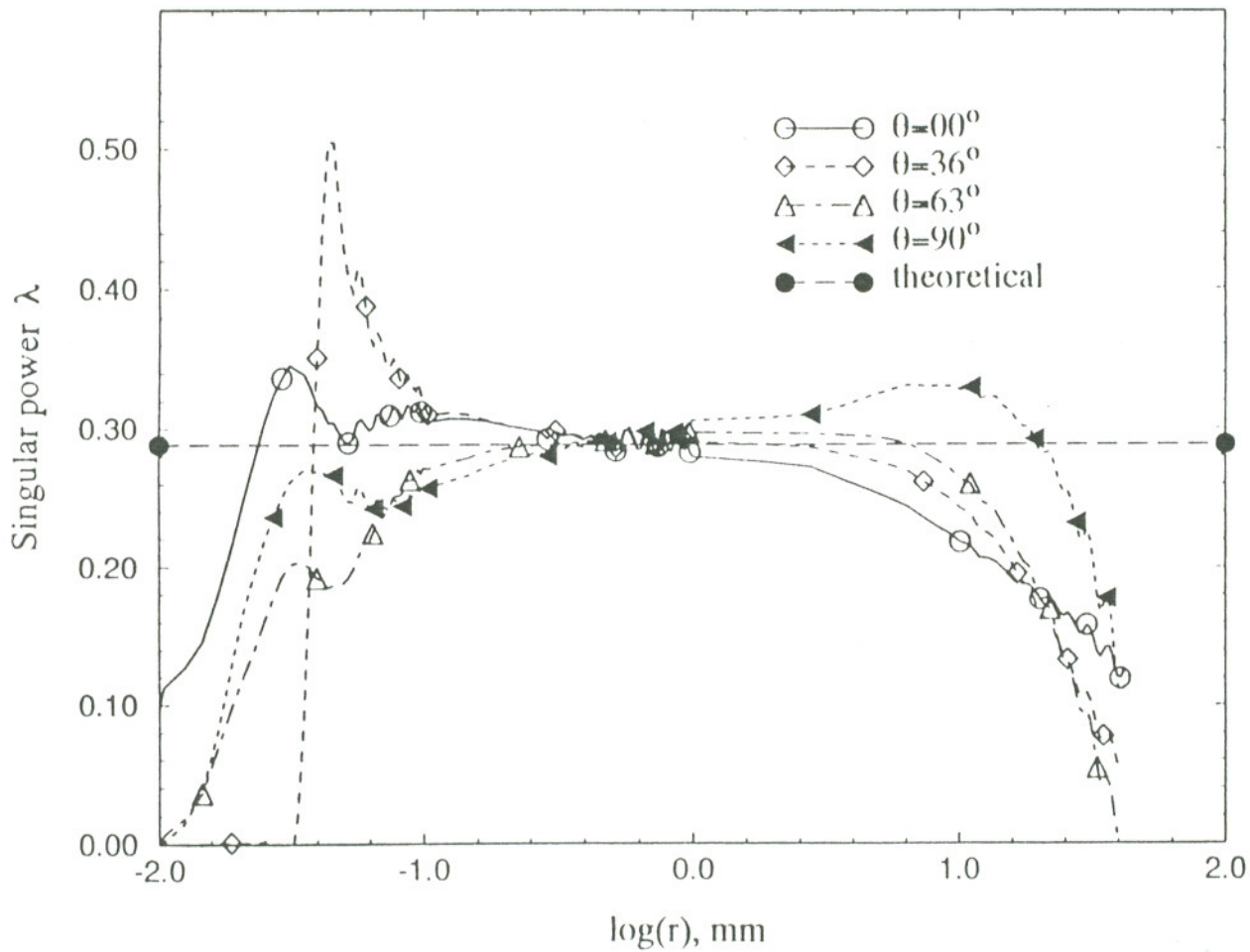

Fig. 2.73 λ distribution along different rays
(E=2632 MPa, ϵ_n=0.0003, t=50 mm, ν=0.35).

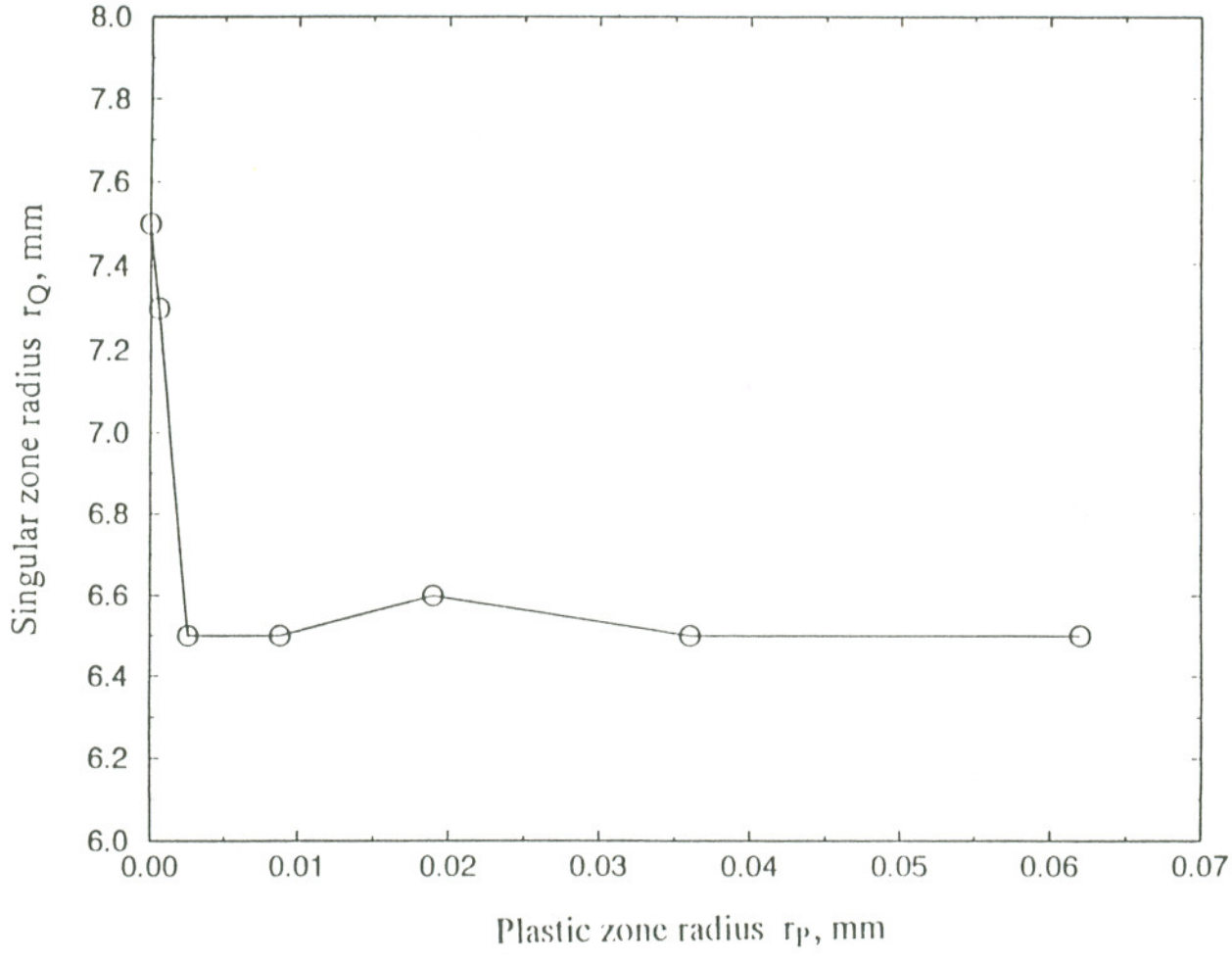

Fig. 3.74 Singular zone vs. plastic zone at $\theta=36°$
(E=2632 MPa, $\epsilon_n=0.0003$, t=50 mm, $\nu=0.35$).

CHAPTER 4
DISCUSSIONS

4.1. Macro-Stress Distributions Inside Adhesive Layers

4.1.1. Selection of Calculation Method

As described in the fore sections of Chapter 3, three methods have been employed to calculate the stress distributions inside adhesive layers of various joints. Generally speaking, closed form solutions are simple, neat and elegant, but cannot capture the features of asymptotic fields. In contrast, numerical methods tend to require more work, to necessitate special facility, to generate many data to process, and to need knowledgeable numerical engineers. In return, numerical work can reveal every detail of the stress distribution as long as the discretization is adequately fine. Concerning the three methods used in this dissertation, comparisons and guidelines can be made as below.

Equations (3.19) and (3.20) from shear lag analysis should be valid for link-joint structures from which they were obtained. Unfortunately, the strength of adhesive joints in link-joint structures is generally not a problem. These two equations are indeed useful to predict transverse tensile and shear stresses for butt joints, but they cannot be used to compute the peel stress (σ_x in Fig. 3.4), which is the dominating stress component in this type of joint. However, the formulae are very useful in fiber pull-out analysis in composites since the linking interface between matrix and fibers is actually the load transfer media. In addition, it suffices to point out that Hart-Smith [38,39] used shear lag principle in conjunction with the plate theory to obtain his closed form solutions for single- and double-lap joints. Because the bending effects have been considered, the

formulae obtained are valid for these situations [57].

Considering the characteristic of adhesive joint Iosipescu specimen, equation (3.55) is applicable for these geometrically special adhesive joints, though it seems that the problem is over-simplified. It is clearly seen from Figs. 3.9-3.11 that the closed-form solutions [equation (3.55)] and the FEM results have an excellent agreement, except for the interface corners where asymptotic fields exist.

Numerical methods, as aforementioned, are the most accurate scheme available to analyze stress distributions in the adhesive layer of different type of adhesive joints. This is because numerical methods do not have to use many assumptions to over-simplify the configuration of the original problem, and they can meet the real boundary conditions to a fairly, if not perfectly, accurate extent. Consequently, many figures plotted from the FEM solutions have been presented in this study to reveal the macro-scale stress behavior of adhesive joint Iosipescu specimens.

4.1.2. Pure Shear Loading

Under pure shear loading, the shear stress component is the dominating, or most interesting, stress for an adhesive joint specimen. Its distribution along the adhesive layer center line and the adherend-adhesive interface can be inspected from Figs. 3.9a, 3.9b, 3.15a and 3.15b. With external force load P of 10 N, the shear stress distribution calculated from finite element analysis (Section 3.1.3) approaches -1 MPa (Figs. 3.9a and 3.15a), which was also obtained from closed form solutions of equation (3.55). However, the shear stresses go to zero at the free surface due to the boundary conditions. Figures 3.9b and 3.15b also show that shear stress is quite uniform along the adherend-adhesive interface except that it deviates from the theoretical value (-1 MPa) when the interface wedge corners are approached because of the singular stress behavior at the interface corners (excluding Type B geometry).

Tensile stresses in the x- (σ_x) and y-direction (σ_y) inside the adhesive layers are

shown in Figs. 3.10, 3.11, 3.16 and 3.17. As postulated from theoretical analysis (Section 3.1.2), they are almost zero under pure shear loading condition (ϕ=0), except at the vicinity of the interface corners because of the singularity stated in the previous paragraph.

By viewing Figs. 3.9-3.11 and 3.15-3.17, it is clear that all of the stress components inside the adhesive layers are quite uniformly distributed under pure shear loading cases. However, with stresses at the interface corners showing their asymptotic behavior (except Type B, more discussion later), it is difficult to obtain, from a mathematical point of view, a uniform stress distribution in adhesive joints.

4.1.3. Biaxial In-Plane Loading

Effects of different loading angles on the stress distributions are illustrated by Figs. 3.12-3.14. From these figures, it is evident that the larger the absolute value of the loading angle, the lower the absolute shear stress (Figs 3.12a and b) but the higher the absolute tensile stresses (Figs. 3.13-3.14). The stress concentrations at wedge corners show the same trend. The shear stress is almost the same inside the adhesive layer irrespective of the sign of the loading angle ϕ; however, the tensile stresses are opposite, with reverse signs at the same loading angles. This can be best interpreted using equations (3.55), (3.59) and (3.60), where it is shown that shear stress is an even function of loading angle ϕ, while tensile stress is an odd function of this angle.

Experimental results on loading angle effects can be viewed in Figs. 3.27-3.30. At the adhesive layer thickness t=1.0 mm, the failure load is higher at ϕ=15° than that under other angles for Type A and B specimens. This observation has also been observed for composite Iosipescu specimens [91], but for type C specimens, the first kink load increases slightly as loading angle ϕ increases while the rupture loads is lowest at ϕ=0°. When t=0.2 mm, both the first kink and final failure loads increase with larger ϕ (Figs. 3.29 and 3.30) for both flexible and rigid adhesive joints (Type A). At a positive ϕ

value, the failure load increase may be due to the fact that the loading mode is compression plus shear, of which the compressive component is beneficial. However, the lack of such an effect for Type C joint requires further investigation to clarify.

A typical case of stress distribution inside the adhesive layer of an adhesive joint Iosipescu specimen under mixed mode loading (ϕ=-30°) is presented in Figs. 3.18, 3.19 and 3.20. The theoretical stresses along the notch root axis in this case are: τ_{xy}=-0.866, σ_x=0.500 and σ_y=0.000 MPa [from equation (3.55)]. Generally speaking, the numerical results coincide well with the closed form solutions inside the adhesive layer, but at interface corners noticeable stress concentrations are observed for Type A specimen. This stress concentration is responsible for crack initiation at these corners. In particular, point B is more likely to be the initial failure spot because stresses are the highest at this point (Figs. 3.18b, 3.19b and 3.20b). Experimental observation has confirmed this prediction (Sections 3.1.4.2 and 3.2.4.2, see Figs. 3.58--3.60).

Equivalent stress [by von Mises definition, equation (3.89)] contours of adhesive joint Iosipescu specimens under mixed mode loading condition of ϕ=30° (shear and compression, Fig. 3.21) show that stress distributions within the adhesive layers are fairly uniform, even if the thicknesses of the adhesive layers are different; however, interface corner B still possesses the maximum value.

4.1.4. Degree of Biaxial Stress Mode Mixing

In the previous section, it was shown that stress distributions inside adhesive layers are intrinsically mode mixed under biaxial loading conditions. In order for the degree of mode mixing of a biaxial stress distribution to be quantitatively evaluated, a measure ξ is proposed for generalized plane stress cases:

$$\xi = sign(\sigma_1\sigma_2)\,\frac{\min(|\sigma_1|,|\sigma_2|)}{\max(|\sigma_1|,|\sigma_2|)} \qquad (4.1)$$

where

$$sign(x) = \begin{cases} 1 & (x \geq 0) \\ -1 & (x < 0) \end{cases} \qquad (4.2)$$

$$\min(x,y) = \begin{cases} x & (x \leq y) \\ y & (x > y) \end{cases} \qquad (4.3)$$

$$\max(x,y) = \begin{cases} x & (x \geq y) \\ y & (x < y) \end{cases} \qquad (4.4)$$

and σ_i (i=1,2) are the principal stresses in a two-dimensional case (The third dimension is not considered here).

By this definition, it is clear that the value of ξ is within the interval [-1,1]. When $\xi=1$, it means that σ_1 equals σ_2, that is, a static water pressure in a two-dimensional sense. With $\xi=-1$, σ_1 and σ_2 have the same value but opposite signs, that is, a pure shear loading situation (equally tensile and compressive biaxial stress state). If $\xi=0$, this is a uniaxial tensile or compressive loading; in other words, no biaxial stress exists.

Using the proposed measure of degree of mode mixing of biaxial stresses, one can easily determine the uniformity of any stress distributions. For instance, using Figs. 3.12-3.14, a plot of the degree of mode mixing of the stresses inside the adhesive layer of a Type A adhesive joint Iosipescu specimen is shown in Fig. 4.1 in the case of t=1.0 mm under various loading angles.

From Fig. 4.1a, it can be seen that, under pure shear loading, the numerical value of ξ is close to the theoretical result (-1) along the adhesive center line OH. For the other

cases, the degree of mode mixing does not change if the loading angles have the same absolute values (Fig. 4.1a). ξ is close to zero along the free surface because of the boundary condition and varies much near the interface corners (Fig. 4.1b), where stress states are complicated. Even under pure shear loading case (ϕ=0), ξ deviates drastically from the theoretical value -1 in the vicinity of the interface corner. Moreover, ξ is around -0.17 at both interface corners A and B irrespective of the loading mode (angle). This may imply that the stress state at a bimaterial wedge corner is mixed mode *per se* no matter what the loading mode is. Also, σ_2 is about 0.17 times of σ_1 at the wedge corner, or *vice versa* and of opposite sign, which suggests that the stress state is of tension-compression.

Based on these observations, it is evident that ξ in equation (4.1) is a good parameter for measuring the degree of biaxial stress mode mixing, since it is capable of reflecting the characteristic of the mixed mode stress fields.

4.1.5. Notch Root Geometry

Stress distribution dependence on notch root geometries is depicted numerically in Figs. 3.9-3.11 and experimentally in Fig. 3.27. For notch root types A and C (see Fig. 2.11b), the only effect along the notch root axis (x=0) that can be seen is that all stress components decrease to zero as the free surface is approached because there is no geometric or physical discontinuity at these points. However, the same argument is not true for the geometry of Type B, where both tensile stresses (σ_x in Fig. 3.10a and σ_y in Fig. 3.11a) are singular at the notch tip which is assumed to be mathematically perfectly sharp (Fig. 3.8b). The shear stress (Fig. 3.9a) at the tip does not exhibit any strong trend of asymptotic behavior. The observation may be explained by Sukumar and Kumosa's work on sharp notch tips [72,74,108]. They have found that, under pure in-plane shear loading condition, the notch root tip singularity disappears if the re-entrant angle of an isotropic notch is greater or equal to 103°. The re-entrant angle for Type B notch is 105°.

The tensile stresses still show some singular behavior, which may be caused by the numerical round-off or truncation errors during the process of computations. These errors, of course, may change a pure mode II loading to a mixed mode loading condition.

The findings are totally different along the interfaces. From Figs. 3.9b, it can be seen that shear stress (τ_{xy}) for specimens A and B displays a "negative" singular behavior, but shear stress in the notch root of Specimen C demonstrates a "positive" singularity. In Figs. 3.10b and 3.11b, tensile stresses (σ_x and σ_y) in the vicinities of the notch roots of geometry Type A and C increase as the wedge corner is approached. They show only limited stress concentration at the interface corner from the viewpoint of the entire interface. In-depth discussions will be addressed in the section of non- and weak-singular bimaterial wedge (Section 4.2.5).

Preliminary experimental results in Figs. 3.27 and 3.28 may demonstrate that notch root geometries do not play an important role in either the first kink load or rupture load, although it seems that Type C is slightly inferior compared with Type A or B. Because the adhesive layer is fairly thick (1 mm), it may contain small defects such as bulbs and micro-cracks. Also, since notch root geometries cannot be made well enough to represent the mathematical roles, more work is necessary before a correct conclusion can be drawn.

4.1.6. Adhesive Type

From the analytical results in equation (3.55), it can be concluded that adhesive type has no influence on the stress distributions inside the adhesive layer, since no material property appears in this equation. Nevertheless, the adhesives used for joints will certainly have an impact on the stress distributions and mechanical behavior. This can be postulated from the asymptotic analysis at bimaterial interface wedge corners (Section 3.2). Equation (3.55) does not consider the mechanical property effects of the

adhesives used because it does not take into account the singular behavior at the interface corners in the analytically deducing process.

From the limited experimental data in Figs. 3.29-3.30, no obvious effects of adhesive types on the joint strength could be inspected. This is rather unusual since the two adhesives used had different mechanical properties, in particular, failure strengths. For the real effects of adhesive types on the joint strengths to be identified, more testings by varying the adhesive types and the adhesive layer thicknesses should be conducted.

4.1.7. Adhesive Layer Thickness

Numerically, shear stresses inside the adhesive layer of a Type A adhesive joint Iosipescu specimen do not change significantly with the adhesive thicknesses under pure shear loading (Fig. 3.15a and b). However, the thinner the adhesive layer, the higher the absolute values of the tensile stresses in the vicinity of the notch root but the lower those values at the adhesive center (Figs. 3.16a and 3.17a). Along the interface, the thickness of the adhesive layer does not show any significant effect on the stress distributions. From these figures (Figs. 3.15-3.17), it is evident that, under pure shear loading mode, adhesive thickness is not a dominant factor in terms of the stress distributions inside the adhesive layer of Type A adhesive joint Iosipescu specimen.

Stress distributions, under a typical mixed mode loading situation of loading angle $\phi=30°$, are shown in Figs. 3.18-3.20. The observation is similar to that in the pure mode II loading condition. Namely, shear stress does not vary much with respect to the adhesive thicknesses (Figs. 3.18a and b). In contrary, tensile stresses change quite a bit when the adhesive thickness varies. The thicker the adhesive layer, the less the variation along the center line OH (Figs. 3.19a and 3.20a); however, little difference is seen along the adherend-adhesive interface (Figs. 3.19b and 3.20b). This also demonstrates that the stresses inside the adhesive layer do not change significantly when the adhesive layer thickness is varied under mixed mode loading conditions for Type A adhesive joint

Iosipescu specimens. Therefore, from the aforementioned observations in this section, it may be deduced that the experimental results will not change significantly when the layer thicknesses are different for Type A adhesive joint Iosipescu specimens.

Adhesive layer thickness effects on the joint strength can be seen from the experimental data in Figs. 3.27-3.30. Here, it is found that both the first kink and rupture loads from the t=0.2 mm group are greater than that from the t=1.0 mm set for Type A specimen made of rigid adhesives. In particular, this effect is more obvious when the loading angle is larger. From the asymptotic analysis on bimaterial wedge interfaces (Section 4.2.3), it has been postulated that a joint with a thinner adhesive layer would have a higher strength than that with a thicker layer because the former would have a higher stress intensity factor. In reality, the higher stress intensity factor at the wedge corners may be easily released by the plastic deformation at the corners with adhesive layer thickness being 1 or 0.2 mm, so that the effect is not as dominant as mathematically predicted. However, if the adhesive layer is thin enough, it may be expected to have such an impact as predicted in Section 4.2.3.

4.2. Asymptotic Fields At Bimaterial Interface Corners

4.2.1. Angular Eigenfunction

The normalized angular displacement eigenfunctions along the x- and y-directions obtained from three methods can be seen in Figs. 3.38a and 3.38b. The normalization in this case assumes the value of the displacement eigenfunction (u_x and u_y) to be unity at a point with $\theta=0°$ and a particular radius r from the wedge corner. Radius r was selected to be 1.0 mm for the analytical calculations, and 1.0 or 0.1 mm for the FEM analysis; for the FEIM computations, it was taken as the maximum distance where convergence was achieved. The analytical data were obtained via a coordinate transform of u_r and u_θ in equations (3.72) and (3.73). The FEM modeling in this study assumed

2t=100 mm in order to create a sufficiently large singular stress zone. The external displacement loads (u_y) were selected such that they were capable of generating a nominal strain of 0.0001 along the y-direction, while the traction along the x-direction was assumed to be zero. The FEIM results of eigenfunctions were extracted when the pre-defined convergence criterion 0.001% [by equation (3.99)] was satisfied. Clearly, the normalized displacement eigenfunction solutions from the analytical and FEIM schemes are in excellent agreement. The FEM results from the r=0.1 mm ring, however, are not as accurate and are even worse along the r=1.0 mm ring. It seems that the ring localized very close to the wedge corner (r=0.1 mm) provides more information about the singular stress field than the other ring (r=1.0 mm). However, when r is too small, the FEM results are also inaccurate and are therefore unacceptable (Fig. 3.37), as will be discussed in Section 4.2.2. It may be stated that whereas the FEM approach has certain drawbacks regarding accuracy, it is capable of generating the absolute value of eigenfunctions with a reasonable degree of accuracy. On the other hand, the FEIM scheme and the theoretical analysis can yield only the relative displacement eigenfunctions. The accuracy of the eigenfunction solutions based on these two methods is excellent.

4.2.2. Singular Power

Initially, focus will be confined to the simplest case: an elastic-rigid bimaterial wedge corner (Figs. 3.39 and 3.41).

An examination of Table 3.1 reveals that the singular power λ does not depend on Young's modulus. It does not depend on the specimen thickness (2t) either, as indicated by the data in Table 3.2 and Table 3.5. When t is 10 or 50 mm, it is obvious that λ remains constant, but when t is smaller, from the FEM results in Table 3.2, it seems that the adhesive layer thickness and the loading conditions do influence the singular power λ. As a matter of fact, they do not have any effect on λ (see Table 3.6), because when t is small, the solution at the interface corner is not accurate enough to

properly model the singular power.

The FEIM results in Tables 3.6 and 3.7 indicate that the singular power λ is an intrinsic characteristic of the interface for a definite material combination. Moreover, it holds the same value no matter how small the thickness or what the loading conditions may be. It may also be inferred that the FEIM is a good and practical method for obtaining stress singular powers in complex conditions. Combining the data in Tables 3.1-3.4, 3.6 and 3.7, it is obvious that λ is only a function of Poisson's ratio for an elastic-rigid bimaterial wedge with a fixed wedge angle.

The second case being discussed is an orthogonal bimaterial wedge made of two elastic isotropic materials (Figs 6.35 and 6.36). The FEIM is the only method used to extract the singular powers because the singular zone in this case is too small to be accurately captured using the FEM (see Section 4.2.4). Attention will be paid to the singular power dependence on singular elastic parameters, namely, Young's modulus ratio E_1/E_2 and Poisson's ratios (ν_1 and ν_2) of the two materials forming the wedge. The resultant data are presented in Figs. 3.42 and 3.43.

Figure 3.42 shows that the ratio of Young's moduli (E_1/E_2) has a significant influence on the value of the singular power when E_1/E_2 approaches unity. For E_1/E_2 values greater than 1000, the singular power is found to be approximately equal to that of the rigid-elastic case just discussed. However, it should be noted that the assumption of a perfectly rigid adherend is generally not valid from an engineering standpoint since the ratio E_1/E_2 would rarely exceed 1000.

The singular power dependence on Poisson's ratios of the bonded materials is presented in Fig. 3.43. Clearly, a varying value of ν_1 (while keeping ν_2=0.35) does not seem to influence the value of λ; on the other hand, if ν_1 is held constant at 0.3, the singular power steadily increases with increasing values of ν_2. This observation seems to suggest that the Poisson's ratio of the so-called "stiffer" material has a relatively smaller effect on the singular power, while that of the "softer" material has a considerably more significant effect on the singular power. Furthermore, comparison of

Figs. 3.42 and 3.43 shows that the ratio of Young's moduli has a larger influence on the singular power than the Poisson's ratios of the individual materials. This is probably caused by the fact that the ratio of Young's moduli E_1/E_2 can undergo considerably large variations while the Poisson's ratios are limited in the range of 0.0 to 0.5. Clearly, the results presented in this case should be taken into account in practical engineering design problems in order to create more tolerant "fail-safe" adhesive joints.

The factors that influence the eigenvalues at the wedge corners for skewed bimaterial wedges, the third case, are addressed separately in Section 4.2.5 because of their complexity and specialty.

In the last case, orthotropic orthogonal bimaterial wedges, more factors exist to influence the singular power, namely, the ratio of Young's moduli, the orthotropic ratios [defined by equation (3.100)] and the Poisson's ratios, than those for the first three cases. In order that the goal of this research dealing with adhesive joints could be met, an orthogonal bimaterial wedge comprised of isotropic (adhesive) and orthotropic (composite adherend) materials, to simulate a joint bonded two elastic orthotropic composite adherends by an elastic adhesive, was considered (Section 3.2.3.4). The results are listed in Tables 3.11 and 3.12 and partly graphed in Figs. 3.49 and 3.50.

When the orthotropic ratio $\omega^{(2)}$ is greater than 0.5, from Fig. 3.49, it is found that the singular power λ does not change noticeably irrespective of the "base value" (kept constant during corresponding computation) of the y-direction Young's modulus $E^{(2)}_{22}$. However, the ratio of $E_1/E^{(2)}_{22}$ has shown an impact on the eigenvalues, *viz.*, the closer it is to unity, the smaller (approaching zero) the eigenvalue; the farther away from unity, the higher the eigenvalue. This is similar to the observations in isotropic bimaterial wedges (Fig. 3.42) where the orthotropic ratio is unity for both materials. When $\omega^{(2)}$ is less than 0.5 and decreases, λ goes up if E_{22} is smaller than 5000 MPa but decreases in the case of $E^{(2)}_{22}$ being greater than 5000. Further, it is observed that the ratio of $E_1/E^{(2)}_{22}$ has a reverse impact on the eigenvalues compared to those if $\omega^{(2)}$ is greater than 0.5. For the artificial materials in Table 3.11, the dependence of the eigenvalues on these

parameters has demonstrated the same trend.

Poisson's ratio $\nu^{(2)}_{12}$ does not demonstrate any significant influence on eigenvalue distributions (Fig. 3.50). Recalling the findings of singular power dependence on Poisson's ratios in case 2 of this section (Fig. 3.43) and considering that both $E^{(2)}_{11}$ and $E^{(2)}_{22}$ are greater than E_1, it is clear that this phenomenon is due to Material 2 having stiffer than Material 1. Nevertheless, it can be expected that Poisson's ratio $\nu^{(2)}_{12}$ will affect λ when Material 2 is softer.

4.2.3. Stress Intensity Factor

An accurate description of the singular stress fields in the adhesive butt joint analyzed in this study (Fig. 3.36) requires an accurate solution of the displacement eigenfunctions. From the previous analytical analysis, it is evident that the displacement eigenfunctions can be determined only when the absolute value of the stress intensity factor Q is known *a priori*. However, since Q is a function of the singular power λ and the external boundary conditions, determination of Q remains impossible without taking the boundary conditions into account. Therefore, only in very special cases (for instance, rigid adherend, orthogonal wedge, and simple boundary conditions [8-9]) can Q be determined analytically. The only other recourse are numerical schemes. Among the existing numerical approaches, the absolute values of the displacement eigenfunctions can be determined only by FEM [and making use of equation (3.88)] to arrive at the solution for Q when the singular stress field is sufficiently large. The FEIM approach, however, fails in this respect since a method for evaluating the stress intensity factor Q, and consequently the displacement eigenfunction, is not presently available for the FEIM schemes. However, all of the aforementioned approaches are capable of producing the relative eigenfunctions of the displacement fields at the terminus of the interfaces in Fig. 3.35.

In addition, from Table 3.5, it is evident that adhesive layer thickness and loading

conditions affect stress intensity factors, and the free edge stress intensity factor is accurately expressed by Reedy's formula [same as equation (3.92)]:

$$Q_y(0) = \sigma^*(2t)^{\lambda} A(\nu) \qquad (4.5)$$

Reedy's free edge stress intensity factor formula characterized the nature of the singular stress field, with A(ν) being a function of the loading condition, whose nature needs to be explored. Moreover, from equation (4.5), it may be speculated that the free edge stress intensity factor will decrease if the adhesive layer becomes thinner. This may explain the common experience that "the best strength of an adhesive joint is no adhesive." However, the fact that experiments conducted so far do not support this effect (Figs. 3.27-3.30) may be because the adhesive layer at the bimaterial wedge corner is not perfectly elastic, rather, plastic deformation at the corner takes place to ease this effect. More experimental work is needed to address this problem correctly.

4.2.4. Singular Zone

It is apparent that when r is very small or fairly large, the data in Fig. 3.37 diverges from the linear relationship. For small values of r, the finite element solutions are not accurate since the polynomial interpolation functions used in the FEM do not represent the r^{λ} curve adequately. On the other hand, when r is large, it is outside the singular stress zone; therefore, equation (3.86) is unable to accurately describe the stress field. Taking these facts into account, it is clear that around the interface corner there exists a singular stress zone, inside which the stresses can be adequately described by equation (3.86).

First, let us analyze a simpler case — the rigid-elastic model (Fig. 3.39) computed in Section 3.2.2.5. As indicated earlier, the singular power is only a function of Poisson's ratio in this situation; thus, the singular zone geometries must also be affected by ν. Figure 3.40a, drawn from the equivalent stress field, shows such an effect.

If r_{Qmax} is denoted as the maximum radius of the singular stress zone and θ_{Qmax} as the angle between the r_{Qmax} and the interface, it can be seen that as ν increases, θ_{Qmax} decreases, as does the singular radius along the interface. r_{Qmax}, however, does not change appreciably. Figure 3.40b shows the negligible effect of Young's modulus on the singular field, as depicted by the numerical data. Also, the eigenvalue does not depend on the Young's modulus. Figure 3.40c shows that the singular zone shapes and sizes will be different if they are extracted from different field parameters, although the wedge geometry, material mechanical properties, external loadings, and boundary conditions are the same. It is found that the equivalent stress field results in the biggest singular zone, while the displacement field along x-direction generates the smallest, and the displacement field along y-direction yields an intermediate value. Figure 3.40d shows a similar trend in the t=50 mm case, implying that the singular stress field differs in different senses. Taking into account the fact that it is necessary to use the equivalent stress to evaluate the plastic zone, it is suggested that the singular zone obtained from the equivalent stress field be treated as the generic one in order to make it convenient to study the interactions between the singular zone and the plastic zone.

For a more complicated case, elastic-elastic bimaterial wedges shown in Figs. 3.35 and 3.36, it is evident from the results shown in Fig. 3.37 that when t is too small, the linearity of the relationship is lost and therefore the singular power λ and the radial stress intensity factor $Q_{ij}(\theta)$ cannot be accurately computed. It appears that the singular stress zone in this case is too small to be adequately described by conventional FEM, as used for the rigid-elastic case. Therefore, as an alternative approach, the singular zone was semi-quantitatively evaluated in Section 3.2.3.5 by applying the FEIM.

The dependence of the singular stress zone on the ratio of Young's moduli is shown in Fig. 3.52 for the case of $\nu_1=0.3$ and $\nu_2=0.35$. Clearly, irrespective of the value of E_1/E_2, the zone in Material 1 is invariably found to be larger than or equal to that of Material 2. The zone is found to be the smallest when E_1/E_2 approaches unity. However, for $E_1/E_2>5$, the zones in both materials do not show any change. An analysis

similar to the rigid-elastic (assuming that Material 1 is rigid, *i.e.*, $E_1/E_2 \rightarrow \infty$), shows that the singular stress zone in Material 2 remains the same for all values of E_1/E_2 greater than 5 (Fig. 3.52).

The singular stress zone size as a function of Poisson's ratios of the two materials is presented in Fig. 3.53. Clearly, for $\nu_2=0.35$, a variation in the value of ν_1 does not lead to any change in the singular zones. However, when ν_1 is held at 0.3 and ν_2 is varied from 0.05 to 0.495, the singular zone size in Material 1 shows an initial increment to attain a maximum in the region $\nu_2=0.30$-0.35 and then decreases rapidly; the singular stress zone in Material 2 on the other hand shows an initial increment and then holds steady at approximately 0.0001 mm.

Taking into account the above results (Figs. 3.52 and 3.53), it may be stated that for adhesive butt joints, when the E_1/E_2 ratio is generally greater than 5 and ν_1, ν_2 are close to 0.3, the singular stress zones do not exhibit any significant change as a result of variation of elastic properties of the bonded materials (adhesive and adherend). Moreover, the singular stress zone in the adherend (Material 1 in this case) is always larger than that of the adhesive.

4.2.5. Non- and Weak-Singular Bimaterial Wedge

The deformed structure of the rectangle with a skewed interface (Fig. 3.33) tends to bend toward the left under uniform tensile loadings if viewed from the left bottom corner, where the dashed line is the contour of the original structure. This is because the upper material (1) is stiffer than the lower one (2), and the slope of the skewed interface is positive with respect to the Cartesian coordinate system used (Fig. 3.31). Consequently, the stiffness of the left edge of the structure is higher than that of the right one. Therefore, it is intuitive by observing that the major deformation will take place in Material 2, the lower portion, since it is softer. Considering the positive slope of the skewed interface, it can be anticipated that the effective strain on the left edge of

Material 2 will be greater than that on the right edge of the same material. That is, during deformation, more energy is dissipated on the interface corner of the left edge (Point A) and less energy is consumed in the near field at Point B in Fig. 3.31. This hypothesis is verified by Fig. 3.34. The highest stress concentration is located in the bimaterial wedge A and the equivalent stress is the smallest at wedge B, which may suggest that the stress field at Wedge B should not be singular. This observation obviously indicates that the initiation point of a failure is most likely to begin from Point A but least probably from Point B. Therefore, it will be desirable to design a bimaterial wedge having the mechanical behavior of the area around Point B.

Further investigations (Tables 3.9 and 3.10, and Figs. 3.47 and 3.48) make it known that a critical interface angle α_c, beyond which the asymptotic stress field totally disappears, universally exists for all material combinations. This angle is about 126°, provided that the convention in Fig. 3.45 and the condition of ratio E_1/E_2 being greater than one are met. This is a very important finding because it means that the bimaterial wedge, with a skewed interface angle greater than the critical angle, will never suffer the stress singularity problem any more, and therefore, is not prone to initiate interfacial cracks and should have a higher safe-failure strength. As a matter of fact, this kind of bimaterial wedge is geometrically similar to and mechanically has the same behavior of Wedge B in Fig. 3.31. In addition, it is also observed that within the range of $40° < \alpha < 65°$, the value of the stress singularity has a regional minimum point (Figs. 3.47 and 3.48). By the general principle that the smaller singular stress power the higher interfacial strength, this regionally minimum point (in the range of $40° < \alpha < 65°$) can be used as the second choice, for designing bimaterial structures with skewed interfaces, if the skewed interface angle can not be selected greater than the critical value 126° in engineering practices. However, the first choice, to choose α being greater than α_c, is always preferred.

The ratio of the Young's moduli (E_1/E_2) has shown effects not only on the value of the stress intensities but also on the critical skewed interface angles, although the latter

is smaller (Table 3.9). From Fig. 3.47, it is noted that the value of λ is higher if ratio E_1/E_2 has a bigger number, and vice versa. This suggests that, from the viewpoint of minimizing the singular power, closer values of Young's moduli (E_1/E_2 approaching unity) between the two materials under consideration are more desirable in real applications. Further, it may suggest a general rule that the smaller the difference between the two materials making up a bimaterial wedge, the smaller stress singularity or the weaker asymptotic stress field at the wedge corner. The Young's modulus ratio E_1/E_2 has such an effect on the critical skewed interface angle α_c that when the ratio approaches infinity, the critical angle is about 126°; otherwise, the critical angle is about 125° (Table 3.9). As a universal result, the former value 126° is taken to be the globally valid critical angle.

With the relationship between the stress singular power λ and the Poisson's ratio of Material 2 in Fig. 3.48, it is found that, only within the range of $40° < \alpha < 125°$ and under the given conditions, λ is noticeably altered while ν_2 is changed. The singular power increases as the Poisson's ratio is increased. When the skewed interface angle is outside the above range ($40° < \alpha < 125°$), no significant difference between the λ's can be observed for various values of ν_2 under consideration. The Poisson's ratio of Material 2 (ν_2) also has an influence on the critical skewed interface angle α_c (Table 3.10). When ν_2 was equal to 0.35 or 0.40, α_c arrived at 126°; but if ν_2 took the value of 0.275 or 0.30, α_c ended up at about 123.75°. However, this does not affect the conclusion that the universal critical angle is 126° from a conservative standpoint. In addition, by comparing Figs. 3.47 and 3.48, it is clear that E_1/E_2 has a greater influence on the stress intensities λ than ν_2 does. This phenomenon coincides with what was observed in Section 4.2.2 [49,118].

4.2.6. Convergence of FEIM

Figure 3.54 shows a typical convergence procedure for the bimaterial wedge

studied in Section 3.2.3.2, from which one can see that the eigenvalues obtained in the first several iterations may diverge, but they will finally converge to the correct value as the iteration procedure proceeds .

In addition, it is noticed that not only the value of the singular power but the convergence rate is also a function of the elastic properties of the bonded materials. Figure 3.55 shows the total number of iterations required to arrive at a converged value of λ as a function of the ratio of Young's moduli (E_1/E_2) of the materials considered. Convergence is also found to be slowest when the ratio (E_1/E_2) approaches unity. It is already shown in Fig. 3.52 that the size of the singular stress zone is smallest for $E_1/E_2 \rightarrow 1$ thereby leading to a slower convergence rate. Fig. 3.56 presents the dependence of convergence rate on the Poisson's ratios of the materials considered. For a constant value of ν_2 (held at 0.35), a varying ν_1 does not seem to influence the convergence rate. However, when ν_1 is fixed at 0.3 and ν_2 is increased from 0.05, the convergence rate shows an initial acceleration until $\nu_2 \approx 0.2$, beyond which it remains constant. Again, comparison with Fig. 3.53 further reinforces the idea of smaller singular stress zones requiring a large number of iterations to achieve convergence.

The fact that, under special conditions, convergence could not be arrived at after many iterations (Fig. 3.57) may imply that the singular powers in these cases are complex [21]. From the analysis of skewed bimaterial wedges, it is evident in Fig. 3.57 that the oscillation of the singular power λ becomes even more severe after the number of iterations is greater than 18. Therefore, a more sophisticated technique is required to extract complex stress singularities [84]. In addition, from Tables 3.9 and 3.10, it is found that as E_1/E_2 becomes smaller, the range with which convergence was not achieved, decreases until it totally disappears; that is, the convergence will be regained when ratio E_1/E_2 declines to the value of 10. The Poisson's ratio of Materials 2 (ν_2), however, does not exhibit any effect on the non-convergent region (Table 3.10 or Fig. 3.48). This is an additional evidence, as stated in the previous paragraph, that Poisson's ratios have less influence on the asymptotic field in the vicinity of a bimaterial wedge

than the ratio of Young's moduli does.

When the solution was real and not close to the non-convergent region, the number of iterations to reach convergence was found to be six or seven, irrespective of the skewed interface angle, the ratio of Young's modulus, and the Poisson's ratios. This may suggest that, provided the conditions, the singular stress zone should not be noticeably influenced by the geometrical and physical properties. However, when the skewed interface angle was near the range of the non-convergent area, the number of iterations needed to arrive at convergence was much larger. It may be speculated that the size of the singular zone of complex stress singularities is much smaller than that of real asymptotic stress field. Nevertheless, further investigation on complex interfacial stress singularities is needed to verify this hypothesis.

4.2.7. Application of Composite Parameters

It was concluded in Section 3.2.1 that for a particular geometry of an isotropic bimaterial wedge, the singular power is only a function of two independent composite parameters α and β as defined by equations (2.52) and (2.53). This could be further verified by the results from the finite element iterative analysis shown in Table 3.8, where ν=0.00001 is used to represent ν=0 and ν=.49999 to represent ν=0.5 in order to conduct the computations. The results demonstrate that any combination of elastic properties of the two media that yield a common set of composite parameters α and β give rise to the same singular power λ. There is one exception, namely, when α=-0.5 and β=-0.25, the λ's obtained by the FEIM scheme are not constant. This is caused by the fact that when λ approaches zero, the numerical errors introduced in the FEIM analysis are large enough to disturb the accuracy of the singular power calculation. This observation indicates that when λ is too small, even the FEIM scheme fails to yield a reasonably accurate result. Nevertheless, perturbations in the values of the singular power become insignificant when λ has a non-trivial value.

A diagram showing the distribution of λ for different composite parameters is shown in Fig. 3.44. It can be seen that the diagram is symmetric about the $\beta=0$ axis. This observation can be supported by equations (3.52) and (3.53), where an interchange of the subscripts leads to a change in the sign of the composite parameters. In addition, it is found that the singularity tends to vanish when α is zero, *i.e.*, material property combinations yielding very small value of α give rise to very small values of the singular power. Therefore, an appropriate selection of bonding materials could prove crucial in enhancing the fracture strength of the adhesive joint. In contrast, the larger the absolute value of α, the larger the singular power λ. Therefore, an adhesive butt joint yielding a large α value may not be a good choice.

From the above observations, it may be concluded that the analytical model described in Section 3.2.1 is valid and the pair of the composite parameters is capable of describing the elastic mechanical behavior of bimaterial media adequately. This conclusion has, in fact, more significance from a practical standpoint because it can be employed in the design of experimental simulations for state-of-the-art materials using relatively inexpensive materials that could give rise to the same composite parameters. Moreover, the fact that a smaller value of α gives rise to a weaker singular power λ may be used as a guideline by design engineers to select material combinations that yield a trivial value of α.

4.3. Plastic Zone at Bimaterial Interface Wedge Corners

4.3.1. Plastic Zone Evaluation Methods

Figure 3.68 demonstrates that the theoretical plastic zone of the second estimation is much larger than the numerical (real) one. Even the area of the plastic zone from the first estimation is larger than that of the numerical one. The shape of the theoretical plastic zone also differs considerably from the numerical one at $\epsilon_n=0.0003$. From Fig.

3.69, it can been seen that when ϵ_n=0.00007, the numerical $\theta^{(n)}_{Pmax}$ almost equals the theoretical $\theta^{(t)}_{Pmax}$. However when ϵ_n becomes bigger, $\theta^{(n)}_{Pmax}$ decreases until it reaches 36° and holds this value. The critical load is about ϵ_n=0.00015. This observation shows that as the load increases, the plastic zone develops toward the interface. This may suggest that the initial failure may take place near the interface since the strain energy of this area is very high. When θ_{Pmax} equals 36°, the plastic zone (Fig. 3.68) is in a fingertip shape, as reported in reference [121]. It is also similar to that of the singular zone (Fig. 3.40). Thus, when the load is big enough, the singular zone controls the plastic zone, which controls the plastic deformation and thus controls the failure path. Although the shapes of the theoretical and numerical plastic zones differ significantly, the theoretical maximum plastic zone radius $r^{(t)}_{Pmax}$ matches the numerical one $r^{(n)}_{Pmax}$ very well before ϵ_n exceeds 0.0007 (as shown in Fig. 3.70). Therefore, $r^{(t)}_{Pmax}$ can be used to represent $r^{(n)}_{Pmax}$ when this value is required in the condition of $\epsilon_n < 0.0007$.

4.3.2. Transition Zone

The effects of the plastic zone on the singular zone can be clearly seen in Fig. 3.71, from which it is convenient to distinguish the wedge corner into a singular zone (I, II and III) and a normal zone (IV) in the elastic case, while in the elastic-plastic case, it appears in four regions: the plastic zone (I), λ=0; the **transition zone** (II), $\lambda \neq$ constant; the singular zone (III), λ=0.2888; and the normal zone (IV), λ decreases.

From Fig. 3.72, it is found that the singular zone becomes smaller as ϵ_n increases since the plastic zone expands. Also, it can be seen that when the load is large enough the singular zone does not exist at all. The critical load is ϵ_n=0.00035, beyond which a plateau of λ=0.2888 cannot be found at all, but the normal zone does not show a notable influence on λ with the load up to ϵ_n=0.0004. Furthermore, it seems that after the singular zone disappears, a critical ring of the radius exists with a value of $r_c \approx 0.97$ mm and a critical angle θ_c=36°. The following observation can be made from a fairly large

area, the transition, singular, and regular zones, around r_c,

$$r < r_c\ ,\ \theta < \theta_c\ ,\ \lambda > 0.2888$$
$$r < r_c\ ,\ \theta > \theta_c\ ,\ \lambda < 0.2888$$
$$r > r_c\ ,\ \theta < \theta_c\ ,\ \lambda < 0.2888$$
$$r > r_c\ ,\ \theta > \theta_c\ ,\ \lambda > 0.2888$$

A schematic drawing displaying this trend is presented in Fig. 4.2.

Larger λ means that stresses change faster (higher $|\partial\sigma_{ij}/\partial r|$) and are more localized, that is, it is expected that failure will be more likely to occur in the area of $r<r_c$ and $\theta<\theta_c$, which is very close to the interface. Singular power λ is also greater than 0.2888 in the region of $r>r_c$ and $\theta>\theta_c$, but because the absolute values of stresses are relatively small, failure is unlikely to occur in this area. The fact that all the cracks initiated at the vicinity of the interface corners (except at notch tips of Type B specimen) may be best explained using this hypothesis irrespective of adhesive types.

As r_P increases, r_Q decreases at first, then stops decreasing until the transition zone wholly overlaps the singular zone (Fig. 3.74). This is because, when the plastic zone emerges, the constraint at the wedge corner is released, resulting in a stress concentration decreasing and hence a smaller singular zone. Although the singular zone geometry change at this stage is not significant, it may still be very beneficial for plastic adhesives to bear higher loads because the stress concentration at the wedge corner is relatively low. However, after the plastic zone expands to a critical value, the singular zone size does not change at all until it disappears. It may be implied that the constraint of the wedge corner is holding at a certain level before the singular zone diminishes; that is, it is possible to use the elastic fracture criteria to predict this type of small yielding plastic layer failure. For the case of t=50 mm, in Fig. 3.35, the critical maximum plastic radius is 0.063 mm and the load at this time is ϵ_n=0.00035, beyond which no singular zone exists.

4.4. Failure Pattern of Adhesive Joint Iosipescu Specimen

4.4.1. Crack Initiation

Direct observation during mechanical testing or from the optical photographs (Figs. 3.58-3.61) indicated that cracks were initiated at the vicinity of the stress singular points. SEM examinations of the fractured surface further verified this assertion.

From Figs. 3.62 and 3.63, the fractured topography strongly implied that the crack started from a point on the line of adhesive-adherend interface intersecting the notch root plateau. Analytical and numerical investigations have already revealed that stresses along this line are very high. Although the stresses in reality could not possess infinite values along this line as mathematically suggested, it is certain that stresses at some points on this line could easily exceed the strength of the joint. Consequently, a crack was initiated. In the case of Type B specimen, the mechanism is the same when a crack was induced at a notch tip as a singular stress field existed there as well.

4.4.2. Crack Propagation

At the tip of a newly formed crack, a more severe stress singularity would drive the crack to propagate [44] if the energy accumulated at the crack tip was greater than that needed to generate new crack surfaces. The crack propagation process would temporarily stop when the strain energy at the tip became smaller than the critical energy release rate. This was caused by the dynamic effect of propagating cracks. In the load-displacement diagram, a kink would be observed. If the speed of consuming energy by the crack propagation was less than or equal to the rate of energy provision by external load, a crack would go all the way from one end to the other end; that is, no kink could be seen. Whether a crack would develop along only a single plane (Fig. 3.65) or step-wise surfaces (3.62--3.64) is determined by many factors, such as loading mode, void

volume percentage, adhesive type, and surface finish grade. Flexible adhesive has such a high critical energy release rate that cracks could not penetrate into it but would develop only along the interface since the adherend (aluminum) also has a higher fracture toughness than the interface. However, rigid adhesive joints showed various fracture profiles (Fig. 3.62--3.64). This may indicate that the interface strength is at the same level as the adhesive. The step-wise and secondary-crack-filled fracture surfaces (Fig. 3.63) of the rigid adhesive may suggest that damage mechanics should be employed to interpret correctly the fracture process of adhesive joint, which is beyond the scope of the present study but will be addressed in the future.

4.5. Optimization of Adhesive Joint Iosipescu Specimen

An optimized adhesive joint Iosipescu specimen, shown in Fig. 4.3, is proposed, based on the investigations on the asymptotic stress fields at bimaterial interface corners (in this presentation) and at sharp notches by Sukumar and Kumosa [72,74,108]. This geometry (Fig. 4.3) consists of both the sharp notch root (in the adhesive) and two bimaterial wedges (involving adhesive and adherend). Based upon Sukumar and Kumosa's work [72,74,108], under pure mode II loading, a critical re-entrant angle of 103° exists. That is, the stress singularities will disappear if the re-entrant angle of an isotropic sharp notch is greater than this critical value, 103°. Since the re-entrant angle of the notch in Fig. 4.3 is 105°, the notch root at Point B will be free of singular stresses. Furthermore, from simple geometric principles, the bimaterial wedge, Point A in Fig. 4.3, would take up a skewed interface angle of 127.5° according to the conventions in Fig. 3.45. That is, this angle is greater than the censorious value of 126° aforementioned. The asymptotic stress field will therefore never appear at the corner of the bimaterial wedges in Fig. 4.3, irrespective of the mechanical properties of the adhesive and adherend. In summary of the discussions in this paragraph, it can be concluded that the adhesive joint Iosipescu specimen proposed in Fig. 4.3 is capable of

introducing a uniform pure shear stress field within its adhesive layer from the standpoint of being free of stress singularities; that is, this geometry will be free of singular stresses both at the notch root and at bimaterial wedges, under pure mode II loading.

In a re-examination of the dimension of the notch root geometry of Type B specimen in Fig. 3.8b, it will be noticed that both Figs. 3.8b (or Fig. 3.23) and Fig. 4.3 look similar. As a matter of fact, they share exactly the same re-entrant angle of 105°. Therefore, the specimen in Fig. 3.23 should be the ideal specimen for adhesive joint testing.

However, finite element results in Figs. 3.9-3.11 showed that, for specimen B, the tensile stresses at the notch tip were singular and were concentrated at the bimaterial wedge corners under pure shearing loading condition. It appears that the numerical observations are against the prediction from asymptotic analysis. Further examination of the conditions of using Sukumar and Kumosa's finding [72,74,108] shows that there is no such contradiction between the FEM (Figs. 3.9-3.11) and asymptotic (Fig. 4.3) outcomes.

It was emphasized that under **pure mode II** loading conditions, the singularity would disappear when the re-entrant angle was greater than 103°. Incidentally, prescribed displacement boundary conditions were employed there [72,74]. In the FEM analysis in Section 3.1.3.1, force couple boundary conditions were used, which may not be able to force the loading condition into a pure shear since theoretically, from Iosipescu's proposal (Fig. 2.8), the pure shear mode only exists at the notch root axis.

If viewing the stress distributions along the notch edge (Fig. 4.4), one can see that there is no stress concentration at the interface corner. From the equivalent stress contours inside the adhesive layer of the optimized specimen under pure shear loading (Fig. 4.5), it can be seen that the maximum equivalent stress occurs a small distance away from the notch tip rather than at the notch tip or the bimaterial wedge corner; that is, no stress singularity exists for this specimen under pure mode II loading. In addition, the distributions of the degree of biaxial stress mode mixing inside the adhesive layer are

presented in Figs. 4.6a and b for different loading conditions. From these diagrams, it is evident that the biaxial stress state within the adhesive layer is fairly uniform under any loading condition, although it is expected that stress singularities will appear at the notch tip when the loading mode is not pure shear. Actually, the singular stress zone at the notch root is almost negligible in Figs. 4.7a, b and c, which are stress contours of Type B specimen from the FEM analysis in Section 3.1.3. From these figures, it can be said that along the notch root axis the stresses are fairly uniform, at least from the view point of practical engineering.

It should be noted that even if the notch tip stress singularity can be avoided by adjusting the loading angle, it is impossible to get such a loading condition in reality anyway. All of these analyses were conducted based on two-dimensional in-plane assumptions, if, more practically, three-dimensional effect [122-124] is taken into account, interface stress singularity inevitably exists at the orthogonal interface wedges. This will mathematically make it impossible to design an adhesive joint free of asymptotic behaviors.

From the above arguments, it is clear that, from the engineering point of view, the new geometry proposed in Fig. 4.1 is capable of generating a quite uniform biaxial stress state inside the adhesive layer. Taking into account the global stress analysis and experimental approaches, Specimen A in Figs. 3.6-3.8 will be another candidate to perform such a task. Specimen C is not a desired choice because of its strong singular behavior at its interface wedge corners.

A modified version of Fig. 4.1, produced by rounding off the sharp tip at the notch root into a small radius but keeping the skewed interface angle as it is, may improve the stress state at the notch root and therefore produces a more uniform stress state within the adhesives. Future work will be focused in this direction.

4.6. Difference Between Micro- and Macro-Mechanical Behavior

Although it was predicted that the optimized specimens of Type B should have a much higher strength compared with those of Type A and C, experimental results did not clearly show such an evidence. Rather, it was found that the joint strengths of all three types of adhesive joint Iosipescu specimens were not strongly affected by the adhesive types, notch root configurations, and adhesive layer thicknesses. Only the loading angle had a slight influence on the joint strength. This is becauset some significant differences exist between the micro- and macro-mechanical behavior at bimaterial wedge corners, which determines the ultimate strength of the adhesive joints.

The analytical or numerical models obviously are in a micro-scale since everything in the bimaterial wedge is assumed to be perfect (see Section 1.3.2), namely, ideally linear elastic materials, straight bondline, perfect interface, smooth notch edge surfaces, and in-plane mechanical behavior. However, the test specimens used in the experiments are in a macro-scale since, the bonding surface is not a perfectly straight line but a zig-zagged surface; there are always some invisible bulbs inside the adhesive layer; the notch edge surfaces are not ideally smooth, rather many micro-cracks and sharp notches exist and the materials that made up the wedge are not 100% elastic but present nonlinear behavior when the equivalent stress exceeds their yield strength. All of these factors make the real test specimen impossible to be accurately simulated by the models. That is, there is a gap between the micro- and macro-mechanical behavior at bimaterial wedge corners. How to fill this gap remains a great challenge in the future studies.

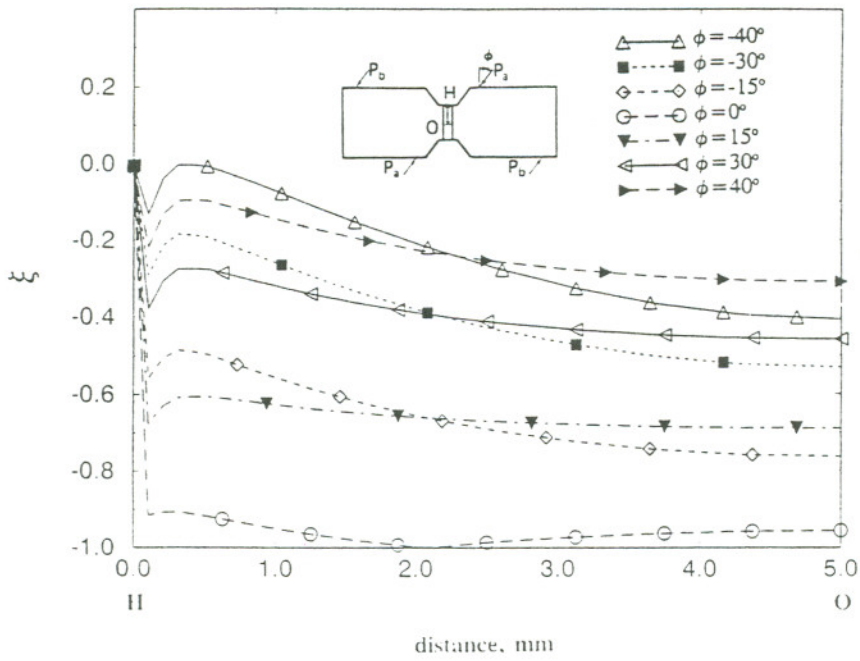

a) along the notch root axis (x=0)

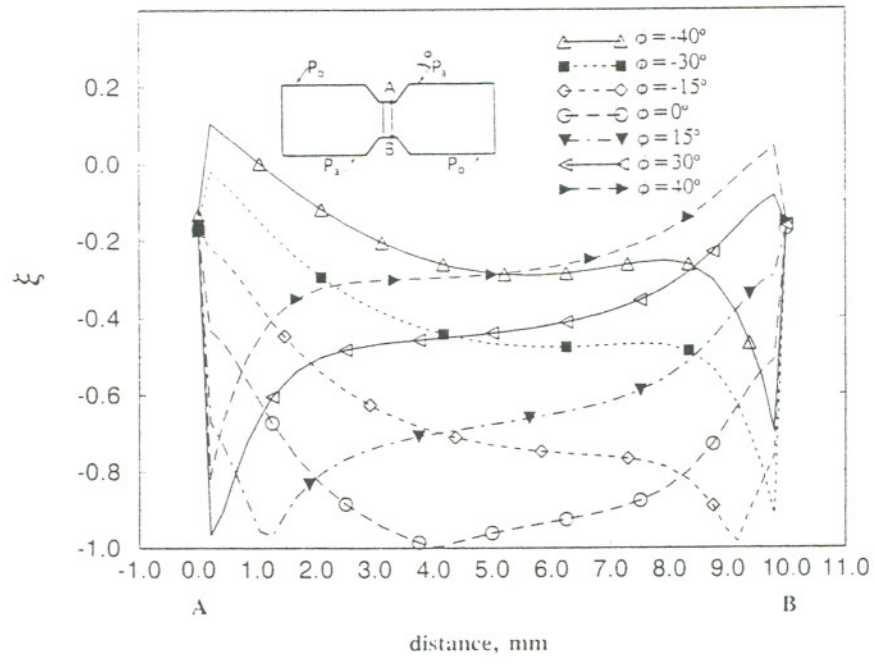

b) along the adhesive-adherend interface (x=0.5)

Fig. 4.1 Degree of biaxial stress mode mixing (Type A, t=1.0 mm)

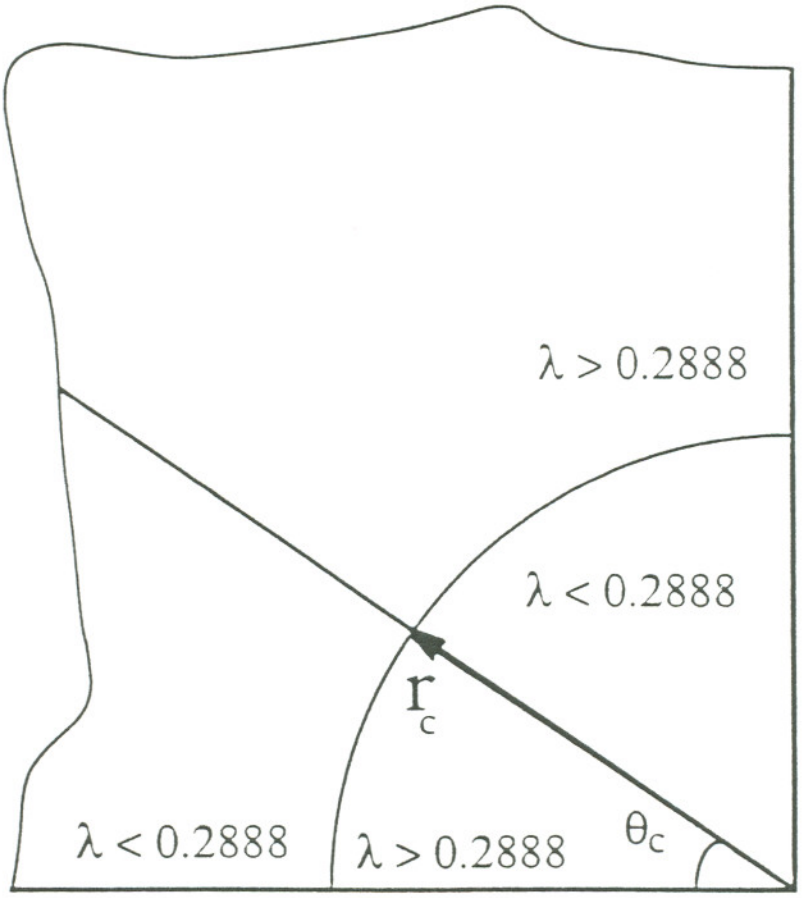

Fig. 4.2 λ distribution inside the plastic and transition zones (E=2632 MPa, ϵ_n=0.0003, t=50 mm, ν=0.35).

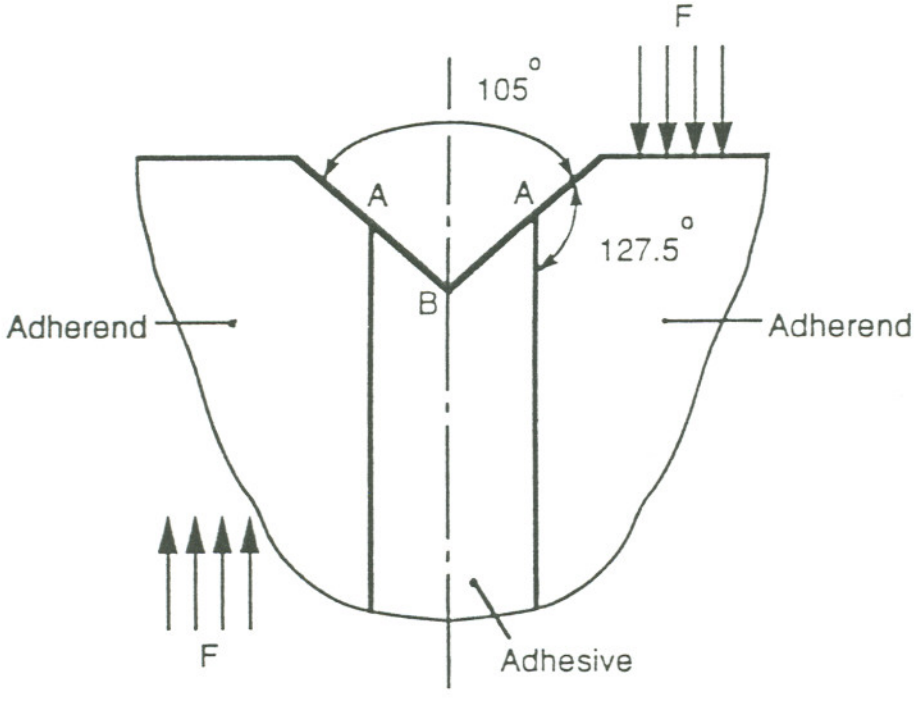

Fig. 4.3 Optimized root geometry of adhesive joint Iosipescu specimen.

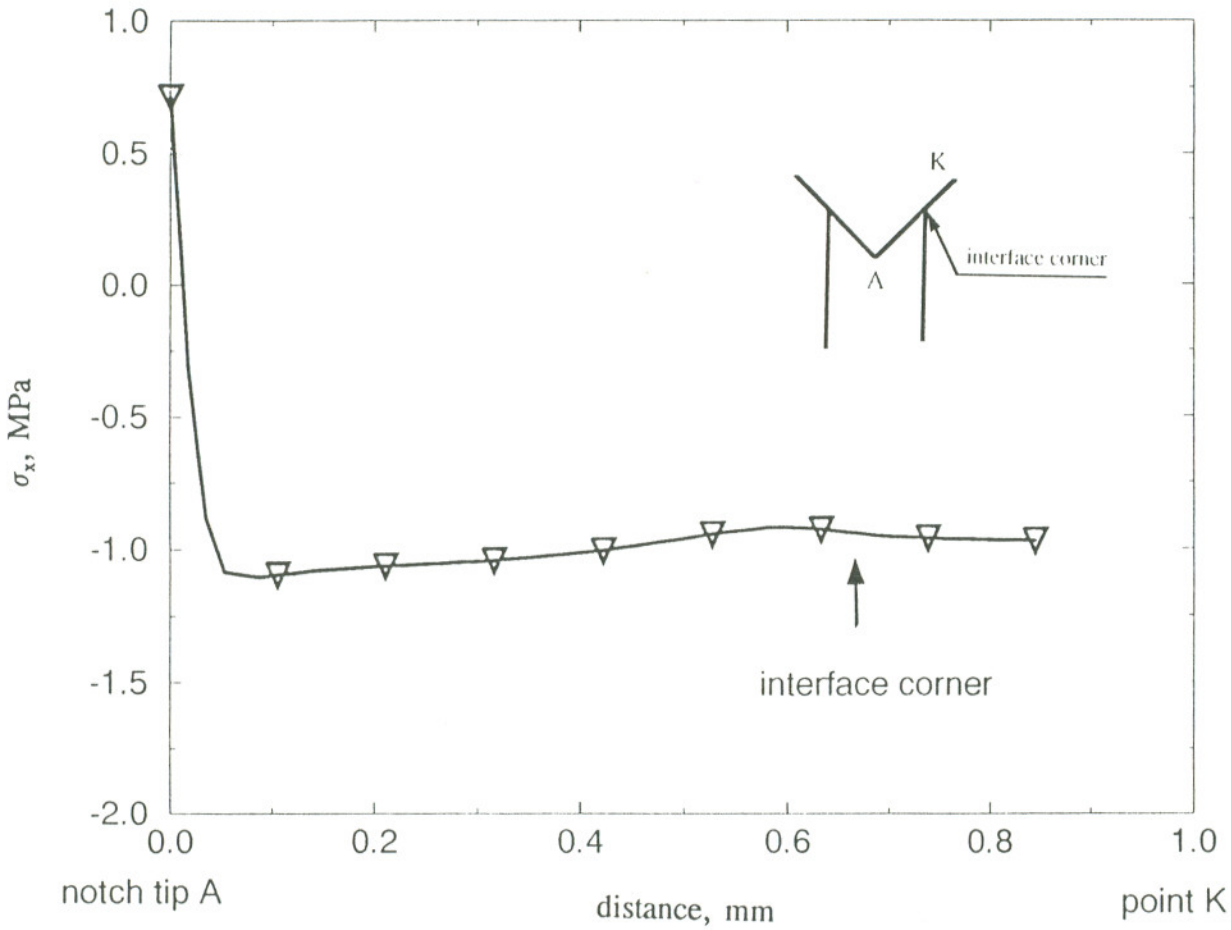

Fig. 4.4 Normal stress distribution along the notch edge (Type B, t=1.0 mm).

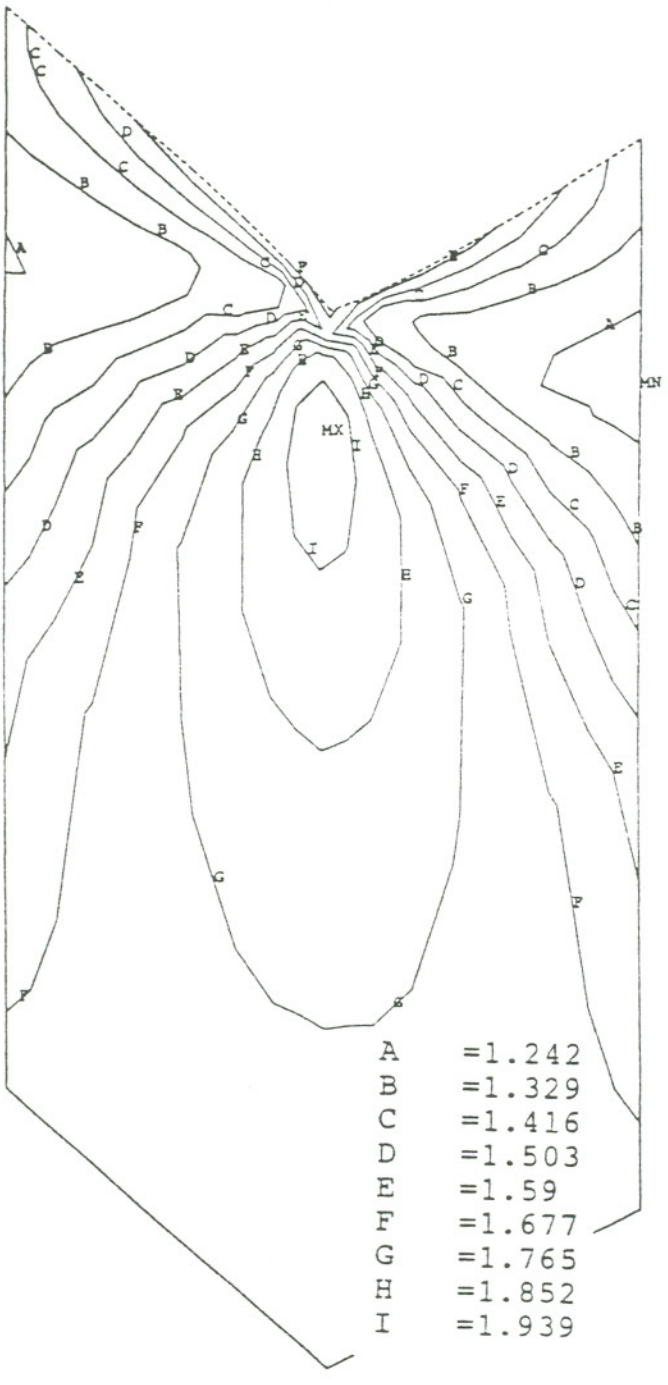

Fig. 4.5 Equivalent stress contours with the adhesive layer under pure shear loading condition (Type B, t=1.0 mm)

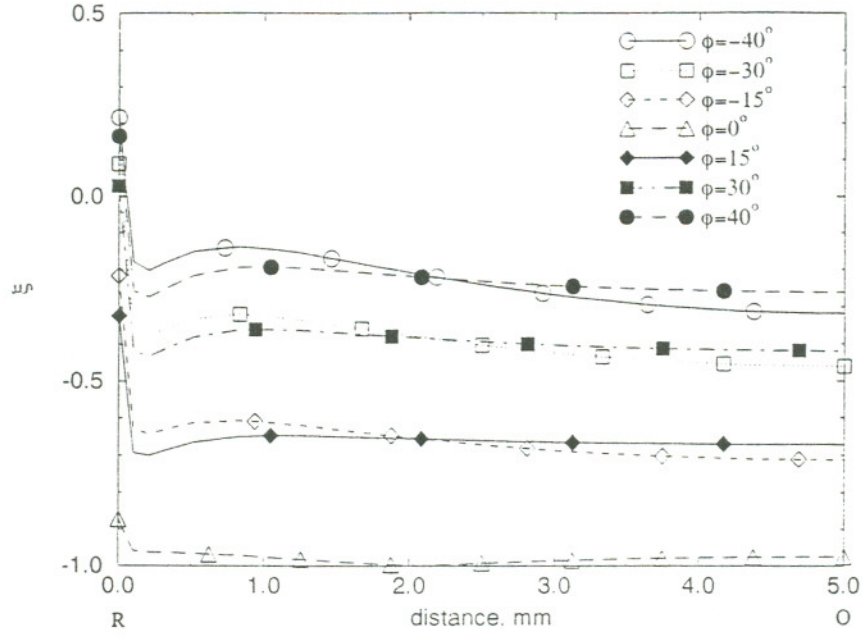

(a) along notch root axis

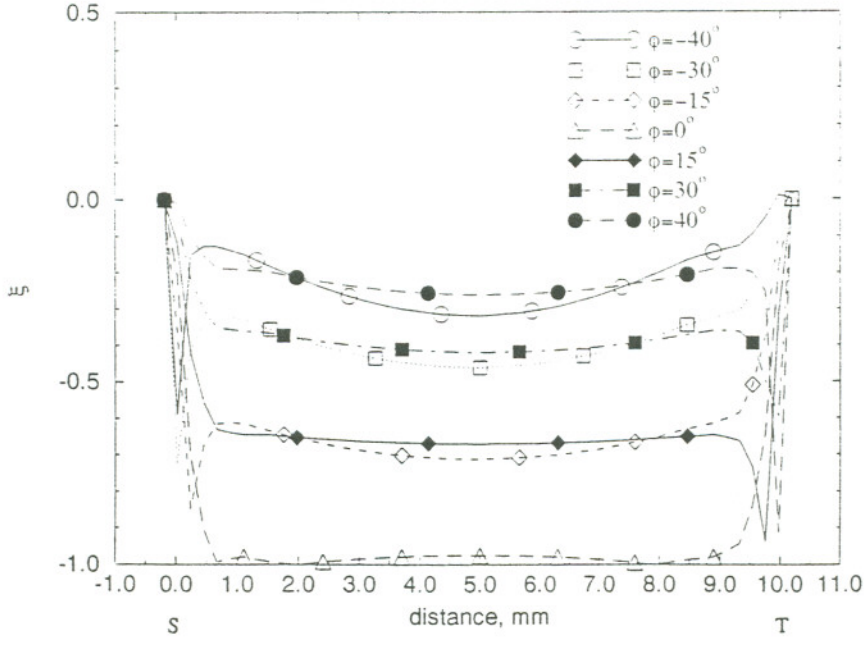

(b) along adhesive-adherend interface

Fig. 4.6 Degree of biaxial stress mode mixing inside the adhesive layer for the optimized specimen under different loading conditions (t=1.0 mm).

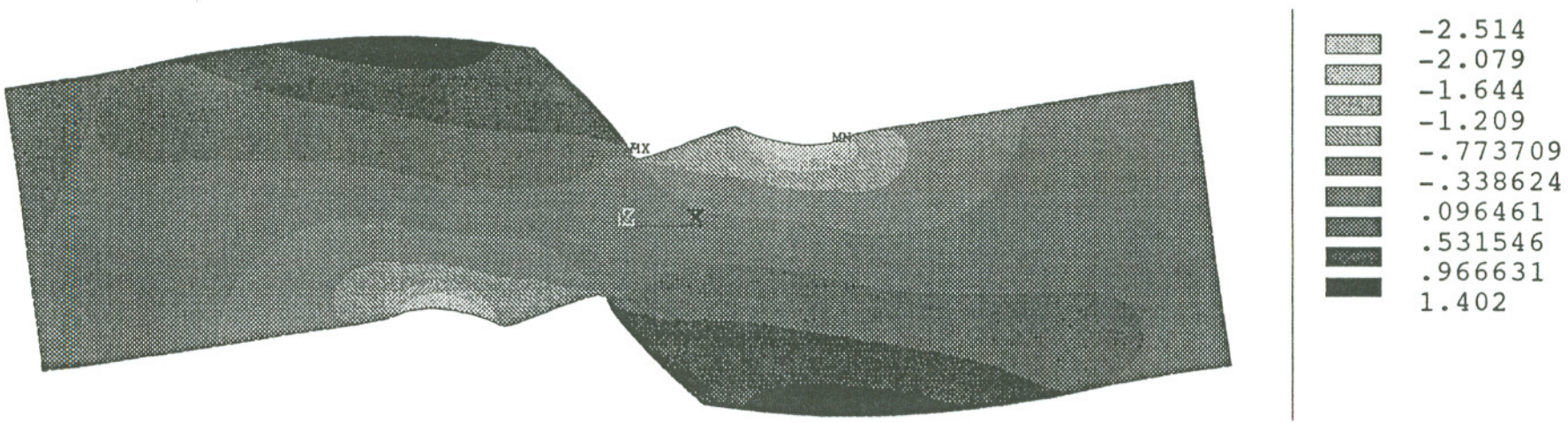

a) σ_x, MPa

Fig. 4.7 Stress contours under pure shear loading condition
(Type B specimen, t=1.0 mm).

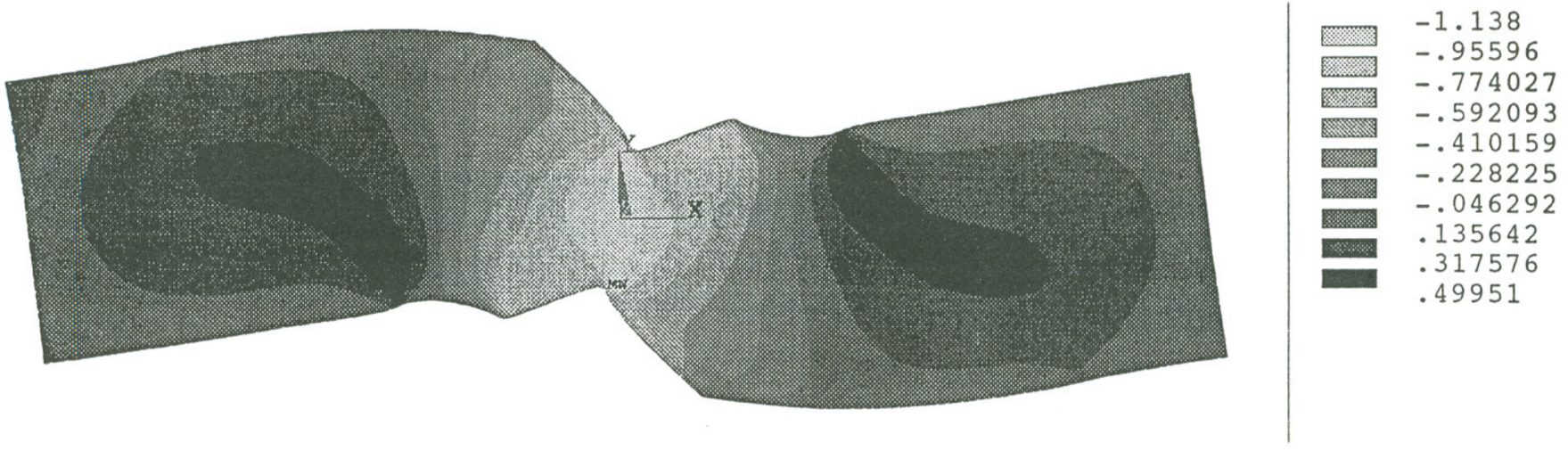

b) τ_{xy}, MPa

Fig. 4.7 (continued)

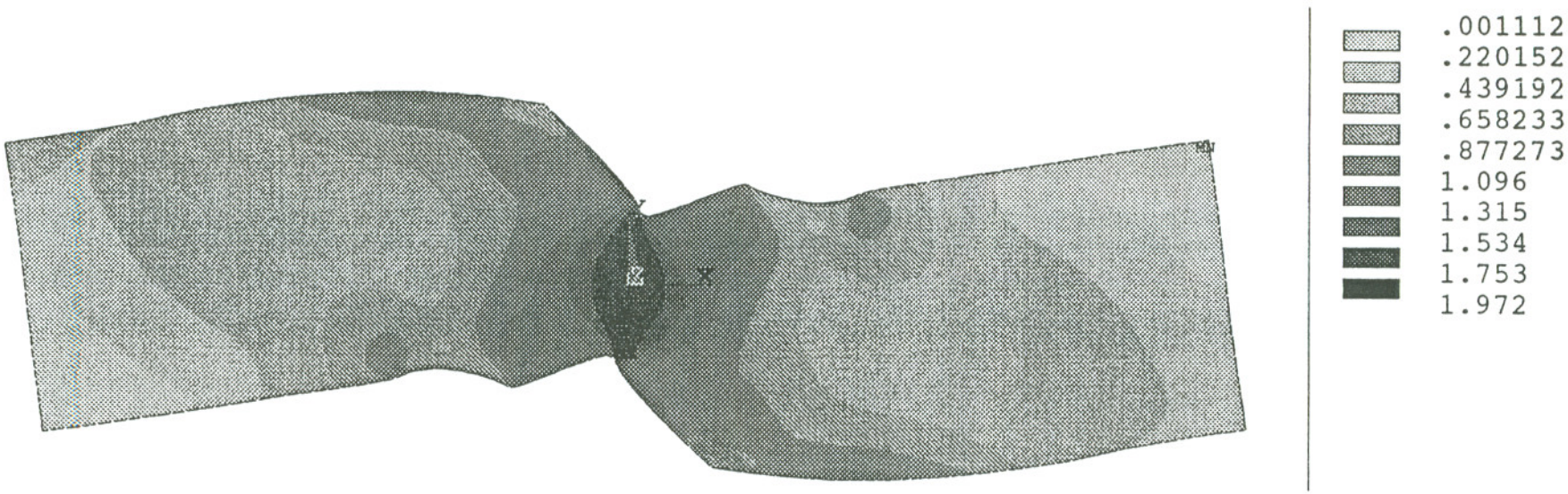

c) σ_e, MPa

Fig. 4.7 (continued)

CHAPTER 5
CONCLUSIONS

(1) A shear lag analysis of adhesive joints was conducted in a two-dimensional situation. The results can best be used to simulate fiber pull-out process in composite materials.

(2) The Airy stress function approach to the stress analysis inside the adhesive layers of adhesive joint Iosipescu specimens can yield fairly good results. It is the only closed form solution so far.

(3) A concept of degree of mode mixing of biaxial stresses has been proposed:

$$\xi = sign(\sigma_1\sigma_2)\frac{\min(|\sigma_1|,|\sigma_2|)}{\max(|\sigma_1|,|\sigma_2|)} \tag{5.1}$$

This formula has been found to be capable of characterizing the biaxial stress state very well.

(4) The singular stress zone geometry at a bimaterial wedge corner is a function of the mechanical properties of the materials, the wedge geometry, and the applied external loads. It can be numerically determined using the proposed criterion of degree of divergence by the FEM or semi-quantitatively estimated by the FEIM with a determined criterion. It is also found that the singular zone in the adherend (stiffer material) is always greater than that in the adhesive (softer material).

(5) The plastic zone geometry at a bimaterial wedge corner can be obtained by

$$r_P = \frac{1}{1-\lambda}\left(\frac{Q_e}{\sigma_y}\right)^{\frac{1}{\lambda}} \tag{5.2}$$

when the load is small. If the load is large, however, the plastic zone resembles the singular zone and should be determined numerically. A transition zone exists between the plastic and the singular zone. When the plastic zone is small, the stress field at the wedge corner can still be described by the elastic solutions. The singular stress field becomes smaller as the plastic zone grows larger. However, when the plastic zone is large enough, the stress field at the wedge corner cannot be said to obey a simple singular rule; rather, it is a more complicated stress field, and at this point, it can be said that the singular stress zone vanishes.

(6) Composite parameters α and β were obtained using simple Williams' Airy stress functions. It had also revealed that the singular behavior of a bimaterial wedge with a fixed geometry can be adequately described by the two independent parameters. Also, in practice, an adhesive joint composed of materials leading to a value of α approximately equal to zero is always desirable since it minimizes the strength of the singular stress field. The observation is very significant in that the eigenvalues will be the same if, for a fixed bimaterial wedge geometry, the material combinations yield the same pair of composite parameters irrespective of the mechanical properties of individual materials, since from a practical point of view it can be used to design experimental simulations for state-of-the-art materials by using relatively inexpensive materials that give rise to the same composite parameters.

(7) A universal critical skewed interface angle 126° has been discovered for a skewed bimaterial interface problem. If the skewed interface angle is greater than 126°,

the asymptotic stress field at the bimaterial wedge will totally disappear irrespective of the mechanical properties of the materials making up the wedge. This finding has corrected the conventional intuition that stresses are singular at any bimaterial wedge with any material combinations.

(8) An optimized adhesive joint Iosipescu specimen has been proposed. This specimen is free of any stress singularity under pure mode II loading conditions. It has also been found that the biaxial stress state inside the adhesive layer of this specimen is uniform. Therefore, this optimized specimen is idea for adhesive joint testing.

(9) Stress singular power at bimaterial wedges depends on, besides geometry, the material properties. The singular power generally increases when E_1/E_2 gets away from unity. The Poisson's ratio of the softer material influences the eigenvalues, but no noticeable change in the singular power can be observed when the Poisson's ratio of the stiffer material is varied. However, the Young's modulus ratio E_1/E_2 has a bigger impact on the variation of the eigenvalue than the Poisson's ratios.

(10) An orthotropic bimaterial wedge has been investigated. It has been observed that the orthotropic ratio of the materials appreciably affects the asymptotic field at the wedge corner.

(11) The FEM can be used to compute the eigenvalues only when the singular stress zone is big; otherwise, this method is unable to represent the asymptotic field accurately. In this case, the FEIM is the best alternative.

(12) The FEIM is an effective numerical scheme to extract bimaterial interface

singular power. However, the stress intensity factor Q can only be obtained by the FEM via the scheme invented in this presentation. Only in the simplest case, an elastic layer bonded to a rigid substrate, can the free edge stress intensity factor be analytically computed from Reedy's formula.

(13) Both the analytical and FEIM approaches are capable of determining the relative displacement eigenfunction solutions and the singular power λ for bimaterial wedge problems with an excellent degree of accuracy. However, only the FEM scheme is capable of extracting the absolute displacement eigenfunctions for generalized bimaterial problems.

(14) The FEIM convergence rate is found to be closely related to the elastic properties of the bonded materials. Specifically, convergence is slowest if E_1/E_2 approaches unity but increases when E_1/E_2 deviates from unity. However, the convergence rate doesn't change if the absolute value of $\log(E_1/E_2)$ is greater than one.

(15) From the global stress analyses, it has been observed that the newly proposed adhesive joint Iosipescu specimens are capable of producing a fairly uniform pure shear or biaxial stress state inside the adhesive layer. Among them, optimized Type B should be the first choice in conducting adhesive joint testing.

(16) From closed form and numerical analysis, the loading angles and adhesive layer thicknesses do not show significant effects on the uniformity of stress distributions inside the adhesive layer. But experimental results show that failure loads reach maximum at 15° loading angle for Specimen A and B with adhesive layer thickness of 1.0 mm. Further, for specimen Type A with adhesive layer thickness t=0.2 mm, both the first kink and rupture loads go up slightly as the loading angle is increased.

(17) The present experimental data do not clearly indicate any relationships between the joint strengths and the other testing parameters, namely, adhesive types, notch root configuration, and adhesive layer thicknesses. Although it seems that loading angle has a slightly effect on the strength. This is because the model used for the analysis is in a micro-scale while the specimens tested are actually in a macro-scale, which are not even close to the analytical model since micro-cracks and micro notches always exist at the notch root surfaces as well as the bonding line is not straight but zig-zagged. These micro-defects greatly influence the ultimate strength of the joints.

(18) Experimental analysis confirmed that cracks initiate their failure from interface corners or sharp notch tips due to the stress singularity. The crack would propagate in a peel-off or zig-zag pattern for rigid adhesive joints. In particular, the fracture topography is of a step-wise manner inside the adhesive layer. However, only the peel-off pattern can be seen for flexible adhesive joints.

(19) Future work should be directed to delicate experimental analyses by varying all influencing parameters, and finding the links between micro- and macro- models, complex stress singularities, and anisotropic adherends.

REFERENCES

1. Cage, C.U. *Adhesive Bonding Techniques and Applications*, McGraw-Hill, 1968.

2. Vinson, J.R. "Adhesive Bonding of Polymer Composites," *Polymer Eng. and Sci.*, Vol. 29, No. 19, 1989, pp. 1325-1331.

3. Hull, D. *An Introduction to Composite Materials*, Cambridge University Press, 1981.

4. Hu, S.M. "Stress-Related Problems in Silicon Technology," *J. Appl. Phys.*, Vol. 70, No. 6, 15 Sept. 1991, pp. R53-R80.

5. Chawla, K.K. *Composite Materials Science and Engineering*, Springer-Verlag, 1987.

6. Knesl, Z.; Sramek, A.; Kadourek, J. and Kroupa, F. "Stress Concentration at the Edges of Coatings on Tensile Specimens," *Acta Tech. CSAV* (Ceskoslovensk Akademie Ved), Vol. 36, No. 5, 1991, pp. 574-593.

7. Knesl, Z. and Kroupa, F. "Delamination Modes Determination at the Edge of a Bimaterial Wedge," *Int. Conf. on Mixed-Mode Fracture and Fatigue*, Vienna, Austria, July 15-17, 1991 (Oral only).

8. Reedy, E.D., Jr. "Intensity of the Stress Singularity at the Interface Corner Between a Bonded Elastic and Rigid Layer," *Eng. Fract. Mech.*, Vol. 36, No. 4, 1990, pp. 575-583.

9. Reedy, E.D., Jr. "Intensity of the Stress Singularity at the Interface Corner of a Bonded Elastic Layer Subjected to Shear" *Eng. Fract. Mech.*, Vol. 38, No. 4/5, 1991, pp. 273-281.

10. Gradin, P.A. "A Fracture Criterion for Edge-Bonded Bimaterial Bodies," *J. Compos. Mat.*, Vol. 16, Nov. 1982, pp. 448-456.

11. Lau, C.W. and Delale, F. "Interfacial Stress Singularities at Free Edge of Hybrid Metal Matrix Composites," *J. Eng. Mat. and Tech.*, Vol. 110, Jan. 1988, pp. 41-47.

12. Theocaris, P.S. "On the Singular Stress Field at a Multiwedge Corner" *Rev. Roum. Sci. Tech. - Mec. Appl.*, Tome, 23, No. 5, Bucarest, 1978, pp. 673-685.

13. Bogy, D.B. "Edge-Bonded Dissimilar Orthogonal Elastic Wedges Under Normal and Shear Loading," *J. Appl. Mech.*, Vol. 35, Sept. 1968, pp. 460-466.

14. Bogy, D.B. "Two Edge-Bonded Elastic Wedges of Different Materials and Wedge Angles Under Surface Tractions," *J. Appl. Mech.*, Vol. 38, June 1971, pp. 377-386.

15. Bogy, D.B. and Wang, K.C. "Stress Singularities at Interface Corners in Bonded Dissimilar Isotropic Elastic Materials," *Int. J. Solids Struct.*, Vol. 7, 1971, pp. 993-1005.

16. Kou, M.C. and Bogy, D.B. "Plane Solutions for Traction Problems on Orthotropic Unsymmetrical Wedges and Symmetrically Twinned Wedges," *J. Appl. Mech.*, Vol. 41, March 1974, pp. 203-208.

17. Hein, V.L. and Erdogan, F. "Stress Singularities in a Two-Material Wedge," *Int. J. Fract. Mech.*, Vol. 7, 1971, pp. 317-330.

18. Spilker, R.L. and Chou, S.C. "Edge Effects in Symmetric Composite Laminates: Importance of Satisfying the Traction-Free-Edge Condition," *J. Compos. Mat.*, Vol. 14, Jan. 1980, pp. 2-20.

19. Walsh, P.F. "The Computation of Stress Intensity Factors by a Special Finite Element Technique," *Int. J. Solids Struct.*, Vol. 7, 1971, pp. 1333-1342.

20. Barsoum, R.S. "Finite Element Solution of the Eigenvalue Problems Associated with the Fracture of Composites," *Proc. of the 4th Int. Conf. on Num. Methods in Fract. Mech.*, Eds. A.R. Luxmoore *et al.*, 1987, pp. 533-550.

21. Barsoum, R.S. "Asymptotic Fields in Adhesive Fracture," *J. Adhesion*, Vol. 29, 1989, pp. 149-166.

22. Szabo, B.A. "Mesh Design for the p-Version of the Finite Element Method," *Computer Method in Appl. Mech. and Eng.*, Vol. 55, 1986, pp. 181-197.

23. Raju, I.S. and Crews, J.H., Jr. "Interlaminar Stress Singularities at a Straight Free Edge in Composite Laminates," *Computers and Structures*, Vol. 14, No. 1-2, 1981, pp. 21-28.

24. Moriya, K. and Ichikawa, T. "A Study on Edge Protection Against Delamination for Composite Laminates (The Effects of Edge Shapes on Stress Singularities for Cross-Ply Laminates)," *JSME Int. J., Series I*, Vol. 31, No. 2, 1988, pp. 209-214.

25. Wang, S.S. and Choi, I. "Boundary-Layer Effects in Composite Laminates: Part 1 — Free-Edge Stress Singularities," *J. Appl. Mech.*, Vol. 49, Sept. 1982, pp. 541-548.

26. Zwiers, R.I.; Ting, T.C.T. and Spilker, R.L. "On the Logarithmic Singularity of Free-Edge Stress in Laminated Composites Under Uniform Extension," *J. Appl. Mech.*, Vol. 49, Sept. 1982, pp. 561-569.

27. Dunders, J. "Effect of Elastic Constants on Stress in a Composite Under Plane Deformation," *J. Compos. Mat.*, Vol. 1, 1967, pp. 310-322.

28. Gradin, P.A. and Groth, H.L. "A Fracture Criterion for Adhesive Joints in Terms of Material Induced Singularities," *Proc. of 3rd Int. Conf. on Num. Methods in Fract. Mech.*, March 26-30, 1984, pp. 711-720.

29. Groth, H.L. "A Method to Predict Fracture in an Adhesively Bonded Joint," *Int. J. Adhesion and Adhesives*, Vol. 5, No. 1, Jan. 1985, pp. 19-22.

30. Groth, H.L "Stress Singularities and Fracture at Interface Corners in Bonded Joints," *Int. J. Adhesion and Adhesives*, Vol. 8, No. 2, April 1988, pp. 107-113.

31. Tracey, D.M. "Analysis of Power Type Singularities Using Finite Elements," *Int. J. for Num. Methods in Eng.*, Vol. 11, 1977, pp. 1225-1233.

32. Whitcomb, J.D.; Raju, I.S. and Goree, J.G. "Reliability of the Finite Element Method for Calculating Free Edge Stresses in Composite Laminates," *Computers and Structures*, Vol. 15, No. 1, 1982, pp. 23-37.

33. Bazant, Z.P. and Estenssoro, L.F. "Surface Singularity and Crack Propagation," *Int. J. Solids Struct.*, Vol. 15, 1979, pp. 405-426.

34. Williams, M.L. "Stress Singularities Resulting From Various Boundary Conditions in Angular Corners of Plates in Extension," *J. Appl. Mech.*, Vol. 19, Dec. 1952, pp. 526-528.

35. Erdogan, F. "Stress Intensity Factors," *J Appl. Mech.*, Vol. 50, Dec. 1983, pp.

992-1002.

36. Timoshenko, S.P. and Goodier, J.N. *Theory of Elasticity*, 3rd edition, McGraw-Hill, 1987.

37. Vasilopoulos, D. "An Algorithm for the Eigenvalues of a Corner with Mixed Boundary Conditions," *Eng. Fract. Mech.*, Vol. 39, No. 6, 1991, pp. 977-1002.

38. Hart-Smith, L.J. "Adhesive-Bonded Double-Lap Joints," *Technical Report for National Aeronautics and Space Administration*, NASA CR112235, Jan. 1973.

39. Hart-Smith, L.J. "Adhesive-Bonded Single-Lap Joints," *Technical Report for National Aeronautics and Space Administration*, NASA CR112236, Jan. 1973.

40. Long, R.S. "Static Strength of Adhesively Bonded ARALL-1 Joints," *J Compos. Mat.*, Vol. 25, April 1991, pp. 391-415.

41. Lancaster, J.F. *Metallurgy of Welding*, 4th edition, Chapman & Hall, 1987, pp. 137-143.

42. Barsoum, R.S. and Chen, T.K. "Three-Dimensional Surface Singularity of an Interface Crack," *Int. J. of Fract.*, Vol. 50, 1991, pp. 221-237.

43. Groth, H.L. and Brottare, I. "Evaluation of Singular Intensity Factors in Elastic-Plastic Materials," *J. Testing and Evaluation*, Vol. 16, No. 3, 1988, pp. 291-297.

44. Broek, D. *Elementary Engineering Fracture Mechanics*, 3rd edition, Martinus Nijhoff Publishers, 1982.

45. Sih, G.C.; Paris, P.C. and Irwin, G.R. "On Cracks in Rectilinearly Anisotropic Bodies," *Int. J. Fract. Mech.*, Vol. 1, 1965, pp. 189-203.

46. Barsoum, R.S. "Cracks in Anisotropic Materials - An Iterative Solution of the Eigenvalue Problem," *Int. J. Fract.*, Vol. 32, 1986, pp. 59-67.

47. Cook, T.S. and Erdogan, F. "Stresses in Bonded Materials With a Crack Perpendicular to the Interface," *Int. J. Eng. Sci.*, Vol. 10, 1972, pp. 677-697.

48. Williams, M.L. "Stress Singularities, Adhesion, and Fracture," *Proc. of the 5th U.S. National Congress of Appl. Mech.*, Minnesota, June 14-17, 1966, pp.

451-464.

49. Ding, S; Meekisho, L. and Kumosa M. "Analysis of Stress Singular Fields at A Bimaterial Wedge," *Eng. Fract. Mech.*, Vol. 49, No. 4, 1994, pp. 569-585.

50. Akin, J.E. "The Generation of Elements with Singularities," *Int. J. Num. Meth. Engng.*, Vol. 10, 1976, pp. 1249-1259.

51. Stern, M. "Families of Consistent Conforming Elements With Singular Derivative Fields," *Int. J. Num. Meth. Engng.*, Vol. 14, 1979, pp. 409-421.

52. Henshell, R.D. and Shaw, K.G. "Crack Tip Finite Elements Are Unnecessary," *Int. J. Num. Meth. Engng.*, Vol. 9, 1975, pp. 495-507.

53. Barsoum, R.S. "On the Use of Isoparametric Finite Elements in Linear Fracture Mechanics," *Int. J. Num. Meth. Engng.*, Vol. 10, 1976, pp. 25-37.

54. Solecki, J.S. *Fracture Mechanics, A Revision 4.4 Tutorial*, Swanson Analysis Systems, Inc., May 1989, pp. 2.1-2.25.

55. PAFEC Ltd., *PAFEC 75 Theory and Results*, Thane Road, Lenton Industrial Estate West, Nottingham, England, 1976, pp. 3.29-3.29.

56. Groth, H.L. and Nordlund, P. "Shape Optimization of Bonded Joints," *Int. J. Adhesion and Adhesives*, Vol. 11, No. 4, Oct. 1991, pp. 204-212.

57. Hart-Smith, L.J. "Joints," *Engineering Materials Handbook: Composites*, ASM International 1987, Metals Park, Ohio 44073.

58. Liechti, K.M. and Liang, Y-M. "The Interfacial Fracture Characteristics of Bimaterial and Sandwich Blister Specimens," *Int. J. Fract.*, Vol. 55, 1992, pp. 95-114.

59. Matthews, F.L.; Kilty, P.F. and Godwin, E.W. "A Review of the Strength of Joints in Fibre-Reinforced Plastics: Part 2. Adhesively Bonded Joints," *Composites*, Vol. 13, Jan. 1982, pp. 29-37.

60. Kirchner, H.P.; Conway, J.C. Jr. and Segall A.E. "Effect of Joint Thickness and Residual Stresses on the Properties of Ceramic Adhesive Joints: I, Finite Element Analysis of Stresses in Joints," *J. Am. Ceram. Soc.*, Vol. 70, No. 2, 1987, pp. 104-109.

61. Zdaniewski, W.A.; Conway, J.C. Jr. and Kirchner, H.P.; "Effect of Joint Thickness and Residual Stresses on the Properties of Ceramic Adhesive Joints: II, Experimental Results," *J. Am. Ceram. Soc.*, Vol. 70, No. 2, 1987, pp. 110-118.

62. Ikegami, K. and Kamiya, K. "Effect of Flaws in the Adhering Interface on the Strength of Adhesive-Bonded Butt Joints," *J. Adhesion*, Vol. 14, 1982, pp. 1-17.

63. Kinloch, A.J. and Shaw, S.J. "The Fracture Resistance of a Toughened Epoxy Adhesive" *J. Adhesion*, Vol. 12, 1981, pp. 59-77.

64. Hattori, T.; Sakata, S.; Hatsuda, T. and Murakami, G. "A Stress Singularity Parameter Approach for Evaluating Adhesive Strength," J*SME Int. J., Series I*, Vol. 31, No. 4, 1988, pp. 718-723.

65. Anderson, G.P.; DeVries, K.L. and Sharon, G. "Evaluation of Tensile Tests for Adhesive Bonds," *Delamination and Debonding of Materials*, ASTM STP 876, Ed. Johnson, W.S., Am. Soc. for Testing and Mat., Philadelphia, 1985, pp. 115-134.

66. Adams, R.D. and Harris, J.A. "The Influence of Local Geometry on the Strength of Adhesive Joints" *Int. J. Adhesion and Adhesives*, Vol. 7, No. 2, Apr. 1987, pp. 69-80.

67. Liechti, K.M.; Freda, T. and Hayashi, T. "Determining the Constitutive and Fracture Properties of Structural Adhesives," *Adhesion Science Review, Proc. 5th Annual Program Review/Workshop*, The Virginia Tech Center for Adhesion Science, Eds. Brinson, H.F. *et al.*, 1987, pp. 199-222.

68. Grant, J.W. "Measurement of In-Situ Adhesive Deformation Properties," *Adhesion Science Review, Proc. 5th Annual Program Review/Workshop*, The Virginia Tech Center for Adhesion Science, Eds. Brinson, H.F. *et al.*, 1987, pp. 187-198.

69. Wysherley, G.W.; Mestan, S.A. and Grabovac, I. "A Method for Uniform Shear Stress-Strain Analysis of Adhesives," *J. of Testing and Evaluation*, Vol. 18, No. 3, May 1990, pp. 203-209.

70. Weissberg, J. and Arcan, M. "Uniform Pure Shear Testing Specimen for Adhesive Characterization," *Adhesively Bonded Joints, Analysis, and Design*, ASTM STP 981, Ed. Johnson, W.S., Am. Soc. Testing and Materials,

Philadelphia, 1988, pp. 28-38.

71. Erdogan, F. and Rizk, A.A. "Fracture of Coated Plates and Shells Under Thermal Shock" *Int. J. Fract.*, Vol. 53, 1992, pp. 159-185.

72. Sukumar, N. *Finite Element Analysis of Mixed Mode Fracture and Failure in Iosipescu Specimens*, Master's Thesis, Oregon Graduate Institute of Science & Technology, Oct. 1992.

73. Erdinc, I. *Singular Stress Fields at Interfaces and Sharp Notches*, Diplom-Thesis, Oregon Graduate Institute of Science & Technology, USA, and University of Paderborn, Germany, Aug. 1992.

74. Sukumar, N. and Kumosa, M. "Application of the Finite Element Iterative Method to Cracks and Sharp Notches in Orthotropic Media," *Int. J. Fract.*, Vol. 58, 1992, pp. 177-192.

75. Theocaris, P.S. "Complex Stress Intensity Factors Evaluated by Pseudocaustics," *Eng. Fract. Mech.*, Vol. 41, No. 5, 1992, pp. 707-720.

76. Dividson, D.L. "A High Resolution Technique for Determination Failure at Interfaces," *Adhesion Science Review, Proc. 5th Annual Program Review/Workshop*, The Virginia Tech Center for Adhesion Science, Eds. Brinson, H.F. *et al.*, 1987, pp. 293-303.

77. Weissberg, V. and Arcan, M. "Invariability of Singular Stress Fields in Adhesive Bonded Joints," *Int. J. Fract.*, Vol. 56, 1992, pp. 75-83.

78. Kumosa, M. *Mixed-Mode Failure Analysis of a Unidirectional Carbon/Epoxy Composite and Adhesively Bonded Composite Systems Using the Modified Iosipescu Test Method*, Dept. of Materials Sci. and Eng., Oregon Graduate Institute, a proposal to the NSF, submitted in Nov. 1990, awarded in July 1991.

79. Kumosa, M. *Mixed Mode Failure Analysis of Composite Materials and Adhesive Joints Subjected to Monotonic and Cyclic Biaxial Loadings*, Dept. of Materials Sci. and Eng., Oregon Graduate Institute, a proposal to the NSF, submitted in Dec. 1993, awarded in Oct. 1994.

80. Anderews, L.C. and Shivamoggi, B.K. *Integral Transforms for Engineers and Applied Mathematicians*, Macmillan Publishing Company, New York, 1988.

81. Dunders, J. "Discussion: Edge-Bonded Dissimilar Orthogonal Elastic Wedges Under Normal and Shear Loading," *J. Appl. Mech.*, Vol. 36, Sept. 1969, pp. 650-652.

82. Theocaris, P.S. *Polymers Properties and Applications*, Springer-Verlag, 1987.

83. Barsoum, R.S. "Theoretical Basis of the Finite Element Iterative Method for the Eigenvalue Problem in Stationary Cracks," *Int. J. Num. Methods Eng.*, Vol. 26, 1988, pp. 531-539.

84. Barsoum, R.S. "Application of the Finite Element Iterative Method for the Eigenvalue Problem in a Crack Between Dissimilar Media," *Int. J. Num. Methods Eng.*, Vol. 26, 1988, pp. 541-554.

85. Barsoum, R.S. "Convergence of the Finite Element Iterative Method for Elastic and Elastic-Plastic Singularity Problems," *Proc. of Int. Conf. on Computer Eng. Sci.*, Eds. S.N. Atluri and G. Yagawa, Vol. 1, Atlanta, GA, Apr. 1988, paper 14.

86. Barsoum, R.S. "The Finite Element Iterative Method - A General Approach to Boundary Value Problems in Fracture Mechanics," *Proc. of the 5th Int. Conf. on Numerical Methods in Fracture Mechanics*, Eds. A.R. Luxmoore and D.R.J. Owen, Freiburg, Germany, Apr. 1990, pp. 345-354.

87. Barsoum, R.S. "Singular Behavior near an Interface Crack Tip of Power Hardening Materials Using the Finite Element Iterative Method," *Int. J. Num. Methods. Eng.*, Vol. 29, 1990, pp. 699-717.

88. Barnes, J.A.; Kumosa, M. and Hull, D. "Theoretical and Experimental Evaluation of the Iosipescu Shear Test," *Compos. Sci. Tech.*, Vol. 28, 1987, pp. 251-268.

89. Kumosa, M. and Hull, D. "Mixed-Mode Fracture of Composites Using Iosipescu Shear Test," *Int. J. Fract.*, Vol. 35, 1987, pp. 83-102.

90. Broughton, W.R.; Kumosa, M. and Hull, D. "Analysis of the Iosipescu Shear Test as Applied to Unidirectional Carbon-Fibre Reinforced Composites," *Compos. Sci. Tech.*, Vol. 38, 1990, pp. 299-325.

91. Bansal, A. and Kumosa, M. "Experimental and Analytical Studies of Failure Modes in Iosipescu Specimens Under Biaxial Loading," *J. Composite Materials*,

No. 2, Feb. 1995, in press.

92. 3M Technical Data, *DP-100 Clear, DP-100 NS Translucent Epoxy Adhesives*, (3M Center, St. Paul, MN 55144-1000) June 1991.

93. 3M Introductory Data, *Structural Adhesives*, DP-100, (3M Center, St. Paul, MN 55144-1000) Jan. 1984.

94. 3M Introductory Data, *Structural Adhesives*, DP-190, (3M Center, St. Paul, MN 55144-1000) Jan. 1984.

95. Shields, J. *Adhesive Handbook*, Newnes-Butterworths, 1976.

96. ASTM, *Annual Book of ASTM Standards*, Vol. 15.06, 1985.

97. Grant, J.W. and Cooper, J.N. "Cone-and-Plate Shear Stress Adhesive Test," *J. Adhes.*, Vol. 21, 1987, pp. 155-167.

98. Arcan, M.; Hashin, Z. and Voloshin, A. "A Method to Produce Uniform Plate-Stress State with Applications to Fibre-Reinforced Materials," *Experimental Mechanics*, Vol. 18, 1978, pp. 141-146.

99. Banks-Sills, L.; Arcan, M. and Bortman, Y. "A Mixed-Mode Fracture Specimen for Mode II Dominant Deformation," *Eng. Fract. Mech.*, Vol. 20, No. 1, 1984, pp. 145-157.

100. Iosipescu, N. "New Accurate Procedure for Single Shear Testing of Metals," *J. Mater.*, Vol. 2, No. 1, 1967, pp. 537-566.

101. Adams, D.F. and Walrath, D.E. "Iosipescu Shear Properties of SMC Composite Materials," *in Composite Materials: Testing and Design (Sixth Conf.)*, ASTM STP 787, Ed. I.M. Daniel, 1982, pp. 19-33.

102. Walrath, D.E. and Adams, D.F. *Analysis of the Stress State in an Iosipescu Shear Test Specimen*, Report UWME-DR-301-102-1, Dept. of Mech. Eng., Univ. of Wyoming, Laramie, Wyoming, June 1983.

103. Walrath, D.E. and Adams, D.F. *Verification and Application of the Iosipescu Shear Test Method*, Report UWME-DR-401-103-1, Dept. of Mech. Eng., Univ. of Wyoming, Laramie, Wyoming, June 1984.

104. Walrath, D.E. and Adams, D.F. *Iosipescu Shear Properties of Graphite Fabric/Epoxy Composite Laminates*, Report UWME-DR-501-103-1, Dept. of Mech. Eng., Univ. of Wyoming, Laramie, Wyoming, June 1985.

105. Walrath, D.E. and Adams, D.F. "Current Status of the Iosipescu Shear Test Method," J. *Compos. Mater.*, Vol. 21, June 1987, pp. 494-507.

106. Walrath, D.E. and Adams, D.F. "Further Developments of the Iosipescu Shear Test Method," *Experimental Mech.*, Vol. 27, June 1987, pp. 113-119.

107. Broughton, W.R. *Shear Properties of Unidirectional Carbon Fibre Composites,* Ph.D. thesis, University of Cambridge, 1989.

108. Sukumar, N. and Kumosa, M. "Stress Singularities at Sharp Notches: Interpolation Formulas," *Int. J. Fract.*, Vol. 58, No. 3, Dec. 1992, pp. R45-R49.

109. Sukumar, N. and Kumosa, M. "Finite Element Analysis of Axial Splits in Composite Iosipescu Specimens," *Int. J. Fract.*, Vol. 62, No. 1, 1993, pp. 55-85.

110. Kumosa, M. "Biaxial Testing of Composites and Adhesive Joints Using the Biaxial Iosipescu Test Method," *Experimental Mech.*, in preparation, 1995.

111. Buchholz, F.-G.; Burger, M.; Kumosa, M. and Eggers, H. "Mixed-Mode Fracture Analysis of Orthotropic Laminates by Local and Global Energy Methods," *Proc. of the 5th Int. Conf. on Numerical Methods in Fracture Mechanics*, Freiburg, Germany, 1990, pp. 353-376.

112. Cox, H.L. "The Elasticity and Strength of Paper and Other Fibrous Materials," *British J. of Appl. Physics*, Vol. 3, 1952, pp. 72-79.

113. Holister, G.S. and Thomas, C. *Fibre Reinforced Materials*, Elsevier Publishing Co. Ltd., 1966.

114. Kumosa, M. private communication, Oregon Graduate Institute of Science & Technology, 1993.

115. Oakite Technical Data, *Product Profile (F.12379R5-486)*, Oakite Products, Inc., 50 Valley Road, Berkeley Heights, NJ, 1993.

116. Arfken, G. *Mathematical Methods for Physicists*, 3rd edition, Academic Press,

Inc., Harcourt Brace Jovanovich, Publishers, 1985.

117. Kreyszig, E. *Advanced Engineering Mathematics*, 6th edition, John Wiley & Sons, Inc., 1988.

118. Ding, S. and Kumosa, M. "Singular Stress Behavior at an Adhesive Interface Corner," *Eng. Fract. Mech.*, Vol. 47, No. 4, 1994, pp. 503-519.

119. Erdinc, I.; Ding, S.; Buchholz, F.-G. and Kumosa, M. "Stress Singularities at Sharp Notch Tips and Skewed Bimaterial Interface Wedges," *7th Int. Conf. on Mech. Behavior of Materials*, the Hague, Netherlands, May 28 - June 2, 1995, in press.

120. Ding, S.; Erdinc, I.; Buchholz, F.-G. and Kumosa, M. "Optimization of the Adhesive Joint Iosipescu Specimen for Pure Shear Test" *Int. J. Fract*, submitted, Mar. 1995.

121. Reedy, E.D., Jr. "Asymptotic Interface Corner Solutions for Butt Tensile Joints," *Int. J. Solids Structures*, Vol. 30, No. 6, 1993, pp. 767-777.

122. Wang, H.; Ding, S.; Buchholz, F.-G. and Rikards, R. "Delamination Analysis for 2D- and 3D-Models of a Cross-Ply Laminated Three-Point Bending Specimen," *Localized Damage III, Computer-Aided Assessment and Control*, Eds. M.H. Aliabadi, A. Carpinteri, S. Kalisky and D.J. Cartwright, Udine, Italy, June 21-23, 1994, pp. 251-258.

123. Ding, S.; Buchholz, F.-G., Bueger, M. and Kumosa, M. "Three-Dimensional Effects on Singularities along a Crack Front," *Int. J. Fract.*, to be submitted.

124. Ding, S.; Buchholz, F.-G., Bueger, M. and Kumosa, M. "3D-Effects on Strain Energy Release Rates, Stresses and Stress Singularities Adjacent to Crack Front Edges" *Int. Con. on Computational Eng. Sci. (ICES-95)*, Hawaii, 30 July - 3 Aug. 1995, accepted and in press.

VITA

The author was born to peasant parents, father Jincai Ding and mother Jinrong Hou, as their first son on the 19th of December, 1963, in Ding Gang, a small village in Henan Province, China. He enrolled in the Department of Mechanical Engineering of Xi'an Jiaotong University, Xi'an, Shaanxi, China, in the fall of 1979 and received his B.S. in 1983 and M.S. in 1986. He was awarded the Daxiue Chen Prize in 1985, a prestigious honor for postgraduate students demonstrating great potential in scientific research. He co-authored one paper and three scientific reports during this time.

After graduation, he joined the Central Research Institute of Building and Construction, Beijing, China, as an Assistant Research Engineer for two years and a Research Engineer until 1990. During this time, he co-authored three papers and many technical reports, co-held one patent, and was co-awarded twice for Scientific Researches and Developments by the Ministry of Metallurgical Industry, China.

The author came to the Oregon Graduate Institute of Science & Technology in the fall of 1990 and began to study composite materials and adhesively bonded composite systems in Dr. Kumosa's group. He spent seven months (10/93-04/94) in the Institute of Applied Mechanics, University of Paderborn, Germany, as a Guest Research Scientist to investigate delamination toughness of laminates and three-dimensional effects on crack front singularities. He has co-authored nine papers based on his graduate research work during the last four years and expects to write at least two more from this work (dissertation).

He married Xiaoyan Zhang in 1989. The happy couple had a son, Anton Z. Ding, on the 3rd of August, 1994. Most of this dissertation was written in the "musical" atmosphere generated by Anton.

The author hopes to find a position in which to continue his research.